

# Identical Emitters, Collective Effects and Dissipation in Quantum Optics

Novel numerical approaches for quantum master equations

vorgelegt von  
M.Sc. Michael Gegg  
geb. in München

von der Fakultät II – Mathematik und Naturwissenschaften  
der Technischen Universität Berlin  
zur Erlangung des akademischen Grades  
Doktor der Naturwissenschaften  
– Dr.rer.nat. –

genehmigte Dissertation

## Promotionsausschuss:

Vorsitzender: Prof. Dr. Thomas Möller  
Gutachter: Prof. Dr. Andreas Knorr  
Gutachter: Prof. Dr. Jan Wiersig  
Gutachter: Dr. Marten Richter

Tag der wissenschaftlichen Aussprache: 6. Oktober 2017

Berlin 2017



---

## Abstract

In this thesis a formalism for indistinguishable multi-level quantum emitters in quantum master equations is developed. The complexity of the approach scales only polynomially in the number of quantum emitters. Complexity here means the number of coupled equations or rather the dimension of the Liouville space. This approach opens new possibilities for calculating open quantum systems. The method is implemented in the PsiQuaSP library, which allows to setup and solve arbitrary master equations, in particular master equations with the reduced polynomial scaling. The introduced tools are utilized to study subradiance in the open Dicke model and various cQED lasers.

One of the main current research goals in quantum optics and quantum information science is the generation and stabilization of quantum coherence between distinct quantum systems. These systems can for instance be photons or quantum emitters, qubits. From a theoretical stance the difficulty with these systems is that their complexity scales in general exponentially with the system size, like the number of quantum emitters. The reduced scaling of the formalism introduced in this thesis stems from the permutation symmetry of the indistinguishable emitters. The method is derived in the context of Lindblad quantum master equations. Lindblad quantum master equations for many identical multi-level systems have been used to study fundamental quantum optical systems, such as lasing and laser like action, various phase transitions, optical bistability, cooperative resonance fluorescence, entanglement, quantum light generation, quantum to classical transitions, super- and subradiance etc. In most of these cases the single emitter, the many emitter and the weak correlation limit can be satisfactorily treated with existing techniques, such as direct integration, phase space methods or cluster expansion. However these techniques are not well suited for the few emitter case with strong correlations. The theory developed in this thesis allows to study all these systems for moderate numbers of quantum emitters and arbitrary correlation strengths, thus filling the gap left open by conventional methods. Even though the theory is developed around Lindblad quantum master equations it is not limited to this case – the requirement of indistinguishability is used to construct symmetrized Liouville space basis states and operators which can also be used to construct other master equations.

In this thesis the general methodology for the polynomial scaling of the many emitter master equation is derived by two different approaches. Generalized permutation symmetric Liouville space states and operators are introduced that allow for the construction of arbitrary master equations and observables. These Liouville space states and operators are translated into a graphical representation that greatly facilitates their usage. This representation is found to have a close connection to Lie algebras as well as graph theory. The whole method is implemented in a general and modular way in a C++ library called PsiQuaSP, which allows to simulate arbitrary master equations based on a number state representation. The design of the library heavily relies on the introduced graphical representation, which greatly facilitates the setup of a simulation. The treatment of non-identical systems with PsiQuaSP is illustrated and further techniques for complexity reduction and computational speedup are discussed. These tools are applied to the two main cases of cQED lasers/spasers and super-, subradiance. In the latter case a new type of phase transition in the open Dicke model is predicted that leads to a deterministic generation of subradiant steady state coherences, with applications in quantum information science. Furthermore the interaction of quantum dots with the dissipative modes at metal interfaces is investigated in order to explain experimental findings.



## Zusammenfassung

In dieser Arbeit wird ein Formalismus für ununterscheidbare Multi-Niveau Quantenemitter in Quanten Mastergleichungen entwickelt. Die Komplexität dieses Ansatzes skaliert nur polynomiell und nicht exponentiell in der Anzahl der Emitter. Komplexität bedeutet hier die Anzahl der gekoppelten Gleichungen bzw. die Dimension des Liouville Raumes. Dieser Ansatz erlaubt neuartige Betrachtungen in offenen, quantenoptischen Systemen. Die Methode wurde in der PsiQuaSP Programmbibliothek implementiert. Diese erlaubt es generelle Quanten-Mastergleichungen numerisch zu lösen, insbesondere Mastergleichungen mit der reduzierten polynomiellen Skalierung. Mit Hilfe der eingeführten Methoden werden Subradianz im offenen Dicke Modell und verschiedene cQED Laser untersucht.

Eines der zentralen, aktuellen Forschungsziele in der Quantenoptik und der Quanteninformations Technologie ist die Generierung und Stabilisierung von Quantenkorrelationen zwischen unterschiedlichen Quantensystemen. Beispiele für solche Quantensysteme sind Photonen oder Quantenemitter, Qubits. Aus theoretischer Sicht liegt die Schwierigkeit mit diesen Systemen in der Tatsache, dass im Allgemeinen ihre Komplexität exponentiell mit der Systemgröße, wie etwa der Anzahl der Quantenemitter, skaliert. Die Reduzierung der Komplexität in dem hier eingeführten Formalismus resultiert aus der Vertauschungssymmetrie der ununterscheidbaren Emitter. Die Methode wird im Kontext von Lindblad Quanten-Mastergleichungen entwickelt. Lindblad Quanten-Mastergleichungen für identische Multi-Niveau Systeme werden verwendet um fundamentale quantenoptische Systeme zu untersuchen, wie etwa Lasing und laserartiges Verhalten, verschiedene Phasenübergänge, optische Bistabilität, Kooperative Resonanzfluoreszenz, Verschränkung, Quantenlicht, Übergang von der Quanten- zur klassischen Physik und Super-, Subradianz. In den meisten dieser Fälle können die Grenzfälle von einzelnen Emittern, vielen Emittern und schwachen Korrelationen mit bestehenden Methoden zufriedenstellend gelöst werden. Diese Methoden sind etwa direkte Integration, Phasenraummethoden oder Cluster Entwicklung. Diese Methoden sind jedoch nicht geeignet für den Fall von mittleren Emitter-Anzahlen mit starken Korrelationen. Der hier entwickelte Formalismus erlaubt es all diese Systeme mit mittleren Emitter-Anzahlen und beliebigen Korrelationsstärken zu berechnen. Somit füllt der Formalismus die Lücke welche von herkömmlichen Methoden zurückgelassen wird.

In dieser Arbeit wird der Formalismus anhand von zwei verschiedenen Betrachtungsweisen entwickelt. Generelle Liouville Raum Operatoren und symmetrisierte Liouville Raum Basiszustände werden eingeführt mit denen beliebige Mastergleichungen und Observablen konstruiert werden können. Diese Zustände und Operatoren werden in eine graphische Darstellung übersetzt welche die Benutzung stark vereinfacht. Die graphische Darstellung hat Verknüpfungen zu Lie Algebren und der Graphentheorie. Der gesamte Formalismus ist in der Bibliothek PsiQuaSP implementiert, welche Simulationsrechnungen für beliebige Mastergleichungen auf Basis von Nummernzuständen erlaubt. Die Bibliothek basiert auf der graphischen Darstellung, was das Implementieren von Simulationen stark vereinfacht. Des weiteren werden die Behandlung von nicht-identischen Emittern in PsiQuaSP sowie zusätzliche Methoden zur Reduzierung der Komplexität vorgestellt. Der Formalismus und die Bibliothek werden auf die zwei Gebiete cQED Laser und Super-, Subradianz angewendet. Im letzteren Fall wird ein neuartiger Phasenübergang im offenen Dicke Modell vorhergesagt, der zur Ausbildung von subradianten Kohärenzen im stationären Zustand führt.

Des weiteren wird die Wechselwirkung von einzelnen Quantenpunkten mit den dissipativen optischen Moden an Metallgrenzflächen untersucht um experimentelle Befunde zu erklären.



## Contents

<b>1</b>	<b>Introduction</b>	<b>1</b>
<b>I</b>	<b>Theoretical Background</b>	<b>5</b>
<b>2</b>	<b>Model systems</b>	<b>7</b>
2.1	Quantum emitters . . . . .	8
2.1.1	Two-level Systems . . . . .	8
2.1.2	Three and more levels . . . . .	10
2.2	Electromagnetic modes in quantum optics . . . . .	11
2.2.1	Electromagnetic modes in vacuum . . . . .	11
2.2.2	Dissipative modes – Quantum optics in media . . . . .	12
<b>3</b>	<b>Open system dynamics</b>	<b>15</b>
3.1	Density matrix . . . . .	15
3.2	Closed quantum systems - von Neumann equation . . . . .	16
3.3	Open quantum systems - Lindblad equation . . . . .	17
3.4	Steady states and the Liouvillian spectrum . . . . .	19
<b>II</b>	<b>Formalism</b>	<b>21</b>
<b>4</b>	<b>Many emitters – Complex quantum systems</b>	<b>23</b>
4.1	Identical two-level emitters . . . . .	24
4.1.1	The product state basis . . . . .	25
4.1.2	The Dicke basis . . . . .	25

4.2	Identical multi-level systems . . . . .	28
4.2.1	Product state basis . . . . .	29
4.2.2	The Lie algebras $su(d)$ . . . . .	30
4.2.3	Dicke states for multi-level systems – $su(d)$ multiplets . . . . .	31
4.3	Conclusion . . . . .	32
<b>5</b>	<b>Permutation symmetry in quantum master equations</b>	<b>33</b>
5.1	Symmetries, size and averages . . . . .	33
5.2	Dissipation vs. symmetry . . . . .	35
5.3	Time evolution of identical multi-level systems . . . . .	37
5.3.1	Time evolution of a simple master equation . . . . .	37
5.3.2	Time evolution – Simplification . . . . .	38
5.3.3	Preventing numerical instability . . . . .	41
5.3.4	Open Dicke model equations of motion . . . . .	43
5.4	Multi-level systems . . . . .	45
5.4.1	Three-level systems . . . . .	45
5.4.2	Multi-level systems . . . . .	47
5.4.3	Two-, three- and four-level laser examples . . . . .	49
5.5	Symmetrized eigenstates of permutation symmetric Liouville space operators . . . . .	54
5.5.1	Permutation symmetric Liouville space operators – Elementary sketches . . . . .	55
5.5.2	Building physically meaningful Liouville space operators . . . . .	56
5.5.3	Lie algebra context . . . . .	58
5.6	Recovering the Dicke states – How to diagonalize the density matrix . . . . .	59
5.7	Conclusion . . . . .	60
<b>A</b>	<b>The PsiQuaSP Library</b>	<b>61</b>
A.1	Using PsiQuaSP – Basic structure of the library . . . . .	62
A.2	Examples . . . . .	63
A.2.1	Example 1: Open Tavis-Cummings relaxation . . . . .	63
A.2.2	Example 2: Three-level systems . . . . .	67
A.3	Template functions versus custom Liouvillians . . . . .	70
A.4	Building arbitrary Liouvillians . . . . .	71
A.5	Performance . . . . .	75
A.6	Some notes on solvers . . . . .	76
A.6.1	Krylov subspaces . . . . .	76
A.6.2	Spectral transformation . . . . .	77
A.7	Conclusion . . . . .	78
<b>III</b>	<b>Results</b>	<b>79</b>
<b>6</b>	<b>Cavity QED Lasers and Spasers</b>	<b>81</b>
6.1	Cluster expansion – Rate equation theory . . . . .	83
6.2	Two-level lasers . . . . .	85
6.3	Three- and Four-level bad cavity lasers – Spasers . . . . .	87
6.4	Conclusion . . . . .	90

<b>7</b>	<b>The open Dicke model</b>	<b>91</b>
7.1	Dicke model physics . . . . .	93
7.2	Bistable effects in quantum optics . . . . .	94
7.3	Superradiant to subradiant phase transition . . . . .	98
7.3.1	Collectivity measure . . . . .	99
7.3.2	Nature of the phase transition . . . . .	100
7.3.3	Robustness test and entanglement properties . . . . .	104
7.4	Dark state cascades . . . . .	105
7.5	Conclusion . . . . .	107
<b>8</b>	<b>Quantum dots on a thin metal film</b>	<b>109</b>
8.1	Spectral response . . . . .	111
8.2	Modeling the surface roughness . . . . .	112
8.3	Conclusion . . . . .	116
<b>9</b>	<b>Further usages of PsiQuaSP</b>	<b>117</b>
9.1	Nonidentical systems . . . . .	117
9.2	Graph theory based optimization . . . . .	119
9.2.1	Graph theory and partitioning in a nutshell . . . . .	119
9.2.2	Reduction of degrees of freedom . . . . .	121
9.3	Conclusion . . . . .	124
<b>IV</b>	<b>Epilogue</b>	<b>125</b>
<b>10</b>	<b>Summary and Outlook</b>	<b>127</b>
<b>11</b>	<b>Acknowledgements</b>	<b>129</b>
<b>B</b>	<b>Properties of the symmetrized Liouville space basis</b>	<b>131</b>
B.1	Scaling . . . . .	131
B.2	Properties of the symmetrized Liouville space basis states . . . . .	132
B.3	Permutation symmetric Liouville space operators $\Gamma$ . . . . .	135
B.4	Block diagonal representation of the density matrix in $su(d)$ multiplets . . . . .	136
B.4.1	Two-level systems . . . . .	136
B.4.2	Multi-level systems . . . . .	138
<b>C</b>	<b>Spin squeezing inequalities</b>	<b>143</b>
C.1	General remarks . . . . .	144
C.2	Definitions and necessary inequalities . . . . .	145
C.3	Proofs . . . . .	147
C.4	Comments . . . . .	148
C.5	Different representation . . . . .	149
<b>D</b>	<b>Equations of motion for the laser examples</b>	<b>151</b>
D.1	Three-level systems . . . . .	151
D.2	Four-level systems . . . . .	154
<b>E</b>	<b>Possible Dissipators</b>	<b>157</b>
	<b>Bibliography</b>	<b>159</b>



# 1 Introduction

The research quest of non-relativistic quantum theory can be regarded as having roughly three categories. The microscopic descriptions of single, elementary entities are the first category: The hydrogen atom, the photon or perhaps for quantum optics the Jaynes-Cummings model [1]. These problems were historically the first to be investigated – they are relatively simple, provide the theoretical footing for a manifold of phenomena and laid the foundation for the success of quantum physics. Second the research focus was widened to collections of (infinitely) many such elementary entities, structured in an very symmetric way. One example is solid state physics, where perfectly identical atoms are placed in perfectly symmetric Bravais lattices<sup>1</sup>. This allows to reduce the problem of an interacting many particle system to the study of a single unit cell – reducing it to a few particle system. For quantum optics the related fields and techniques are Glauber’s photonic and Arecchi’s atomic coherent states [2, 3], the related phase space formulation of quantum optics like the positive P representation and the whole notion of quantum to classical transition in quantum optics [4, 5, 6]. These techniques describe large quantum optics setups – many atoms and large photon numbers. In general these theories and concepts of this second category aim to explain our macroscopic world from a microscopic quantum viewpoint. However in order to be able to describe large quantum systems the requirement of symmetry and large size is crucial: These requirements are used to reduce the exponential complexity of interacting quantum systems to something manageable.

Third, after the micro and the macro limits have been established we are now faced with the challenge of the world in between: Mesoscopic systems are now at the focus of attention since micro- and nanofabrication tools have made tremendous progress and have opened a world of size dependent physics. Omitting the limits invented for well ordered macro objects requires new

---

<sup>1</sup>There is also disorder in solid state physics, but this disorder is usually treated as a perturbation, thus a small deviation from the symmetric case.

methodologies. At first sight when dealing with a mesoscopic interacting quantum system we are left with the exponentially scaling Hilbert space. This limits full, straightforward modeling of interacting  $N$  body problems to very small numbers  $N$ .

However progress has been made in various directions: DMRG and other matrix product state based methods [7, 8], correlation and cluster expansion, mean field theory [9], perturbative methods [10, 11], etc. and sometimes exactly solvable toy models [10, 12]. These methods each harvest specialized symmetries, facilitating properties and/or use truncation in order to bypass solving a system of exponential complexity. Almost all these methods are numerical recipes, heavily relying on the power of modern computers.

A mesoscopic quantum optical system may consist of a set of quantum emitters coupled to quantized and/or classical radiation modes. In these systems not only the problem of an exponential Hilbert space needs to be addressed but also system bath interaction is generally important [13]. Thus an open system description is needed which further complicates the mathematical problem. The methods commonly used in the field may solve these systems in certain limits – most prominently the weak correlation and large system size limits [4, 6, 9]. However for quantum optical systems with moderate emitter numbers and strong correlations these approaches are not suitable. Since quantum correlations are believed to be essentially important in exactly this few particle limit [14] a method for investigating strong correlations in few particle open quantum systems is highly desirable.

In this thesis an exact formalism for indistinguishable quantum emitters is developed that fills the gap between the large and the small system size limits and works up to arbitrary correlation strengths. The formalism utilizes the permutation symmetry induced by the indistinguishability of the emitters and is formulated in a Lindblad quantum master equation context. This treatment reduces the exponential complexity of the interacting many emitter setup to a polynomial complexity, thus greatly enhancing the application range of numerical treatments in these systems.

In quantum optics Lindblad quantum master equations for setups involving many quantum emitters have been studied in a vast number of different contexts, such as lasing and laser like action [15, 16, 17], various phase transitions [18, 19, 20], optical bistability [21], cooperative resonance fluorescence [19], entanglement [22], quantum light generation [23, 24], quantum to classical transitions [5], super- and subradiance etc [16, 5, 25]. The presented formalism allows to treat all these phenomena on an equal theoretical footing and is especially advantageous over existing techniques in the few particle and strong correlation limit.

The formalism is derived by directly investigating the equations of motion and is then reformulated using symmetrized Liouville space basis states and elementary operators acting on these basis states. This allows for maximal flexibility in the construction of master equations to fully harvest all the possibilities of this formalism. This treatment in principle also allows for open system formulations other than the Born-Markov approximation in the Lindblad equation. One of the main features in the present discussion is the translation of these Liouville space states and operators into a graphical representation that greatly facilitates the usage. The resulting sketches are found to have close connections to the Lie algebras  $su(N)$  and graph theory. The whole method is implemented in a general and modular way in a C++ library called PsiQuaSP, which allows to simulate arbitrary master equations based on a number state representation, especially those involving indistinguishable quantum emitters. PsiQuaSP is an acronym for *Permutation symmetry for identical Quantum Systems Package* and the library has been made publicly available [26, 27].

The method and the library are applied to the two main cases of cQED lasers and super-/subradiance. In the latter case a new type of phase transition is predicted that leads to a deterministic generation of dark states through cavity assisted coherences. Additional symmetries

---

in quantum master equations and various techniques for complexity reduction and computational speedup that are compatible with the method and the library are also discussed. In addition the effects of dissipative quantum optical modes in media, more precise at metal interfaces, on the emission properties of individual quantum dots are investigated using a non-perturbative system bath interaction theory. Further possible applications, especially the connection of the indistinguishable emitter formalism and the PsiQuaSP library to dissipative quantum modes in media are discussed.

## Structure of the thesis

This thesis is structured in four parts: In Part I the theoretical foundations for the following discussion are laid out: In Chapter 2 the theoretical description of the model systems considered in this thesis are presented, namely multi-level systems for quantum emitters and various treatments for quantized electromagnetic fields. In Chapter 3 the standard open system description of quantum optics, namely the Lindblad equation, is introduced and some properties and concepts of this theory are explained.

In Part II the permutation symmetric, open few and many emitter formalism is introduced and the usage of the PsiQuaSP library is explained. Chapter 4 is an introduction to the closed system formulation of identical quantum emitters in quantum optics. Also basic concepts of Lie algebras are introduced that are relevant to the present discussion. The derivation of the open system theory is presented in Chapter 5. Here two different approaches are presented that together give a comprehensible view on the possibilities and the mathematical as well as physical properties of the approach. In this discussion the sketch representation is introduced using many examples. The extensive discussion of the formalism, especially the sketches, allows to completely omit any equations of motion thereafter. Directly after this discussion in Appendix A the direct translation of this formalism into numerical simulations using the PsiQuaSP library is explained. Furthermore a discussion on performance and different solution strategies for quantum master equations is presented that covers modern, state-of-the-art Krylov subspace methods.

The application of the formalism and the library is presented in Part III. The discussion starts with various cQED laser and spaser examples in Chapter 6. Thereafter collective effects in the open Dicke model are investigated in Chapter 7. In this chapter a new type of phase transition is predicted that leads to a deterministic generation of subradiant states through cavity assisted coherences. In Chapter 8 a collaboration with an experimental group is presented, investigating the effect of thin metal films on the radiative lifetimes of individual quantum dots. In this chapter a theory for dissipative quantized electromagnetic modes, including strong system bath interactions is used to explain the experimental findings. In Chapter 9 further usages of the library are presented: The treatment of non-identical quantum emitters and a graph theory based algorithm for reduction of numerical effort are presented.

The last Part IV summarizes the findings and provides additional detailed information through the appendices.



# **I Theoretical Background**



## 2 Model systems

The field of quantum optics is concerned with the generation and manifestation of quantum light or quantum light matter coupling [28]. Light is emitted and absorbed by matter, such as atoms, molecules, quantum dots, lattice defects in solids, etc. In full generality these emitters usually live in an infinite Hilbert space with a complex overall structure. However for the understanding of the light matter interaction it is often sufficient to use simple approximations of these systems: In order to describe the interaction of such a system with a single mode of the electromagnetic field one may just consider the two states of the Hilbert space that form a resonant transition with this mode. Hence, depending on experimental conditions, a generic quantum emitter can be approximated by a two-level system. If needed the model can always be extended to more levels, forming three-, four- and multi-level systems.

The modes of the electromagnetic field considered in quantum optics were historically mostly vacuum fields: Classical coherent electromagnetic waves, as approximately produced by a single mode laser, and canonically quantized cavity modes. Together with the multi-level system description of matter this leads to a non-relativistic or low-energy version of quantum electrodynamics, which is called cavity quantum electrodynamics (cQED). Sparked by the advances in nanofabrication tools this focus has widened and nowadays also electromagnetic fields and modes in media are considered. For example strips of dielectrics – also called waveguides – support traveling electromagnetic or photonic modes, two-dimensional dielectric slabs with holes arranged in a regular Bravais lattice form photonic crystals, where photon modes have a two-dimensional band structure. Also metallic nanostructures exhibit classical and quantized elementary excitation modes: Surface plasmons and surface plasmon polaritons are quasiparticle like excitations at metal interfaces and metal nanoparticles bear localized surface plasmons. In all these systems dispersion and dissipation is present, which gives rise to new interesting physics but also poses a more challenging mathematical problem.

In this chapter the theoretical quantum optical concepts and model systems used in this thesis

are introduced: Multi-level systems for quantum emitters and classical electromagnetic waves, photon modes as well as dispersive modes for surface plasmons.

## 2.1 Quantum emitters

The simplest model for a quantum emitter is the two-level system. Two-level systems can be used to describe a huge variety of different physical systems, like quantum dots [29], nitrogen or silicon vacancy centers in diamond [30], dye molecules and electron or nuclear spins in solid state environments [31], see Fig. 2.1. The interaction of single two-level systems with the electromagnetic field is one of the most fundamental problems in quantum optics. The dressed states of the Jaynes-Cummings model, Rabi oscillations and the Purcell effect can be explained on this level of theory [1, 32]. Well known physical effects in three-level systems are coherent population trapping, stimulated Raman adiabatic passage (STIRAP) and electromagnetically induced transparency [15, 33]. An example for a four-level system effect is the quantum dot biexciton cascade [34, 24].

These quantum emitters can either couple to the electromagnetic field, but also directly coupled emitters without considering photonic degrees of freedom are studied. Examples range from many body models such as spin chains [35] or the Lipkin-Meshkov-Glick model [10] to electronically addressed spins in quantum information science [36]. Material platforms that are of interest for related experiments are for instance adatoms on topological superconductors or electronic and nuclear spins in silicon.

Overall there is a huge variety of actual physical laboratory systems and theoretical questions centered around quantum emitters or multi-level systems.

### 2.1.1 Two-level Systems

The simplest nontrivial quantum mechanical system is the two-level system. Probably due to its simplicity it is one of the most popular systems in quantum optics and quantum information theory. It is described by two quantum states  $|0\rangle$  and  $|1\rangle$ , which are drawn in Fig. 2.2 (a). The dynamics of a single two-level system can be described by the four spin matrices

$$\begin{aligned}\sigma_{11} &= |1\rangle\langle 1|, & \sigma_{01} &= |0\rangle\langle 1|, \\ \sigma_{10} &= |1\rangle\langle 0|, & \sigma_{00} &= |0\rangle\langle 0|.\end{aligned}\tag{2.1.1}$$

The matrices  $\sigma_{11}$  and  $\sigma_{00}$  describe the population in the upper and lower level. Thus the Hamiltonian of a single two-level system can be written as

$$H_0 = \hbar\omega\sigma_{11}.\tag{2.1.2}$$

This is equivalent to setting the energy of the lower state  $|0\rangle$  to zero<sup>1</sup>.

The matrices  $\sigma_{10}$ ,  $\sigma_{01}$  describe the transition or flip processes between the two states

$$\sigma_{01}|0\rangle = 0, \quad \sigma_{01}|1\rangle = |0\rangle, \quad \sigma_{10}|0\rangle = |1\rangle, \quad \sigma_{10}|1\rangle = 0.$$

These matrices obey the commutation relations

$$[\sigma_{10}, \sigma_{01}] = \sigma_{11} - \sigma_{00}, \quad [\sigma_{10}, \sigma_{11}] = -\sigma_{10}, \quad [\sigma_{01}, \sigma_{11}] = \sigma_{01},\tag{2.1.3}$$

which are the commutation relations of the  $su(2)$  Lie algebra [42].

---

<sup>1</sup>Some authors prefer to set the zero of energy between these levels, arriving at  $H_0 = \frac{\hbar\omega}{2}(\sigma_{11} - \sigma_{00}) = \hbar\omega\sigma_z$ . Since in quantum mechanics one usually only deals with relative energies this choice is arbitrary and in this work the convention Eq. (2.1.2) will be used throughout.

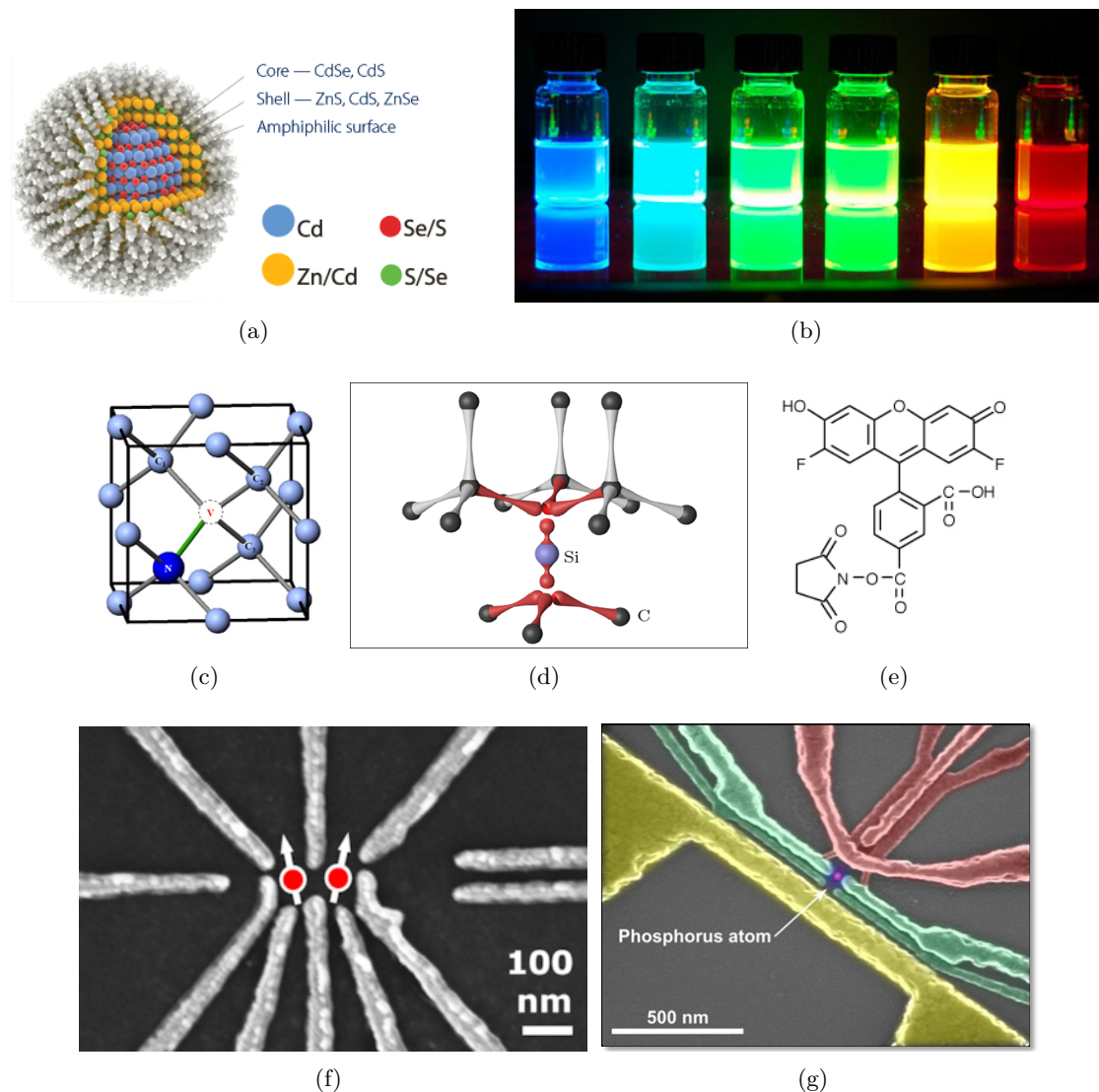


**Figure 2.1 – Material platforms for quantum optics and quantum information:** (a) Sketch of a colloidal core-shell quantum dot. (b) Photoluminescence of colloidal quantum dot solutions. Depending on size and composition the energy spectrum of these nano-objects changes. Taken from [37]. (c) Nitrogen vacancy center in diamond and (d) Silicon vacancy center in diamond. Taken from Ref. [38]. Diamond vacancy centers are popular in quantum optics due to their long coherence times and small incoherent broadening. (e) Oregon Green organic dye molecule. This dye was used by Nogoniiov *et al.* in their spaser setup [39]. Taken from Ref. [40]. (f) Two electronic spins close to each other in a solid state setup. Taken from Ref. [41]. (g) A single phosphorous atom in a solid state atom allows to couple the electron and nuclear spin and to prepare them in entangled states. Taken from Ref. [36]. Depending on experimental conditions, all these systems can be treated as either two-, three-, or multi-level systems.

### 2.1.2 Three and more levels

Three and more levels introduce more complexity into the theory, give rise to new physical phenomena and also provide a more realistic picture in most cases<sup>2</sup>.

Three level systems are represented by three levels  $|0\rangle$ ,  $|1\rangle$  and  $|2\rangle$ . The dynamics of such a three-level system is then described by the *nine* matrices

$$\begin{aligned}\sigma_{22} &= |2\rangle\langle 2|, & \sigma_{12} &= |1\rangle\langle 2|, & \sigma_{02} &= |0\rangle\langle 2|, \\ \sigma_{21} &= |2\rangle\langle 1|, & \sigma_{11} &= |1\rangle\langle 1|, & \sigma_{01} &= |0\rangle\langle 1|, \\ \sigma_{20} &= |2\rangle\langle 0|, & \sigma_{10} &= |1\rangle\langle 0|, & \sigma_{00} &= |0\rangle\langle 0|.\end{aligned}\tag{2.1.4}$$

These matrices obey the commutation relations,

$$\begin{aligned}[\sigma_{xy}, \sigma_{yx}] &= \sigma_{xx} - \sigma_{yy}, \\ [\sigma_{xy}, \sigma_{yz}] &= \sigma_{xz}, \\ [\sigma_{xy}, \sigma_{xx}] &= -\sigma_{xy},\end{aligned}$$

which, in group theoretic language, corresponds to a  $su(3)$  algebra [42]. Thus the matrices Eq. (2.1.4) are equivalent to the Gell-Mann matrices of quantum chromodynamics. In quantum optics these three-level systems are usually distinguished as  $\Lambda$ ,  $V$  and  $\Xi$  systems, depending on the relative alignment of the energies of the three states, see Fig. 2.2

Generally, a  $d$ -level system is described by the state  $|0\rangle, \dots, |d-1\rangle$  and its dynamics can be described using the  $d^2$  matrices

$$\sigma_{xy} = |x\rangle\langle y|,\tag{2.1.5}$$

which obey the commutation relations

$$[\sigma_{xy}, \sigma_{yx}] = \sigma_{xx} - \sigma_{yy},\tag{2.1.6}$$

$$[\sigma_{xy}, \sigma_{zz}] = \sigma_{xz}\delta_{yz} - \sigma_{zy}\delta_{xz},\tag{2.1.7}$$

$$\tag{2.1.8}$$

and zero otherwise, which is equivalent to the  $su(d)$  algebra. As an example consider the quantum dot biexciton cascade which is usually represented by a four-level system, see Fig. 2.2 d).

---

<sup>2</sup>In principle the term multi-level system just refers to a quantum system with a finite dimensional Hilbert space. So essentially, whenever a computer simulation is run for an arbitrary quantum system based on *discrete* basis states, whatever quantum system is considered is approximated by a multi-level system, since the computer always uses a finite excerpt of Hilbert space. Hence also any simulation involving photon number states essentially approximates that photon mode by a multi-level system. For identical two-level systems this has a connection to the Holstein-Primakoff approximation and the giant quantum oscillator [43].

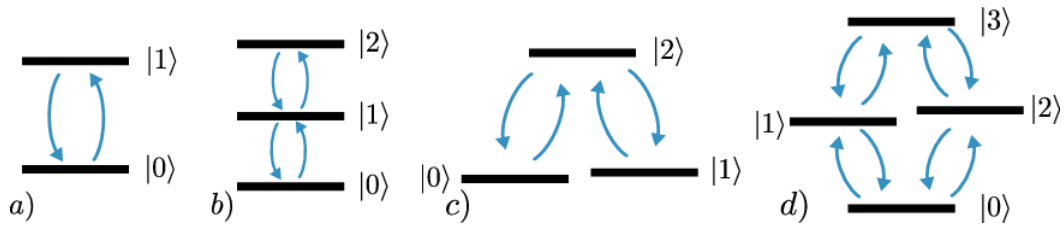


**Figure 2.2 – Multi-level systems:** a) Sketch of a two-level system. The upper and lower level occupations can be expressed with the sigma matrices  $\sigma_{11}$  and  $\sigma_{00}$ , the transition between the levels can be represented by the spin matrices  $\sigma_{01}$  and  $\sigma_{10}$ . b)  $\Xi$  system with, which is used for e.g. three-level lasers. c)  $\Lambda$  system which is important for effects like electronically induced transparency and coherent population trapping. d) Four level system with energy structure typical for a quantum dot biexciton cascade.

## 2.2 Electromagnetic modes in quantum optics

In the early days of quantum optics the considered modes of the electromagnetic field usually were classical coherent waves, as approximately produced by a single mode laser, and cavity modes, both classically and quantum mechanically [28, 15, 32]. All these modes are vacuum modes and laid the foundation to the field of cavity quantum electrodynamics (cQED). The experimentally available systems at that time were lasers and macroscopic mirror cavities and these modes provide the proper theoretical description for these setups.

Confining free space modes is limited by the diffraction limit, therefore in the quest for miniaturization in quantum optical and photonic systems dielectric and metal nanostructures have gained a lot of interest [44, 45]. Metal interfaces have the possibility of confining electromagnetic fields well below the diffraction limit and some of the elementary excitations at these interfaces have quantum properties, such as surface plasmons, surface plasmon polaritons and localized surface plasmons [45, 46, 47].

The quantum effects of the quantized electromagnetic modes are in fact quite elusive [48]. Many of the effects in quantum optics can be described with classical light, just the matter needs to be quantized. A famous and ironical example for this is the photo effect, which was one of the first effects that were "explained" using the photons postulated by Einstein [49]. The quest of finding "true" quantum behavior is even more challenging in the field of plasmonics where dissipation and strong dephasing induced by intrinsic system scattering events and confinement effects causes rapid decay of quantum coherences [47].

In this section the theory for the two scenarios of free space modes and modes supported by metal nanostructures are sketched, not trying to give an exhaustive discussion but highlighting the differences between them.

### 2.2.1 Electromagnetic modes in vacuum

In free space the modes of the electromagnetic field satisfy the homogeneous Maxwell equations. It is convenient to work in the Coulomb gauge, where the vector potential  $\mathbf{A}(\mathbf{r}, t)$  is chosen to be divergence free [28, 32]

$$\nabla \mathbf{A}(\mathbf{r}, t) = 0. \quad (2.2.1)$$

The remaining part of the vector potential is called the transverse vector potential, which satisfies the wave equation

$$\nabla^2 \mathbf{A}(\mathbf{r}, t) - \frac{1}{c^2} \partial_t^2 \mathbf{A}(\mathbf{r}, t) = 0. \quad (2.2.2)$$

The solutions of this wave equation are plane waves, normalized using periodic boundary conditions

$$\mathbf{A}(\mathbf{r}, t) = \frac{1}{L^{3/2}\varepsilon_0^{1/2}} \sum_{\mathbf{k}} \mathcal{A}_{\mathbf{k}}(t) e^{i\mathbf{k}\mathbf{r}}, \quad (2.2.3)$$

where  $L$  is the periodicity length of the normalization condition that fixes the normalization and we sum over all allowed Fourier components  $\mathbf{k}$ . By replacing the canonical momentum and position variables in these waves by the canonical position and momentum operators and postulating commutation relations these modes can be quantized. Using the relation for the internal energy of the free field

$$U = \frac{1}{2} \int_{L^3} (\varepsilon_0 \mathbf{E}^2(\mathbf{r}, t) + \frac{1}{\mu_0} \mathbf{B}^2(\mathbf{r}, t)) \quad (2.2.4)$$

together with the relations

$$\mathbf{E}(\mathbf{r}, t) = -\partial_t \mathbf{A}(\mathbf{r}, t), \quad \mathbf{B}(\mathbf{r}, t) = \nabla \times \mathbf{A}(\mathbf{r}, t), \quad (2.2.5)$$

one can derive the Hamiltonian of the free field

$$H = \sum_{\mathbf{k}} \hbar\omega_{\mathbf{k}} (b_{\mathbf{k}}^\dagger b_{\mathbf{k}} + \frac{1}{2}), \quad (2.2.6)$$

where  $b_{\mathbf{k}}, b_{\mathbf{k}}^\dagger$  are the usual bosonic raising and lowering operators for the mode  $\mathbf{k}$ . Considering a one dimensional cavity is equivalent to imposing the boundary conditions in one dimension only and the problem reduces to

$$H = \sum_k \hbar\omega_k (b_k^\dagger b_k + \frac{1}{2}), \quad (2.2.7)$$

where the  $k$  index is now a scalar instead of a vector. Obviously that removes the electromagnetic degrees of freedom in the other two dimensions which have to be treated differently, for instance using a Lindblad quantum master equation, see Chapter 3.

### 2.2.2 Dissipative modes – Quantum optics in media

In the discussion above the approach for mode quantization of the free, transverse field in vacuum was presented. However vacuum is often not a justified assumption in modern experimental setups. Setups like DBR micropillars [50], waveguides [44], photonic crystals [51], metal nanoparticles [52] and the vast field of meta materials [53] open material platforms with rich (quantum) optical properties that do not live in mere vacuum. Therefore new theoretical approaches are needed.

In this work, aside from the vacuum modes, mainly the field of plasmonics or rather metal nanostructures is considered. There are roughly two different approaches in literature on how to treat metal nanostructures in a quantum dynamical way. These two will be shortly outlined in the following. As in the vacuum case, all these derivations start from the Maxwell equations and then introduce commutation relations.

#### Phenomenological quantization

The bulk plasmon can be derived as a collective excitation of the Fermi sea from microscopic interaction Hamiltonians in solid state theory – it has a sound theoretical footing [54]. The surface plasmon counterpart lacks this theoretical footing, up to date it could not be derived from

such a microscopic theory, it remains more or less a fact from experimental experience [46]. Since there is no microscopic derivation there have been various approaches for a phenomenological quantization or quantum description of the surface plasmon of varying sophistication. In the following the most straightforward approach will be briefly outlined. The details of the derivation vary from author to author but the overall assumptions are the same. Due to its simplicity this approach has been widely used [45, 55, 56, 46, 57, 17].

Assuming a spherical metal nanoparticle with radius  $r \sim 10^0 - 10^1$  nm, that is excited at optical frequencies  $\lambda \sim 10^2$  nm: The field that the metal nanoparticle experiences can be assumed to be spatially homogeneous, which is called time harmonic approximation. The field of the metal nanoparticle is then approximated by a simple dipole field along the external field axis, which amounts to truncating the multipole expansion at the dipole level and then neglecting the two dipole modes that are perpendicular to the external field. The field of the metal nanoparticle  $\mathbf{E}_{np}$  is then given by

$$\mathbf{E}_{np} \propto \underbrace{\frac{\epsilon_h - \epsilon(\omega)}{2\epsilon_h + \epsilon(\omega)}}_{=g(\omega)} \mathbf{G}_i(\mathbf{r}), \quad (2.2.8)$$

where  $\epsilon_h$  is the dielectric constant of the medium surrounding the metal nanoparticle and  $\epsilon(\omega)$  is the frequency dependent dielectric function of the metal, which can be described by Drude theory [54] but is usually taken from experimental data [58], and  $\mathbf{G}_i(\mathbf{r})$  is the spatial dependence of a electric dipole field. The response coefficient  $g(\omega)$  can be approximated by a Lorentzian around the dipole, surface plasmon resonance

$$\epsilon(\omega = \omega_{sp}) = -2\epsilon_h, \quad (2.2.9)$$

which minimizes the real part of the denominator in  $g(\omega)$ . This is called the Fröhlich condition for dipolar plasmon resonance [45]. A Lorentzian in frequency domain is represented by a damped harmonic oscillator in time domain. For the quantization one neglects the damping, computes the internal energy of the oscillation and introduces commutation relations as in the vacuum case, arriving at

$$H_0 = \hbar\omega_{sp}b^\dagger b \quad (2.2.10)$$

and

$$\mathbf{E}_{np} \propto \mathbf{G}_i(\mathbf{r})(b^\dagger + b). \quad (2.2.11)$$

The finite lifetime can be reintroduced using open system theory e.g. the Lindblad equation. For more information on this approach please refer to Ref. [57]. In Chapter 6 this approach will be used to investigate the influence of three- and four-level emitters on the threshold behavior of the spaser – surface plasmon amplification by stimulated emission of radiation [59, 60].

### Dissipative modes

The approach described above is simple and gives a first estimate on the system behavior, but it is lacking in many regards. For instance it is not applicable for larger and nonspherical structures and cannot describe effects like the size dependence of the plasmon resonance of metal nanoparticles. Also the inclusion of higher multipole modes in this quantum theory is not straightforward. Furthermore the strong system bath interaction is not well described by a Lindblad equation, which is based on a second order perturbation theory. Thus another more sound and sophisticated theoretical approach is needed. The methodology presented in the following was introduced by Welsch *et al.* [61, 62].

In the vacuum setting the starting point were the free Maxwell equations. Here the starting

point are the Maxwell equations in media [63]. One then introduces the electric and magnetic field operators  $\hat{\mathbf{E}}$  and  $\hat{\mathbf{B}}$  that satisfy the Maxwell equations

$$\begin{aligned}\nabla \cdot \hat{\mathbf{B}}(\mathbf{r}, \omega) &= 0 \\ \nabla[\epsilon_0 \epsilon(\mathbf{r}, \omega) \hat{\mathbf{E}}(\mathbf{r}, \omega)] &= \hat{\rho}(\mathbf{r}, \omega) \\ \nabla \times \hat{\mathbf{E}}(\mathbf{r}, \omega) &= i\omega \hat{\mathbf{B}}(\mathbf{r}, \omega) \\ \nabla \times \hat{\mathbf{B}}(\mathbf{r}, \omega) &= -i\frac{\omega}{c^2} \epsilon(\mathbf{r}, \omega) \hat{\mathbf{E}}(\mathbf{r}, \omega) + \mu_0 \hat{\mathbf{j}}(\mathbf{r}, \omega).\end{aligned}\quad (2.2.12)$$

Here  $\epsilon(\mathbf{r}, \omega)$  is the complex dielectric function of the system, explicitly allowing general geometries. The operators  $\hat{\rho}(\mathbf{r}, \omega)$  and  $\hat{\mathbf{j}}(\mathbf{r}, \omega)$  are the noise charge and noise current densities, which are related to the noise polarization operator  $\hat{\mathbf{P}}(\mathbf{r}, \omega)$  as

$$\begin{aligned}\hat{\rho}(\mathbf{r}, \omega) &= -\nabla \cdot \hat{\mathbf{P}}(\mathbf{r}, \omega) \\ \hat{\mathbf{j}}(\mathbf{r}, \omega) &= -i\omega \hat{\mathbf{P}}(\mathbf{r}, \omega).\end{aligned}\quad (2.2.13)$$

The noise polarization operator  $\hat{\mathbf{P}}(\mathbf{r}, \omega)$  is defined as

$$\hat{\mathbf{P}}(\mathbf{r}, \omega) = i\sqrt{\frac{\hbar\epsilon_0}{\pi}} \epsilon_I(\mathbf{r}, \omega) \hat{\mathbf{f}}(\mathbf{r}, \omega).\quad (2.2.14)$$

Thus all noise operators are proportional to the imaginary part of the dielectric function  $\epsilon_I(\mathbf{r}, \omega)$ , which indicates an absorptive, dissipative process that cannot be described in the vacuum setting. The  $\hat{\mathbf{f}}(\mathbf{r}, \omega)$  are the actual underlying operators of the quantization procedure in this approach, their three spatial components obey the standard bosonic commutation relations

$$\begin{aligned}[\hat{f}_i(\mathbf{r}, \omega), \hat{f}_j^\dagger(\mathbf{r}', \omega')] &= \delta_{ij} \delta(\mathbf{r} - \mathbf{r}') \delta(\omega - \omega') \\ [\hat{f}_i(\mathbf{r}, \omega), \hat{f}_j(\mathbf{r}', \omega')] &= 0.\end{aligned}\quad (2.2.15)$$

This approach is more technical but allows to treat a variety of different systems on a solid theoretical footing. The expression for the electric field reads

$$\hat{\mathbf{E}}(\mathbf{r}, \omega) = \hat{\mathbf{E}}^{(+)}(\mathbf{r}, \omega) + \hat{\mathbf{E}}^{(-)}(\mathbf{r}, \omega),\quad (2.2.16)$$

with  $\hat{\mathbf{E}}^{(+)}(\mathbf{r}, \omega) = (\hat{\mathbf{E}}^{(-)}(\mathbf{r}, \omega))^\dagger$  and

$$\hat{\mathbf{E}}^{(-)}(\mathbf{r}, \omega) = i\sqrt{\frac{\hbar}{\pi\epsilon_0}} \frac{\omega^2}{c^2} \int d^3\mathbf{r}' \sqrt{\epsilon(\mathbf{r}', \omega)} \mathbf{G}(\mathbf{r}, \mathbf{r}', \omega) \hat{\mathbf{f}}(\mathbf{r}', \omega),\quad (2.2.17)$$

where the  $\omega^2/c^2$  is a spherical coordinates prefactor. The strength of this formalism lies in the fact that the electric field operator depends on the *classical* dyadic Green's function  $\mathbf{G}(\mathbf{r}, \mathbf{r}', \omega)$  satisfying the equation

$$\left[\frac{\omega^2}{c^2} \epsilon(\mathbf{r}, \omega) - \nabla \times \nabla \times\right] \mathbf{G}(\mathbf{r}, \mathbf{r}', \omega) = -\boldsymbol{\delta}(\mathbf{r} - \mathbf{r}').\quad (2.2.18)$$

These classical dyadic Green's functions have been derived for a multitude of different geometries and can also be calculated numerically using partial differential equation solvers [64, 65, 66]. Deriving a full quantum theory, including Fock states for the elementary bosonic excitations in the system, is quite involved, but there has been recent progress in this direction [67]. However in the weak excitation limit the bosonic operators  $\hat{\mathbf{f}}(\mathbf{r}, \omega)$  can be eliminated and closed equations of motion can be obtained. This approach will be used in Chapter 8 to explain experimental findings of lifetimes of quantum dots in the vicinity of different silver surfaces.

# 3 Open system dynamics

The dynamics of non-relativistic, closed quantum systems can be described with a Schrödinger equation [11]

$$i\hbar\partial_t|\psi(t)\rangle = H(t)|\psi(t)\rangle. \quad (3.0.1)$$

There exists a scalar product for the eigenfunctions of this equation and different eigenfunctions to different eigenvalues are orthonormal, since the Hamiltonian  $H(t)$  is hermitian. Thus, if a countable number of eigenfunctions is considered, the eigenfunctions form a Hilbert space basis and closed system quantum mechanics essentially reduces to linear algebra. In this picture the state of the system is always described by a Hilbert space vector  $|\psi(t)\rangle$ , a pure state. Statistical mixtures, such as thermal distributions cannot be described at this level.

In this chapter the density matrix is introduced and its necessity when dealing with statistical mixtures is explained. This leads to the concepts of mixed states and open quantum systems. The von-Neumann and the Lindblad quantum master equations are introduced, which describe the time evolution of density matrices in closed and open systems. Furthermore some general properties of the Lindblad equation are explained.

## 3.1 Density matrix

In quantum mechanics pure states are described by Hilbert space vectors  $|\psi\rangle$  and their time evolution is governed by the Schrödinger equation. A mixed state cannot be described by a state vector, as by definition it lives in multiple states simultaneously. In this context one uses a state *matrix* – the density matrix  $\rho$  [15, 68, 13, 57]. It can be defined as follows

$$\rho = \sum_{i,j} \rho_{ij} |\psi_i\rangle\langle\psi_j|, \quad (3.1.1)$$

where the  $|\psi_i\rangle$  form a complete set of basis states. The density matrix is hermitian and has trace class 1

$$\rho^\dagger = \rho, \quad \text{tr}(\rho) = 1. \quad (3.1.2)$$

Since the density matrix is hermitian it can always be diagonalized. The expectation value of any operator  $\hat{O}$  can be calculated as

$$\langle \hat{O} \rangle = \text{tr}(\hat{O}\rho). \quad (3.1.3)$$

Coming back to the distinction between pure and mixed states: It is possible to define a density matrix for a pure state, say the state  $|\phi\rangle$ . The probability of finding a pure state  $|\phi\rangle$  in the state  $|\phi\rangle$  is, of course, equal to 1. Therefore from Eqs. (3.1.1) we can write

$$\rho_{\text{pure}} = |\phi\rangle\langle\phi|. \quad (3.1.4)$$

This is a matrix of potentially infinite dimension (depending on the number of basis states), which has one diagonal entry equal to 1 and all other entries are 0. However the choice of basis is arbitrary and we could transform this density matrix into an arbitrary basis via unitary transformations. Since the property of diagonalizability and the eigenvalues persevere under unitary transformations a pure state can be defined by looking at the eigenvalues of the density matrix. If the density matrix has only one nonzero eigenvalue, which has to be 1 due to Eq. (3.1.2), it represents a pure state. A mixed state on the other hand is any density matrix with more than one nonzero eigenvalue. As an example for a mixed state we could think of a quantum system of finite dimension  $N$  with uniform distribution along the diagonal, i.e.

$$\rho_{\text{mixed}} = \sum_{i=1}^N \frac{1}{N} |\psi_i\rangle\langle\psi_i|, \quad (3.1.5)$$

which is a matrix that has  $N$  nonzero eigenvalues.

Diagonalization/diagonalizability is a nice theoretical concept, however actual, numerical diagonalization of density matrices might be (very) expensive if the dimension of the density matrix is large. To circumvent exact diagonalization it is a popular approach to just look at the purity  $\gamma$  which is defined as

$$\gamma \equiv \text{tr}(\rho^2). \quad (3.1.6)$$

The purity has an upper and lower bound

$$\frac{1}{N} \leq \gamma \leq 1, \quad (3.1.7)$$

where the upper bound holds for pure states and the lower bound holds for equipartitioned states, with  $N$  being the dimension of the Hilbert space, c.f. Eqs. (3.1.4) and (3.1.5).

## 3.2 Closed quantum systems - von Neumann equation

As stated above, the dynamics of a pure state is described by the Schrödinger equation [13, 57]

$$i\hbar\partial_t|\psi(t)\rangle = H(t)|\psi(t)\rangle. \quad (3.2.1)$$

From this it follows that the time evolution of a state  $|\psi(t)\rangle$  can be written in terms of a unitary time-evolution operator  $U(t, t_0)$

$$|\psi(t)\rangle = U(t, t_0)|\psi(t_0)\rangle \quad (3.2.2)$$

with

$$U(t, t_0) = T_{\leftarrow} \exp\left[-\frac{i}{\hbar} \int_{t_0}^t H(t') dt'\right], \quad (3.2.3)$$

where  $T_{\leftarrow}$  refers to time ordering. We assume that at some initial time  $t_0$  the density matrix of the system can be written as

$$\rho(t_0) = \sum_{\alpha} \omega_{\alpha} |\psi_{\alpha}(t_0)\rangle \langle \psi_{\alpha}(t_0)|, \quad (3.2.4)$$

with the  $|\psi_{\alpha}\rangle$  forming a complete basis in the Hilbert space. Multiplying this expression with  $U(t, t_0)$  from the left and  $U^{\dagger}(t, t_0)$  from the right, the time evolution of the density matrix is given by

$$\begin{aligned} \rho(t) &= \sum_{\alpha} \omega_{\alpha} U(t, t_0) |\psi_{\alpha}(t_0)\rangle \langle \psi_{\alpha}(t_0)| U^{\dagger}(t, t_0) \\ &= U(t, t_0) \rho(t_0) U^{\dagger}(t, t_0). \end{aligned} \quad (3.2.5)$$

Since the eigenvalues of a matrix are invariant under unitary transformations, this result implies that a closed system in a pure (mixed) state will remain in a pure (mixed) state for all times. Even the purity as a quantitative measure for mixedness is invariant under unitary time evolution.

Differentiating Eq. (3.2.5) with respect to  $t$  immediately results in the von-Neumann equation

$$\partial_t \rho(t) = \frac{i}{\hbar} [\rho(t), H(t)]. \quad (3.2.6)$$

### 3.3 Open quantum systems - Lindblad equation

In the previous section the theory for time evolution of a closed quantum system was outlined. However a closed system approach is neither realistic, as every real system is embedded in an environment, nor is it able to describe physical processes like dissipation. An atom spontaneously emitting a photon into the photonic environment, driving the system with an external source, coupling the system to a thermal reservoir are all processes that cannot be described using a state vector representation of the system alone. Taking into account the full Hilbert space of system and environment would allow to treat these processes, however this would result in an unacceptably huge Hilbert space and thus complexity of the associated equations.

The standard approach in order to catch these physical processes while not treating the bath explicitly is the Lindblad quantum master equation formalism. Here the derivation is briefly outlined, for a more thorough treatment please refer to the literature [4, 15, 13, 69].

The complete Hamiltonian of both system and environment reads

$$H = H_S + H_E + H_I. \quad (3.3.1)$$

Here  $H_S$ ,  $H_E$  and  $H_I$  are the system, environment and interaction Hamiltonians, where the interaction Hamiltonian can be explicitly time dependent, i.e.  $H_I = H_I(t)$ , c.f. Fig. 3.1. The density matrix of the combined system and environment shall be denoted as  $\chi$  and  $R_0$  respectively, the latter is assumed to be constant or rather the environment should be large enough to be unaffected by the coupling to the system. The density matrix  $\rho$  of the system is recovered by tracing over the environment degrees of freedom

$$\rho = \text{tr}_E(\chi). \quad (3.3.2)$$

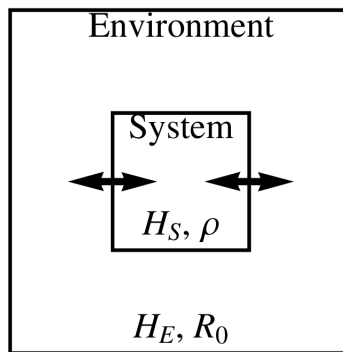


**Figure 3.1 – Scheme of an open quantum system:** System and bath are each described by a Hamiltonian and density matrix, the interaction is described by an interaction Hamiltonian and tracing out the bath degrees of freedom in the Born-Markov approximation results in the Lindblad equation.

Even if the total state  $\chi$  of system and environment is in a pure state, the action of the partial trace generally results in mixed state of the system. The partial trace only then results in a pure state of the system if the reduced density matrices of system and bath factorize, which is equivalent to the absence of quantum correlations. For finite interaction strengths between system and bath this will never occur. Formally integrating the von-Neumann equation (Eq. (3.2.6)) in the interaction picture, reinserting the result and tracing over the environment results in

$$\dot{\tilde{\rho}} = -\frac{1}{\hbar^2} \int_0^t dt' \text{tr}_E [H_I(t), [H_I(t'), \tilde{\chi}(t')]], \quad (3.3.3)$$

where the  $\tilde{\cdot}$  indicates interaction picture representation. The integration constants can be shown to be zero (see for example Ref. [4]).

The next step in the derivation is a Born approximation (second order perturbation theory): Contributions higher than second order in  $H_I$  in this equation are neglected, i.e. one writes  $\tilde{\chi}(t) = \tilde{\rho}(t)R_0 + \mathcal{O}(H_I)$  and drops the  $\mathcal{O}(H_I)$  term. Furthermore the time evolution of the system due to the system-bath interaction is assumed to be Markovian, i.e. the replacement  $\tilde{\chi}(t') \rightarrow \tilde{\chi}(t)$  in the above equation is made. This results in the Born-Markov quantum master equation in the interaction picture

$$\dot{\tilde{\rho}} = -\frac{1}{\hbar^2} \int_0^t dt' \text{tr}_E [H_I(t), [H_I(t'), \tilde{\rho}(t)R_0]]. \quad (3.3.4)$$

Evaluating the integral in its most general form results in the Lindblad equation [70]

$$\dot{\rho} = \mathcal{L}\rho = \frac{i}{\hbar} [\rho, H] + \underbrace{\sum_{k=1}^{N^2-1} \frac{\gamma_k}{2} (2A_k \rho A_k^\dagger - A_k^\dagger A_k \rho - \rho A_k^\dagger A_k)}_{\mathcal{D}_k(\rho)}. \quad (3.3.5)$$

Here  $A_k^\dagger$  and  $A_k$  are general system operators, the damping constants  $\gamma_k$  are positive, real valued and  $N^2 - 1$  is the dimension of the Liouville space associated to the system degrees of freedom ( $N = \dim(H_S)$ ). The terms  $\mathcal{D}_k(\rho)$  are often called Lindblad dissipators and describe the system bath interaction. The general (super-) operator or Liouvillian  $\mathcal{L}$  defines a linear operator on the Liouville space – the space of density matrices. Linear mappings are the topic of linear algebra, thus also finding the solution of a Lindblad equation boils down to linear algebra, see next Section 3.4.

Looking at the expectation value of a general system operator  $J$  and using the cyclic property of the trace i.e.  $\text{tr}(J\rho) = \text{tr}(\rho J)$  it is possible to write down the Heisenberg picture Lindblad equation [71]

$$\dot{J} = \mathcal{L}^\dagger J = -\frac{i}{\hbar}[J, H] + \sum_{k=1}^{N^2-1} \frac{\gamma_k}{2} (2A_k^\dagger J A_k - A_k^\dagger A_k J - J A_k^\dagger A_k). \quad (3.3.6)$$

A direct consequence of this expression is that the trace of the density matrix is conserved [72]: The trace is the expectation value of the Hilbert space identity  $I$ :  $\text{tr}(\rho) = \text{tr}(I\rho)$ . Since  $\dot{I} = \mathcal{L}^\dagger I = 0$  it follows that  $\partial_t \text{tr}(I\rho) = 0$ . Generally, any operator  $O$  that commutes with the Hamiltonian and the operators in the Lindblad dissipators represents a conserved quantity of the system, since its expectation value has derivative zero

$$[O, H] = [O, A_k] = [O, A_k^\dagger] = 0 \quad \rightarrow \quad \partial_t \text{tr}(O\rho) = 0. \quad (3.3.7)$$

This observation will become important in Part II when identifying the actual degrees of freedom of quantum optical systems described by a Lindblad equation. Please note that the reverse argument does not hold, it is possible that  $\partial_t \text{tr}(O\rho) = 0$  even though the operator does not commute with all the ingredients of the Liouvillian  $H$ ,  $A_k$  and  $A_k^\dagger$ .

### 3.4 Steady states and the Liouvillian spectrum

For a closed system described by the von-Neumann equation, each eigenstate of the Hamiltonian represents a steady state of the system: If  $H|\psi_i\rangle = E_i|\psi_i\rangle$  then  $|\psi_i\rangle$  is a steady state of the system, since  $[|\psi_i\rangle\langle\psi_i|, H] = 0$ . If there are  $N$  eigenstates of the Hamiltonian, there are  $N$  possible distinct steady states<sup>1</sup>.

A single two-level system subject to spontaneous emission is described by the Lindblad equation

$$\dot{\rho} = \mathcal{L}\rho = \frac{\gamma}{2}(2\sigma_{01}\rho\sigma_{10} - \sigma_{11}\rho - \rho\sigma_{11}). \quad (3.4.1)$$

From physical intuition alone it is clear that the steady state of this system has to be the ground state. Thus even though the dimension of the Liouville space is 3 the steady state is unique [72]. This raises the question when, why and how the steady state of a Lindblad master equation is unique, whether there are possibilities of multiple steady states and how they occur.

Contrary to the Hamiltonian the Liouvillian  $\mathcal{L}$  is not hermitian (compare  $\mathcal{L}$  and  $\mathcal{L}^\dagger$  in Eqs. (3.3.5) and (3.3.6)). Thus  $\mathcal{L}$  it is not necessarily diagonalizable, its eigenvalues do not need to be real and are generally not real for physically relevant systems [69]. However there are some general known properties about the eigenvalues of the Liouvillian  $\mathcal{L}$  [72, 69, 71]: (i) the real parts of the eigenvalues are zero or negative, (ii) there is always at least one zero eigenvalue and the associated density matrix is the steady state density matrix  $\rho_{ss}$

$$\dot{\rho}_{ss} = \mathcal{L}\rho_{ss} = 0 \quad (3.4.2)$$

and (iii) there always exists a real valued eigenvalue  $\lambda_1$  with largest, non-zero magnitude, which represents the slowest steady state convergence time  $\lambda_1^{-1}$ , see Fig. 3.2. The absolute value of this eigenvalue, which is the difference between  $\lambda_0 = 0$  and  $\lambda_1$  is called the Liouvillian gap  $\Delta$ . If this eigenvalue  $\lambda_1$  goes to zero (the Liouvillian gap closes) a new steady state is formed. If this happens due to a change in system parameters this phenomenon is called a dissipative phase transition (DPT). This nomenclature is inspired by the field of quantum phase transitions

<sup>1</sup>If there are degenerate eigenstates  $|\psi\rangle$  and  $|\phi\rangle$ , there may be steady state coherences  $|\phi\rangle\langle\psi|$ .

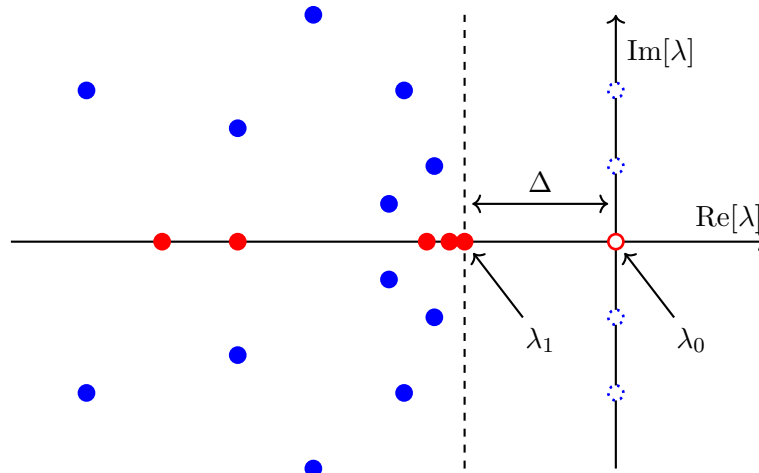


**Figure 3.2 – Liouvillian spectrum:** All the eigenvalues are located in the negative, complex half-plane. The red circle is the  $\lambda_0 = 0$  eigenvalue, corresponding to the steady state(s). The Liouvillian gap  $\Delta$  is determined by the smallest magnitude non-zero eigenvalue  $\lambda_1$ . Red dots correspond to real eigenvalues describing monotonous decay, blue dots correspond to complex eigenvalues describing oscillatory decay and blue, dotted circles are possible steady state coherences (Did not occur in this thesis, but included here for completeness sake).

which occur, when the first excited state and the ground state become degenerate, i.e. when the Hamiltonian gap closes [73].

Having multiple steady states results in quantum memory: Each steady state lives in a subspace of Liouville space and the subspaces of different steady states do not interact with each other according to the master equation. The existence of such non-interacting subspaces is a necessary condition for the existence of multiple steady states – the steady state is determined by the initial conditions [72]. If there are non-interacting subspaces then in the final state of the system information about the initial state is preserved and this information can be associated to a conserved quantity in the system.

## **II Formalism**



## 4 Many emitters – Complex quantum systems

In quantum optics and quantum information theory many works involve not single quantum emitters but collections of quantum emitters. There are many experimental setups where many emitters are present: In lasers and related devices more emitters lead to more gain and thus to higher possible output powers and sometimes more emitters are needed just to overcome the lasing threshold. Irradiating a sample with randomly distributed quantum dots on a substrate or in solution using a diffraction limited laser spot will result in measuring multiple dots simultaneously.

From a theoretical perspective these systems can be split in two categories: The laser example corresponds to an additive logic, more emitters lead to more yield [15, 74], or more philosophical the sum is just the sum and nothing more. However there are also situations where more emitters lead to not only more yield but rather new physics altogether. Such behavior is usually referred to as collective or sometimes emergent behavior. Examples for such truly collective behavior in quantum optical setups are super- and subradiance [25, 75, 76, 77, 78], (multipartite) entanglement [79, 80, 81, 82] or the scaling behavior at phase transitions [83, 18, 19, 14, 84, 85, 86, 20]. In this chapter the operators and Hilbert space basis states for collections of identical, indistinguishable multi-level systems are introduced. There are two different types of basis states, individual and collective. For two-level systems these two are the direct product basis and the Dicke basis.



**Figure 4.1 – Schematic representation of the product state basis** for two two-level systems. One writes down all possible excitation configurations and assigns a state to each of these configurations.

## 4.1 Identical two-level emitters

A set of  $N$  identical two-level systems is described by the collective operators

$$\begin{aligned} J_{11} &= \sum_{i=1}^N \sigma_{11}^i, & J_{01} &= \sum_{i=1}^N \sigma_{01}^i, \\ J_{10} &= \sum_{i=1}^N \sigma_{10}^i, & J_{00} &= \sum_{i=1}^N \sigma_{00}^i. \end{aligned} \quad (4.1.1)$$

These matrices obey the same commutation relations as the individual  $\sigma_{xy}$  matrices, which were introduced in Chapter 2, thus also these operators form a  $su(2)$  algebra [42]. However comparing products of the single  $\sigma$  matrices, e.g.

$$\sigma_{10}\sigma_{01} = \sigma_{11} \quad (4.1.2)$$

with the products of their collective counterparts  $J$

$$J_{10}J_{01} = \sum_{i,j} \sigma_{10}^i \sigma_{01}^j = J_{11} + \underbrace{\sum_{i \neq j} \sigma_{10}^i \sigma_{01}^j}_A \neq J_{11} \quad (4.1.3)$$

it becomes apparent that these identities are violated for collections of two-level systems: The  $A$  term distinguishes a collection of two-level systems from a single two-level system – it introduces a coupling or crosstalk between different two-level systems, which lies at the heart of collective effects such as superradiance.

In this thesis a numerical method for solving master equations with many multi-level systems is introduced. In order to solve a master equation numerically, first one needs to define a basis in which to expand the density matrix and the whole master equation. Thus replacing the operator equation by a  $c$  number equation, since this is all that numerics can handle.

The start of the discussion is the definition of the collective ground state of the system<sup>1</sup>

$$|0\rangle_N = \bigotimes_{i=1}^N |0\rangle_i. \quad (4.1.4)$$

Excited states can be constructed from the collective ground state by applying the raising operator. Since there are two different raising operators, the individual  $\sigma_{10}^i$  and the collective  $J_{10}$ , there are two different basis representations. Constructing excited states from the individual spin matrices results in the product state basis and constructing basis states from the collective spin matrices results in the collective Dicke basis states. These two types of states behave quite

<sup>1</sup>In the presence of strong coupling or quantum phase transitions this state may not be the ground state anymore. However this is not important, any state can be used in order to construct a basis, if the raising and lowering operators are known. In group theory this state would be called *highest weight state* – it is a standard procedure to construct the Hilbert space from a single known highest weight state. See Ref. [42].

differently when interacting with a radiation mode.

For the closed system the proper choice of basis is the Dicke basis, it reduces the complexity dramatically and directly explains effects like super- and subradiance. However including dephasing in an open system description seemingly does not allow to use the Dicke states, favoring the product state basis. In the following the two types of basis states are introduced.

#### 4.1.1 The product state basis

Applying the individual raising operator  $\sigma_{10}^i$  once to the collective ground state results in a singly excited state

$$\sigma_{10}^i |0\rangle_N = |1\rangle_i \bigotimes_{j \neq i} |0\rangle_j \equiv |1, \{i\}\rangle_N. \quad (4.1.5)$$

The last expression means that a single two level-system is excited and the excited two-level system is the two-level system  $i$ . and applying the raising operator to  $n$  different two-level systems results in higher excited states

$$\bigotimes_{i \in \mathbf{u}_n} \sigma_{10}^i |0\rangle_N = \bigotimes_{i \in \mathbf{u}_n} |1\rangle_i \bigotimes_{j \notin \mathbf{u}_n} |0\rangle_j \equiv |n, \mathbf{u}_n\rangle_N \quad (4.1.6)$$

where  $\mathbf{u}_n = \{i_1, \dots, i_n\}$  is the set containing all two level systems that are in the excited state and  $n$  is the number of two-level systems that are excited. If the two-level systems are identical there is a binomial degeneracy  $D$  for  $|n, \mathbf{u}_n\rangle_N$

$$D = \binom{N}{n} \quad (4.1.7)$$

and the total size of the Hilbert space scales exponentially

$$\sum_{n=0}^N \binom{N}{n} = 2^N, \quad (4.1.8)$$

which is a direct consequence of the binomial theorem [87]. The complete product space basis for two two-level systems is drawn in Fig. 4.1.

Looking at the spontaneous emission rate from such a state

$$A \propto \langle n, \mathbf{u}_n | J_{01} J_{10} | n, \mathbf{u}_n \rangle = N \quad \text{for } n > 0 \quad (4.1.9)$$

it is clear that  $N$  emitters prepared in such a state decay individually. The rate of photon emission is constant for all states, resulting in a simple exponential decay, see Fig. 4.2.

#### 4.1.2 The Dicke basis

Dicke pointed out that the radiation of a two-level atom is affected if additional, resonant two-level atoms are placed in its vicinity [25, 28]. In this case the two-level atoms interact via the common radiation mode and states analogous to the spin multiplet states of molecular and atomic physics are created. In the context of quantum optics these states are called Dicke states. The Dicke basis states are simultaneous eigenstates of the two operators

$$J_z = \frac{1}{2}(J_{11} - J_{00}), \quad (4.1.10)$$

$$J^2 = \frac{1}{4}(J_{01} J_{10} + J_{10} J_{01}) + J_z^2, \quad (4.1.11)$$

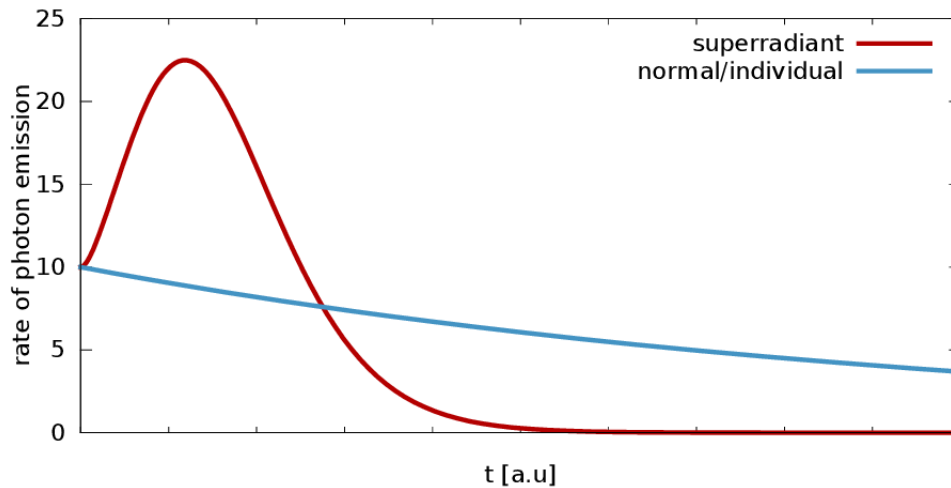


**Figure 4.2 – Superradiant burst vs. individual decay:** Rate of photon emission Eqs. (4.1.9) and (4.1.15) for  $N = 10$  two-level systems. The system is prepared in the fully excited state and relaxes spontaneously towards the ground state. The superradiant decay results in a burst since the collective dipole element is maximal for the half excited states ( $m = 0$ ). Overall this leads to a fast depletion of excitation. The individual decay reproduces the naive expectation that  $N$  emitters radiate at  $N$  times the individual emitters decay rate, but still follow a simple exponential decay. Curves generated with the PsiQuaSP library [26, 27], see Appendix A.

with corresponding quantum numbers  $m$  and  $l(l+1)$ .  $J^2$  is often called the pseudo spin operator since its eigenvalue in molecular and atomic physics gives the total spin of the multi-electron system and  $l$  is thus called the total (pseudo) spin quantum number. Dicke states are the  $N$  particle generalization of the Bell states.

Dicke states are usually labeled as  $|l, m\rangle$ . The quantum number  $m$  is called inversion quantum number: It equals  $-N/2$  in the ground state and  $N/2$  in the fully excited state.  $m$  and  $l$  are bounded by

$$\begin{aligned} 0, \frac{1}{2} \leq l \leq \frac{N}{2}, \\ -l \leq m \leq l, \end{aligned} \quad (4.1.12)$$

where the zero holds for even and the  $1/2$  holds for odd  $N$ . The actions of the collective raising and lowering operators on the Dicke states are

$$\begin{aligned} J_{01}|l, m\rangle &= \sqrt{(l+m)(l-m+1)}|l, m-1\rangle \\ J_{10}|l, m\rangle &= \sqrt{(l-m)(l+m+1)}|l, m+1\rangle. \end{aligned} \quad (4.1.13)$$

In the closed system the interaction of a set of *identical* two-level systems to an electromagnetic mode is mediated by the collective raising and lowering operators<sup>2</sup>. Thus in the closed system the optical selection rules are

$$\Delta m = \pm 1, \quad \Delta l = 0. \quad (4.1.14)$$

Hence if only collective optical transitions are considered the Hilbert space splits into non-interacting subspaces of dimension  $2l+1$ , with  $l$  being the eigenvalue of the  $J^2$  operator. All

<sup>2</sup>This also requires that short ranged, direct coupling between the two-level systems, such as dipole-dipole coupling, can be neglected. This induces some restraints on experimental realizations.

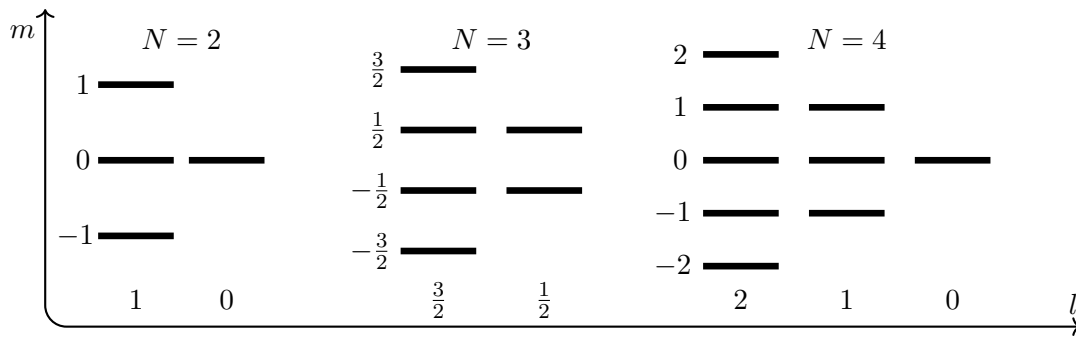


**Figure 4.3** – Schematic representation of the Dicke state basis for 2, 3 and 4 two-level systems. The lowest state of the  $l_{max} = N/2$  subspace is the ground state Eq. (4.1.4) and the lowest state in each subspace is dark, if the two-level systems couple collectively to the electromagnetic surroundings. The different  $l$  subspaces do not couple to each other through collective interactions, therefore in a closed system description the dynamics of the system is generally restricted to the superradiant subspace, characterized by  $l_{max} = N/2$ .

collective operators commute with this operator. Therefore, if the dynamics of the system is expressible in collective operators only, the system will stay in the respective  $l$  subspace. This is equivalent to  $l$  being a conserved quantity as explained in Chapter 3. This also holds for open systems if only collective decay is considered.

Looking at the spontaneous emission rate from a Dicke state

$$A \propto \langle l, m | J_{01} J_{10} | l, m \rangle = (l + m)(l - m + 1) \propto \begin{cases} N^2 & \text{for } l = \frac{N}{2}, m = 0, \\ 0 & \text{for } m = -l. \end{cases} \quad (4.1.15)$$

it becomes clear that the interaction between a set of  $N$  emitters prepared in a Dicke state behaves highly collective: The half excited states in the  $l = l_{max} = N/2$  subspace decay with rates that scale with  $N^2$  while the lowest states in each  $l$  subspace ( $m = -l$ ) are dark, even though only the lowest state in the  $l_{max}$  subspace is the ground state, and the other  $m = -l$  states are excited states. This observation coins the concepts superradiance and subradiance: In general a superradiant emission process of a collection of  $N$  emitters is characterized by a spontaneous emission rate that scales superlinear in  $N$  and a subradiant emission process is characterized by a spontaneous emission rate that scales sublinear in  $N$ . Since the collective dipole moment is maximal for half excited states, a set of initially excited two-level systems decays in a burst if the two-level systems interact collectively with the electromagnetic surrounding, see Fig. 4.2. Since the ground state is part of the  $l_{max} = \frac{N}{2}$  subspace – also called superradiant subspace – it is a popular approach to restrict the dynamics of the  $N$  two-level system setup to this subspace. This amounts to a dramatic reduction in the degrees of freedom, from  $2^N$  to  $N + 1$ . However, in the open system, when dephasing and individual decay is included these subspaces couple to each other and this restriction no longer holds. In this case the straightforward approach would be to expand the density matrix in the direct product states Eq. (4.1.6) resulting in an exponential complexity. Luckily this can be circumvented as will be seen in the next chapter. The  $m > l$  Dicke states can be constructed from the  $l$  subspace ground states  $|l, -l\rangle$  by repeated application of the collective raising operator

$$|l, m\rangle = \left( \frac{(l - m)!}{(2l)!(l + m)!} \right) J_{10}^{(m+l)} |l, -l\rangle. \quad (4.1.16)$$

Looking at the total number of different Dicke states

$$\sum_l 2l + 1 \propto N^2 \quad (4.1.17)$$

it is clear that some of these states have to be highly degenerate, since the total size of the Hilbert space is still exponential, see Eq. (4.1.8). The degeneracy  $D_l$  of a Dicke state just depends on  $l$  and  $N$  and is given by

$$D_l = \frac{(2l + 1)N!}{(\frac{1}{2}N + l + 1)!(\frac{1}{2}N - l)!}. \quad (4.1.18)$$

From this expression it follows that the superradiant subspace  $l = N/2$  always has degeneracy 1. This immediately shows that the superradiant subspace is very small compared to the whole Hilbert space for moderate or large  $N$  ( $N + 1$  vs  $2^N$ ), which will become important in Chapter 7.

The construction of arbitrary Dicke states even for moderate  $N$  is a tedious task, since even the explicit form of the lowest Dicke states  $|l, -l\rangle$  is complicated for  $l < l_{max} = N/2$ . However constructing the states of the superradiant subspace is quite simple, they are just the normalized, totally symmetric superposition states of matching excitation, i.e.

$$|\frac{N}{2}, n - \frac{N}{2}\rangle = \binom{N}{n}^{-\frac{1}{2}} \mathcal{S} |n, \mathbf{u}_n\rangle_N. \quad (4.1.19)$$

Here  $\mathcal{S}$  is the symmetrization operator [11]

$$\mathcal{S} = \sum_P \hat{P}, \quad (4.1.20)$$

which is a sum over all permutations  $P$  generated by the permutation operator  $\hat{P}$ . As an example consider the two two-level system product state  $|1, \{1\}\rangle = |1\rangle_1 |0\rangle_2$ : The action of the symmetrization operator produces the symmetric Bell state: Using Eq. (4.1.19)

$$\binom{2}{1}^{-\frac{1}{2}} \mathcal{S} |1, \{1\}\rangle = \frac{1}{\sqrt{2}} \sum_P \hat{P} |1\rangle_1 |0\rangle_2 = \frac{1}{\sqrt{2}} (\hat{P}_{12} + \hat{P}_{21}) |1\rangle_1 |0\rangle_2 = \frac{1}{\sqrt{2}} (|1\rangle_1 |0\rangle_2 + |0\rangle_1 |1\rangle_2).$$

The other Dicke states for  $l < N/2$  involve anti-symmetric superpositions generated by the anti-symmetrization operator  $\mathcal{A}$  which is known from fermionic Fock states [11]. One of the difficulties of constructing arbitrary Dicke states stems from the fact that for two-level systems there are no totally anti-symmetric states for  $N > 2$ . Mixed symmetric anti-symmetric states are complicated as pointed out before.

## 4.2 Identical multi-level systems

As for the two-level systems collections of identical  $d$ -level systems can be described with the collective operators

$$J_{xy} = \sum_{i=1}^N \sigma_{xy}^i, \quad (4.2.1)$$

where the  $\sigma_{xy}^i$  are the  $d^2$  individual spin matrices or  $su(d)$  generators [42]. Again, the collective  $d$ -level operators obey the same commutation relations as their individual  $\sigma$  matrix counterparts

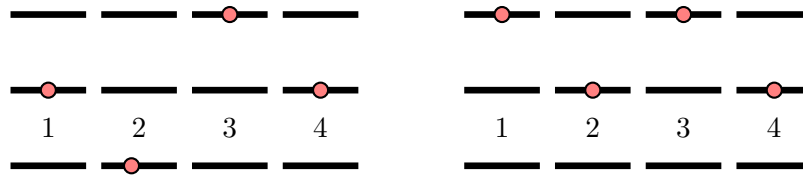


**Figure 4.4 – Three-level system product states:** Schematic representation of two product states for four three-level systems. The left state is given by Eq. (4.2.6).

and again the difference between individual and collective operators can be seen at the level of the operator products

$$\sigma_{xy}\sigma_{yx} = \sigma_{xx} \quad (4.2.2)$$

with the products of their collective counterparts

$$J_{xy}J_{yx} = \sum_{i,j} \sigma_{xy}^i \sigma_{yx}^j = J_{xx} + \underbrace{\sum_{i \neq j} \sigma_{xy}^i \sigma_{yx}^j}_A \neq J_{xx}. \quad (4.2.3)$$

The collective ground state can be written as (no ultra-strong coupling effects are considered)

$$|0\rangle_N = \bigotimes_{i=1}^N |0\rangle_i \quad (4.2.4)$$

and a complete basis can be defined by the repeated application of the raising operators,  $\sigma_{xy}^i$  or  $J_{xy}$ . The individual raising operators again result in a direct product state basis. The collective raising operators for general  $d$ -level systems lead to collective states. In a Lie algebraic context these collective states are called multiplet states, Arecchi *et al.* called these states Gelfand-Tsetlein basis states in the context of quantum optics [88]. However these basis states have only been explicitly derived in the fully symmetrical case in the quantum optics context, to the best of my knowledge, and furthermore have hardly received any attention at all. Maybe with the advent of cold atom, NV center and Rydberg atom experiments and ever more control in these systems this will change in the future. An example where the symmetric three-level system states have been used is Hayn *et al.* [89]. There the closed system three-level counterpart of the ultra-strong coupling phase transition in the Dicke model – called the superradiant phase transition – was studied in the fully symmetrical subspace of the collective three-level system basis states using  $su(3)$  Holstein-Primakoff bosons<sup>3</sup>.

### 4.2.1 Product state basis

The basis states of the individual  $d$ -level system are  $|0\rangle_i, \dots, |d-1\rangle_i$ . As for the two-level systems the simplest choice of basis is the product state basis which can be constructed using the individual flip operators  $\sigma_{xy}^i$

$$\begin{aligned} |n_1, \mathbf{u}_1, n_2, \mathbf{u}_2, \dots, n_{(d-1)}, \mathbf{u}_{(d-1)}\rangle &= \bigotimes_{i \in \mathbf{u}_1} \sigma_{10}^i \bigotimes_{j \in \mathbf{u}_2} \sigma_{20}^j \dots |0\rangle_N \\ &= \bigotimes_{i \in \mathbf{u}_1} |1\rangle_i \bigotimes_{j \in \mathbf{u}_2} |2\rangle_j \dots \bigotimes_{k \notin \mathbf{u}_1 \cup \mathbf{u}_2 \dots} |0\rangle_k, \end{aligned} \quad (4.2.5)$$

<sup>3</sup>Bosonization techniques are popular algebraic techniques since commutation relations of bosons are generally simpler than  $su(n)$ , fermionic commutation relations. Therefore these techniques often allow for analytic solutions. Other bosonization techniques are the Jordan-Schwinger bosonization and the hard sphere bosonization [90, 91].

where the sets  $\mathbf{u}_x$  are disjoint, e.g.  $\mathbf{u}_x \cap \mathbf{u}_y = \emptyset$ . This slightly lengthy looking expression is actually not very complicated, one example for a product state of a four three-level system collection is

$$|2, \{1, 4\}, 1, \{3\}\rangle = |1\rangle_1 |0\rangle_2 |2\rangle_3 |1\rangle_4, \quad (4.2.6)$$

which is shown in Fig. 4.4. The degeneracy of one of these states is given by a multinomial coefficient

$$\binom{N}{\{n_d\}} = \frac{N!}{n_0! n_1! \dots n_{(d-1)}!}, \quad (4.2.7)$$

where  $\{n_d\} = \{n_0, n_1, n_2, \dots, n_{(d-1)}\}$  is the set containing all numbers  $n_x$  that obey the relation

$$N = \sum_{x=0}^{d-1} n_x, \quad (4.2.8)$$

which stems from the fact that all the sets  $\mathbf{u}_x$  are mutually disjoint, or rather that each multi-level system is represented by exactly one Ket in Eq. (4.2.5). This can be used to recover the number of multi-levels in the ground state

$$n_0 = N - n_1 - n_2 \dots \quad (4.2.9)$$

The total Hilbert space dimension is recovered from

$$\sum_{n_d + \dots + n_0 = N} \binom{N}{\{n_k\}} = (d+1)^N, \quad (4.2.10)$$

which is a direct consequence of the multinomial theorem [87]. Here the sums runs over all possible sets/numbers  $\{n_d\} = \{n_0, n_1, n_2, \dots, n_{(d-1)}\}$  that obey Eq. (4.2.8).

### 4.2.2 The Lie algebras $su(d)$

In the introduction it was stated that the  $d$ -level system operators form a  $su(d)$  Lie algebra<sup>4</sup>. At the level of individual spins this statement is somewhat trivial: The  $d$ -level system operators can be represented by  $d \times d$  matrices and *any* basis in the (Liouville) space spanned by  $d \times d$  matrices forms a  $su(d)$  algebra – there is nothing to be learned from Lie algebras for individual spins. The situation changes when collections of identical  $d$ -level systems are considered: In the last section the collective two-level system operators were introduced, which still obey the same commutation relations as the single spin matrices. This means that also the collections of two-level systems form a  $su(2)$  algebra. It became clear that there are two ways to construct a Hilbert space basis for these collections – direct product states and Dicke states.

The Dicke states were introduced around the realization that the operator  $J^2$  commutes with all the other collective operators. Therefore its eigenstates can be used to construct simultaneous eigenstates with one of the other operators. Looking at this operator

$$J^2 = \frac{1}{4}(J_{01}J_{10} + J_{10}J_{01}) + J_z^2 = J_x^2 + J_y^2 + J_z^2 \quad (4.2.11)$$

it becomes clear that it is a second order polynomial of all the collective spin operators. The collective operators are also called the generators and the  $J^2$  operator is called the Casimir

<sup>4</sup>The convention in group theoretic, Lie algebraic contexts is to label the algebras with a capital  $N$ , i.e.  $su(N)$ , however  $N$  usually refers to the total number of multi-level systems in this thesis. Therefore I write  $su(d)$  instead of  $su(N)$ .

operator  $C_1$  of the Lie algebra  $su(2)$ .

Generally a  $su(d)$  Lie algebra representing a collection of  $N$   $d$ -level systems has  $d - 1$  Casimir operators  $C_1, C_2, \dots, C_{(d-1)}$  that are polynomials of order 2, 3,  $\dots, d$  in the generators/collective operators [42]. All these Casimirs commute with each other and all other generators or collective operators of the Lie algebra. Therefore these Casimirs can be used to construct simultaneous eigenstates with the Casimirs and  $d - 1$   $J_{kk}$  collective density operators<sup>5</sup>. Completely analogous to the Dicke basis the collective operators  $J_{kl}$  do not couple the subspaces spanned by the eigenvalues of the Casimir operators since they commute with the Casimirs. These subspaces are called the multiplets of  $su(d)$ . These are the same multiplets known from e.g. spectroscopy in atomic and molecular physics. Therefore a system of indistinguishable  $d$ -level systems in a closed system, governed by a von-Neumann time evolution, will always live in *only one* of these multiplets as long as the  $d$ -level systems are indistinguishable. The dimension of these multiplets scales only polynomially in the number of individual systems as compared to the exponential scaling of the direct product basis, which makes these considerations very powerful.

### 4.2.3 Dicke states for multi-level systems – $su(d)$ multiplets

The Dicke states are the multiplets of  $su(2)$ : By applying the collective raising and lowering operators only a subspace of the Hilbert space can be constructed, the  $su(2)$  multiplet. These subspaces are labeled by the quantum number  $l$ , which results from the Casimir operator  $J^2$ . States from different multiplets cannot be transferred into each other by the actions of the collective operators alone, thus states from different multiplets are noninteracting if only collective interactions are considered. This is realized e.g. in the closed system dynamics of indistinguishable two-level systems. These multiplets do not only occur in quantum optics, but also in particle physics and atomic/molecular spectroscopy: Consider two electrons in a molecular orbital with antiparallel spin orientation: Exciting the electron represents a singlet state, the total spin of both electrons is zero. If, by some process, the spin in the excited state is flipped, a spin triplet is formed. This triplet can have three different spin orientations or three different states, therefore the name triplet. The spin triplet cannot return to the spin singlet ground state unless another spin flip occurs, which usually happens on slow time scales, which is why these states are long lived. This is completely analogous to the  $N = 2$  Dicke (or Bell) states, with the difference that in the spectroscopy context all states are excited states. In the Dicke model context the lowest state in the triplet subspace represents the total ground state. Considering more electrons with spin  $1/2$  each results in more different multiplets, as in the Dicke case, see Fig. 4.3.

The notion of spin multiplets is not restricted to the spin-1/2 or two-level system case. Arecchi *et al.* called the generalization of the Dicke states to multi-level systems in quantum optics the Gelfand-Tsetlin states [88]. They have by far not attracted the same popularity as their two-level system counterparts. As seen from the discussion above from a Lie algebraic, group theoretic stance, it is quite straightforward that these states have to exist. However even for two-level systems the explicit construction of the  $l < N/2$  subspaces is difficult and just the form of the higher Casimir operators  $C_{>2}$  is not trivial. Therefore one usually constructs these multiplets by finding a single state in the multiplet and by applying the raising and lowering operators on this state all other states of the multiplet can be constructed. The collective ground state is part of the totally symmetric multiplet and the symmetric multiplet is just the normalized superposition of all direct product states of equal excitations  $n_k$  in level  $k$ . Therefore this

---

<sup>5</sup>One can leave one of the  $d$   $J_{kk}$  operators out in the definition of the basis states since the total number of multi-level systems is fixed. In the two-level system case there is one quantum number for the excitation.

multiplet is easily constructed:

$$|n_1, n_2, \dots, n_{d-1}\rangle = \left( \binom{N}{\{n_k\}} \right)^{-\frac{1}{2}} \mathcal{S} |n_1, \mathbf{u}_1, n_2, \mathbf{u}_2 \dots n_{(d-1)}, \mathbf{u}_{(d-1)}\rangle. \quad (4.2.12)$$

The dimensionality of this subspace is given by the number of possible numbers  $n_0, n_1, \dots$  that satisfy

$$N = \sum_{k=0}^{d-1} n_k, \quad (4.2.13)$$

which is given by

$$\binom{N+d-1}{N} \propto \frac{1}{(d-1)!} N^{d-1}. \quad (4.2.14)$$

This observation has two important consequences: First, if a master equation with only collective interactions is considered, the dynamics can always be reduced to the totally symmetric multiplet. This greatly reduces numerical effort. Second, in the next section we will find that even if non-collective effects are considered, the dimension of the Liouville space does not scale exponentially but polynomially, if the individual emitters are indistinguishable. This is then found to be equivalent to the density matrix being block diagonal in the spin multiplet states. This result is very useful for density matrix diagonalization, since in a block diagonal matrix each block can be diagonalized independently and the size of these blocks only scales polynomially. This dramatically reduces numerical effort.

### 4.3 Conclusion

In this chapter the Hilbert space basis states for collections of identical multi-level systems were introduced. It became clear that depending on the choice of raising and lowering operators there are two different types of basis states – individual and collective basis states. The choice of operators is closely linked to the considered interaction, whether the interaction Hamiltonian can be constructed from individual or collective operators. The collective basis states were found to be the  $su(d)$  multiplets and their interaction strength with e.g. a bosonic mode strongly depends on the quantum numbers.

## 5 Permutation symmetry in quantum master equations

While from an experimental perspective it is often more challenging to reduce the number of emitters, or rather have a more controlled sample/setup, it is usually more challenging from a theoretical perspective to go to higher numbers of emitters. In order for experiment and theory to meet in the mesoscale both sides have to make an effort.

From the theoretical side the difficulty to treat more systems stems from the fact that just straightforwardly extending the microscopic, single emitter theory to a few or many emitter theory results in an overwhelming complexity and information content. There are plenty of examples for this explosion in complexity: For instance the memory requirement for storing a numerically computed wavefunction for a many particle system even using a moderate spacial grid easily exceeds to storage capacity of a normal computer, server or of all hard drives in the world [92]. This is due to the fact that the complexity for straightforwardly solving these systems scales exponentially in system size. Scaling can mean both scaling in storage requirement and computation time.

### 5.1 Symmetries, size and averages

Luckily there are good and very general arguments as to why one should not try to approach these problems in such a straightforward way. They can be understood e.g. from classical statistical mechanics: The first argument is that even if explicitly solving a system of overwhelming complexity was feasible it would not be a good idea to do so since we would not understand the answer. If a simulation prints an output on the order of Terabytes at each run humans will have a very hard time to get an intuitive understanding of what is going on. Or, more specific, calculating the trajectory of a number of gas particles on the order of the Avogadro constant will

hardly tell us what we want to know, what we are able to perceive and grasp, things like pressure and temperature. Another argument, again from classical statistical mechanics, formulated as a question is: How come the trajectories of a unfathomable number of water molecules can all together be described by an equation depending on only three spatial coordinates – the Navier-Stokes equation [93]? The short answer is: Collective behavior, symmetries and averaging leads to a reduction of degrees of freedom. Collective behavior such as temperature, pressure and volume emerge from the behavior of the individual particles and would be impossible to grasp by only looking at full microscopic treatments.

In quantum mechanics the quantities of interest are different from classical statistical mechanics – there are quantities like states, populations and quantum correlations but also classical averages and correlations. The underlying principles of the scaling in complexity are similar albeit more severe in quantum mechanics [94]: The Hilbert space of an interacting quantum system scales exponentially in system size or is always infinite in the case of e.g. photons. However, also in quantum mechanics, the solution of this overwhelmingly (or infinitely) complex system is neither needed nor would it be a good idea even if possible. For instance dynamical processes of electrons and holes in semiconductors can be very efficiently described by a truncation in the hierarchy expansion of Heisenberg equations of motion, called cluster expansion. In many instances this in principle infinite expansion series can be truncated at the lowest order, called singlet, and still give remarkably accurate results [9]. In this context the many body background of the solid state induces effective dephasing at the single and few particle level thus leading to the destruction of higher order correlations in the hierarchy expansion and thus allowing to truncate at a low level [9]. A popular approach in metals is the use of the Boltzmann equation for e.g. electrical transport, which is a technique comparable to a low order cluster expansion [95]. Thus in these systems the many body contributions reduce the complexity of the studied effect.

There are uncontrolled, disordered, chaotic, non-symmetric systems that can be understood by looking at averages (electron dynamics in solids [9, 95]) and there are highly symmetrical systems, where the symmetry induces a reduction of degrees of freedom (fluids and the Navier-Stokes equation [93]). Both scenarios reduce the complexity of the straightforward solution.

In this chapter a method for treating identical multi-level systems in an open system setting including dephasing is derived. The method is exact and non-approximate – it uses a symmetry to reduce the number of degrees of freedom. The exploited symmetry is the permutation symmetry: Interchanging any two indistinguishable multi-level systems leaves the equations of motion invariant. This leads to the observation that a multinomial number of density matrix elements are identical, which in turn reduces the numerical complexity from exponential to polynomial. The strength of the method is that it is able to treat *all* correlations – in fact it is equivalent to a cluster/correlation expansion to maximal order in the multi-level system degrees of freedom [4]. The permutation symmetry and the resulting reduction in degrees of freedom for two-level system master equations has been independently observed by a variety of authors using varying levels of sophistication [96, 97, 98, 99, 100, 17, 101, 102]. The strength of the discussion presented in this chapter compared to treatments of other authors is the developed sketch representation: After many pages of derivations the sketches allow for a simple and intuitive treatment of the formalism and associated master equations. The sketches are simple to draw, allow to omit the explicit derivation of the equations of motion and at the same time provide a deeper understanding of the involved processes. The sketch representation provides the foundation of the PsiQuaSP library. This library allows to directly translate the sketches into code, which greatly speeds up code development time while still providing a clear and direct view on the actual processes in the master equation. PsiQuaSP is an acronym for *Permutation symmetry for identical Quantum Systems Package*. The library is introduced in Appendix A

directly after this chapter.

The chapter is organized as follows: First in Section 5.2 the problem is motivated by looking at a simple master equation for two-level systems. In Section 5.3 the permutation symmetry is identified in the explicit equations of motion, the reduction of degrees of freedom is derived for two-level systems and the sketches are introduced. In Section 5.4 the findings are generalized to multi-level systems. In Section 5.5 the findings are generalized and translated into a mathematically more formal context that allows for more flexibility. This is important for the library since it provides the foundation for implementing arbitrary master equations. Finally in Section 5.6 the connection to the collective Dicke and general multi-level system multiplet states is presented, which not only provides an interesting viewpoint on the whole methodology but also is very useful for density matrix diagonalization.

## 5.2 Dissipation vs. symmetry

In the last chapter the Hilbert space basis states for identical multi-level systems and the operators acting on these were introduced. For a closed system description this would be sufficient. In this chapter the theory will be extended to the open system scenario. Therefore Liouville space basis states and Liouville space operators are introduced.

Generally in this thesis Lindblad quantum master equations for indistinguishable emitters are considered, which means that all the parameters describing the physical properties of these emitters in the master equation are identical. As an example  $N$  two-level systems coupled to a single bosonic mode are considered. This system is called Dicke or Tavis-Cummings model [25, 12]. The whole setup is coupled to the electromagnetic environment, leading to spontaneous emission and dissipation, see Fig. 5.1. The master equation for this setup reads

$$\dot{\rho} = \frac{i}{\hbar}[\rho, H] + \mathcal{D}_{1 \rightarrow 0}(\rho) + \mathcal{D}_{ph}(\rho) \quad (5.2.1)$$

with the Hamiltonian

$$H = \hbar\omega_0 b^\dagger b + \hbar\omega_1 J_{11} + \hbar g(J_{10}b + J_{01}b^\dagger) \quad (5.2.2)$$

and the Lindblad dissipators

$$\mathcal{D}_{1 \rightarrow 0}(\rho) = \frac{\gamma}{2} \sum_i (2\sigma_{01}^i \rho \sigma_{10}^i - \sigma_{11}^i \rho - \rho \sigma_{11}^i), \quad (5.2.3)$$

$$\mathcal{D}_{ph}(\rho) = \frac{\kappa}{2} (2b\rho b^\dagger - b^\dagger b\rho - \rho b^\dagger b). \quad (5.2.4)$$

Here  $\mathcal{D}_{1 \rightarrow 0}(\rho)$  describes individual spontaneous decay of the two-level systems from the excited state to the ground state, through e.g. spontaneous photon emission into the surrounding vacuum and  $\mathcal{D}_{ph}(\rho)$  describes the cavity loss when the cavity has non-perfect mirrors. Using the bare dissipators and the rotating wave approximation (RWA) in this master equation means that it is only valid as long as ultra-strong coupling effects can be neglected, i.e.  $g \ll \omega_0, \omega_1$  [103].

Looking at these expressions it becomes apparent that all contributions in this master equation acting on the two-level systems can be expressed in collective two-level system operators  $J_{kl}$ , Eq. (4.1.1), except for the first term in Eq. (5.2.3):

$$\mathcal{D}_{1 \rightarrow 0}(\rho) = \frac{\gamma}{2} \sum_i (2\sigma_{01}^i \rho \sigma_{10}^i - \sigma_{11}^i \rho - \rho \sigma_{11}^i) = \frac{\gamma}{2} (2 \underbrace{\sum_i \sigma_{01}^i \rho \sigma_{10}^i}_{\text{symmetry breaking}} - J_{11} \rho - \rho J_{11}).$$

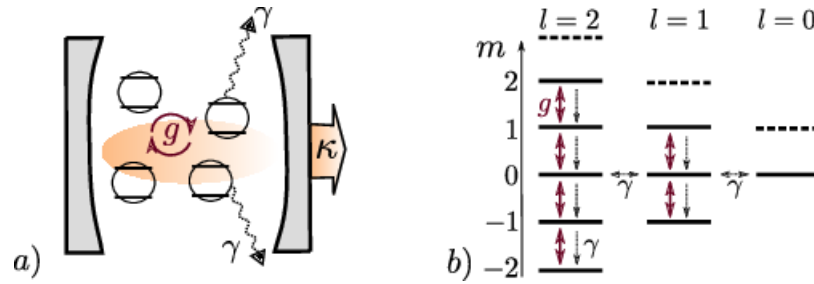


**Figure 5.1 – Illustration of the open Dicke model:** a) A variable number of two-level emitters interacts with a bosonic cavity mode and both mode and two-level systems are subject to loss and decay. b) The Dicke states and the actions of the different contributions in the master equation are shown. Only the individual spontaneous emission couples different Dicke subspaces, because of the  $J^2$  symmetry breaking.

Since the collective operators commute with the Casimir operator  $J^2$ , all contributions in the master equation except the first term in this equation commute with the  $J^2$  operator Eq. (4.1.11). As explained Chapters 3 and 4, without this term the expectation value of  $J^2$  would be a conserved quantity (see Eq. (3.3.7)) and the dynamics of the whole setup could be confined to the superradiant subspace. The  $J^2$  symmetry breaking term is the only term in the master equation that couples the superradiant Dicke states to other states and therefore this master equation cannot be solved by expanding the master equation only in the symmetric Dicke states. At first glance expanding this master equation in the direct product states Eq. (4.1.6) results in an exponential complexity, the dimension of the Hilbert space Eq. (4.1.8) squared:

$$(2^N)^2 = 4^N. \quad (5.2.5)$$

This complexity would limit numerical simulations to very few emitters. Fortunately it is possible to exploit the fact that the two-level systems are indistinguishable in order to reduce the exponential complexity to a polynomial one. Depending on parameters and how many bosonic modes are considered this allows to simulate up to hundreds of two-level systems on modern computers. However the application of this method is only advisable in the range up to 50 emitters, since for larger emitter numbers the phase space formulation of quantum optics, like the positive P representation, is the proper choice of method [104, 14, 4].

The underlying symmetry that leads to this reduction in degrees of freedom is the permutation symmetry of the indistinguishable emitters. The arguments are very general and can directly be applied to arbitrary multi-level systems. In the following this scaling will be derived using two different approaches: First by expanding the density matrix and the master equation in the direct product states and looking at the resulting equations of motion and second by introducing symmetrized Liouville space basis states and general operators acting on these states. These operators then again form a Lie algebra and the symmetrized eigenstates form the symmetric multiplet of this algebra. Both approaches are equivalent, however the first approach is physically more intuitive and simple and the second approach is mathematically more general and allows for more flexibility and a higher theoretical perspective. Investigating the connection of the symmetrized Liouville space basis states to the Dicke states or  $su(d)$  multiplets reveals that a density matrix describing indistinguishable multi-level systems is block diagonal in this basis. This then reveals the close intrinsic connection between the closed system Hilbert space multiplets discussed in the last chapter and the formalism introduced in this chapter. For two-level systems the statement that the density matrix is block diagonal in the Dicke basis is equivalent to the statement that the  $J^2$  symmetry breaking contribution in Eq. (5.2) introduces (diagonal)

coupling between different Dicke subspaces, see Fig. 5.1 b).

Here the RWA is used for reasons of brevity, Eq. (5.2.1) is only valid for moderate coupling strengths  $g$ . The RWA has no influence on the scaling behavior of the permutation symmetric method. The Non-RWA terms simply lead to more terms and require finer time discretization in numerical integration algorithms. For direct steady state computations the difference in runtime is negligible<sup>1</sup>. Also the ground state may change in systems where the RWA fails, however the existence of the quantum phase transition in the Dicke model, the superradiant phase transition [18, 85], is still a matter of active debate [105, 106]. Furthermore the system environment coupling should then be treated in the proper eigenbasis of the Hamiltonian [103]. Nonetheless the Non-RWA terms do not affect the applicability of the permutation symmetric method.

## 5.3 Time evolution of identical multi-level systems

In the following the master equation Eq. (5.2.1) will be expanded in the direct product states Eq. (4.1.6) and by carefully looking at the resulting equations of motion the reduction in the degrees of freedom will be derived. The arguments developed in this discussion are then applied to the general multi-level system case. The resulting quantities are discussed and a sketch representation is developed that provides a more intuitive view on the possible processes and their actions. Furthermore these sketches allow to identify additional symmetries that further reduce the complexity without any approximation. The derivation and discussion presented in this section were published in M. Gegg, M. Richter, *New J. Phys.* 043037 (2016) [101].

### 5.3.1 Time evolution of a simple master equation

The expansion of the density matrix (and thus the Lindblad equation) in the two-level system product state basis introduced in the last chapter, Eq. (4.1.6), is given by

$$\langle m, \mathbf{u}_m | \rho | n, \mathbf{u}_n \rangle. \quad (5.3.1)$$

Here  $m$  and  $n$  are again the number of excited two-level systems in the respective state and  $\mathbf{u}_n$ ,  $\mathbf{u}_m$  are the associated sets of two-level system indices. The aim is to arrive at a Liouville space basis, which is a basis in the space of square matrices. The expansion of the density matrix in this basis is performed using a Hilbert-Schmidt inner product:

$$\begin{aligned} \langle m, \mathbf{u}_m | \rho | n, \mathbf{u}_n \rangle &= \text{tr} [|n, \mathbf{u}_n\rangle \langle m, \mathbf{u}_m| \rho] \\ &\equiv \langle |n, \mathbf{u}_n\rangle \langle m, \mathbf{u}_m| \rangle. \end{aligned} \quad (5.3.2)$$

Here the matrices

$$|n, \mathbf{u}_n\rangle \langle m, \mathbf{u}_m| \quad (5.3.3)$$

form a complete basis in the Liouville space of the set of  $N$  two-level systems. The total number of these operators is  $(2^N)^2 = 4^N$ , which is the brute force complexity of this problem.

In Eq. (5.3.3) every two-level system is represented by one ket  $|k\rangle_i$  and one bra  $\langle l|_i$ , which results in a spin matrix  $|k\rangle_i \langle l|_i$  for two-level system  $i$ :

$$|n, \mathbf{u}_n\rangle \langle m, \mathbf{u}_m| = \dots |i\rangle_k \dots \langle j|_k \dots = \dots \underbrace{|i\rangle_k \langle j|_k}_{=\sigma_{ij}^k} \dots \quad (5.3.4)$$

---

<sup>1</sup>This is only true as long as both RWA and Non-RWA Liouvillians do not have an explicit time dependence. The use of eigenvalue based steady state solvers requires a constant Liouvillian. If there is an explicit time dependence then direct steady state computation requires techniques such as pseudo time stepping (or direct integration using Runge-Kutta), see Section A.6.

There are four possible single two level system operators:  $\sigma_{11}^i$ ,  $\sigma_{10}^i$ ,  $\sigma_{01}^i$ , and  $\sigma_{00}^i$ , see Eq. (2.1.1). It is beneficial to proceed by counting the number of two-level systems that are represented by the four different spin matrices: let  $n_{11}$  be the number of two-level systems that are represented by  $\sigma_{11}^i$  in Eqs. (5.3.3), (5.3.4) and let  $\mathbf{u}_{11}$  be the set of the respective labels. Analogous  $n_{10}$ ,  $n_{01}$ ,  $n_{00}$  and  $\mathbf{u}_{10}$ ,  $\mathbf{u}_{01}$ ,  $\mathbf{u}_{00}$  are the numbers and sets for the other three cases. Since every two-level system is represented by exactly one spin matrix these quantities obey the relations

$$N = n_{11} + n_{10} + n_{01} + n_{00} \quad (5.3.5)$$

and

$$\mathbf{u}_N = \mathbf{u}_{11} \cup \mathbf{u}_{10} \cup \mathbf{u}_{01} \cup \mathbf{u}_{00}, \quad (5.3.6)$$

where  $\mathbf{u}_N = \{1, \dots, N\}$  is the set containing all two-level system indices/labels. Rewriting the basis element (5.3.3) using these quantities yields

$$\begin{aligned} |n, \mathbf{u}_n\rangle \langle m, \mathbf{u}_m| &= |n_{11} + n_{10}, \mathbf{u}_{11} \cup \mathbf{u}_{10}\rangle \langle n_{11} + n_{01}, \mathbf{u}_{11} \cup \mathbf{u}_{01}| \\ &\equiv |n_{11}, \mathbf{u}_{11}, n_{10}, \mathbf{u}_{10}\rangle \langle n_{11}, \mathbf{u}_{11}, n_{01}, \mathbf{u}_{01}|. \end{aligned} \quad (5.3.7)$$

So far everything amounts to relabeling. Please note that  $n_{00}$  and  $\mathbf{u}_{00}$  do not enter this expression: As in the definition of the excited state (vector) basis (4.1.6), the two-level systems in the ground state can be omitted, because the total number of two-level systems is fixed and thus the information about the ground state two-level systems can be recovered (from (5.3.5) and (5.3.6)). An important quantity is the number of basis elements for fixed  $n_{11}$ ,  $n_{10}$ ,  $n_{01}$  but variable sets  $\mathbf{u}_{11}$ ,  $\mathbf{u}_{10}$ ,  $\mathbf{u}_{01}$ . It is given by the multinomial coefficient [87], using Eq. (5.3.5)

$$\begin{aligned} \mathcal{C}(n_{11}, n_{10}, n_{01}) &= \binom{N}{n_{11}, n_{10}, n_{01}, n_{00}} \\ &= \frac{N!}{n_{11}! n_{10}! n_{01}! (N - n_{11} - n_{10} - n_{01})!}. \end{aligned} \quad (5.3.8)$$

The Hilbert space completeness relation in this notation is given by

$$I_H = \sum_{n=0}^N \mathcal{S} |n, \mathbf{u}, 0, \emptyset\rangle \langle n, \mathbf{u}, 0, \emptyset|, \quad (5.3.9)$$

where  $\emptyset = \{\}$  is the empty set and the symmetrization operator  $\mathcal{S}$  creates a sum over all possible sets  $\mathbf{u}$ .

In the following the time evolution of the density matrix elements associated to the basis in (5.3.7) according to the master equation Eq. (5.2.1) will be derived and the effects of the permutation symmetry will be identified, which results in the polynomial complexity.

### 5.3.2 Time evolution – Simplification

The equations of motions are obtained by expanding the quantum master equation in the excited state basis by using

$$\partial_t \langle \hat{O} \rangle = \text{tr} [\hat{O} \partial_t \rho] = \frac{i}{\hbar} \text{tr} [\hat{O} [\rho, H]] + \text{tr} [\hat{O} \sum_i \mathcal{D}[A_i]], \quad (5.3.10)$$

where  $\hat{O}$  will be the basis elements defined in (5.3.7). The derivation will be illustrated by discussing the spontaneous emission contribution Eq. (5.2.3) in the quantum master equation Eq. (5.2.1), since it is the only term that breaks the symmetry of the Dicke states and therefore

the only reason why the whole discussion of this chapter has any benefit. The whole set of equations arising from the open Dicke model example will be discussed in Section 5.3.4. Here the cavity mode is omitted as it is not necessary for spontaneous emission into vacuum<sup>2</sup>.

Inserting Eqs. (5.2.3) and (5.3.7) into Eq. (5.3.10) and rearranging the matrices in the trace using  $\text{tr}[ABC] = \text{tr}[CAB]$  yields

$$\begin{aligned} \partial_t \langle |n_{11}, \mathbf{u}_{11}, n_{10}, \mathbf{u}_{10}\rangle \langle n_{11}, \mathbf{u}_{11}, n_{01}, \mathbf{u}_{01}| \rangle \Big|_{\mathcal{D}_1 \rightarrow 0(\rho)} &= \\ \gamma \sum_j \left[ \langle \sigma_{10}^j |n_{11}, \mathbf{u}_{11}, n_{10}, \mathbf{u}_{10}\rangle \langle n_{11}, \mathbf{u}_{11}, n_{01}, \mathbf{u}_{01}| \sigma_{01}^j \rangle \right. \\ &\quad - \frac{1}{2} \langle |n_{11}, \mathbf{u}_{11}, n_{10}, \mathbf{u}_{10}\rangle \langle n_{11}, \mathbf{u}_{11}, n_{01}, \mathbf{u}_{01}| \sigma_{11}^j \rangle \\ &\quad \left. - \frac{1}{2} \langle \sigma_{11}^j |n_{11}, \mathbf{u}_{11}, n_{10}, \mathbf{u}_{10}\rangle \langle n_{11}, \mathbf{u}_{11}, n_{01}, \mathbf{u}_{01}| \rangle \right]. \end{aligned} \quad (5.3.11)$$

This equation of motion has three contributions: The first term on the rhs of Eq. (5.3.11) is the  $J^2$  symmetry breaking contribution, the single system operators act on both sides (bra and ket) of the basis element simultaneously. The other two terms act on only one side each (bra or ket). Looking at the operator actions of the first, symmetry breaking term in Eq. (5.3.11) for two-level system  $j$  by rearranging the expression as in Eq. (5.3.4)

$$\sigma_{10}^j |n_{11}, \mathbf{u}_{11}, n_{10}, \mathbf{u}_{10}\rangle \langle n_{11}, \mathbf{u}_{11}, n_{01}, \mathbf{u}_{01}| \sigma_{01}^j = \dots \sigma_{10}^j \sigma_{kl}^j \sigma_{01}^j \dots = \dots \sigma_{11}^j \delta_{k0} \delta_{l0} \dots$$

it becomes clear that each two-level system is represented by a product of three spin matrices. This product is nonzero only if  $\sigma_{kl}^j = \sigma_{00}^j$  and yields  $\sigma_{11}^j$ , therefore summing over all two-level systems results in exactly  $n_{00}$  terms where in each term the single two-level system  $j$  has been raised to the  $\sigma_{11}^j$ . The remaining two terms are non-zero if the two-level system is excited on the right or on the left side respectively. Hence the  $J^2$  symmetry breaking term acts on both sides of the individual spin matrices and the  $J^2$  symmetry preserving terms act only on one side at a time<sup>3</sup>.

This can be expressed in terms of the different sets of two-level systems represented by the different spin matrices  $\mathbf{u}_{11}, \dots$  (cf. (5.3.5), (5.3.6) and (5.3.7)):

$$\begin{aligned} \partial_t \langle |n_{11}, \mathbf{u}_{11}, n_{10}, \mathbf{u}_{10}\rangle \langle n_{11}, \mathbf{u}_{11}, n_{01}, \mathbf{u}_{01}| \rangle \Big|_{\mathcal{D}_1 \rightarrow 0(\rho)} &= \\ \gamma \left[ \sum_{j \in \mathbf{u}_{00}} \langle |n_{11} + 1, \mathbf{u}_{11}^{+j}, n_{10}, \mathbf{u}_{10}\rangle \langle n_{11} + 1, \mathbf{u}_{11}^{+j}, n_{01}, \mathbf{u}_{01}| \rangle \right. \\ &\quad - \frac{1}{2} \sum_{j \in \mathbf{u}_{11} \cup \mathbf{u}_{10}} \langle |n_{11}, \mathbf{u}_{11}, n_{10}, \mathbf{u}_{10}\rangle \langle n_{11}, \mathbf{u}_{11}, n_{01}, \mathbf{u}_{01}| \rangle \\ &\quad \left. - \frac{1}{2} \sum_{j \in \mathbf{u}_{11} \cup \mathbf{u}_{01}} \langle |n_{11}, \mathbf{u}_{11}, n_{10}, \mathbf{u}_{10}\rangle \langle n_{11}, \mathbf{u}_{11}, n_{01}, \mathbf{u}_{01}| \rangle \right], \end{aligned} \quad (5.3.12)$$

where  $\mathbf{u}_{11}^{+j} = \{i_1, \dots, i_{n_{11}}, j\}$  is the set  $\mathbf{u}_{11}$  including the additional element  $j$ . The rhs of (5.3.12) consists of three sums over two-level system labels  $j$ .

<sup>2</sup>This amounts to taking the partial trace of the density matrix  $\text{tr}_b[\rho]$  over the bosonic degrees of freedom.

<sup>3</sup>This is the basic difference between the closed system symmetry preserving contributions and the contributions that break this symmetry. Closed system symmetry means that the Hamiltonian of identical  $d$ -level systems commutes with the  $su(d)$  Casimir operators. Thus the eigenvalues corresponding to these Casimirs are constants of motion and the dynamics of the system is confined to the symmetric multiplet.

These sums have  $n_{00}$ ,  $n_{11} + n_{10}$ , and  $n_{11} + n_{01}$  summands regardless of the specific sets of unique two-level system labels  $\mathbf{u}_{11}, \dots$ . In fact the whole equation does not depend on the specific sets as long as the parameter of the Liouvillian  $\gamma$  is the same for all two-level systems. This holds for all contributions arising from the Lindblad equation. Upon further requiring that at some initial time all density matrix entries of the form  $\langle |n_{11}, \mathbf{u}_{11}, n_{10}, \mathbf{u}_{10}\rangle \langle n_{11}, \mathbf{u}_{11}, n_{01}, \mathbf{u}_{01}| \rangle$  with the same numbers  $n_{11}$ ,  $n_{10}$ ,  $n_{01}$  but different sets  $\mathbf{u}_{11}, \dots$  are equal, the information about the sets is redundant, since the equations of motion for all these states are identical. This requirement is fulfilled if the system starts in the ground state or a thermal equilibrium state.

If the information about the sets is redundant it may be omitted and the density matrix elements can be replaced by

$$\langle |n_{11}, \mathbf{u}_{11}, n_{10}, \mathbf{u}_{10}\rangle \langle n_{11}, \mathbf{u}_{11}, n_{01}, \mathbf{u}_{01}| \rangle \equiv \rho[n_{11}, n_{10}, n_{01}]. \quad (5.3.13)$$

These quantities contain all information about the system. The action of all Liouvillians on the density matrix elements defined by (5.3.13) ( $n_{xy}$  fixed,  $\mathbf{u}_{xy}$  variable) is the same. The total number of these elements (for  $n_{xy}$  fixed) is given by (5.3.8).

The number of different  $\rho[n_{11}, n_{10}, n_{01}]$ , i.e. the total number degrees of freedom of the system is

$$\frac{1}{6}(N+1)(N+2)(N+3) \sim \frac{1}{3!}N^3 \quad (5.3.14)$$

The permutation symmetry of quantum master equations of indistinguishable two-level systems has been used by other authors as well: To our knowledge the first two published mentions of this method were reported by Sarkar and Satchell in 1987 [96, 97]. They contributed to the discussion of optical bistability in the few emitter case, since the phase space formulation of master equations like Eq. (5.2.1) breaks down as emitter numbers become as small as 50 [14, 97]. Therefore for the few emitter regime ( $\leq 50$ ) the formalism introduced here is the proper choice of method and in the many emitter regime ( $> 50$ ) the phase space methods, like the positive P representation [104], are the proper choice of method. The phase space methods result in a Fokker-Planck equation or associated quantum Langevin equation of five dimensions for the open Dicke model example, which can even be solved analytically in some cases [4]. In reference to the works of Sarkar and Satchell, Carmichael provides an explanation of this scaling in his book based on an operator expectation value hierarchy expansion [4]. However this method did not receive much attention until in 2012 Hartmann found this scaling behavior by exploiting a  $su(4)$  symmetry of the quantum master equation using group theory [100, 107]. We derived this scaling for two-level systems independently using the equation of motion approach presented above [17]. Also Chase, Geremia and Baragiola independently discovered this methodology in 2008 by directly expanding the density matrix in the full Dicke basis and realizing that the density matrix is block diagonal in this basis [98, 99]. Also in the context of quantum tomography it was pointed out that a density matrix describing indistinguishable, permutation symmetric two-level systems leads to similar reductions in degrees of freedom [108, 109]. In recent years this method has received more attention and is now used in various contexts [110, 111, 112, 102, 113]. The derivation in this section comes from simple and accessible arguments and the direct product state representation gives a clear view on the underlying physics, especially in the context of coherences/collectivity vs dephasing/individualization [20]. Furthermore the equations of motion are easily derived and the generalization to multi-level systems is straightforward. Especially the sketch representation introduced in the following will prove useful compared to other treatments.

The lack of popularity back then and the popularity of this method now can probably be explained by the increase of computational power in the meantime: Sarkar and Satchell adiabatically eliminated the cavity mode in an equation similar to Eq. (5.2.1) and were able to compute

the Liouvillian gap for up to  $N = 12$  two-level systems on a Cray-1 supercomputer in 1987 [97]. This corresponds to a partial diagonalization of a  $455 \times 455$  non-hermitian matrix. Thirty years later, using our code and modern Krylov subspace methods we are able to (partially) diagonalize these same non-hermitian matrices up to order  $10^6 \times 10^6$  on a standard personal computer. Inserting (5.3.13) into (5.3.12) yields

$$\begin{aligned} & \partial_t \rho[n_{11}, n_{10}, n_{01}] \Big|_{\mathcal{D}_{1 \rightarrow 0}(\rho)} \\ &= \frac{\gamma}{2} \left[ 2(N - n_{11} - n_{10} - n_{01}) \rho[n_{11} + 1, n_{10}, n_{01}] \right. \\ & \quad \left. - (2n_{11} + n_{10} + n_{01}) \rho[n_{11}, n_{10}, n_{01}] \right]. \end{aligned} \quad (5.3.15)$$

The action of this Liouvillian on the density matrix element  $\rho[n_{11}, n_{10}, n_{01}]$  contains in- and out-scattering contributions: The in-scattering contribution (first term,  $J^2$  symmetry breaking) stems from a density matrix element that has a higher number of emitters in the excited state, i.e.  $n_{11} + 1$ . The out-scattering contribution (second term,  $J^2$  symmetry preserving) is proportional to the same density matrix element  $\rho[n_{11}, n_{10}, n_{01}]$ . Such a process, where a state with a higher excitation number scatters into a state with a lower excitation number, describes an exponential decay of excitation. The part proportional to  $n_{10} + n_{01}$  describes the dephasing. Both contributions together describe spontaneous radiative decay. The decrease in excited two-level systems is reflected in the diagonal elements ( $n_{10} = n_{01} = 0$ ) and the loss of coherence in the off-diagonals ( $n_{10} \neq 0 \neq n_{01}$ ).

Using the definition Eq. (5.3.13) it is possible to derive closed equations of motion for all conceivable permutation symmetric two-level system quantum master equations. In principle one could stop here and implement a simulation based on the quantity  $\rho[n_{11}, n_{10}, n_{01}]$ . However at this level there are issues concerning the numerical stability, which will be explained and solved in the following.

### 5.3.3 Preventing numerical instability

The density matrix contains all accessible information about a quantum system [5]. However this information is in general only indirectly accessible to an experimenter through measurable observables. Thus in order to make meaningful predictions operator expectation values have to be calculated. For instance looking at the excited state population expectation value  $\langle J_{11} \rangle$ , using (5.3.9)

$$\begin{aligned} \langle J_{11} \rangle &= \left\langle \sum_i \sigma_{11}^i \sum_{n=0}^N \mathcal{S} |n, \mathbf{u}, 0, \emptyset\rangle \langle n, \mathbf{u}, 0, \emptyset| \right\rangle \\ &= \sum_{n=0}^N \binom{N}{n} \left\langle \sum_i \sigma_{11}^i |n, \mathbf{u}, 0, \emptyset\rangle \langle n, \mathbf{u}, 0, \emptyset| \right\rangle \\ &= \sum_{n=0}^N \binom{N}{n} n \rho[n, 0, 0]. \end{aligned} \quad (5.3.16)$$

Even though the information about the sets is redundant there is still a multinomial number of basis elements for each  $\rho[i, j, k]$ , which is a binomial in this case, since  $j = k = 0$ .

From a numerical point of view this expression is problematic: When evaluating the binomial for e.g. 100 two-level systems one needs to calculate and store numbers of dramatically different

magnitudes i.e.  $\binom{100}{50} \sim 10^{29}$  vs.  $\binom{100}{100} = 1$ . This reduces numerical accuracy or makes computation impossible altogether: The larger binomial coefficients grow faster than exponentially in  $N$ , thus quickly leaving reasonable number storage formats. Furthermore since the trace of the density matrix is conserved, i.e.

$$\text{tr}[\rho] = \sum_{n=0}^N \binom{N}{n} \rho[n, 0, 0] = 1, \quad (5.3.17)$$

it is clear that the magnitudes of those elements  $\rho[n, 0, 0]$  that are associated with large binomial coefficients become (less than) exponentially small. Multiplying larger than exponentially large numbers with smaller than exponentially small numbers on a finite precision machine results in enormous numerical errors.

Fortunately, this problem can be conveniently circumvented by accounting for the multinomial number of  $\rho[\dots]$  at the level of the equations of motion. Simply multiplying the equations of motion (like (5.3.15)) by the multinomial number of elements  $\rho[n_{11}, n_{10}, n_{01}]$  Eq. (5.3.8)) and defining

$$\mathcal{P}[n_{11}, n_{10}, n_{01}] = \binom{N}{n_{11}, n_{10}, n_{01}, n_{00}} \rho[n_{11}, n_{10}, n_{01}] \quad (5.3.18)$$

transforms Eq. (5.3.15) into

$$\begin{aligned} \partial_t \mathcal{P}[n_{11}, n_{10}, n_{01}]|_{\mathcal{D}_1 \rightarrow 0(\rho)} &= \frac{\gamma}{2} \left[ 2(n_{11} + 1) \mathcal{P}[n_{11} + 1, n_{10}, n_{01}] \right. \\ &\quad \left. - (2n_{11} + n_{10} + n_{01}) \mathcal{P}[n_{11}, n_{10}, n_{01}] \right]. \end{aligned} \quad (5.3.19)$$

Thus only the prefactor of the first rhs term changes (5.3.15), which is due to

$$\binom{N}{n_{11}, \dots} \binom{N}{n_{11} + 1, \dots, n_{00} - 1}^{-1} \mathcal{P}[n_{11} + 1, \dots] = \frac{n_{11} + 1}{n_{00}} \mathcal{P}[n_{11} + 1, \dots].$$

This definition fixes the numerical issues since the excited state expectation value

$$\langle J_{11} \rangle = \sum_{n=0}^N n \mathcal{P}[n, 0, 0]. \quad (5.3.20)$$

and the trace

$$\text{tr}(\rho) = \sum_{n=0}^N \mathcal{P}[n, 0, 0]. \quad (5.3.21)$$

are numerically well behaved. The physical interpretation of  $\mathcal{P}[n_{11}, n_{10}, n_{01}]$  is also more accessible than  $\rho[n_{11}, n_{10}, n_{01}]$ :  $\mathcal{P}[n, 0, 0]$  gives the full, incoherent probability of finding the system in a state with  $n$  two-level systems excited and  $N - n$  unexcited and for  $n_{10}, n_{01} \neq 0$   $\mathcal{P}[n_{11}, n_{10}, n_{01}]$  gives the full polarization/transition probability between adjacent states.

Our aim with this method is to use it for numerics. The method is quite general – any permutation symmetric master equation of two- (or multi-) level systems can be solved. It would be tedious and error prone to derive equations of motion for every specific master equation and then implement these equations by hand. Therefore we developed a sketch representation of the elements  $\mathcal{P}[\dots]$  in which we can visualize the processes of the master equation and designed the implementation of this method in PsiQuaSP in a way that allows to directly translate these sketches into code. The sketch illustrating the spontaneous decay Eq. (5.3.19) is shown in Fig.

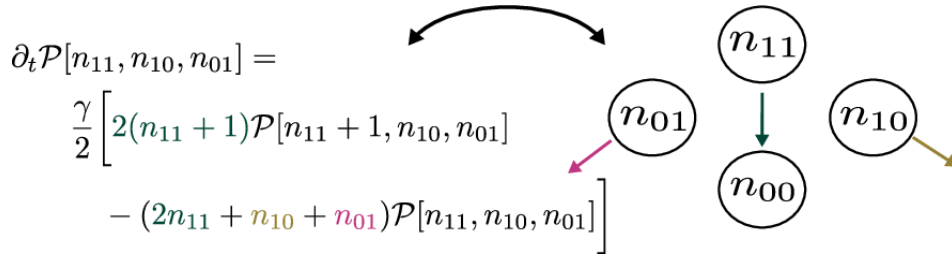


**Figure 5.2 – Sketch representing the action of the spontaneous emission Liouvillian:** Each bubble represents a degree of freedom, each arrow a process. Arrows and corresponding terms have the same color. The green (black) arrow depicts the loss of excitation, states with higher numbers  $n_{11}$  decay into states with higher numbers  $n_{00}$ . There are two terms responsible for this process – one in- and one out-scattering term – since the total probability has to be conserved. The yellow and purple (gray) arrows depict the dephasing or "coherence out-scattering". The offdiagonal elements ( $n_{10}, n_{01} \neq 0$ ) are purely damped. The corresponding arrows point to the outside, indicating this loss.

5.2. The arrow pointing from the  $n_{11}$  to the  $n_{00}$  circle depicts the process in which states with higher numbers  $n_{11}$  of excited two-level systems (and thus lower  $n_{00}$ ) decay to the states with higher  $n_{00}$  (and thus lower  $n_{11}$ ), which results in a reduction of the excited state population. The arrows pointing from the  $n_{10}$  and  $n_{01}$  circles to the outside depict the destruction of quantum coherence. In the next section the full equations of motion for open Dicke model example Eq. (5.2.1) are discussed.

### 5.3.4 Open Dicke model equations of motion

In order to discuss the full time evolution of the open Dicke model example Eq. (5.2.1) a basis for the photon mode needs to be introduced. This is treated by the usual photon number states  $|k\rangle$  and the basis for the joint system is constructed via

$$|k\rangle|n, \mathbf{u}_n\rangle \rightarrow \mathcal{P}[n_{11}, n_{10}, n_{01}; k, p], \quad (5.3.22)$$

where  $k$  and  $p$  are the photon degrees of freedom, i.e.  $\langle \dots |k\rangle\langle p| = \mathcal{P}[\dots; k, p]$ .

The contributions of the Lindblad dissipators to the equations of motion are the spontaneous emission Eq. (5.3.19) and

$$\partial_t \mathcal{P}[n_{11}, n_{10}, n_{01}; k, p]_{\mathcal{D}_{ph}(\rho)} = \frac{\kappa}{2} \left[ 2\sqrt{(k+1)(p+1)} \mathcal{P}[n_{11}, n_{10}, n_{01}; k+1, p+1] - (k+p) \mathcal{P}[n_{11}, n_{10}, n_{01}; k, p] \right] \quad (5.3.23)$$

for the cavity photon decay. The contribution of the Dicke interaction Hamiltonian in the RWA Eq. (5.2.2) to the quantum master equation is given by

$$\begin{aligned}
& \partial_t \mathcal{P}[n_{11}, n_{10}, n_{01}; k, p] \Big|_{H_I} \\
&= ig[(n_{01} + 1)\sqrt{k+1} \mathcal{P}[n_{11} - 1, n_{10}, n_{01} + 1; k + 1, p] \\
&\quad + (n_{00} + 1)\sqrt{k+1} \mathcal{P}[n_{11}, n_{10} - 1, n_{01}; k + 1, p] \\
&\quad + (n_{10} + 1)\sqrt{k} \mathcal{P}[n_{11}, n_{10} + 1, n_{01}; k - 1, p] \\
&\quad + (n_{11} + 1)\sqrt{k} \mathcal{P}[n_{11} + 1, n_{10}, n_{01} - 1; k - 1, p] \\
&\quad - (n_{10} + 1)\sqrt{p+1} \mathcal{P}[n_{11} - 1, n_{10} + 1, n_{01}; k, p + 1] \\
&\quad - (n_{00} + 1)\sqrt{p+1} \mathcal{P}[n_{11}, n_{10}, n_{01} - 1; k, p + 1] \\
&\quad - (n_{01} + 1)\sqrt{p} \mathcal{P}[n_{11}, n_{10}, n_{01} + 1; k, p - 1] \\
&\quad - (n_{11} + 1)\sqrt{p} \mathcal{P}[n_{11} + 1, n_{10} - 1, n_{01}; k, p - 1]], \tag{5.3.24}
\end{aligned}$$

where  $n_{00} = N - n_{11} - n_{10} - n_{01}$  is used for visual clarity. The terms are all associated to processes where one excitation in the two-level systems is destroyed (created) while a photon is created (destroyed). The eight terms correspond to two operators in the interaction Hamiltonian Eq. (5.2.2), each acting from the left and the right and making a distinction between two sets each  $n_{11}, n_{10}$  or  $n_{11}, n_{01}$ . This results in  $2 \times 2 \times 2 = 8$  terms. Including the Non-RWA terms therefore leads to  $4 \times 2 \times 2 = 16$  terms. Further including a pure dephasing contribution

$$\mathcal{D}_z(\rho) = \gamma' \sum_{i=1}^N (\sigma_z^i \rho \sigma_z^i - \rho) \tag{5.3.25}$$

which can be used to model e.g. line broadening due to phonons [114] results in

$$\partial_t \mathcal{P}[n_{11}, n_{10}, n_{01}; k, p] \Big|_{\mathcal{D}_z(\rho)} = -\gamma'(n_{10} + n_{01})\mathcal{P}[n_{11}, n_{10}, n_{01}; k, p]. \tag{5.3.26}$$

Again in Eq. (5.3.25) the contribution where individual spin matrices act on both sides of the density matrix simultaneously (the first rhs term) is breaking the  $J^2$  symmetry of the closed system. The sketch of the action of the Dicke interaction Hamiltonian on the two-level systems is given in Fig. 5.3 b): Every arrow corresponds to one term in (5.3.24). Occupation is exchanged between the two levels 0 and 1 via the build up of quantum coherences, as opposed to the action of the Lindblad dissipators, which are inherently incoherent contributions, cf. Fig. 5.3 a).

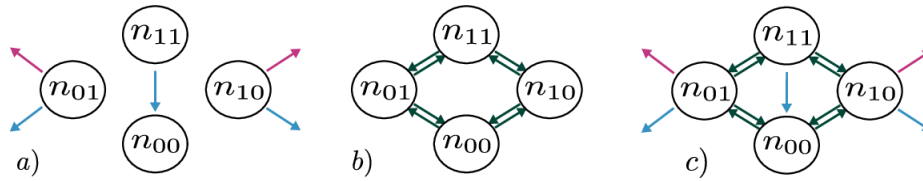


**Figure 5.3 – Sketch of the actions of the different contributions of the open Dicke model:** Arrows pointing from circle  $A$  to circle  $B$  correspond to a build up of density matrix entries with higher number in  $B$  and lower number in  $A$ . Arrows pointing from a circle to the outside correspond to dephasing, i.e. a pure decay of the respective (offdiagonal) density matrix entry. a) Action of the Lindblad dissipators: blue (solid) arrows describe spontaneous emission, purple (dashed) arrows incoherent pumping and yellow (dot-dashed) arrows pure dephasing. b) Tavis-Cummings Hamiltonian (electron-photon coupling): densities are exchanged between  $n_{11}$  and  $n_{00}$  via the build up of quantum coherence  $n_{10}$  and  $n_{01}$ . c) The combination of all processes describes the gain medium dynamics of a laser setup [17].

## 5.4 Multi-level systems

The dimension of the full Liouville space associated to  $N$   $d$ -level systems is  $d^{2N}$ , it scales only polynomially in  $d$ , but still this renders simulations impossible even for moderate  $d$  and  $N$ . Fortunately the arguments developed in the previous section are general and not limited to the two-level system case: The action of the quantum master equation on groups of elements of the density matrix was found to be identical and the number of degrees of freedom was greatly reduced. Thus also for multi-level systems the exponential complexity can be reduced to a polynomial one. This section starts by outlining the formal derivation for the three- and general multi-level systems. Thereafter the sketches and the application of the method is discussed using several laser examples.

### 5.4.1 Three-level systems

The simplest extension of the theory is to consider three-level systems. Three level systems are often divided into the three categories  $V$ ,  $\Lambda$ ,  $\Xi$  according to the relative energies of the levels [15, 9]. Three level systems are used for realistic laser theories [115], noise induced coherences [116, 117], electromagnetically induced transparency [118], coherent population trapping [15], STIRAP [33] or for more realistic quantum dot models including e.g. multiple single exciton or the trion state [119, 120].

In the previous chapters the spin matrices for three-level systems  $\sigma_{kl}^i$  and the corresponding many emitter product basis states

$$|n_1, \mathbf{u}_{n_1}, n_2, \mathbf{u}_{n_2}\rangle = \bigotimes_{i \in \mathbf{u}_{n_1}} \sigma_{10}^i \bigotimes_{j \in \mathbf{u}_{n_2}} \sigma_{20}^j |0\rangle_N, \quad (5.4.1)$$

were introduced. Here the three-level systems in  $\mathbf{u}_{n_1}$  and  $\mathbf{u}_{n_2}$  are in state  $|1\rangle$  and  $|2\rangle$  respectively. The two sets  $\mathbf{u}_{n_2}$  and  $\mathbf{u}_{n_1}$  are disjoint  $\mathbf{u}_{n_2} \cap \mathbf{u}_{n_1} = \emptyset$ . A conceivable Hamiltonian is

$$H_0 = \hbar \sum_m \omega_m b_m^\dagger b_m + \hbar \sum_{k=0}^2 \omega_k J_{kk} \quad (5.4.2)$$

$$H_I = \hbar \underbrace{\sum_{k \neq l} \sum_m g_{kl}^m (J_{kl} + J_{lk})(a_m^\dagger + a_m)}_{H_{kl}}, \quad (5.4.3)$$

including an arbitrary number of electromagnetic (cavity) modes. Possible Lindblad dissipators are again spontaneous radiative and non-radiative decay between individual levels, incoherent pumping and pure dephasing, where again the parameter needs to be identical for all individual three-level systems. For more information please refer to Appendix E.

The associated Liouville space is spanned by the basis elements

$$|n_1, \mathbf{u}_{n_1}, n_2, \mathbf{u}_{n_2}\rangle \langle m_1, \mathbf{u}_{m_1}, m_2, \mathbf{u}_{m_2}|. \quad (5.4.4)$$

Here  $n_2$  gives the number of three-level systems that are in the Ket state  $|2\rangle_i$  in above expression, the associated labels are contained in set  $\mathbf{u}_{n_2}$ . The associated Bra state to three-level system  $i$  can either be  $\langle 2|_i$ ,  $\langle 1|_i$ , or  $\langle 0|_i$ , hence the set and the numbers will be split into three. Analogously to the previous section distinguishing these cases results in

$$n_1 = n_{10} + n_{11} + n_{12}, \quad \mathbf{u}_{n_1} = \mathbf{u}_{n_{10}} \cup \mathbf{u}_{n_{11}} \cup \mathbf{u}_{n_{12}}. \quad (5.4.5)$$

The other numbers and sets split into

$$\begin{aligned} n_2 &= n_{20} + n_{21} + n_{22}, & \mathbf{u}_{n_2} &= \mathbf{u}_{n_{20}} \cup \mathbf{u}_{n_{21}} \cup \mathbf{u}_{n_{22}} \\ m_1 &= n_{01} + n_{11} + n_{21}, & \mathbf{u}_{m_1} &= \mathbf{u}_{n_{01}} \cup \mathbf{u}_{n_{11}} \cup \mathbf{u}_{n_{21}} \\ m_2 &= n_{02} + n_{12} + n_{22}, & \mathbf{u}_{m_2} &= \mathbf{u}_{n_{02}} \cup \mathbf{u}_{n_{12}} \cup \mathbf{u}_{n_{22}}. \end{aligned}$$

The contributions for the ground state population ( $\sigma_{00}^i$ )  $n_{00}$  and  $\mathbf{u}_{n_{00}}$  can be defined through the equalities

$$\begin{aligned} \mathbf{u}_N &= \mathbf{u}_{00} \cup \mathbf{u}_{01} \cup \dots \cup \mathbf{u}_{22}, \\ N &= n_{00} + n_{01} + \dots + n_{22}. \end{aligned} \quad (5.4.6)$$

The fact that the number  $n_{00}$  and set  $\mathbf{u}_{00}$  can be expressed through the other 8 numbers and sets allows the omission. As long as the number of three- (or general multi-) level systems is fixed this elimination is possible and the selection of  $\sigma_{00}$  is merely convention<sup>4</sup>.

Again if the parameters in the master equation are identical for all three-level systems, the information about the sets is redundant. In complete analogy to the previous section closed equations can be obtained by introducing the quantities

$$\begin{aligned} &tr [ |n_1, \mathbf{u}_{n_1}, n_2, \mathbf{u}_{n_2}\rangle \langle m_1, \mathbf{u}_{m_1}, m_2, \mathbf{u}_{m_2} | \rho ] \\ &\equiv tr [ |n_{10}, \mathbf{u}_{10}, n_{11}, \mathbf{u}_{11} \dots n_{22}, \mathbf{u}_{22}\rangle \langle n_{01}, \dots n_{22}, \mathbf{u}_{22} | \rho ] \\ &\equiv \rho [ n_{22}, n_{21}, \dots n_{01} ] \end{aligned} \quad (5.4.7)$$

and

$$\mathcal{P}[n_{22}, n_{21}, \dots n_{01}] = \mathcal{C}(n_{22}, n_{21}, \dots n_{01}) \rho [n_{22}, n_{21}, \dots n_{01}] \quad (5.4.8)$$

with the multinomial coefficient

$$\mathcal{C}(n_{22}, n_{21}, \dots n_{01}) = \frac{N!}{n_{22}! n_{21}! \dots n_{01}! n_{00}!}. \quad (5.4.9)$$

The total number of degrees of freedom of this theory is

$$\binom{N+8}{N} = \frac{1}{8!} (N+8)(N+7) \dots (N+1) \propto \frac{1}{8!} N^8. \quad (5.4.10)$$

---

<sup>4</sup>The label 00 does not have to refer to the ground state, by relabeling the levels in the multi-level system this can refer to any level.

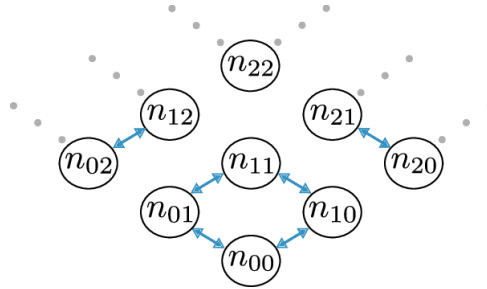


**Figure 5.4 – Sketch of the action of a three-level system interaction Hamiltonian:**

It is apparent that there are, additionally to the two-level system case, contributions exchanging quantum coherence between  $n_{20}$ ,  $n_{21}$  and  $n_{02}$ ,  $n_{12}$ , which are completely separated from the other dynamics of the system. The representation is simplified with respect to Fig. 5.3 to a single arrow with two heads. This also corresponds to the usage in PsiQuaSP. In the RWA this corresponds to two terms in the equations of motion (cf. (5.3.24) and Fig. 5.3 b)), without RWA there are four. The dots indicate the transition to higher multi-level system dynamics. The proper rules for constructing these sketches are given in Section 5.4.3.

The interaction of levels 0 and 1 with a single cavity mode is described by the Hamiltonian (cf. (5.4.3))

$$H_{10} = \hbar g_{10}(a^\dagger + a)(J_{10} + J_{01}). \quad (5.4.11)$$

In Fig. 5.4 the sketch for this process is shown. The sketch has  $3^2 = 9$  circles and from Eq. (5.4.6) one degree of freedom can be eliminated leading to a  $\propto N^{9-1} = N^8$  scaling. Additional degrees of freedom (bubbles) arise compared to the two-level system case and additional exchange of quantum coherence (arrows). Please note that the additional exchange of coherence is completely decoupled from the other dynamics. This will become important in Section 5.4.3, where the application of the permutation symmetric expansion scheme is discussed at the level of the sketches by looking at different laser setups.

## 5.4.2 Multi-level systems

There is a large application range for multi-level systems: Four-level systems describe gain in optical devices with reduced thresholds or are model systems to study the quantum-dot biexciton cascade [34, 24]. Generally more realistic descriptions of quantum optical systems such as (coupled) quantum dots require multi-level systems [120, 121], which leads to increasingly complex quantum dynamics [122, 123].

Again starting from the product space basis for the Hilbert space of the collection of  $d$ -level systems Eq. (4.2.5)

$$|n_1, \mathbf{u}_{n_1}, \dots, n_{(d-1)}, \mathbf{u}_{n_{(d-1)}}\rangle = \bigotimes_{i \in \mathbf{u}_{n_1}} |1\rangle_i \bigotimes_{j \in \mathbf{u}_{n_2}} |2\rangle_j \dots \bigotimes_{k \notin \mathbf{u}_{n_1} \cup \mathbf{u}_{n_2} \dots} |0\rangle_k, \quad (5.4.12)$$

the direct product Liouville space basis is given by

$$|n_1, \mathbf{u}_{n_1}, \dots, n_{(d-1)}, \mathbf{u}_{n_{(d-1)}}\rangle \langle m_1, \mathbf{u}_{m_1}, \dots, m_{(d-1)}, \mathbf{u}_{m_{(d-1)}}|. \quad (5.4.13)$$

Analogous to two- and three-level systems the numbers  $n_1, \dots, m_1, \dots$  and the associated sets  $\mathbf{u}_{n_1}, \dots, \mathbf{u}_{m_1}, \dots$  are divided into  $d^2$  different numbers  $n_{kl}$  and sets  $\mathbf{u}_{kl}$  – one per spin matrix

$\sigma_{kl}^i$  Eq. (2.1.5):

$$\begin{aligned}
n_1 &= n_{10} + n_{11} \dots n_{1(d-1)}, & \mathbf{u}_{n_1} &= \mathbf{u}_{n_{10}} \cup \mathbf{u}_{n_{11}} \dots \mathbf{u}_{n_{1(d-1)}} \\
&\vdots & & \\
n_{(d-1)} &= n_{(d-1)0} + n_{(d-1)1} \dots, & \mathbf{u}_{n_{(d-1)}} &= \mathbf{u}_{n_{(d-1)0}} \cup \mathbf{u}_{n_{(d-1)1}} \dots \\
m_1 &= n_{01} + n_{11} \dots n_{(d-1)1}, & \mathbf{u}_{m_1} &= \mathbf{u}_{n_{01}} \cup \mathbf{u}_{n_{11}} \dots \mathbf{u}_{n_{(d-1)1}} \\
&\vdots & & \\
m_{(d-1)} &= n_{0(d-1)} + n_{1(d-1)} \dots, & \mathbf{u}_{m_{(d-1)}} &= \mathbf{u}_{n_{0(d-1)}} \cup \mathbf{u}_{n_{1(d-1)}} \dots
\end{aligned} \tag{5.4.14}$$

and

$$\begin{aligned}
\mathbf{u}_N &= \mathbf{u}_{00} \cup \mathbf{u}_{01} \cup \dots \mathbf{u}_{(d-1)(d-1)}, \\
N &= n_{00} + n_{01} + \dots n_{(d-1)(d-1)},
\end{aligned} \tag{5.4.15}$$

which ensure conservation of the number of multi-level systems and allow to eliminate one degree of freedom,  $n_{00}$ , which reduces the scaling by one power i.e.  $N^m \rightarrow N^{m-1}$ . Closed equations for permutation symmetric Lindblad equations are obtained for

$$\begin{aligned}
&tr[[n_1, \mathbf{u}_{n_1}, \dots] \langle m_1, \mathbf{u}_{m_1}, \dots | \rho \rangle \\
&\equiv tr[[n_{10}, \mathbf{u}_{10}, \dots] \langle n_{01}, \mathbf{u}_{01}, \dots | \rho \rangle \\
&\equiv \rho[n_{(d-1)(d-1)}, \dots].
\end{aligned} \tag{5.4.16}$$

Equivalently, numerical stability favors the  $\mathcal{P}$  representation

$$\mathcal{P}[n_{(d-1)(d-1)}, \dots n_{01}] = \mathcal{C}(n_{(d-1)(d-1)}, \dots n_{01}) \rho[n_{(d-1)(d-1)}, \dots n_{01}], \tag{5.4.17}$$

where  $\mathcal{C}(n_{(d-1)(d-1)}, \dots n_{01})$  is again the multinomial coefficient

$$\mathcal{C}(n_{(d-1)(d-1)}, \dots n_{01}) = \frac{N!}{n_{(d-1)(d-1)}! \dots n_{01}! n_{00}!}. \tag{5.4.18}$$

The number of degrees of freedom of the many  $d$ -level system solution is fixed by the number of indices counting the basis elements, i.e. the number of different sets  $\{n_{kl}\} = \{n_{(d-1)(d-1)}, \dots\}$  satisfying the relation

$$N = \underbrace{\sum_{k,l} n_{kl}}_{m \text{ summands}}, \tag{5.4.19}$$

which is

$$\binom{N+m}{N} \propto \frac{1}{(m-1)!} N^{m-1}. \tag{5.4.20}$$

The sketch of such a basis representation/master equation would have  $m$  circles, and the scaling of the permutation symmetric method is always proportional to  $N$  to the power of the number of circles in the sketch minus one, i.e.  $\propto N^{m-1}$ . Hence the full solution of the many  $d$ -level system scales as

$$\binom{N+d^2-1}{N} \tag{5.4.21}$$

since  $d^2$  is the number of spin matrices for the individual  $d$ -level system. This scaling relation looks strikingly familiar when looking back at the discussion of the Gelfand-Tsetlin basis states

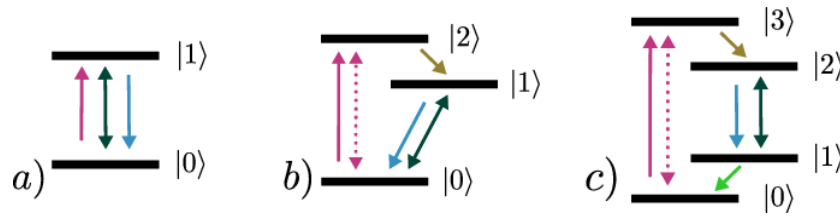


**Figure 5.5 – Level schemes for the different laser setups:** a) two-level, b) three-level and c) four-level optical emitters (cf. (5.4.23) and (5.4.29)). The dotted arrows indicate optical pumping.

or symmetric  $su(d)$  multiplets in Chapter 4. In fact it will turn out that the Liouville space basis discussed in this section also represents a symmetric multiplet, just in Liouville instead of Hilbert space, and the associated Lie algebra is  $su(m)$ , with  $m$  as in Eq. (5.4.19). This will be explained in Section 5.5.

In the next section the application of the permutation symmetric formalism is illustrated by looking at different laser setups. The discussion will be centered around the sketches, which illustrates that equations and formula can be omitted.

### 5.4.3 Two-, three- and four-level laser examples

In this section the application of the permutation symmetric method is illustrated and especially the use of the sketch representation using different setups for two-, three- and four-level system based laser setups. This serves as an introduction to the sketch usage. The aim of this treatment is to completely omit deriving any equations of motion: The permutation symmetric method was implemented in the PsiQuaSP library [26, 27] based on this sketch representation. There the user does not derive any equations of motion but translates the master equation into the sketch representation introduced above – a matter of a few minutes – and then directly translates these sketches into code. The library was made publicly available on GitHub: <https://github.com/modmido/psiquasp> and a manual/introduction was published in M. Gegg, M. Richter arXiv:1707.01079 (2017). Please refer to Appendix A directly after this chapter for details on PsiQuaSP.

The range of applicability of the permutation symmetric method to laser theory is the cQED laser limit: Few emitters (1 – 100) and relatively low cavity photon numbers, the range where in principle quantum correlations are expected to be important. The cavity degrees of freedom and the full equations of motion are omitted in this section, as they do not benefit the understanding of the sketches. Further, some spontaneous emission contributions and all conceivable pure dephasings are omitted for reasons of brevity. The scalings/complexities of the solutions of the respective quantum master equation do not change if these contributions were included. The only difference in the results are more terms in the equations of motion, but it does not affect the numerical scaling. The spontaneous emission of the lasing transition into non-lasing modes is included, as this rate is crucial for a definition of the  $\beta$  factor, a central parameter in laser theory [17, 84, 124].

The full equations are given in Appendix D. Please note that the results or rather the numerical scalings observed in this section are valid for both RWA and Non-RWA treatments, thus all conclusion of this section are valid in both cases.

Five different setups are discussed: incoherently driven two-level systems and incoherently as well as coherently driven three- and four-level systems. For a two-level system laser theory incoherent pumping is mandatory since otherwise no population inversion can be achieved.

The master equation for the two-level laser is given by (omitting the cavity decay and  $H_0$  for

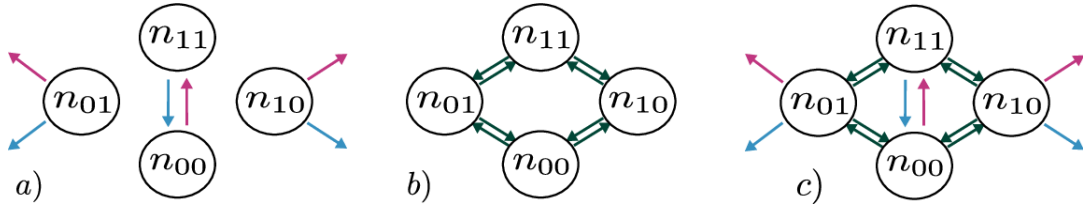


**Figure 5.6 – Two-level laser sketch:** The only difference to the open Dicke model Fig. 5.3 is the purple upward arrow that results from the incoherent driving. The scaling is  $\sim N^3$ ,  $N$  to the power of the number of circles minus one. The sketch can be directly translated into code using the PsiQuaSP library.

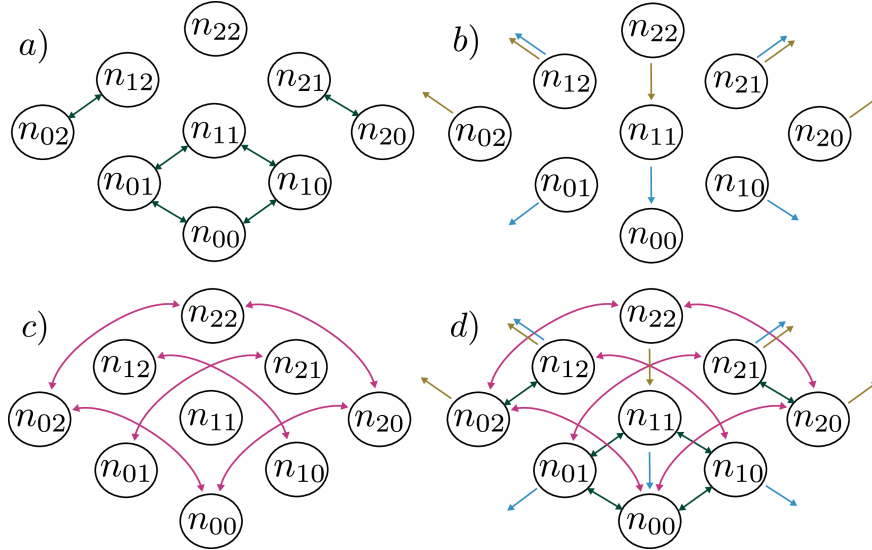


**Figure 5.7 – Sketch representation of the coherently pumped three-level laser:** Compare to Eq. (5.4.23) and Fig. 5.5 b). a) The Hamiltonian of the lasing transition  $H_{10}$  Eq. (5.4.11), b) the system-bath contributions of  $\mathcal{D}_{2\rightarrow 1}(\rho)$  (yellow) and  $\mathcal{D}_{1\rightarrow 0}(\rho)$  (blue), c) the pumping Hamiltonian  $H_P$  Eq. (5.4.24), and d) the full dynamics. The combination of  $H_{10}$  and  $H_{20}$  couples all polarization degrees of freedom to density degrees of freedom, hence the full  $\sim N^8$  scaling is needed to describe these dynamics.

brevity)

$$\dot{\rho} = \frac{i}{\hbar}[\rho, H_{10}] + \frac{\gamma_{10}}{2}\mathcal{D}_{1\rightarrow 0}(\rho) + \frac{P}{2}\mathcal{D}_{0\rightarrow 1}(\rho), \quad (5.4.22)$$

where  $H_{10}$  is the interaction Hamiltonian between the two-level systems and the mode, the term proportional to  $\gamma_{10}$  is the spontaneous emission and the term proportional to  $P$  is the incoherent pumping term, see Fig. 5.5 a). The scaling of this master equation is  $\sim N^3$ , see Fig. 5.6.

The quantum master equation for an optically pumped three-level laser scheme is

$$\dot{\rho} = \frac{i}{\hbar}[\rho, H_{10} + H_P] + \frac{\gamma_{21}}{2}\mathcal{D}_{2\rightarrow 1}(\rho) + \frac{\gamma_{10}}{2}\mathcal{D}_{1\rightarrow 0}(\rho), \quad (5.4.23)$$

Here  $H_{10}$  is the interaction with the cavity mode (cf. Eq. (5.4.11)),  $H_P$  is the optical pumping of the system (using a suitable rotating frame)

$$H_P = \hbar E(J_{20} + J_{02}). \quad (5.4.24)$$

The term proportional to  $\gamma_{21}$  is the incoherent relaxation process that brings occupation into the upper lasing level and the term proportional to  $\gamma_{10}$  is again the spontaneous emission into

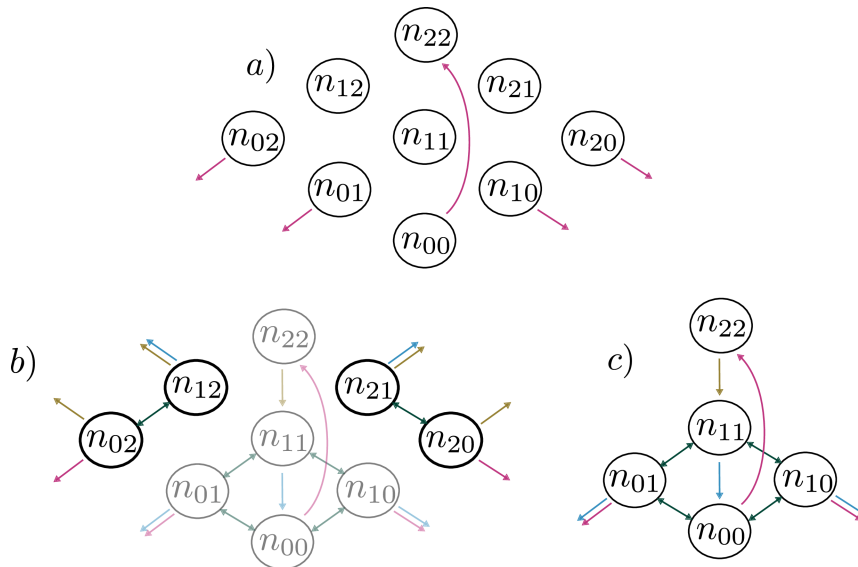


**Figure 5.8 – Sketch representation of the incoherently driven three-level laser:** Eq. (5.4.25). a) The dynamics of  $\mathcal{D}[\sigma_{20}]\rho$ , b) the full dynamics of the system: Some polarizations are completely decoupled from the rest of the dynamics and can therefore be omitted. c) The full laser dynamics can be described by a  $\sim N^4$  theory.

non-lasing modes. The level scheme of this setup is shown in Fig. 5.5 b). The associated sketches are shown in Fig. 5.7. The dissipator contributions – Fig. 5.7 b) – connect density degrees of freedom ( $\sim n_{ii}$ ) with densities, polarization degrees of freedom ( $\sim n_{ij}, i \neq j$ ) are only dephased. At this level the polarizations are decoupled from the densities and one could omit the polarizations entirely, as will become clear below. However, the Hamiltonians  $H_{10}$  and  $H_P$  connect all polarization degrees of freedom to densities, see Figs. 5.7 a) and c), so that the system has full complexity.

This behavior changes when replacing the pumping Hamiltonian  $H_P$  by an incoherent pumping Lindblad dissipator, omitting intermediate quantum coherences. The corresponding master equation is

$$\dot{\rho} = \frac{i}{\hbar}[\rho, H_{10}] + \frac{\gamma_{21}}{2}\mathcal{D}_{2\rightarrow 1}(\rho) + \frac{\gamma_{10}}{2}\mathcal{D}_{1\rightarrow 0}(\rho) + \frac{P}{2}\mathcal{D}_{0\rightarrow 2}(\rho). \quad (5.4.25)$$

The incoherent setup corresponds to the solid upward arrow in Fig. 5.5 b). This emphasizes that densities are directly transferred between the levels by the Lindblad dissipator and not via the build up of polarizations as in the  $H_P$  case.

In Fig. 5.8 a) the sketch for this Liouvillian is shown. Combining all occurring processes in a single sketch shows that four polarization degrees of freedom (i.e.  $n_{20}, n_{21}, n_{02}, n_{01}$ ) are completely decoupled from the other system dynamics, see Fig. 5.8 b). This can be used to greatly reduce the numerical complexity and the scaling with the system size  $N$ : Coherences can only be driven by coupling to densities. Starting in a state that has no quantum coherences implies that the density matrix entries for  $n_{20}, n_{21}, n_{02}, n_{01} \neq 0$  remain zero throughout the whole time evolution. Furthermore, regardless of the initial state the density matrix elements for  $n_{20}, n_{21}, n_{02}, n_{01} \neq 0$  will be zero in the steady state since they are dephased. Therefore this quantum master equation for three-level systems is *exactly* described by the quantity

$$\mathcal{P}[n_{22}, n_{11}, n_{10}, n_{01}], \quad (5.4.26)$$

where now the new relation

$$N = n_{22} + n_{11} + n_{10} + n_{01} + n_{00} \quad (5.4.27)$$

holds. From Eq. (5.4.20) it follows that this solution scales with

$$\binom{N+4}{N} \sim \frac{1}{4!} N^4. \quad (5.4.28)$$

This scaling is considerably lower than that of the coherently driven three level systems Eq. (5.4.23),  $\sim N^8$  and of course also the brute force solution  $\sim 3^{2N}$ . Please bear in mind that this does not correspond to a Hilbert/Liouville space truncation or approximation of any kind – the argument is solely that some off-diagonal density matrix elements are not connected to diagonal elements and thus remain zero and thus do not need to be computed. This still represents the full non-approximate density matrix.

With the help of the sketches the exact solution can be directly implemented (in PsiQuaSP) and the additional simplification can be seen without deriving a single equation of motion. This makes these sketches very useful. Bolaños and Barberis-Blostein [125] came to a similar decoupling in complexity: By calculating the commutation relations of the  $9^2 = 81$   $su(9)$  generators for three-level systems they observed that the master equation could be described by a  $su(3)$  subalgebra, if they only considered spontaneous emission contributions between the levels (see Section 5.5.3 for more information). This is exactly the same situation as the sketch in Fig. 5.7 b): This sketch itself could be reduced to a  $\sim N^3$  theory. However the sketches are very simple to draw – at least compared to calculating commutation relations of 81 abstract operators – and furthermore give an intuitive picture. Therefore also for a more formal Lie algebra approach these sketches are very useful, this connection will be explained in more detail below.

The coherently driven four-level laser theory would be constructed with the master equation

$$\dot{\rho} = \frac{i}{\hbar} [\rho, H_P + H_{21}] + \frac{\gamma_{32}}{2} \mathcal{D}_{3 \rightarrow 2}(\rho) + \frac{\gamma_{21}}{2} \mathcal{D}_{2 \rightarrow 1}(\rho) + \frac{\gamma_{10}}{2} \mathcal{D}_{1 \rightarrow 0}(\rho), \quad (5.4.29)$$

where the pump  $H_P$  is now between levels 3 and 0. For the incoherent driving the master equation reads

$$\dot{\rho} = \frac{i}{\hbar} [\rho, H_{21}] + \frac{\gamma_{32}}{2} \mathcal{D}_{3 \rightarrow 2}(\rho) + \frac{\gamma_{21}}{2} \mathcal{D}_{2 \rightarrow 1}(\rho) + \frac{\gamma_{10}}{2} \mathcal{D}_{1 \rightarrow 0}(\rho) + \frac{P}{2} \mathcal{D}_{0 \rightarrow 3}(\rho). \quad (5.4.30)$$

The level scheme for both setups is shown in Fig. 5.5 c). In Fig. 5.9 a) and b) the processes included in the Hamiltonians and Lindblad dissipators of the four-level laser with coherent pump are sketched. Again some of the polarization degrees of freedom decouple. The corresponding elements  $\mathcal{P}[n_{kl}, \dots]$  are zero, cf. Figs. 5.9 c) and d) and thus do not need to be computed. Consequently the complexity of this solution does not scale with  $\sim N^{15}$  but with  $\sim N^7$  instead. Interestingly this is even lower than in the three-level system case: The symmetry of the four levels allows for a more efficient decoupling of polarization degrees of freedom compared to the three-level systems, where all polarization degrees of freedom are connected to densities.

Again a further reduction is achieved via an incoherent pump term Eq. (5.4.30). The solution of this setup scales with  $\sim N^5$ , see Fig. 5.10.

The general rules for constructing the sketches are: (i) an interaction Hamiltonian connecting the levels  $x$  and  $y$  results in arrows connecting all circles  $n_{xz}$ ,  $n_{yz}$  and  $n_{zx}$ ,  $n_{zy}$ . For RWA treatments there are always two arrows connecting two circles in back and forth direction. For Non-RWA treatments there are four arrows each. (ii) a individual spontaneous decay from level  $x$  to level  $y$  results in a single arrow from  $n_{xx}$  towards  $n_{yy}$  and dephasing arrows for all circles  $n_{xz}$  and  $n_{zx}$ . These rules becomes apparent by looking at the full equations of motion in Appendix D or by the discussion in the following section.

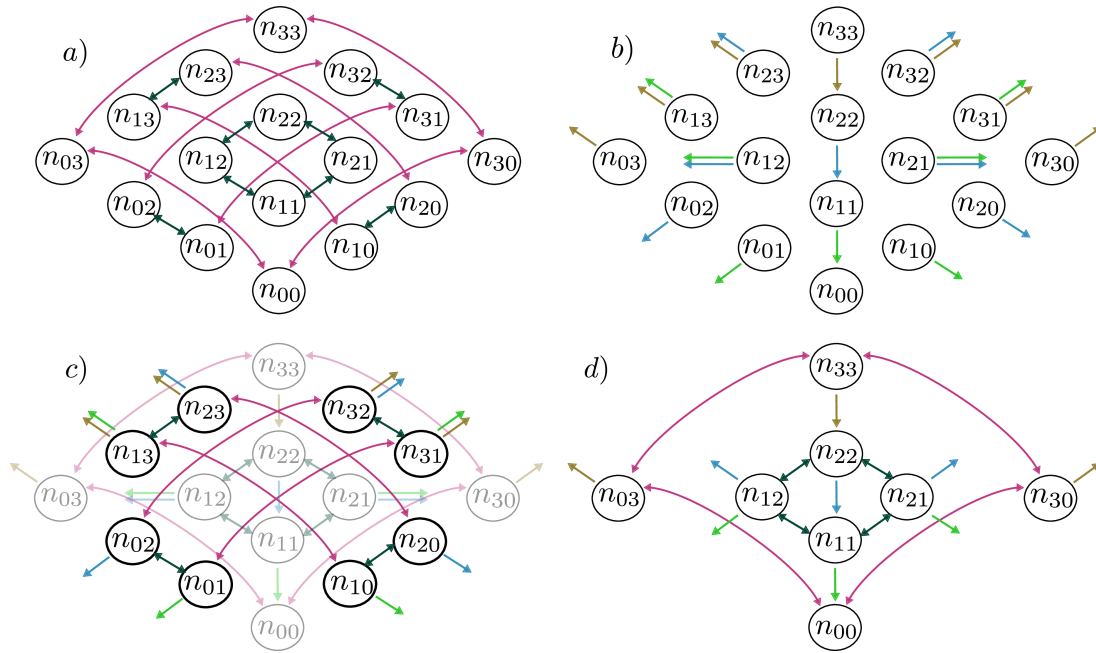


**Figure 5.9 – Sketch for the coherently driven four-level laser:** Eq. (5.4.29) and Fig. 5.5 b): a) Pumping Hamiltonian  $H_{30}$  (purple) and interaction with the lasing mode  $H_{21}$  (green), b) depletion of lower lasing level  $\mathcal{D}_{1 \rightarrow 0\rho}$  (blue), spontaneous emission into non-lasing modes  $\mathcal{D}_{2 \rightarrow 1}(\rho)$  (green), and filling of the upper lasing level  $\mathcal{D}_{3 \rightarrow 2}(\rho)$  (yellow). c) The full dynamics: Again some polarizations decouple from the rest and thus d) describes the full, non-approximate dynamics. The solution then scales as  $N^7$  as opposed to the full  $N^{15}$  scaling of the many four-level system method.

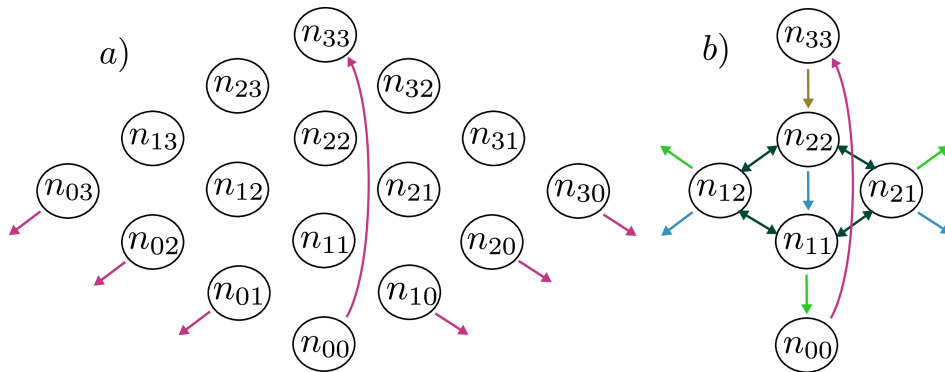


**Figure 5.10 – Sketch for the incoherently driven four-level laser:** Eq. (5.4.30): a) The dynamics of the incoherent pump term  $\mathcal{D}_{0 \rightarrow 3\rho}$ . b) The full laser dynamics can be described by a  $\sim N^5$  theory.

In this section the usefulness of the sketch representation of the permutation symmetric multi-level system method was illustrated. The sketches for the individual contributions in the master equation are easy to draw and sketches for the full quantum master equation provide an easy and quick tool to identify simplifications and to calculate the scaling behavior for a specific setup.

Even if the diagrams for the full quantum master equation dynamics may appear complicated at first sight, their construction is straightforward. Furthermore the PsiQuaSP library allows to directly translate these sketches into numerical code, which completely removes the necessity to derive equations of motion. Please bear in mind that, from a mathematical point of view, all presented solutions, representations are (numerically) exact.

The methodology presented in the last sections provides a physically intuitive picture. However it is not very general since for each Hamiltonian, or rather, each Liouville space operator a sketch representation needs to be introduced and also implemented in the PsiQuaSP library. For the Hamiltonians and dissipators discussed above this is not very difficult, however for operators like  $J_{xy}^n$  these sketches can become quite cumbersome. Therefore in order to utilize the full generality of the permutation symmetric method for quantum master equations a more flexible approach is needed. This approach will be presented in the following.

## 5.5 Symmetrized eigenstates of permutation symmetric Liouville space operators

In the previous section the permutation symmetry in the master equations was identified and exploited by directly looking at the equations of motion resulting from an expansion of the density matrix in a direct product state basis. General density matrix elements  $\rho[\dots]$  and  $\mathcal{P}[\dots]$  were introduced and the action of the Liouvillians were found to either leave these elements invariant or transform them into another one of these elements. Therefore closed equations of motion could be achieved.

In this section the findings of the previous section will be generalized: The expansion of the master equation in the  $\mathcal{P}[\dots]$  representation is equivalent to expanding the master equation in symmetrized Liouville space states. These states are the eigenstates of special permutation symmetric Liouville space operators and other permutation symmetric operators serve as flip operators between these states. These operators form a  $su(n)$  Lie algebra, with  $n$  being the number of necessary individual spin matrices  $\sigma_{kl}^i$ . The symmetrized eigenstates represent the associated totally symmetric multiplet, similar to the (totally symmetric) superradiant Dicke or Gelfand-Tsetlin states but in Liouville space instead of Hilbert space. These states and the actions of the symmetrized Liouville space operators can again be represented by simple sketches. This more formal treatment allows to realize that the permutation symmetric Liouville space operators serve as elementary building blocks that can be utilized to construct arbitrary Liouville space operators. This can be used to construct arbitrary quantum master equations and observables (that are permutation symmetric). This is implemented in the PsiQuaSP library [26] to provide maximal flexibility in constructing arbitrary master equations. This approach is necessary because the theory of the last section allows to implement arrows for *specific* Hamiltonians and dissipators but the permutation symmetric method is in principle applicable to *any* permutation symmetric master equation. Since it is not possible to write ready made functions for all conceivable permutation symmetric Liouville space operators there needs to be another, more flexible approach. Exactly this is provided by the approach presented in this section. Furthermore the more formal treatment of this section also allows to identify generalizations and more general, theoretical properties and possibilities of the method. Parts of the discussion in this section were published in the PsiQuaSP publication M. Gegg and M. Richter, *arXiv:1707.01079*

[27].

The definition of the  $\mathcal{P}[\dots]$  representation derived in the last sections is

$$\mathcal{P}[\{n_{kl}\}] = \binom{N}{\{n_{kl}\}} \rho[\{n_{kl}\}] = \binom{N}{\{n_{kl}\}} \text{tr}[|\dots n_{kl}, \mathbf{u}_{kl} \dots\rangle \langle \dots | \rho], \quad (5.5.1)$$

where  $\{n_{kl}\} = \{n_{(d-1)(d-1)}, \dots\}$  is a short hand notation, it is the set of all numbers  $n_{kl}$ . In this expression the Hilbert-Schmidt product of a single, direct product Liouville space state with the density matrix is computed and multiplied with the total number of direct product states that yield the same Hilbert-Schmidt product. In the following this expression will be rewritten as a sum over all these direct product basis states.

Expressing these Liouville space basis state directly in terms of the spin matrices results in

$$\begin{aligned} |\dots n_{kl}, \mathbf{u}_{kl} \dots\rangle \langle \dots| &= \dots \underbrace{\sigma_{kl}^{i_1} \otimes \sigma_{kl}^{i_2} \dots \otimes \sigma_{kl}^{i_{n_{kl}}}}_{\equiv \sigma_{kl}^{\otimes n_{kl}}} \dots \\ &= \bigotimes_{k,l} \sigma_{kl}^{\otimes n_{kl}}. \end{aligned} \quad (5.5.2)$$

This expression does not contain the information about the sets, the ordering of the individual spin matrices is not uniquely defined – there are many permutations of spin matrix indices that can be written as such a product of spin matrices, characterized by the numbers  $\{n_{kl}\}$ . However it is possible to construct a unique basis state by forming a symmetric superposition of all possible basis states for fixed  $\{n_{kl}\}$ :

$$\hat{\mathcal{P}}[\{n_{kl}\}] \equiv \mathcal{S} \bigotimes_{k,l} \sigma_{kl}^{\otimes n_{kl}}, \quad (5.5.3)$$

where  $\mathcal{S}$  is again the symmetrization operator

$$\mathcal{S} = \sum_P \hat{P}, \quad (5.5.4)$$

with  $\hat{P}$  being the permutation operator and the sum runs over all possible permutations  $P$  of multi-level system indices  $i$ . The number of possible permutations is again the multinomial coefficient Eq. (5.4.18)

$$\binom{N}{\{n_{kl}\}} = \frac{N!}{n_{00}! n_{01}! \dots}. \quad (5.5.5)$$

Since the trace has the property  $\text{tr}[A + B] = \text{tr}[A] + \text{tr}[B]$  it follows that

$$\mathcal{P}[\{n_{kl}\}] = \text{tr}[\hat{\mathcal{P}}[\{n_{kl}\}]\rho]. \quad (5.5.6)$$

Hence the expansion of the density matrix found in the previous section is equivalent to defining a basis of totally symmetric superpositions of direct product Liouville space basis states.

### 5.5.1 Permutation symmetric Liouville space operators – Elementary sketches

As stated above there are two types of permutation symmetric Liouville space operators  $\Gamma$ : Operators to which the symmetrized basis states Eq. (5.5.3) are eigenstates and general flip operators that transform one eigenstate into the other. These two types of  $\Gamma$  operators can be defined via their action on the symmetrized basis states  $\hat{\mathcal{P}}[\{n_{kl}\}]$

$$\Gamma_{mm}^{nn} \hat{\mathcal{P}}[\{n_{kl}\}] \equiv \sum_i \sigma_{mm}^i \hat{\mathcal{P}}[\{n_{kl}\}] \sigma_{nn}^i \quad (5.5.7)$$

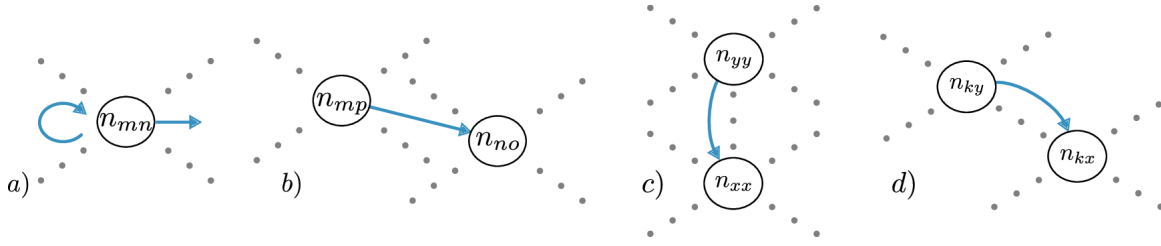


**Figure 5.11 – Modular sketches for identical multi-level systems:** a) The nonconnecting arrow can represent the phase oscillations arising from the self energy Hamiltonians (curved arrow) and it can describe dephasing (straight arrow). The self energy Hamiltonian was omitted in the discussion of the last section. b) The connecting arrow connects two different circles. It can represent density relaxation c) and elements of flip operators d).

and

$$\Gamma_{mn}^{op} \hat{\mathcal{P}}[\{n_{kl}\}] \equiv \sum_i \sigma_{mn}^i \hat{\mathcal{P}}[\{n_{kl}\}] \sigma_{op}^i, \quad (5.5.8)$$

requiring that  $m \neq n$  and  $o \neq p$ . It can be shown that

$$\Gamma_{mm}^{nn} \hat{\mathcal{P}}[\{n_{kl}\}] = n_{mn} \hat{\mathcal{P}}[\{n_{kl}\}], \quad (5.5.9)$$

hence the symmetrized Liouville space states are in fact eigenstates of the permutation symmetric Liouville space operators. The action of the other operators is given by

$$\Gamma_{mn}^{op} \hat{\mathcal{P}}[\{n_{kl}\}] = (n_{mp} + 1) \hat{\mathcal{P}}[\dots n_{mp} + 1 \dots n_{no} - 1 \dots], \quad (5.5.10)$$

hence they serve as generalized flip operators. The commutation relations for these operators are given by

$$\begin{aligned} [\Gamma_{mn}^{op}, \Gamma_{qq}^{rr}] &= +\Gamma_{mn}^{op} \delta_{nq} \delta_{or} - \Gamma_{mn}^{op} \delta_{mq} \delta_{pr}, \\ [\Gamma_{mn}^{op}, \Gamma_{qr}^{st}] &= +\Gamma_{mr}^{sp} \delta_{nq} \delta_{to} - \Gamma_{qn}^{ot} \delta_{rm} \delta_{ps} \end{aligned} \quad (5.5.11)$$

and zero otherwise. The corresponding proofs can be found in Appendix B.2.

The corresponding sketches are shown in Fig. 5.11: In all the sketches so far there were two different types of arrows – connecting and non-connecting arrows. Non-connecting arrows just point from one circle away, representing a dephasing process and the connecting arrows connect two circles. It turns out that a single non-connecting arrow corresponds to a  $\Gamma_{mn}^{nn}$  operator and a single connecting arrow corresponds to a  $\Gamma_{mn}^{op}$  connecting arrow. Thus these complicated looking operators are just the formal, mathematical formulation of the individual arrows in the sketches<sup>5</sup>, which again is not very complicated and the (PsiQuaSP) user just needs to draw these sketches. These sketches already imply some interesting identities/sum rules, which are needed to construct physically meaningful operators (sketches) from these elementary operators (arrows).

### 5.5.2 Building physically meaningful Liouville space operators

In the discussion above the elementary Liouville space operators and the corresponding sketches were introduced. Here the necessary relations to construct physically meaningful operators are

<sup>5</sup>In the case of the emitter-cavity coupling the arrows also implicitly represented actions on the mode degrees of freedom, which is not the case here.

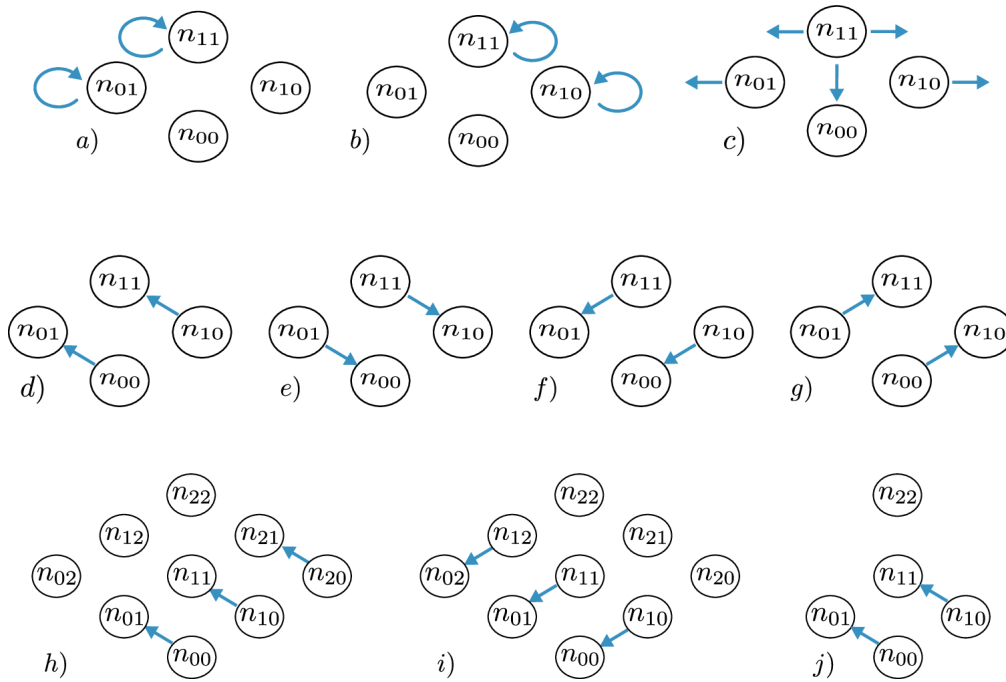


**Figure 5.12 – Building complex Liouvillians from elementary sketches:** a) and b) correspond to the two operators  $J_{11}^L$  and  $J_{11}^R$ . c) The spontaneous emission Liouvillian in the elementary picture. d) - g) The sketches corresponding to  $J_{10}^L$ ,  $J_{01}^L$ ,  $J_{10}^R$ ,  $J_{01}^R$  for two-level systems. h) - j) three-level system operators:  $J_{10}^L$ ,  $J_{10}^R$  and  $J_{10}^L$  for reduced complexity.

introduced. For this purpose it is useful to use the  $R, L$  algebra notation for Liouville operators [126], which is defined by

$$O\rho \equiv O^L\rho, \quad \rho O \equiv O^R\rho. \quad (5.5.12)$$

Using this notation there are four relevant Liouville space operators based on the collective spin operators  $J_{\dots}$ :  $J_{kk}^L$ ,  $J_{kk}^R$  and  $J_{kl}^L$ ,  $J_{kl}^R$ . The relations between these operators and the elementary  $\Gamma$  operators are

$$\begin{aligned} J_{kk}^L &= \sum_n \Gamma_{kk}^{nn} = \sum_n \sum_i \sigma_{kk}^i \dots \sigma_{nn}^i, \\ J_{kk}^R &= \sum_n \Gamma_{nn}^{kk} = \sum_n \sum_i \sigma_{nn}^i \dots \sigma_{kk}^i, \\ J_{kl}^L &= \sum_n \Gamma_{kl}^{nn} = \sum_n \sum_i \sigma_{kl}^i \dots \sigma_{nn}^i, \\ J_{kl}^R &= \sum_n \Gamma_{nn}^{kl} = \sum_n \sum_i \sigma_{nn}^i \dots \sigma_{kl}^i. \end{aligned} \quad (5.5.13)$$

The corresponding proof of these relations are shown in Appendix A, while explaining how to construct arbitrary operators in PsiQuaSP. With this set of results it is clear how to construct e.g. a von-Neumann equation for a general self energy Hamiltonian  $H_0 = \hbar\omega J_{kk}$

$$\dot{\rho} \sim i/\hbar[\rho, H_0] = i/\hbar(H_0^R - H_0^L)\rho = i\omega \sum_n (\Gamma_{nn}^{kk} - \Gamma_{kk}^{nn})\rho \quad (5.5.14)$$

or a general individual dissipator

$$\begin{aligned} \mathcal{D}\rho &= \frac{\gamma}{2} \left( \sum_i 2\sigma_{kl}^i \rho \sigma_{ik}^i - J_{ll} \rho - \rho J_{ll} \right) = \frac{\gamma}{2} \left( \sum_i 2\sigma_{kl}^{i,L} \sigma_{ik}^{i,R} - J_{ll}^L - J_{ll}^R \right) \rho, \\ &= \frac{\gamma}{2} \left( 2\Gamma_{kl}^{lk} - \sum_n \Gamma_{ll}^{nn} - \sum_n \Gamma_{nn}^{ll} \right) \rho. \end{aligned} \quad (5.5.15)$$

In Fig. 5.12 a) - c) the corresponding sketches are shown for two-level systems. Fig. 5.12 d) - g) represent the two-level system flip operators  $J_{10}^{L,R}$   $J_{01}^{L,R}$  and Fig. 5.12 h) - j) show different flip operators for three-level systems.

The construction of equations of motion from these expressions is done by multiplying with  $\hat{P}[\dots]$  from the left performing the trace operation, see Appendix A for details and the corresponding PsiQuaSP implementation.

### 5.5.3 Lie algebra context

The commutation relations Eq. (5.5.11) are the same commutation relations as the ones found for the multi-level systems (Eq. (2.1.8)), thus the  $\Gamma$  operators form a Lie algebra and the symmetrized basis states Eq. (5.5.3) are the totally symmetric multiplet (or irreducible representation) of this algebra. The order of the Lie algebra is  $su(d^2)$  for identical  $d$ -level systems, or lower if coherences decouple as in Section 5.4.3. The only difference between the  $\hat{\mathcal{P}}$  basis and the Gelfand-Tsetlin basis states of Chapter 4 is that the  $\hat{\mathcal{P}}$  are Liouville space basis states and not Hilbert space basis states. This raises the question whether antisymmetric Liouville space basis states are of interest: The definition of the trace or rather the Hilbert space identity

$$I_H = \sum_{\{n_{kk}\}} \hat{\mathcal{P}}[\{n_{kk}\}], \quad (5.5.16)$$

is included in the symmetric basis states and not in the (partially) anti-symmetric basis states. Here  $\{n_{kk}\} = \{n_{11}, n_{22}, \dots\}$  is the set of all density like quantum numbers. Also the ground state  $\hat{\mathcal{P}}[0, 0, \dots]$  is part of the symmetric and therefore not the (partially) anti-symmetric multiplets. Thus confining the system to an anti-symmetric multiplet is probably unphysical. Including all multiplets symmetric and anti-symmetric should recover the full exponential complexity of the individual direct product Liouville space basis.

A direct consequence of this formulation is that it is possible to apply analytic Lie algebra techniques like bosonization techniques, such as the Holstein-Primakoff bosons or the Jordan-Schwinger bosons [91]. In the Holstein-Primakoff bosonization the  $su(n)$  operators are replaced by  $n - 1$  bosonic mode operators, while the Jordan-Schwinger bosonization requires  $n$  bosons. These techniques often allow for analytic solutions. Please note that this technique is usually used for Hilbert space operators, applying these transformations to the operators introduced here corresponds to a Liouville space bosonization ansatz. For a simple three-level system setup the Jordan-Schwinger bosons were successfully used in Ref. [125].

In general the minimal group for the permutation symmetric formalism is  $su(2)$  e.g.

$$\hat{\mathcal{P}}[n_{11}] = \mathcal{S} \sigma_{11}^{\otimes n_{11}} \sigma_{00}^{\otimes n_{00}} \quad (5.5.17)$$

which is a valid basis for e.g. individually decaying two-level systems described by the master equation

$$\dot{\rho} = \frac{\gamma}{2} \sum_i (2\sigma_{01}^i \rho \sigma_{10}^i - \sigma_{11}^i \rho - \rho \sigma_{11}^i). \quad (5.5.18)$$

This can be seen from the sketches, e.g. Fig. 5.11 c). There the polarization degrees of freedom decouple. This result is obtained without explicitly computing commutation relations, thus also

in the group theoretic context the sketch representation is useful.

This basis is the symmetric  $su(2)$  multiplet in Liouville space. Thus the individual spontaneous decay of a set of indistinguishable two-level systems is governed by the Liouville space analogue of the superradiant Dicke states (symmetric  $su(2)$  multiplets). Inclusion of coherent, collective properties always results in adding two quantum numbers  $n_{xy}$  and  $n_{yx}$ . Of course this is merely a toy example but this illustrates the flexibility of the approach.

## 5.6 Recovering the Dicke states – How to diagonalize the density matrix

The results presented so far are useful if one seeks the solutions to a quantum master equation: The number of different symmetrized basis states is given by Eq. (5.4.20)

$$D = \binom{N+m}{N} \propto \frac{1}{m!} N^m, \quad (5.6.1)$$

therefore we can implement equations of motion which represent a set of  $D$  coupled linear homogeneous differential equations, which means that the Liouvillian  $\mathcal{L}$  of the master equation

$$\dot{\rho} = \mathcal{L}\rho \quad (5.6.2)$$

can be written as a  $D \times D$  matrix, see Appendix A and B. This can be used for time-integration or direct steady state computation, e.g. via iterative Krylov-subspace methods. This corresponds to a vectorized representation of the master equation, meaning the density matrix is represented by a vector in this picture, which is also the underlying representation in PsiQuaSP (see Appendix B.2 for details on vectorized representation).

If one wishes to compute for example the von-Neumann entropy [94]

$$S = -\text{tr}(\rho \ln \rho) \quad (5.6.3)$$

it is necessary to diagonalize the density matrix since the logarithm of a matrix is only defined in the diagonal form. Using the  $\hat{\mathcal{P}}$  representation to reconstruct the density *matrix* in the direct product state basis Eqs. (5.3.3) and 5.4.13 would again result an exponentially scaling density matrix  $d^N \times d^N$  for  $d$ -level systems. Many of the entries in this matrix are identical, but still, the diagonalization or even storage of such a matrix is not feasible even for moderate  $N$ . Fortunately there is a way to find a block diagonal representation of the density matrix

$$\rho = \begin{pmatrix} \rho_1 & 0 & 0 & \dots \\ 0 & \rho_2 & 0 & \dots \\ 0 & 0 & \rho_3 & \dots \\ \vdots & \vdots & \vdots & \ddots \end{pmatrix}, \quad (5.6.4)$$

where each of the sub-blocks scales at most polynomially in  $N$  for identical  $d$  level systems. The basis states in which the density matrix is block diagonal are the  $su(d)$  multiplet states, i.e. for two-level systems the density matrix is block diagonal in the Dicke basis. For two-level systems this was shown by Xu and Holland [110] and Chase, Geremia and Baragiola [98, 99]. For multi-level systems this result has not been published so far in quantum optics, to the best of my knowledge<sup>6</sup>. The details of how to reconstruct the Dicke states and the proof for the

<sup>6</sup>From a group theoretic stance this relation seems very fundamental, thus it is likely that this relation does exist somewhere in group theory. The group theoretic formulation of the statement would be: The block diagonal representation a matrix of  $N$  identical  $d$ -level systems in the  $su(d)$  multiplets is equivalent to the totally symmetric multiplet of  $su(d^2)$ .

equality for multi-level systems are outlined in Appendix B.2. Please note that this result is independent of what kind of master equation is considered, the only requirement is that the multi-level systems are indistinguishable.

For two-level systems this means that only matrices of order  $N \times N$  need to be diagonalized, for multi-level systems the blocks scale at most polynomially, which is a dramatic reduction in complexity. The block size in the Dicke basis is defined by the quantum number  $l$ , each block corresponds to the number of possible  $m$  values  $2l + 1$ , meaning that each block has  $(2l + 1)^2$  entries. In fact the sum over all the block entries recovers the scaling found from the permutation symmetry

$$\sum_{l=0,1/2}^{N/2} (2l + 1)^2 = \frac{1}{6}(N + 1)(N + 2)(N + 3). \quad (5.6.5)$$

Hence the two statements (i) "the density matrix is block diagonal in the Dicke basis", (ii) "the master equation bears permutation symmetry" and (iii) "the multi-level systems are indistinguishable" are equivalent. From an intuitive perspective this can be understood as follows: The contributions of the Hamiltonian part of the master equation do not couple different Dicke subspaces, only the  $J^2$  symmetry breaking dissipator terms do so. Dissipators should not induce coherences therefore the density matrix should be block diagonal, since if it wasn't block diagonal the dephasing would induce nonzero off-diagonal elements.

## 5.7 Conclusion

The discussion in this chapter showed that the inclusion of (individual) dissipation of the multi-level systems breaks the symmetry of the  $su(n)$  Casimir operators. This means that the system of identical multi-level systems cannot be described by the symmetric  $su(n)$  multiplet states alone, which at first glance seems to result in an exponential complexity of the underlying equations of motion/Liouville space. However it was shown that the permutation symmetry imposed by the requirement of indistinguishable multi-level systems reduces this complexity again to a polynomial complexity. This can be shown by directly looking at the equations of motion or by introducing symmetrized Liouville space states and permutation symmetric Liouville space operators. The first approach provides a simple and accessible treatment, while the second approach is more general and mathematically sound. This treatment is then found to be identical to a block diagonal representation of the density matrix in the  $su(d)$  multiplet states for  $d$ -level systems. This is an incredibly useful relation for density matrix diagonalization.

The sketch representation introduced in this chapter provides a simple and intuitive approach to the methodology and makes it possible to completely omit any equations of motion. The sketches also provide a very powerful tool to identify further symmetries in the setup, which could in principle also be derived from the Lie algebraic considerations, but the sketch representation makes these considerations much more simple. Thus both for intuition and sound mathematical treatments the sketch representation provides a major benefit. Furthermore the sketch representation was used to design the PsiQuaSP library that allows to translate these sketches directly into code, which greatly reduces code development time.

## **A** The PsiQuaSP Library

In the last chapter the permutation symmetric method for quantum master equations was introduced and a sketch representation was developed. In this chapter the library PsiQuaSP is presented, which is an object oriented C++ implementation of this method. PsiQuaSP is an acronym for *Permutation symmetry for identical Quantum Systems Package*. It is based on the PETSc library for iterative sparse matrix methods and differential equations. The library was made publicly available on GitHub: <https://github.com/modmido/psiquasp> and an introduction/manual was published: M. Gegg and M. Richter, *arXiv:1707.01079* [27]. The following discussion is a close adaptation from this publication.

The main design feature of PsiQuaSP is that it allows to translate the sketch representation of the permutation symmetric method directly into code. The user does not need to derive any equation of motion. The bubbles and arrows can each be set by single function calls and the whole setup of the equations of motion is handled internally by PsiQuaSP. Solving these equations is then entirely handled by PETSc and related packages such as SLEPc. The internal design of PsiQuaSP allows to write scalable, efficient code while being very user friendly. There are several examples in the `example/` directory introducing the basic and advanced possibilities that PsiQuaSP provides. Overall, library and examples, PsiQuaSP contains over 20000 lines of code in  $\sim 50$  source code files, it has been implemented for  $> 10$  different master equations and successfully tested on Linux and macOS operating systems. It uses recursive GnuMake to facilitate the installation procedure. The comments in the source code are written in Doxygen [127] formatting, providing a comprehensible and easily accessible documentation in a html website format, see Fig. A.1.



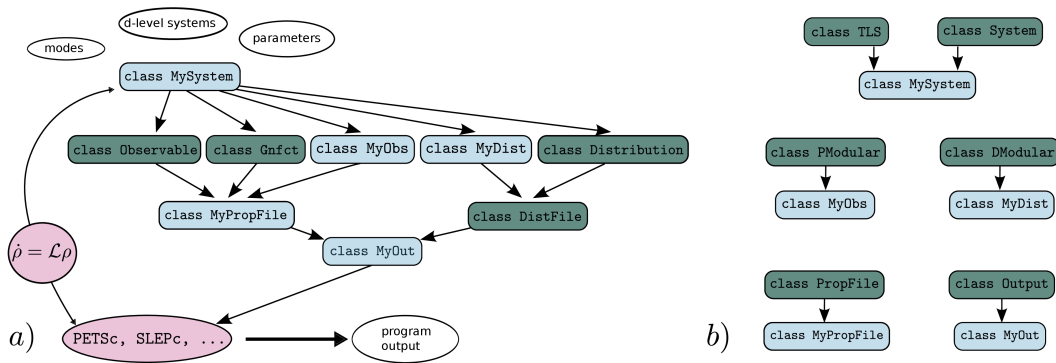


**Figure A.2 – Structure of the PsiQuaSP library:** a) Schematic representation of the general structure of a PsiQuaSP application code: `MySystem` contains all the relevant information about the system and is used to construct the master equation and the output. The output is organized in three layers, the first layer consists of objects that can compute the desired properties of the system, like `Observable`, `Distribution`, the correlation functions `Gnfct` and the custom types `MyObs` and `MyDist`. The second layer groups these objects into output files, each managed by another object. The third layer consists of the `MyOut` class, which groups all output files and provides a clean interface to PETSc. Classes that need to be derived from base classes have blue boxes, green boxes indicate ready to use classes. b) Base class diagram for the derived classes in a). Only for `MySystem` there are two possibilities: `TLS` for two-level system setups and `System` for all other purposes like  $d$ -level systems.

setting up the master equation. The output of the program is managed by the `Output` class, which can manage a set of user defined output files, containing observables, correlation functions, distributions, etc, see Fig. A.2 a). Please note that even though PsiQuaSP is intended and designed for solving permutationally symmetric master equations, the library is not limited to this application. It may also be used for efficient treatments of nonidentical multi-level systems as well as Hamiltonian diagonalizations, see Chapter 9.

Installation instructions for PsiQuaSP and PETSc are given in the `README.md` and `INSTALL.md` files in the PsiQuaSP folder. PsiQuaSP uses Doxygen commenting. Doxygen translates the comments in the source code into a structured website representation, which is extremely useful for getting to know the library. Read `doc/README.md` for further information.

## A.2 Examples

The setup of PsiQuaSP simulations will now be illustrated by discussing examples. All source codes of the examples and many more can be found in the `example/` directory in the PsiQuaSP directory.

### A.2.1 Example 1: Open Tavis-Cummings relaxation

The first example will be the master equation introduced at the beginning of Chapter 5: Eqs. (5.2.1), (5.2.2) and (5.2.3), which was the starting point of the whole derivation of the  $\hat{\mathcal{P}}$  formalism. The equation describes the Dicke Hamiltonian, including spontaneous emission and cavity loss

$$\dot{\rho} = \frac{i}{\hbar}[\rho, H] + \mathcal{D}_{1 \rightarrow 0}(\rho) + \mathcal{D}_{ph}(\rho), \quad (\text{A.2.1})$$

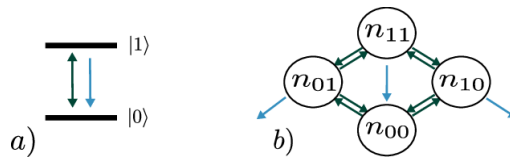


**Figure A.3 – Open Tavis-Cummings relaxation:** a) The level scheme for the individual two-level system and b) the sketch for the  $\mathcal{P}$  representation of this master equation.

with the Dicke Hamiltonian in RWA

$$H = \hbar\omega_0 b^\dagger b + \hbar\omega_1 J_{11} + \hbar g(J_{10}b + J_{01}b^\dagger) \quad (\text{A.2.2})$$

and the Lindblad dissipators

$$\mathcal{D}_{1\rightarrow 0}(\rho) = \frac{\gamma}{2} \sum_i (2\sigma_{01}^i \rho \sigma_{10}^i - \sigma_{11}^i \rho - \rho \sigma_{11}^i), \quad (\text{A.2.3})$$

$$\mathcal{D}_{ph}(\rho) = \frac{\kappa}{2} (b\rho b^\dagger - b^\dagger b\rho - \rho b^\dagger b). \quad (\text{A.2.4})$$

In Fig. A.3 the level scheme and the corresponding sketch are shown. It is the setup of a basic Tavis-Cummings/Dicke model including individual spontaneous decay of the two-level systems and a cavity loss term. The example code computes the temporal dynamics of this master equation using direct Runge-Kutta time integration. The source code can be found in `example/ex1a`. `example/ex1b` solves the same equation with an adaptive step width Runge-Kutta and at the same time shows the application of more advanced PETSc routines. Since there is no pump term in this master equation the steady state will be the ground state and we need to prepare the system initially in an excited state in order to observe nontrivial dynamics.

*System/Master equation setup:* First a derived class for the system under consideration is declared:

```
class OTC: public TLS
{
public:
void Setup(Vec * dm, Mat * L);
};
```

This class just defines a setup function. This is the standard procedure for all user derived classes in PsiQuaSP, i.e. in most cases user derived classes just define a setup function. Here the base class TLS is used, which provides enhanced tools for master equations only involving two-level systems. Here the setup function will create a vector `Vec * dm` and a matrix `Mat * L`, which are the density matrix and the Liouvillian of the system. PsiQuaSP uses a vectorized version of the master equation. The two types `Vec` and `Mat` are defined by PETSc. Both can be either serial or parallel, `Mat` is sparse by default (but dense types are available if needed), leading to efficient memory usage and reduction in computation time.

In the `OTC::Setup(...)` function we call the functions

```
TLSAdd(ntls,ntls,ntls,tlsenergy);
ModeAdd(m0+1,dm0,modeenergy);
PQSPSetup(dm,1,L);
```

to tell PsiQuaSP that `ntls` two-level systems and one bosonic mode with maximum Fock state `m0` are considered. `TLSAdd(...)` adds the two-level system quantum numbers  $n_{11}$ ,  $n_{10}$  and  $n_{01}$ , c.f. Fig. A.3 b). The  $n_{00}$  quantum number is not needed, as explained in the previous chapter. The three arguments `ntls,ntls,ntls` specify the maximum number for the three indices  $n_{11}$ ,  $n_{10}$ ,  $n_{01}$ . This allows for a truncation of the three individual quantum numbers.

`tlsenergy` and `modeenergy` are the transition energies for exciting a two-level system and the photon energy, which are needed for preparing the system in a thermal equilibrium state. These energy parameters are independent of the parameters used for the equation of motion since rotating frame representations might be used. After this the user needs to call `PQSPSetup()`, the setup function for all internal structures which creates the density matrix vector `dm` and the Liouvillian matrix `L`. Now the master equation is specified. This is done by calling

```
AddTLSHO(*L, NULL, NULL, 1, domega_tls*PETSC_i);
AddTavisCummingsHamiltonianRWA(*L, NULL, NULL, 1, 0, gcouple*PETSC_i);
AddTLSSpontaneousEmission(*L, NULL, NULL, 1, gamma/2.0);
AddLindbladMode(*L, NULL, NULL, 1, 0, kappa/2.0);
```

Here each line adds the contributions of a different term of the master equation to the Liouvillian matrix `L`. The sketch for `AddTLSSpontaneousEmission(...)` is represented by the blue arrows in Fig. A.3 b) and `AddTavisCummingsHamiltonianRWA(...)` is represented by the green arrows in Fig. A.3 b).

Mode related Liouvillians like `AddLindbladMode(...)` are not represented in sketches and the `AddTLSHO(...)` is given by the combination of sketches Fig. A.7 a) and b). In this example a rotating frame representation is used and `domega_tls` is the detuning of the two-level systems from the cavity mode, on resonance `domega_tls = 0.0` holds<sup>2</sup>. The next step is to specify initial conditions, here we prepare the system in an excited state:

```
PetscInt qnumbers [5] = {n11, n10, n01, mket, mbra};
DMWritePureState(*dm, qnumbers);
```

The `qnumbers` array contains the quantum numbers of the desired state. This setup function can prepare the density matrix in any of the permutation symmetric basis states equation (5.5.3). However only for `n10 = n01 = 0` and `mket = mbra` the state corresponds to a physically meaningful population. This function addresses the different quantum numbers in the order they have been set: As stated above the `TLSSAdd(...)` function call adds the two-level system quantum numbers in the order  $n_{11}$ ,  $n_{10}$ ,  $n_{01}$  and the function `ModeAdd(...)` always adds first the ket and then the bra quantum number of  $|m_{\text{ket}}\rangle\langle m_{\text{bra}}|$ . Adding two modes in this example via two successive calls to `ModeAdd(...)` would require to address an individual state with an array like

```
PetscInt qnumbers [7] = {n11, n10, n01, m0ket, m0bra, m1ket, m1bra};
```

`PsiQuaSP` internally labels the modes with numbers starting from 0 in the order of creation.

To create an object of the system specification class `OTC`, e.g. in the main routine the constructor and the setup function are called

```
OTC otc;
otc.Setup(&dm, &L);
```

The `otc` object has two purposes: It creates all ingredients to the master equation and after successful setup it contains all necessary information about the system. Afterwards the object is used to build observables and to specify the output data.

*Defining the output:* The expectation value of a collective operator like  $J_{11}$  (Eq. (4.1.1)), which represents the mean occupation of the excited states of all two-level systems

$$\langle J_{11} \rangle = \text{tr}[J_{11}\rho] = \sum_{n=0}^N \sum_m n \mathcal{P}[n, 0, 0; m, m] \quad (\text{A.2.5})$$

can be defined using the `Observable` class:

<sup>2</sup>On resonance we could in principle leave out the `AddTLSHO(...)` setup function, however PETSc solvers require that the diagonals of every sparse matrix are explicitly set, even if they are zero. Since `AddTLSHO(...)` adds all these diagonal elements it should always be included, or the user calls the function `AddDiagZeros(...)` that could be used instead of `AddTLSHO(...)` on resonance.

```
Observable *pdens11 = new Observable();
MLSDim n11 (1,1);
pdens11->SetupMlsOccupation(otc,n11);
```

Here `n11` is an identifier referring to the  $n_{11}$  degree of freedom and the function `SetupMlsOccupation()` can be used to define all  $\langle J_{kk} \rangle$  observables for two-level systems

$$\langle J_{kk} \rangle = \sum_{n_{kk}=0}^N \sum_{\dots} n_{kk} \mathcal{P}[\dots n_{kk} \dots], \quad (\text{A.2.6})$$

where the second sum runs over all density degrees of freedom, e.g. a partial trace. The `MLSDim` and `ModeDim` classes provide a way to access different degrees of freedom within the application code. Output files that print observables, distributions etc. at every  $n$ th time step are also managed by classes,  $n$  is equal to 30 by default and can be changed with the `-tev_steps_monitor newvalue` command line option. For files printing observables like  $J_{kk}$  the user creates a derived class like

```
class ObservablesFile: public PropFile
{
public:
void SetupMyObsFile(OTC * otc, std::string name);
};
```

As in the `OTC` class only the definition of a setup function is required. `name` is the name for the output file. This class is derived from the `PropFile` class. Classes derived from this class allow the user to print an arbitrary number of user specified properties that are related to operator expectation values. This includes standard (already implemented) observables of the `Observable` class, correlation functions  $g^{(n)}(\tau)$  (`Gnfct` class) and user defined custom observables (`PModular` class). Within this setup function the `Observable` object needs to be created as above and added to the output file with the command

```
AddElem(pdens11, "<J_11>");
```

The second argument is the name of this quantity will have in the header of the output file. This observables file including an arbitrary number of other user specified output files is bundled into the `MyOut` class

```
class MyOut: public Output
{
public:
void SetupMyOut(OTC * system);
};
```

The setup function includes the following function calls

```
ObservablesFile *obsfile = new ObservablesFile;
obsfile->SetupMyObsFile(system, "observables.dat");
AddOFile(obsfile);
```

The user can specify an arbitrary number of different output files for customized purposes by either providing multiple setup functions in one class or deriving a new class with a single setup function for each file. Aside from files managing observables the `DistFile` class is used for number state distributions of the modes and the multi-level systems, as well as more complicated (also custom made) distributions like the `DickeDistribution`. The usage of the `DistFile` class is straightforward and can be seen in the example codes.

As for the `OTC` class e.g. in the main file we need to call

```
MyOut *out = new MyOut;
out->SetupMyOut(&otc);
```

These function calls create the whole output structure of the program bundled into one object.

Generally PsiQuaSP provides functionality for setting up vectors and matrices and to create the output object (`out`). These three types of objects (`Vec`, `Mat` and `MyOut`) then provide the input fed into the PETSc (SLEPc, ...) solution routines. Please note that PETSc vectors are not always density matrices and matrices are not always Liouvillians for the master equation. For example the trace operation and therefore any computation of an observable can be defined as a PETSc vector which is subsequently applied to the density matrix via a scalar product using the PETSc routine `VecDot(...)`: Defining a custom observable  $\langle \hat{O} \rangle$  usually is done by setting the matrix for the Liouvillian corresponding to the action of  $\hat{O}\rho$ , multiplying it with the trace vector and storing the resulting vector. The computation of the observable is then given by the scalar product of this vector with the density matrix vector (`VecDot(...)`). This is shown in `example/ex2a`. This is also the proper choice for multi-level system observables.

*Solution using PETSc:* The numerical solution is handled by PETSc, which in this example is done by simple time integration using a normal fourth order Runge-Kutta in `example/ex1a` and an adaptive time step Runge-Kutta in `example/ex1b`. The basic setup of a time integration using PETSc is as follows:

```
TS ts;
TSCreate(PETSC_COMM_WORLD,&ts);
TSSetType(ts,TSRK);
```

This creates the PETSc time stepper context `TS` and sets it to Runge-Kutta. `PETSC_COMM_WORLD` is the PETSc MPI communicator. PsiQuaSP is fully parallelized by default by using the PETSc routines, but it can of course always be run on a single processor. With the commands

```
TSSetRHSFunction(ts,NULL,TSComputeRHSFunctionLinear,NULL);
TSSetRHSJacobian(ts,L,L,TSComputeRHSJacobianConstant,NULL);
```

one tells PETSc that the right hand side of the differential equation ( $\dot{\rho} = \mathcal{L}\rho$ ) is given by a constant matrix and that this matrix is the `L` matrix. The output of the PETSc time steppers is handled by a monitor function, which is a function with a defined interface that PETSc calls at every integration step:

```
TSMonitorSet(ts,MyOut::GenMonitor,out,NULL);
```

The function `MyOut::GenMonitor` is the general purpose monitor function of PsiQuaSP. It prints a single line into each specified output file by computing all user specified observables and distributions in each individual file. By default this function prints a single line at every 30th time step. This can be changed with the command line option `-tev_steps_monitor newvalue`. The command

```
TSSolve(ts,dm);
```

solves the time dynamics, `dm` contains always the current time step density matrix. In Fig. A.4 (a) the mean excitation in the two-level systems and the mode during this relaxation is shown: Initially the dynamics are fast due to Rabi oscillations between bright Dicke states and the mode. Afterwards the dynamics is governed by the slow, monotonous spontaneous emission, since only the dark Dicke states remain excited. In Fig. A.4 (b) the population in these Dicke states is shown.

### A.2.2 Example 2: Three-level systems

In the two-level system example above the base class `TLS` was used. For three- and general multi-level systems specialized classes are not provided, instead there is the multi purpose class `System` (the base class of `TLS`). In Figs. A.5 b) and d) two different three-level system sketches are shown, which correspond to the three-level system setups Fig. A.5 a) and c): A.5 b) connects all degrees of freedom while in A.5 d) four degrees of freedom can be eliminated, resulting in a  $\sim N^4$  scaling instead of an  $\sim N^8$  scaling for A.5 b). The decoupling of some basis states and

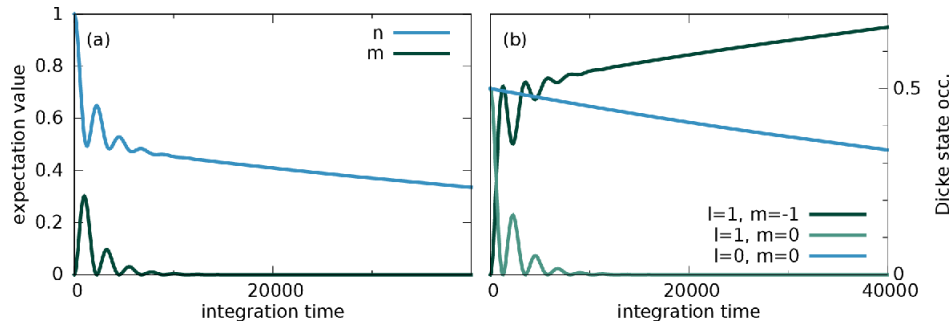


**Figure A.4 – Time dynamics of the open Tavis-Cummings relaxation:** Using the code of `example/ex1b`: a) mean excitation in the two-level systems  $n = \langle J_{11} \rangle$  and mean photon number  $m = \langle b^\dagger b \rangle$  for 2 two-level systems prepared in the state  $\mathcal{P}[1, 0, 0; 0, 0]$ . This corresponds to the entanglement distillation setup[139]. The bright superradiant states couple to the cavity mode and cause Rabi oscillations, while the dark subradiant state does not couple to the cavity and just decays via individual spontaneous emission[28, 20], c.f. Eq. (A.2.3). b) Dicke state occupations  $\langle |l, m\rangle \langle l, m| \rangle$ : temporal dynamics of the states of the superradiant subspace (green) vs the single dark state in the subradiant subspace (blue).

the resulting reduction in degrees of freedom is the main reason why PsiQuaSP does not provide specialized classes for multi-level systems.

For the two-level system example we called `TLSAdd(a, b, c, energy)` which internally calls

```
MLSAddDens(n11, a+1, energy);
MLSAddPol(n10, b+1);
MLSAddPol(n01, c+1);
```

where `MLSAddDens(...)` adds a density degree of freedom, corresponding to a quantum number  $n_{xx}$ , and `MLSAddPol(...)` adds a polarization degree of freedom, corresponding to a quantum number  $n_{xy}$ ,  $x \neq y$ . Thus setting the degrees of freedom for three-level systems (Fig. A.5 b)) is done with the function calls (without truncation)

```
MLSAddDens(n22, n+1, energy2);
MLSAddPol(n21, n+1);
MLSAddPol(n20, n+1);
MLSAddPol(n12, n+1);
MLSAddDens(n11, n+1, energy1);
MLSAddPol(n10, n+1);
MLSAddPol(n02, n+1);
MLSAddPol(n01, n+1);
```

or for Fig. A.5 d) with

```
MLSAddDens(n22, n+1, energy2);
MLSAddDens(n11, n+1, energy1);
MLSAddPol(n10, n+1);
MLSAddPol(n01, n+1);
```

Here `n` represents the number of three-level systems considered. This number can also be lower than the number of treated three-level systems, which corresponds to a truncation of the number of three-level system basis states. A truncation should always be tested if it is applicable in the given situation (parameter dependent), but it can reduce the numerical cost considerably (Example: strong dephasing in driven systems can reduce the number of needed offdiagonals (`nxy`) considerably). The `nxy` objects are again the `MLSDim` identifiers and are created with e.g.

```
MLSDim n21 (2, 1);
```

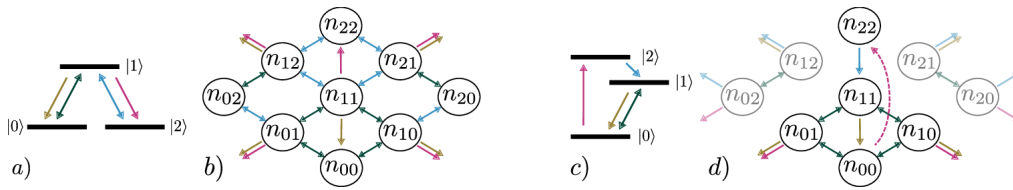


**Figure A.5 – Different three-level system setups:** a), b) The level scheme and the sketch for the Lambda system setup. c), d) The three level laser of Section 5.4.3.

As in the two-level system example, after setting all multi-level system degrees of freedom the user can add bosonic modes with the command

```
ModeAdd(m0+1, dm0, modeenergy);
```

This order of `ModeAdd(...)` after the `MLSAdd...` function calls is mandatory, `PsiQuaSP` returns an error message if these routines are not called in the right order. Setting e.g. the spontaneous emission between levels 1 – 0 for Fig. A.5 b) is done with

```
AddLindbladRelaxMLS(L, NULL, NULL, 1, n11, n00, gamma/2.0);
AddLindbladDephMLS(L, NULL, NULL, 1, n10, gamma/2.0);
AddLindbladDephMLS(L, NULL, NULL, 1, n01, gamma/2.0);
AddLindbladDephMLS(L, NULL, NULL, 1, n21, gamma/2.0);
AddLindbladDephMLS(L, NULL, NULL, 1, n12, gamma/2.0);
```

and for Fig. A.5 d) it is

```
AddLindbladRelaxMLS(L, NULL, NULL, 1, n11, n00, gamma/2.0);
AddLindbladDephMLS(L, NULL, NULL, 1, n10, gamma/2.0);
AddLindbladDephMLS(L, NULL, NULL, 1, n01, gamma/2.0);
```

The parameter `gamma/2.0` is the same parameter as appearing in the master equation and each function call corresponds to exactly one of the arrows in the sketches. The incoherent pumping is added by calling

```
AddLindbladRelaxMLS(L, NULL, NULL, 1, n00, n22, pump/2.0);
```

and the respective calls to `AddLindbladDephMLS()`. The interaction of the three-level systems with the mode for Fig. A.5 b) is added by calling

```
AddMLSModeInt(AA, NULL, NULL, 1, n20, n21, mbra, -gcouple*PETSC_i);
AddMLSModeInt(AA, NULL, NULL, 1, n10, n11, mbra, -gcouple*PETSC_i);
AddMLSModeInt(AA, NULL, NULL, 1, n00, n01, mbra, -gcouple*PETSC_i);
AddMLSModeInt(AA, NULL, NULL, 1, n02, n12, mket, gcouple*PETSC_i);
AddMLSModeInt(AA, NULL, NULL, 1, n01, n11, mket, gcouple*PETSC_i);
AddMLSModeInt(AA, NULL, NULL, 1, n00, n10, mket, gcouple*PETSC_i);
```

and for Fig. A.5 d) omitting the arrows of the disconnected part of the sketch

```
AddMLSModeInt(AA, NULL, NULL, 1, n10, n11, mbra, -gcouple*PETSC_i);
AddMLSModeInt(AA, NULL, NULL, 1, n00, n01, mbra, -gcouple*PETSC_i);
AddMLSModeInt(AA, NULL, NULL, 1, n01, n11, mket, gcouple*PETSC_i);
AddMLSModeInt(AA, NULL, NULL, 1, n00, n10, mket, gcouple*PETSC_i);
```

`mket` and `mbra` are the identifiers for the mode degrees of freedom and are created by calling

```
ModeDim mket (0, photonnumber);
ModeDim mbra (1, photonnumber);
```

`photonnumber` is the index of the mode. Modes are numbered internally starting from zero in the order they are created with an `AddMode()` call. Hamiltonian contributions that change the right index of the `MLSdim` and/or act on the bra side of the mode expansion come with a minus sign. This stems from the commutator in the von-Neumann part of the quantum master equation, see section A.4 for more details. The generation of the output as well as the solution

example/	System, concepts, techniques
ex1a	Open Tavis-Cummings model, simple observables, distributions, time-integration
ex1b	ex1a with thermal bath, PETSc concepts, adaptive time integration, Dicke distribution
ex2a	Two-level laser, incoherent pump, custom observables
ex2b	Direct steady state/null space computation using SLEPc Krylov-Schur algorithm
ex2c	Two-level laser with Non-RWA terms
ex3a	Lambda system setup, multi-level system usage
ex3b	Three-level laser
ex4a	Phonon laser/laser cooling setup, custom Liouvillians
ex5	Same as ex3a, using ParMETIS graph partitioning to exploit $U(1)$ symmetry, leading to a reduction from $N^8$ to $\sim N^7$

**Table A.1 – Overview over the example codes** and the concepts explained/introduced in these examples. **ex2b** requires an additional SLEPc installation and for **ex5** it is necessary to build PETSc with the `-download-parmetis` flag.

stage is completely analogous to the two-level system example. Further examples, illustrating other master equations, custom observables, custom distributions, custom Hamiltonians and Liouvillians as well as other solution techniques and advanced, graph theory based reduction of degrees of freedom are provided in the examples in the `example/` folder as well as in section A.4. An overview of the examples and the concepts explained in them is given in Table A.1.

### A.3 Template functions versus custom Liouvillians

PsiQuaSP has roughly two types of usages. The first usage was presented in the previous section: There are ready-made functions for setting arrows of common Hamiltonians and Lindblad dissipators. Generally a single function call to one of these functions represents a single arrow in one of the sketches. First the user draws the sketch representation of the master equation and then directly translates the sketch into code. In the case of two-level systems it is even simpler – a single function call is sufficient to set a Hamiltonian or dissipator contribution. The implemented contributions are shown in Table A.2.

In the second usage form the user defines elementary Liouville space operators and constructs arbitrary master equations, observables, distributions, etc. from these elementary operators: The permutation symmetric methodology is in principle applicable to *any* permutation symmetric quantum master equation and using the general framework of PsiQuaSP one can solve in principle *any* quantum master equation in a number state representation (there is no support for coherent state basis etc.). Since we cannot provide template setup functions for every conceivable Liouvillian matrix there needs to be another, more flexible approach for this: In the second type of usage the user defines elementary Liouville operators like

$$J_{xy}\rho \hat{=} J_{xy}^L\rho, \quad \rho J_{xy} \hat{=} J_{xy}^R\rho. \quad (\text{A.3.1})$$

Here again the  $L, R$  algebra was used [126]: For any Hilbert space operator one defines a Liouville space operator by distinguishing whether it acts on the left or right side of the density matrix, i.e.  $A\rho = A^L\rho$  and  $\rho A = A^R\rho$ . As in the first type of usage the setup of these elementary Liouville operators is done by first drawing a sketch for each needed operator and then adding all needed arrows by single function calls. Based on these elementary operators the user then can define arbitrary interaction Hamiltonians and dissipators as well as custom observables,

Liouvillian	System function	Examples
$H = \hbar\omega_0 b^\dagger b$	AddModeHO()	ex3a
$H = \hbar\omega_{xx} J_{xx}$	AddMLSHO()	ex1a, ex1b
$H = \hbar g(J_{xy} + J_{yx})(b^\dagger + b)$	AddMLSMODEINT()	ex2c
$H = \hbar g(J_{xy} b^\dagger + J_{yx} b)$	AddMLSMODEINT()	ex1a, ex1b
$H = \hbar E(J_{xy} e^{i\omega t} + J_{yx} e^{-i\omega t})$	AddMLSCohDrive()	ex3a
$H = \hbar E(b e^{i\omega t} + b^\dagger e^{-i\omega t})$	AddModeCohDrive()	none
$\mathcal{D} = \frac{\gamma}{2} \sum_i (2\sigma_{xy}^i \rho \sigma_{yx}^i - \sigma_{yy}^i \rho - \rho \sigma_{yy}^i)$	AddLindbladRelaxMLS()	
$\mathcal{D} = \delta \sum_i (\sigma_{xy}^{z,i} \rho \sigma_{yx}^{z,i} - \rho)$	AddLindbladDephMLS()	ex1a, ex1b
$\mathcal{D} = \frac{\kappa}{2} (b\rho b^\dagger - b^\dagger b\rho - \rho b^\dagger b)$	AddLindbladMode()	ex1a
$\mathcal{D} = \frac{\kappa}{2} ((\bar{m} + 1)(b\rho b^\dagger - b^\dagger b\rho - \rho b^\dagger b) + \bar{m}(b^\dagger \rho b - b b^\dagger \rho - \rho b b^\dagger))$	AddLindbladModeThermal()	ex1b

**Table A.2 – Overview over the general ready-made Liouvillian setup functions** of the `System` class. Please look into the TLS class documentation to see the derived, specialized two-level system functions. The Hamiltonian contributions always refer to the  $i/\hbar[\rho, H]$  terms. Using  $\sigma_{xy}^{z,i} = 1/2(\sigma_{xx} - \sigma_{yy})$ .

distributions, basis transformations etc. For instance using Eq. (A.3.1) the definition of a collective spontaneous emission Liouvillian from level  $x$  to level  $y$  would be

$$\mathcal{D}(\rho) = \frac{\Gamma}{2} (J_{yx} \rho J_{xy} - J_{xy} J_{yx} \rho - \rho J_{xy} J_{yx}) = \frac{\Gamma}{2} (J_{yx}^L \cdot J_{xy}^R - J_{xy}^L \cdot J_{yx}^L - J_{yx}^R \cdot J_{xy}^R) \rho, \quad (\text{A.3.2})$$

here the combination of the  $R/L$  operators  $\cdot$  is performed by the standard matrix-matrix product, provided by the PETSc function `MatMatMult()`. Hence the user first defines elementary matrices and then uses the PETSc matrix multiplication and addition tools to construct every conceivable Liouville operator. The details for this type of application are explained in the next section.

## A.4 Building arbitrary Liouvillians

In this section the formalism that allows to setup all possible Liouvillians that are consistent with the permutation symmetric method is discussed. It closely resembles the treatment in the Sections 5.5.1 and 5.5.2. There are separate setup functions for multi-level system and mode degrees of freedom, e.g. for  $J_{xy}^L$  or  $b^R$ . These elementary matrices can be used to construct more complicated operators such as  $J_{xy}^L + J_{yx}^R$  and  $J_{xy}^L b^L$  by using the PETSc tools for matrix multiplication and addition. Defining such setup functions for the mode degrees of freedom is straightforward and is based on textbook physics [140]. For the symmetric basis states of PsiQuaSP the treatment is a bit more difficult. The following discussion is technical, it involves the permutation symmetric Liouville space operators of the previous section. The usage however is then very simple, it again results in drawing simple sketches and directly implementing single arrows by single function calls.

*Technical details:* As defined in Eq. (A.1.2) PsiQuaSP uses an expansion of the density matrix in Liouville space. Expansion coefficients can be obtained via the Hilbert-Schmidt inner product

$$\mathcal{P}[\{n_{kl}\}] = \text{tr}[\hat{\mathcal{P}}[\{n_{kl}\}]\rho] \quad (\text{A.4.1})$$

The actions of any operators  $A, B$  on the density matrix  $A\rho B$  are handled by PsiQuaSP like applying these operators to  $\hat{\mathcal{P}}[\{n_{kl}\}]$ :

$$\text{tr}[\hat{\mathcal{P}}[\{n_{kl}\}]A\rho B] = \text{tr}[B\hat{\mathcal{P}}[\{n_{kl}\}]A\rho]. \quad (\text{A.4.2})$$

Hence one needs to find a general recipe to construct arbitrary operators  $B\hat{\mathcal{P}}[\{n_{kl}\}]A$  expressed in the permutation symmetric basis, for all  $A\rho B$  that live in the permutation symmetric subspace. In order to do this there are two steps: First the elementary processes/Liouville operators need to be identified and second the recipes how to construct physically relevant operators, like e.g. a collective raising operator for a four-level system acting from the left, from these elementary operators need to be formulated. The permutation symmetry demands that only those processes can be included that are based on spin matrices acting *indistinguishably* on the left and/or right side of the density matrix. These elementary operators should be representable by arrows.

*Defining elementary processes/arrows:* Looking at the sketches two general types of arrows appear: Connecting and nonconnecting arrows. A connecting arrow represents a coupling between two different symmetric basis states Eq. (5.5.3), corresponding to an in- or out-scattering process, and a nonconnecting arrow just acts on the state itself, leaving it unchanged. This is quite analogous to the actions of the interacting and non-interacting parts of a Hamiltonian acting on a Hilbert space state, or rather that the symmetrized basis states  $\hat{\mathcal{P}}$  Eq. (5.5.3) are eigenstates of the operators corresponding to the nonconnecting arrows. It turns out that these are the only possible two types. The general mathematical expressions are given by the  $\Gamma$  matrices introduced in the previous chapter

$$\sum_i \sigma_{xx}^i \hat{\mathcal{P}}[\dots] \sigma_{yy}^i = n_{xy} \hat{\mathcal{P}}[\dots] \quad (\text{A.4.3})$$

for a single nonconnecting arrow and

$$\sum_i \sigma_{xy}^i \hat{\mathcal{P}}[\dots] \sigma_{kl}^i = (n_{xl} + 1) \hat{\mathcal{P}}[\dots n_{xl} + 1 \dots n_{yk} - 1 \dots] \Theta(n_{yk}), \quad (\text{A.4.4})$$

for a connecting arrow, where  $\Theta(n)$  is equal to one for  $n > 0$  and zero otherwise. Here we write down only the changed numbers  $n_{xl}$  and  $n_{yk}$ . Multiplying these equations with the density matrix and taking the trace results again in equations of motion. Using these two types of arrows it is possible to construct every permutationally symmetric multi-level system Liouville operator. The PsiQuaSP functions for adding one of these arrows to a given matrix are `AddMLSSingleArrowNonconnecting(...)` and `AddMLSSingleArrowConnecting(...)`. The sketch representation for these two types is shown in Fig. A.6 a) and d): Eq. (A.4.3) describing nonconnecting arrows can represent two different types of processes depending on the corresponding prefactor in the master equation. If the prefactor is imaginary the term corresponds to a Hamiltonian part  $H_0$ , or if it is negative and real it corresponds to dephasing, caused e.g. by a dissipator (Fig. A.6 b) and c)). The two arrows are the looped and the outward pointing arrows in Fig. A.6 a). The connecting arrow Eq. (A.4.4) usually also represents two different processes: One sided flip operator actions arising from interaction Hamiltonians (Fig. A.6 e) and f)) and density relaxation caused by individual spontaneous emission, decay dissipators (Fig. A.6 g)).

*Constructing physical operators:* Looking at the collective flip operator acting from the right

$$\begin{aligned} \text{tr}[\hat{\mathcal{P}}[\dots] \rho J_{xy}] &= \text{tr}[J_{xy} \hat{\mathcal{P}}[\dots] \rho] \\ &= \text{tr}[\sum_i \sigma_{xy}^i \hat{\mathcal{P}}[\dots] \sum_k \sigma_{kk}^i \rho] \\ &= \sum_k (n_{xk} + 1) \mathcal{P}[\dots n_{xk} + 1 \dots n_{yk} - 1 \dots] \Theta(n_{yk}) \end{aligned} \quad (\text{A.4.5})$$

amounts to summing over all possible individual connecting arrows, see Fig. A.6 e). Here in the second line the Hilbert space identity for each individual  $d$ -level system was inserted

$$I^i = \sum_k \sigma_{kk}^i. \quad (\text{A.4.6})$$

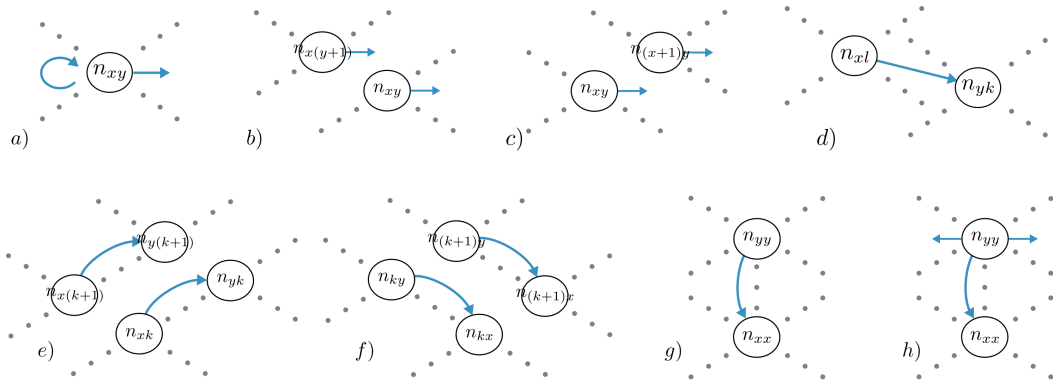


**Figure A.6 – Modular sketches for multi-level systems:** a) The nonconnecting arrow can represent the phase oscillations arising from the self energy Hamiltonians (curved arrow) and it can describe dephasing (straight arrow). b) and c) the sketches corresponding to dephasing  $\dot{\rho} \propto J_{xx}^R \rho$  and  $\dot{\rho} \propto J_{yy}^L \rho$ . d) The connecting arrow can represent flip operators and density relaxation. e) and f) the arrows corresponding to the flip operators  $\dot{\rho} \propto J_{xy}^R \rho$  and  $\dot{\rho} \propto J_{xy}^L \rho$ , c.f. Eqs. (A.4.5) and (A.4.7). g) The density relaxing arrow caused by an individual spontaneous emission like dissipator  $\dot{\rho} \propto \sum_i \sigma_{xy}^i \rho \sigma_{yx}^i = \Gamma_{xy}^{yx} \rho$ . h) The density relaxation arrow introduced in Fig. 5.2 called by the function `AddLindbladRelaxMLS()` consists of three arrows in the elementary picture, two nonconnecting and one connecting arrow.

The actions of the  $\sigma_{xy}^i$  matrices in Eq. (A.4.5) change each individual spin matrix  $\sigma_{yk}^i$  into a spin matrix  $\sigma_{xk}^i$ . The  $k$  sum of the  $\sigma_{kk}^i$  matrices results in a sum over all possible right  $k$  indices in  $n_{yk}$  and  $n_{xk}$ . In the last step Eq. (A.4.4) was inserted and the trace was computed. From this expression it can already be seen that the resulting matrix will be sparse, since there are at most  $k$  nonzero entries in each line of this matrix.

The same operator acting from the left results in a sum over all possible left  $k$  indices

$$\begin{aligned} \text{tr}[\hat{\mathcal{P}}[\dots] J_{xy} \rho] &= \text{tr} \left[ \sum_k \sum_i \sigma_{kk}^i \hat{\mathcal{P}}[\dots] \sigma_{xy}^i \rho \right] \\ &= \sum_k (n_{ky} + 1) \mathcal{P}[\dots n_{ky} + 1 \dots n_{kx} - 1 \dots] \Theta(n_{yk}). \end{aligned} \quad (\text{A.4.7})$$

These two operators can be implemented by repeatedly calling the single connecting arrow function `AddMLSSingleArrowConnecting(...)` – once for every possible  $k$  value, see Fig. A.6 e) and f). The action of a collective projection or diagonal operator  $J_{xx}$  is given by

$$\begin{aligned} \text{tr}[\hat{\mathcal{P}}[\dots] \rho J_{xx}] &= \text{tr} \left[ \sum_k \sum_i \sigma_{xx}^i \hat{\mathcal{P}}[\dots] \sigma_{kk}^i \rho \right] \\ &= \sum_k n_{xk} \mathcal{P}[\dots] \end{aligned} \quad (\text{A.4.8})$$

and

$$\begin{aligned} \text{tr}[\hat{\mathcal{P}}[\dots] J_{xx} \rho] &= \text{tr} \left[ \sum_k \sum_i \sigma_{kk}^i \hat{\mathcal{P}}[\dots] \sigma_{xx}^i \rho \right] \\ &= \sum_k n_{kx} \mathcal{P}[\dots], \end{aligned} \quad (\text{A.4.9})$$

which can be implemented by repeatedly calling `AddMLSSingleArrowNonconnecting(...)` – again once for every possible  $k$  value, see Fig. A.6 b) and c). This discussion also serves as a

$b\rho$	AddModeLeftB(...)	$\rho b$	AddModeRightB(...)
$b^\dagger\rho$	AddModeLeftBd(...)	$\rho b^\dagger$	AddModeRightBd(...)
$b^\dagger b\rho$	AddModeLeftBdB(...)	$\rho b^\dagger b$	AddModeRightBdB(...)
$bb^\dagger\rho$	AddModeLeftBBd(...)	$\rho bb^\dagger$	AddModeRightBBd(...)
$b\rho b^\dagger$	AddModeLeftBRightBd(...)	$b^\dagger\rho b$	AddModeLeftBdRightB(...)

**Table A.3** – List of all available functions for setting elementary mode Liouvillians: The redundant functions allow faster and easier code development – actually all Liouvillians could be constructed from the first two.

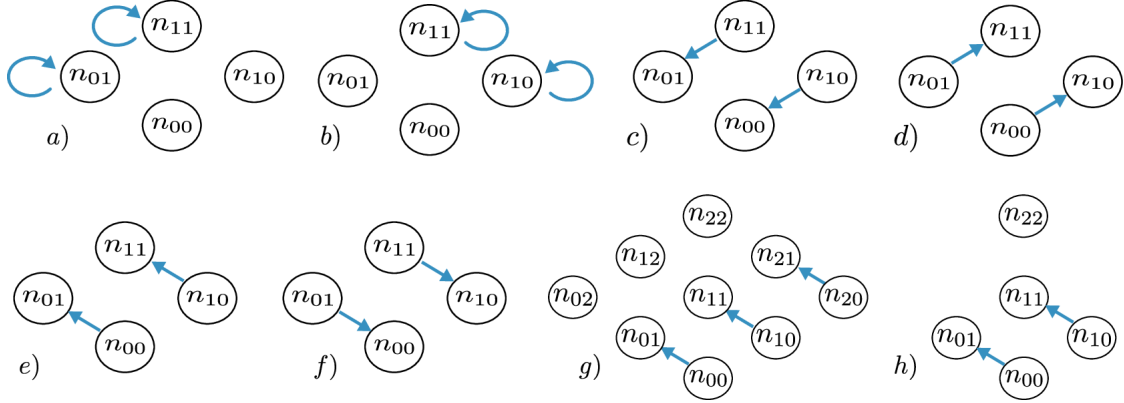


**Figure A.7** – Sketches needed for the phononlaser example code: From a) to f): Sketches corresponding to  $J_{11}^L$ ,  $J_{11}^R$ ,  $J_{10}^R$ ,  $J_{01}^R$  and  $J_{10}^L$ ,  $J_{01}^L$ . When the operator acts on the left (right) side of the density matrix, it acts on the right (left) index of the  $n_{xy}$ , c.f. Eq. (A.4.2). Two versions of the  $J_{10}^L$  operators for the full and reduced three level system dynamics, c.f. Fig. A.5 b) and d).

proof for the sum rules for the  $\Gamma$  operators in the last chapter.

With this set of results it is clear how to construct a general self energy Hamiltonian  $\dot{\rho} \sim i/\hbar[\rho, H_0]$  or a general individual dissipator

$$\mathcal{D}\rho = \frac{\gamma}{2} \left( \sum_i \sigma_{xy}^i \rho \sigma_{yx}^i - J_{yy}\rho - \rho J_{yy} \right), \quad (\text{A.4.10})$$

where the first term is set by a single call to `AddMLSSingleArrowConnecting(...)`, see Eq. (A.4.4), and the second and third term are set as in Eqs. A.4.8 and A.4.9. Please note that the possibility of a decoupling of some coherence degrees of freedom as in Fig. A.5 d) is the main reason why PsiQuaSP does not provide generalized setup functions for operator actions of  $J_{xy}$  and  $J_{xx}$ , since it would result in unnecessary numerical cost, if the decoupled basis elements were included. The other reason is that the elementary arrow representation also provides maximal freedom for the application programmer, whereas any encapsulation/facilitation would always be associated with a cut in generality.

The sketches corresponding to simple operators like  $J_{xy}$  and  $J_{xx}$  are simple to draw. Sketches corresponding to Liouville operators like  $J_{xy}\rho J_{yx}$  or  $J_{xy}^n\rho$  are more complicated and it is not recommended to implement these sketches by hand. Rather we recommend to define the elementary processes like  $J_{xy}$  and  $J_{xx}$ , set the corresponding matrices and then use the PETSc tools `MatMatMult()` and `MatAXPY(...)` to construct more complicated operators. In order to

do so the following identities are useful

$$\begin{aligned} A\rho B &\hat{=} A^L \cdot B^R \rho = B^R \cdot A^L \rho, \\ AB\rho &\hat{=} A^L \cdot B^L \rho, \quad \rho AB \hat{=} B^R \cdot A^R \rho, \end{aligned} \quad (\text{A.4.11})$$

where the  $\cdot$  operation is given by the `MatMatMult()` operation. The elementary Liouville space operators for the bosonic modes can be set by calling the functions shown in Table A.3.

*Simple example:* In `example/ex4a` the phonon laser/laser cooling master equation from Refs. 141, 142 is implemented

$$H = \hbar\Delta J_{11} + \hbar\omega_{ph} b^\dagger b + \hbar g J_{11} (b + b^\dagger) + \hbar E (J_{10} + J_{01}). \quad (\text{A.4.12})$$

Here  $\Delta = \omega_{11} - \omega_L$  is the detuning of the two-level systems from the driving laser. For positive detuning near the Stokes resonance this corresponds to laser cooling and for negative detuning at the anti-Stokes resonance this corresponds to phonon lasing. The master equation includes individual spontaneous emission and finite phonon lifetime through the dissipators

$$\begin{aligned} \mathcal{D}_1(\rho) &= \frac{\gamma}{2} \sum_i (\sigma_{01}^i \rho \sigma_{10}^i - \sigma_{11}^i \rho - \rho \sigma_{11}^i), \\ \mathcal{D}_2(\rho) &= \frac{\kappa}{2} (b\rho b^\dagger - b^\dagger b\rho - \rho b^\dagger b). \end{aligned} \quad (\text{A.4.13})$$

In this example six two-level system operators are needed to construct the master equation:  $J_{11}^{L,R}$ ,  $J_{10}^{L,R}$  and  $J_{01}^{L,R}$ . Each of these matrices are defined by two calls to the single nonconnecting arrow functions `AddMLSSingleArrowNonconnecting(...)` for  $J_{11}^{L,R}$  and the connecting arrow functions `AddMLSSingleArrowConnecting(...)` for  $J_{10}^{L,R}$  and  $J_{01}^{L,R}$ . The sketches for these matrices are shown in Fig. A.7. From these matrices and the respective phonon matrices we can construct the Liouvillian and also possible additional observables.

## A.5 Performance

The two main advantages of PsiQuaSP are the reduction of complexity due to the symmetrized basis states and the manifold of solvers provided through PETSc and e.g. SLEPc.

*Overall complexity:* In Fig. A.8 a) the number of basis elements of the density matrix for the full exponential density matrix is compared to the polynomial, symmetrized PsiQuaSP density matrix for two- and three-level systems. This corresponds to the overall complexity since both the storage requirement and the number of coupled equations scale like the number of basis elements.

*Steady state computation:* In Fig. A.8 b) the convergence time for steady state calculations for a two-level laser as discussed in the last chapter and implemented in the examples `example/ex2a` and `example/ex2b` for different solvers is shown: the fixed time step fourth order Runge-Kutta is by far the slowest solver. The adaptive time step and the direct null space computation using the SLEPc package outperform this standard routine. The speedup of the shift and invert spectral transformation solver compared to the RK4 method amounts almost to a factor of 5000. Please note that these numbers and the relative performance of these solvers is parameter and system size dependent, it is possible to find examples where the difference is even higher but it is also possible to find examples where the difference is less pronounced. Especially for iterative solvers like the SLEPc Krylov-Schur eigenvalue solver convergence time is highly dependent on the spectrum of the matrix and on chosen solver specific parameters. Please refer to the PETSc and SLEPc documentations for the specifics of these methods.

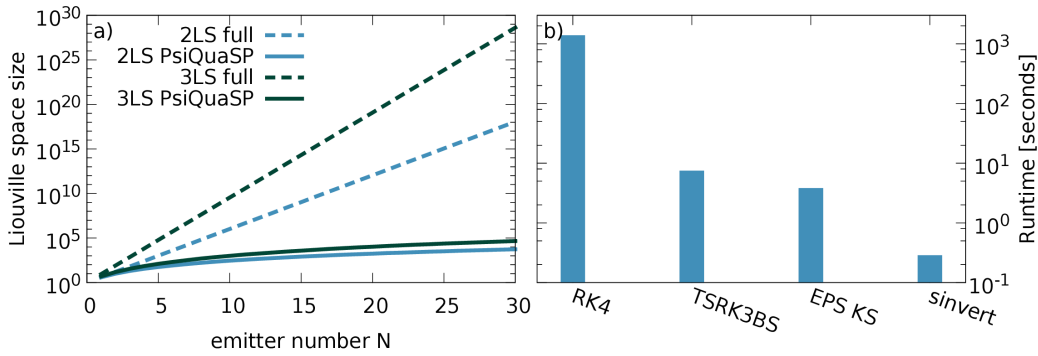


**Figure A.8 – PsiQuaSP performance:** a) The scaling of storage space and overall computation time for two-level systems and three-level systems using the full exponential approach vs. the permutation symmetric PsiQuaSP approach. b) Runtime comparison between different solution methods for steady state calculations for a two-level laser setup: fixed time step fourth order Runge-Kutta (RK4), adaptive time step Runge-Kutta (TSRK3BS), SLEPc Krylov-Schur null space computation (EPS KS) and SLEPc Krylov-Schur null space computation with exact shift and invert spectral transformation (sinvert). Please refer to the PETSc and SLEPc documentation and the discussion in this section for details to these solvers.

## A.6 Some notes on solvers

In the last section the performance of different solvers for steady state computation was compared. There are in principle two different questions that can be answered by numerically solving a quantum master equation

$$\dot{\rho} = \mathcal{L}\rho. \quad (\text{A.6.1})$$

The first question is "How does the system evolve in time?" and the second question is "What is the steady state?". Depending on the question the solver should be chosen.

For a constant Liouvillian steady states should be computed using steady state solvers and only if the time dependency is of interest then one should resort to direct integration. Time evolution should be calculated with an adaptive step width Runge-Kutta: The step width is adaptively chosen by comparing the solutions of two different Runge-Kutta algorithms of different order, for instance a second and a third order Runge-Kutta. As seen in Fig. A.8 b) this alone provides a dramatic speedup.

There is a large variety of different steady state solvers: PETSc provides generally two different approaches: (i) pseudo time stepping, which is a fake time integration that directly computes the steady state and the intermediate time steps are unphysical. This in principle allows also for explicitly time-dependent Liouvillians (not used in this thesis), and (ii) a huge variety of iterative Krylov subspace methods (through the KSP object). Krylov subspace methods are somewhat the standard for iterative sparse matrix diagonalization and have been used a lot in this thesis.

### A.6.1 Krylov subspaces

A Krylov subspace  $\mathcal{K}$  of a complex vector space  $\mathbb{C}^n$ , is constructed from a matrix/operator  $A \in \mathbb{C}^{n \times n}$  and a column vector  $q \in \mathbb{C}^n$  [143]

$$\mathcal{K} = \mathcal{K}(A, q) = \mathcal{K}_m(A, q) = \text{span}\{q, Aq, A^2q, \dots, A^{m-1}q\}. \quad (\text{A.6.2})$$

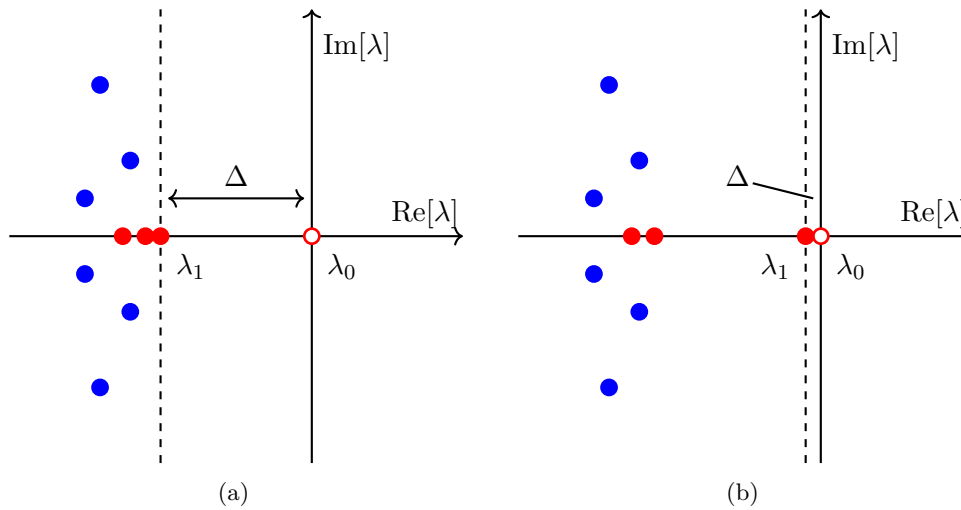


**Figure A.9 – Two different Liouvillian spectra:** a) This spectrum makes the gap  $\Delta$  computation expensive. b) Gap and steady state computation are (relatively) expensive.

The main idea is that the eigenvectors of  $A$  are usually part of the Krylov subspace and if one can find the desired eigenvector in a Krylov subspace with  $m \ll n$  then the dimensionality/complexity of the problem is greatly reduced. Also the inverse of a non-singular matrix is part of the Krylov subspace. The null space is however not contained in the Krylov-subspace, a singular matrix also does not have an inverse (except for the Moore-Penrose pseudoinverse). Therefore Krylov subspace algorithms often have a null space correction included. There is a large variety of different iterative algorithms that utilize exactly this property, one rather well known example is GMRES – generalized minimal residual method. This solver is however not suited for the Liouvillians considered in this work. Throughout this work the Krylov-Schur algorithm of the SLEPc package is used for steady state computations.

## A.6.2 Spectral transformation

Normally for sparse matrices only an excerpt of the spectrum is computed, since a large matrix has a lot of eigenvalues and usually only few of those are of actual interest. In the case of quantum master equations it is usually the null space and the smallest magnitude non-zero eigenvalue/vector that are of interest. As stated in Section 3.4 the spectrum of the matrix influences the convergence time of the iterative solvers: Generally, if there are other eigenvalues in the vicinity of the desired eigenvalue the convergence is slow: In Fig. A.9 a) and b) two different spectra are shown. In Fig. A.9 a) there are many eigenvalues close to the  $\lambda_1$  eigenvalue making the computation of the Liouvillian gap  $\Delta$  expensive, because it requires  $\lambda_1$ , computing only the null space is cheap. In Fig. A.9 b)  $\lambda_1$  and  $\lambda_0$  are close to each other (dissipative phase transition), which makes the steady state computation more expensive, but computing the gap is equally expensive.

In order to bypass these difficulties there are the spectral transformation techniques: One transforms the eigenvalue problem

$$Ax = \lambda x \quad (\text{A.6.3})$$

into a problem that has a "nicer" spectrum but is still equivalent to the original problem. The easiest spectral transformation is the shift transformation

$$Ax = \lambda x \quad \rightarrow \quad (A - \sigma I)x = (\lambda - \sigma)x. \quad (\text{A.6.4})$$

This however does not change the fact that the eigenvalues are too close to each other, therefore one uses shift and invert

$$Ax = \lambda x \quad \rightarrow \quad (A - \sigma I)x = (\lambda - \sigma)x \quad \rightarrow \quad (A - \sigma I)^{-1}x = (\lambda - \sigma)^{-1}x \quad (\text{A.6.5})$$

The  $1/x$  function is well suited to separate the eigenvalues even if the  $\lambda_i$  are close to each other. In the case of Liouvillians the shift is mandatory since the Liouvillian is singular and thus does not have an inverse without a shift. Furthermore the shift  $\sigma$  should be chosen positive to ensure that all eigenvalues are unequal to zero (because the Liouvillian spectrum lives in the negative half plane).

Thus shift and invert speeds up the convergence, see Fig. A.8 b). The drawback of this method is that computing the inverse requires a  $LU$  factorization, which in requires a lot of storage and the standard PETSc  $LU$  factorization only works in single processor operation. For instance for the steady states computed in Chapter 7 the shift and invert spectral transformation was used and for larger systems ( $N = 9$ ) with photon number states up to 50 the storage requirement exceeded 100 giga bytes. This corresponds to a matrix of the order  $10^5 \times 10^5$  to  $10^6 \times 10^6$ . Processing 100 giga bytes on a single cpu is far from efficient. Therefore in order to go to even larger systems/matrices parallel  $LU$  factorization provided by the external packages MUMPS or SuperLU should be used.

## A.7 Conclusion

A library was introduced that enables the setup of master equations for identical multi-level systems. The library provides ready-made setup functions for density matrices as well as Liouville operators. The design of these functions is centered around the sketch representation of the Liouville operators or master equation introduced in in Chapter 5. This has the advantage that implementing an arbitrary master equation does not require calculating any equations of motion but can be done by directly implementing the sketches. There is a simplified usage for two-level systems and ready-made Liouvillian setup routines and an advanced usage where the user can construct arbitrary permutation symmetric Liouvillians from simple sketches.

## III Results



## 6 Cavity QED Lasers and Spasers

In Chapter 5 the usage of the sketch representation was illustrated using different laser examples. In this chapter these examples are applied. The range of application of the permutation symmetric method in the context of lasers is the small system size, cQED laser – meaning one to few emitters and moderate photon numbers. The cQED lasers are the small or mesoscopic counterparts to the classical lasers, which usually involve macroscopic setups: Two mirrors and a macroscopic gain medium like an atomic gas discharge lamp in between, see Fig. 6.1 (a). The classical, conventional lasers usually involve thousands, millions or more emitters/electrons that serve as gain medium and usually have very high photon output rates. Contrary examples for cQED lasers are quantum dots in micropillar structures: These micropillars contain only few quantum dots that are on resonance with the cavity mode and the cavity mode is not formed between two standard macroscopic mirrors but rather by the distributed Bragg reflector (DBR) structure of the micropillar, see Fig. 6.1 (b).

Apart from the typical output powers and the size of the setup there is one striking difference in the behavior of cQED lasers compared to conventional, macroscopic lasers: In conventional lasers the lasing threshold and the start of the stimulated emission process can be seen in a simple input-output curve – Increasing the pump rate leads to a sudden "explosion of stimulated emission" [84], which manifests itself in a stark sudden increase in the cavity output. This can be observed experimentally and serves as a demonstration of lasing action. However in cQED lasers this sudden increase is (almost) absent, the cavity output increases linearly with the pump rate, there is no real indication where the lasing action starts in a simple input-output curve. This has sparked a vivid discussion about threshold-less lasing, since at first sight it seems that the threshold for lasing action goes to zero pump power [84]. However by looking at the statistics of the emitted cavity photons it becomes clear that this is not the case, there remains a finite threshold at which the photons become coherent or rather Poissonian and the absence of the threshold is attributed to a pronounced spontaneous emission contribution. The quantity that

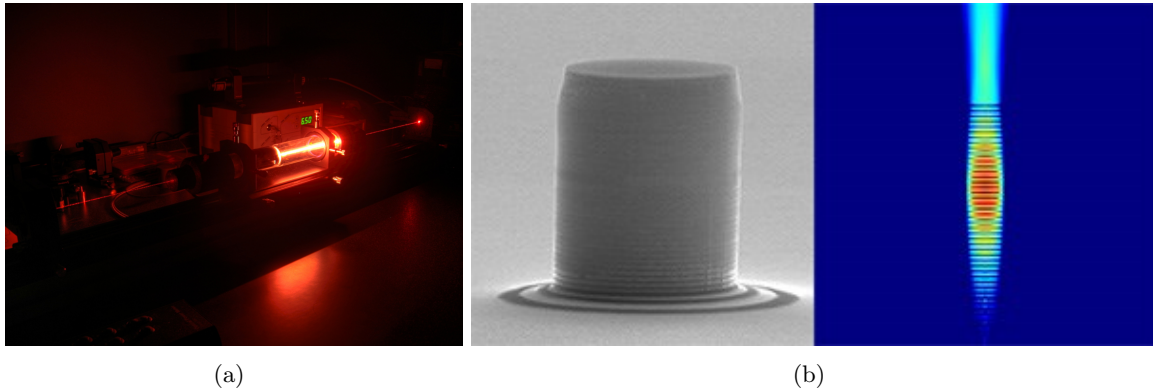


**Figure 6.1 – Different types of lasers:** (a) A Helium-Neon Laser is a macroscopic setup. Image taken from [144]. (b) A DBR Micropillar with corresponding mode structure. Such a micropillar has usually a spatial dimension of a few microns, it is not visible to the naked eye. Image taken from [145]

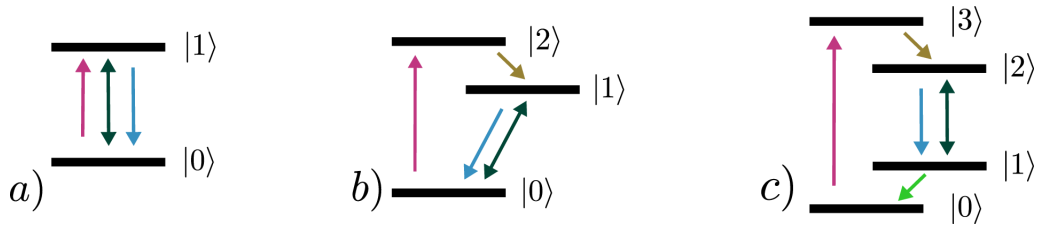


**Figure 6.2 – Level schemes** for the a) two-, b) three and c) four-level laser setup considered in this chapter.

distinguishes between these two cases is the  $\beta$  factor, which is defined as the ratio of spontaneous emission into the lasing mode  $\gamma_l$  to the total spontaneous emission rate  $\gamma_l + \gamma_{nl}$

$$\beta = \frac{\gamma_l}{\gamma_l + \gamma_{nl}}. \quad (6.0.1)$$

In macroscopic lasers usually  $\gamma_{nl} \gg \gamma_l$  holds and in cQED lasers usually  $\gamma_{nl} \sim \gamma_l$  and even  $\gamma_{nl} \ll \gamma_l$ , which results in  $\beta$  factors of  $\beta \sim 10^{-6}$  for conventional lasers and  $\beta \sim 0.1 - 1$  for cQED lasers [84]. In fact the  $\beta$  factor can be used as a measure to define the system size in lasers, with the  $\beta = 1$  defining the atomistic laser and  $\beta \rightarrow 0$  defining the thermodynamic limit, the macroscopic laser [84].

In this chapter three different laser setups are discussed, namely the incoherently driven two-, three- and four-level laser. The two-level laser theory will be used to explore the standard range of cQED lasers. The three- and four-level laser theories will be used to further investigate the findings of M. Richter, M. Gegg, T.S. Theuerholz, A. Knorr published in Phys. Rev. B 035306 (2015) [17]: The spaser – *surface plasmon amplification by stimulated emission of radiation* [59, 60] can be approximated by a bad cavity (short photon lifetime) laser with relatively high emitter-light coupling strength [57]. In Ref. [17] it was found that threshold pump rates for spasing action based on a two-level system bad cavity laser model are unrealistically high, since they need to overcome the tremendous plasmonic losses. Therefore it might be interesting to investigate three- and four-level laser theories.

The sketches and level schemes for the two-, three- and four-level laser setups considered in this chapter are shown in Figs. 6.2 and 6.3. They all include an incoherent drive, which reduces

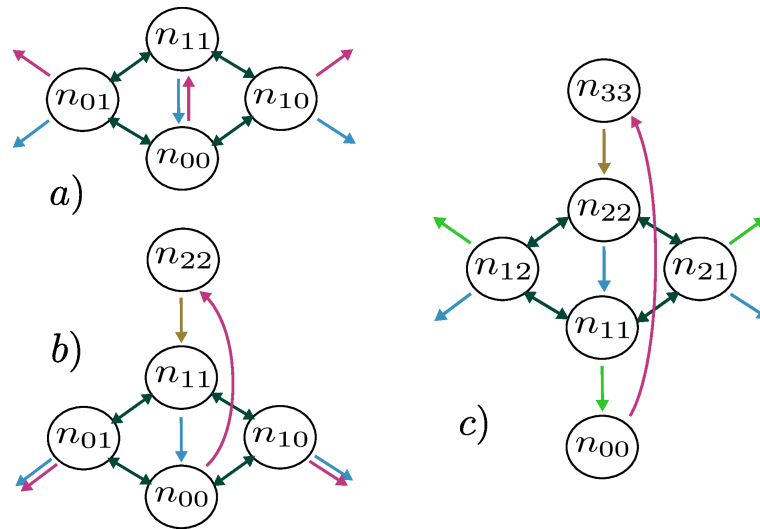


**Figure 6.3** – Sketches for the a) two-, b) three and c) four-level laser setup considered in this chapter. The four-level laser does not have a pump-rate dependent dephasing. These sketches were directly translated into code using the PsiQuaSP library [26, 27], see Appendix A.

numerical cost and enhances comparability.

Parts of the discussion in this chapter were presented at the PQE 2016 and NOEKS 2016 conferences.

## 6.1 Cluster expansion – Rate equation theory

Even though the permutation symmetric method is efficient compared to the brute force solution it still can be quite involved. Therefore it is beneficial to first derive a simplified theory gives estimates for parameter ranges. Here, especially the lasing threshold is of interest. For this purpose it is customary to derive a rate equation theory, which is equivalent to a low order cluster expansion.

In the following the derivation is shortly outlined: The starting point are expectation values of operators like  $b^\dagger b$  and  $J_{xx}$ , the mean cavity and excited state populations. Here  $x$  refers to the upper level of the lasing transition, see Figs. 6.2 and 6.3. Equations of motion for the expectation values can be derived by looking at the time-derivative of these quantities and inserting the Lindblad equation (Schrödinger picture, see Section 3.3)

$$\partial_t \text{tr}[O\rho] = \text{tr}[O\dot{\rho}] = \text{tr}[O\mathcal{L}\rho] \quad (6.1.1)$$

and then calculating all necessary commutation relations. For the mean cavity mode population this yields

$$\partial_t \langle b^\dagger b \rangle = 2g \text{Im} \langle J_{xy} b^\dagger \rangle - \kappa \langle b^\dagger b \rangle, \quad (6.1.2)$$

where  $g$  is the light matter interaction strength,  $\kappa$  is the cavity decay rate,  $J_{xy}$  is the flip operator corresponding to the lasing transition, where  $y$  is the upper and  $x$  is the lower level of the lasing transition, see Figs. 6.2 and 6.3. In order to proceed one then derives the equation of motion for the new operator  $\langle J_{xy} b^\dagger \rangle$

$$\langle J_{xy} b^\dagger \rangle \propto ig \langle (J_{yy} - J_{xx}) b^\dagger b \rangle, \quad (6.1.3)$$

which in turn couples to another operator product. This is called hierarchy problem [9]: Through the interaction Hamiltonian the expectation values of operators couple to expectation values of higher operators, where higher means a product of (more) operators. In principle this hierarchy would go to infinity (since the Hilbert space of the bosons is not bounded), but in the rate equation theory one assumes that quantum correlations are small and thus the assisted quantities are factorized

$$\langle (J_{yy} - J_{xx})b^\dagger b \rangle \sim \langle J_{yy} - J_{xx} \rangle \langle b^\dagger b \rangle. \quad (6.1.4)$$

This results in closed equations of motion. For two-, three- and four-level systems this approach results in three, four and five coupled equations respectively. These can be solved analytically in the stationary limit

$$\partial_t \langle O \rangle = 0 \quad (6.1.5)$$

and results in a second order polynomial equation for the mean cavity number  $m = \langle b^\dagger b \rangle$

$$(\kappa m)^2 + b(P)(\kappa m) + c(P) = 0, \quad (6.1.6)$$

where  $\kappa^{-1}$  is the photon lifetime and the parameters  $b(P)$  and  $c(P)$  are functions of all system parameters, especially of the pump rate  $P$ . Eq. (6.1.6) defines a parabola and the zeroes of the parabola determine the cavity photon number: One solution is always negative, thus there is always exactly one physical solution. The system starts lasing if the parameter  $b(P)$  becomes negative, see Fig. 6.4 (a) and (b). Please note that there are parameter ranges in which  $b(P)$  is strictly positive for all  $P$ , which means that some systems just never will cross the lasing threshold. This is for example the case if the cavity lifetime is too short, or if the emitter cavity coupling or the number of emitters is too small, or for three- and four-level system setups if the incoherent processes that populate the upper lasing level and depopulate the lower lasing level are too slow compared to the other parameters. Generally there needs to be a stable population inversion and a sufficient assisted polarization  $Im\langle J_{xy}b^\dagger \rangle$  in order to spark and maintain the stimulated emission of the laser/spaser.

The functional dependency of this  $b$  parameter strongly influences the behavior of the laser and varies for the three different setups: For a two-level system it is a parabola, which is always opened to the top

$$b(P) = qP^2 + rP + s, \quad q > 0 \quad (6.1.7)$$

for a three level system it asymptotically behaves like a linear function of positive slope

$$b(P) = \frac{qP^2 + rP + s}{tP + u}, \quad q > 0. \quad (6.1.8)$$

The constants in these expressions  $q, r, s, t, u$  depend on the parameters in the master equation, however their explicit form is not of interest for the present discussion. These two laser theories will always only have a lasing window with respect to the pump-rate  $P$ : The dephasing introduced by the incoherent pump term eventually leads to a strong damping of the assisted polarization  $Im\langle J_{xy}b^\dagger \rangle$ ,  $b(P)$  is always positive for large  $P$  and the lasing action dies. Contrary the  $b$  parameter of the four-level laser theory behaves asymptotically like a constant function

$$b(P) = \frac{qP + r}{sP + t}, \quad s > 0, \quad (6.1.9)$$

where  $q$  in this case can be negative and also should be for the lasing action. Thus for a negative  $q$  (of sufficient magnitude) the system enters the lasing regime and then stays in the lasing regime for increasing  $P$ . The  $q$  parameter depends on the difference between the spontaneous

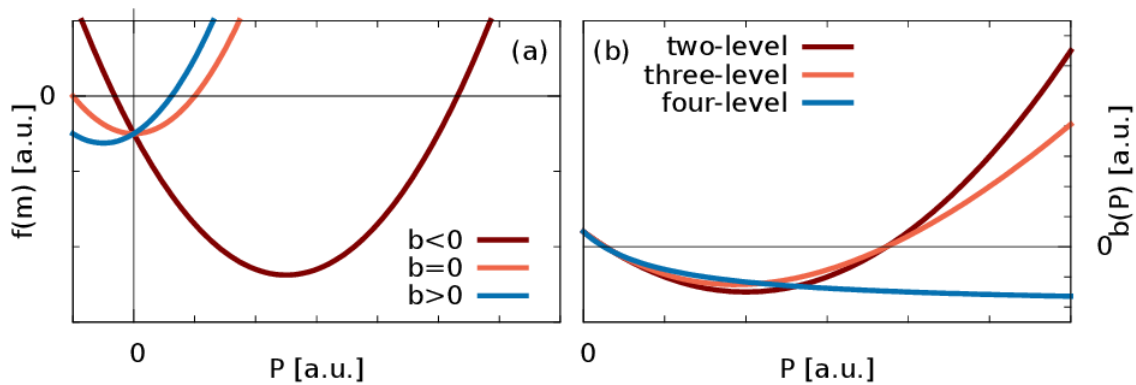


**Figure 6.4 – Identifying the lasing threshold:** (a) The zero of the parabola only goes to high positive values if  $b(P)$  becomes negative. (b)  $b$  as a function of  $P$  for two-, three- and four-level lasers. It is apparent that for two- and three-level systems there is a window of lasing which is due to the fact that for these two cases the pump  $P$  introduces strong dephasing in the lasing transition, which in ultimately quenches photon generation. The four-level laser theory does not have this dephasing effect and thus does not turn off for large  $P$ . This can also be seen in the sketches Fig. 6.3.

emission rate into nonlasing modes  $\gamma_{2 \rightarrow 1}$  and the depopulation rate of the lower lasing transition  $\gamma_{1 \rightarrow 0}$ <sup>1</sup>

$$q \propto N g^2 (\gamma_{2 \rightarrow 1} - \gamma_{1 \rightarrow 0}), \quad (6.1.10)$$

with  $N$  being the number of four-level systems. This indicates that the relative values of these two decay processes are crucial for the system to start lasing. The three different functional dependencies of the  $b$  parameter are shown in Fig. 6.4 (b). For two- and three-level lasers  $b$  always approaches  $+\infty$  for  $P \rightarrow \infty$  since the pumping introduces dephasing in the lasing transition, which leads to quenching for high pump rates. Thus these two systems always only have a lasing window. The four-level laser does not experience this dephasing and  $b$  is constant for  $P \rightarrow \infty$  and therefore the laser does not turn off for high pump powers.

## 6.2 Two-level lasers

The two-level laser is somewhat a limiting case for the three-level laser: If the transition rate from level 2 to level 1 (the yellow arrow in Figs. 6.2 b) and 6.3 b)) is fast compared to all other processes, the three-level laser essentially reduces to a two-level laser since population in upper level should be close to zero and correlations are not involved. Thus the two-level laser is a convenient theoretical concept but in real physical systems more than two-levels are needed in order to realize lasing action, since the stable generation of a population inversion is generally not possible with only two levels<sup>2</sup>

In Fig. 6.5 (a) the normalized mean excitation  $\langle J_{11} \rangle / N$  is plotted: As the number of emitters is increased the system passes the lasing threshold and the shape of the curve changes to a characteristic double S shape, which indicates lasing [147]. The mean intracavity photon number, Fig. 6.5 (b), experiences a drastic increase in the range of the "second" S, between the pump

<sup>1</sup>Here, for simplicity, it was assumed that the rate of population of the upper lasing level  $\gamma_{3 \rightarrow 2}$  and the rate of depopulation of the lower lasing level  $\gamma_{1 \rightarrow 0}$  are identical.

<sup>2</sup>There is also the notion of inversion less lasing, which is particularly interesting for high energy radiation lasers, i.e. ultra-violet and x-ray, since the inversion less lasing schemes are more energy efficient and require lower pump rates [146]. However this rather specific topic is not considered in this thesis.

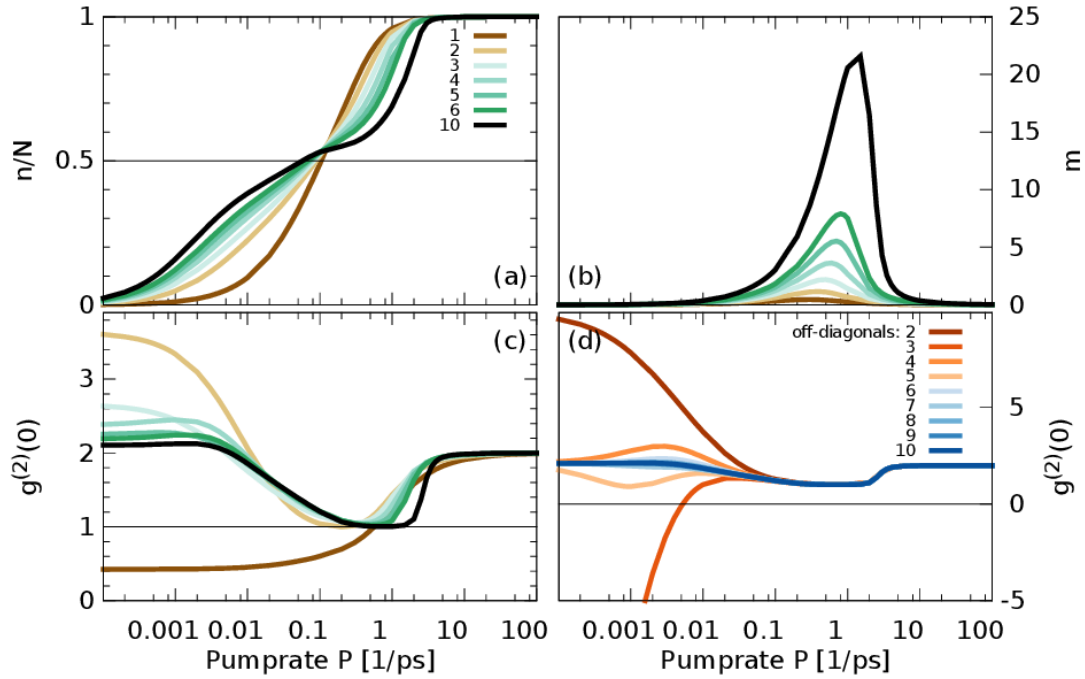


**Figure 6.5 – cQED two-level laser:** (a) The normalized mean excitation of the two-level systems  $n/N = \langle J_{11} \rangle / N$  for varying  $N$  shows the emergence of a characteristic double S shape, which indicates the lasing action. (b) The intracavity photon number  $m = \langle b^\dagger b \rangle$  grows in the lasing window for increasing emitter numbers. The quenching of the photons in the high pump limit results from the strong dephasing of the lasing transition due to the incoherent pump. (c) The second order correlation function  $g^{(2)}(0)$  shows that in the lasing window for  $N > 1$  the system indeed reaches a Poissonian distribution. (d) The importance of the off-diagonal elements for  $N = 10$ : Truncating the elements  $\mathcal{P}[n, k, l]$  with  $k + l < x$  for various  $x$ . Below the lasing threshold the two-level system coherences are important, however above the lasing threshold the coherences can almost be entirely neglected.

rates  $P = 0.1 \text{ ps}^{-1}$  and  $P = 10 \text{ ps}^{-1}$ . This is merely an indication for lasing action since the rate equation does not provide any information about the statistics of the photons. However looking at the equal time second order correlation function [32]

$$g^{(2)}(0) = \frac{\langle b^\dagger b^\dagger b b \rangle}{\langle b^\dagger b \rangle^2} \quad (6.2.1)$$

in Fig. 6.5 c) it becomes clear that the system indeed starts lasing. Coherent radiation implies constant intensity, which in a photon detection experiment should yield a Poissonian number state distribution, see e.g. Ref. [148]. The correlation functions [28]

$$g^{(n)}(0) = \frac{\langle (b^\dagger)^n b^n \rangle}{\langle b^\dagger b \rangle^n} \quad (6.2.2)$$

are the moments of this distribution. Even though a second order correlation function equal to one is in principle not a sufficient criterion for a Poissonian number state distribution, from practical experience it becomes clear that in the regions where  $g^{(2)}(0) = 1$  usually also the other correlation functions  $g^{(n)}(0)$  approach unity, which is a sufficient criterion.

In the discussion of the rate equation theory it became clear that the assisted polarization

$Im\langle J_{xy}b^\dagger \rangle$  is a crucial quantity in laser theory. However the strength of the permutation symmetric method lies in the fact that it is able to treat all inter two-level system correlations exactly: Looking at the importance of quantum coherence between the individual two-level systems represented by the offdiagonal elements of the two-level system part of the density matrix – the  $\mathcal{P}[n, k, l]$  terms for  $k, l > 0$  – we see that above the lasing threshold these coherences are not important, see Fig. 6.5 d). Artificially truncating the offdiagonal elements  $\mathcal{P}[n, k, l]$  with  $k + l < x$  for varying  $x$  shows that below the lasing threshold these off diagonal elements are important in order to achieve converged results, it even can produce completely unphysical behavior like negative  $g^{(2)}(0)$ . However above the transition no influence can be detected. This indicates that the lasing action is essentially a classical effect, at least at the level of the gain medium, which may explain the success of (semi-) classical laser theories such as the rate equation theory presented in the previous section.

In fact the full quantum solution more or less just verified the expectations of the rate equation theory: If the intra-cavity photon number becomes large the system eventually starts lasing. However quantitatively determining the threshold is not possible with the rate equation theory, since it is unclear at which photon number the second order correlation function actually reaches unity. Sometimes intra-cavity photon numbers as large as 20 are needed for the  $g^{(2)}(0)$  function to reach unity [17]. Therefore common estimates like "The system starts lasing if the intra-cavity mean photon number reaches/exceeds unity" are very rough estimates in the cQED laser limit. The findings in this section reproduce the findings of Ref. [84] that in the cQED limit the second order correlation function is indispensable for identifying the lasing threshold. Murray Holland et al. [110, 149] call the sub-threshold regime of the two-level laser the super-radiant regime, since here the inter two-level system correlations are important, which indicates collective behavior (see Chapter 7 for details). They have investigated the physics of the sub-threshold laser using a quantum trajectory version of the formalism of Hartmann [100, 107]. In recent years also the connection of lasing action and collective effects such as super-, subradiance in quantum dot based micropillars has been investigated explicitly including semiconductor effects [16, 150].

### 6.3 Three- and Four-level bad cavity lasers – Spasers

In the paper of M. Richter, M. Gegg, T.S. Theuerholz, A. Knorr, published in Phys. Rev. B 035306 (2015) [17] the spaser – surface plasmon amplification by stimulated emission of radiation [59, 60] was investigated using the permutation symmetric method: A set of identical two-level systems coupled to a bosonic surface plasmon mode of a spherical metal nanoparticle [151]. The whole setup is inspired by the experiment of Noginov *et al.* from 2009 [39]. This paper received considerable attention as it promised a new laser like light source with spatial dimensions below the diffraction limit, which is impossible using conventional light resonator designs. However, nowadays, their findings are at best controversially discussed in the field [152, 153].

The treatment in Ref. [17] is equivalent to a bad cavity (short boson lifetime) two-level laser setup with (relatively) high two-level system mode interaction strength. The main reason for the short plasmon lifetime are ohmic losses in the metal, which in turn results in heat generation. It was found that the system could in principle start spasing, however the pump rates and gain required to overcome the plasmonic losses are so high that the system very likely would melt before coming near the spasing threshold [154]. Thus the spaser setup proposed by Bergman, Stockman and measured by Noginov *et al.* can be regarded as an efficient nanosized optical to thermal energy converter.

However the question occurred whether three- or four-level laser theories might be able to partly overcome the intrinsic shortcomings of the spaser design. In fact Noginov *et al.* used dye

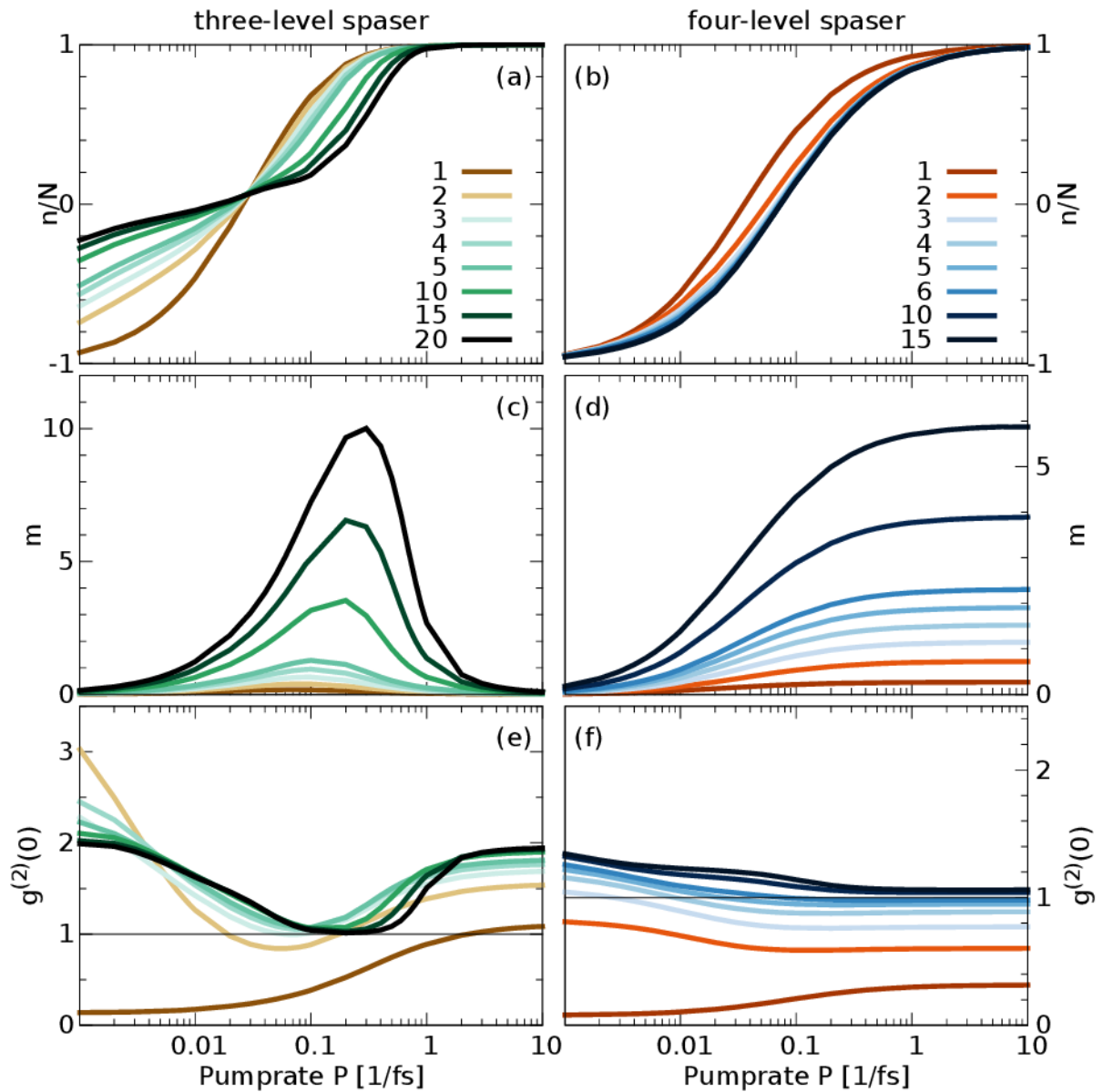


**Figure 6.6 – Three- and four-level spasers:** Left column three-level spaser and right column four-level spaser. (a) and (b) The mean, normalized population inversion of the lasing transition  $n/N$ . Double and single S shape curves for three- and four-levels respectively. (c) and (d) the plasmon number  $m = \langle b^\dagger b \rangle$ . Quenching for three-level systems and no quenching for four-level systems, due to the different pump dependent dephasing actions in these two setups. (e) and (f) the second order correlation function  $g^{(2)}(0)$ . In the lasing window of the three-level systems the system indeed reaches a Poissonian distribution. For the four-level systems it is not entirely clear from the second order correlation function alone whether this should be called spasing action.

molecules as gain medium in their setup – dye lasers are the standard example for four-level lasers. Thus for a correct quantum description of their findings a four-level gain theory should be applied. Furthermore this serves as a proof of principle that the permutation symmetric method and PsiQuaSP [26, 27] are in fact able to handle multi-level systems.

As stated in the discussion of the rate equation theory expectations the three-level laser and the two-level laser are similar setups, thus there is not much difference to be expected. However the four-level laser is intrinsically different since the pump does not introduce dephasing in the lasing transition and therefore the quenching effect should be absent. It is crucial to realize that in three- and four-level laser theories the additional relaxation processes that are related to the population of the upper lasing level and the depopulation of the lower lasing level (Fig. 6.3 b) and c)) are material parameters and should therefore be kept constant in the simulation. This however introduces material limitations to the gain and thus lasing action that are absent in the two-level laser theory.

As expected from the rate equation considerations, the three-level laser behaves quite similar to the two-level laser, Fig. 6.6: There is a maximum in the plasmon output  $\propto m$  and the system starts spasing for sufficiently high emitter numbers. At high pump rates the dephasing of the lasing transition quenches plasmon generation (compare to Figs. 6.4 (b) and 6.5 (b)). Contrary the four-level spaser does not experience this dephasing and thus does not have a maximum in the plasmon number. However the plasmon generation saturates for high pump powers which is a result of the material limitations due to the constant rates for  $\gamma_{3\rightarrow 2}$  and  $\gamma_{1\rightarrow 0}$ , i.e. the population rate of the upper lasing level and the depopulation rate of the lower lasing level. Interestingly it is not clear at all whether the four-level setup crosses the threshold at all: For  $N = 6$  it seems as if the setup starts spasing, the number of plasmons is above unity (which is a rather common criterion for lasing action, as discussed above) and the  $g^{(2)}(0)$  function equal to one for  $P > 0.1 \text{ fs}^{-1}$ . Normally this would be associated to spasing/lasing. However increasing the number of emitters, which is equivalent to increasing the gain results in higher numbers of plasmons *and*  $g^{(2)}(0)$  values. So even though the number of plasmons increases the statistics becomes less Poissonian when increasing the gain. For higher numbers of emitters it might even grow further and thus completely leaving the coherent regime. This should clearly be attributed to sub-threshold behavior, because above the threshold an increase in gain should lead to better lasing performance rather than worse. This further supports the observation that identifying the lasing threshold for cQED lasers is a complex task and should therefore be done with caution and proper theoretical methods.

Overall the three- and four-level spaser schemes do not provide major benefits compared to the two-level spaser: The threshold is still unrealistically high and the problem of high losses remains the same. Generally it is theoretically expected that the metal nanoparticle melts when the plasmon number roughly reaches one [154], which is also confirmed by experimentalists working in the field [152]. However the three-level spaser theory expects spasing at plasmon numbers of  $m > 5$ , thus in an unrealistic parameter regime. Generally there is an active discussion in the plasmonics community of how to overcome the problem of high plasmonic losses. Jacob Khurgin proposed to use the "high  $Q$  window" of the noble metals gold and silver: As stated in Chapter 2 the dielectric constant of the surrounding medium  $\epsilon_h$  has a large impact on the dipole plasmon resonance  $\omega_{sp}$ , due to the Fröhlich condition [155, 45]

$$\text{Re}(\epsilon(\omega = \omega_{sp})) = -2\epsilon_h. \quad (6.3.1)$$

here  $\epsilon(\omega)$  is the dielectric function of the metal. Due to this resonance condition the plasmon frequency shifts to lower energies for higher host dielectric constants  $\epsilon_h$ . However the dielectric constants needed to provide  $Q$  factors of  $\sim 100$  are of the order  $\epsilon_h \geq 10$ , which is a value that is difficult to obtain. Furthermore Khurgin pointed out that surface scattering plays an important

role in nanosized metal particles, which also reduces plasmon lifetimes [47].

Generally the model assumptions made in the present spaser theory are hardly justified but serve as an extreme version of a best-case scenario – there is no reason to expect that a more noisy/complicated/realistic model would give a better performance, bypass the intrinsic shortcomings and overcome the losses. This expectation is supported by literature: As stated in Chapter 2 the plasmonic theory employed is very rough, considering only one mode is not justified since the plasmonic structure supports multipole modes that are especially important in the closely packed geometry of the Noginov design. In fact the measured threshold behavior could be reproduced theoretically as a sub threshold mode competition effect between these multipole modes, which however further degrades the prospects of spasing action [153]. Furthermore the assumption of identical coupling is not justified for randomly distributed emitters in a strongly spatially varying near field mode. Yuang Zhang, Klaus Mølmer and Volkhard May investigated this spaser geometry using a three-level gain theory as in the discussion above [156] and randomly oriented emitters using a explicitly spatially dependent coupling parameter [157]. However the authors found that the inclusion of the spatial dependence further degrades the performance of the device.

## 6.4 Conclusion

In this chapter the permutation symmetric method was successfully applied to different laser setups, namely two-, three- and four-level laser theories. It was identified at the rate equation theory level that two- and three-level lasers should behave similarly, they both experience pump dependent quenching of the lasing output, while this effect is absent in a four-level laser. Generally the qualitative expectations of the rate equation theory were confirmed using the exact permutation symmetric method and PsiQuaSP. This serves as a prove of principle that the library is in fact able to handle multi-level system setups.

In the discussion of the two-level cQED laser it was found that the strength of the permutation symmetric method in fact lies in describing the sub-threshold behavior of the system: The inclusion of the off-diagonal elements in the two-level system part of the density matrix is only important below the lasing threshold. This is the so-called superradiant regime of the laser [110, 149]. Generally this setup is somewhat the simplest meaningful setup for the permutation symmetric method. All results in this chapter were obtained using direct time-integration, the transient dynamics converge fast, thus there is no need for steady state solvers. Furthermore it turns out that the two-level system part of the density matrix of the two-level system laser only scales like  $\propto N^2$  instead of the expected  $\propto N^3$ , thus further simplifying this setup. The details of this reduction of degrees of freedom are discussed in Chapter 9.

The investigation of the multi-level spaser theories revealed that even the inclusion of more realistic and involved gain medium theories cannot overcome the intrinsic design shortcomings of the spaser setup: Plasmonic losses are too high, heating destroys the samples and downscaling introduces further losses due to surface or bound state scattering [47].

## 7 The open Dicke model

In this chapter the permutation symmetric method will be applied to the open Dicke model: A set of identical two-level systems coupled to a bosonic mode. This is in fact the same setup as in the two-level laser discussed in the previous chapter. However in this chapter the two-level systems will be coherently driven by an external, cw laser and the focus of the investigation will be the population of the various Dicke states, especially the subradiant and dark states as discussed in Chapter 4. Furthermore the distinction of individual and collective behavior in this system under the presence of dephasing is elucidated.

A simple rate equation description of the model predicts a bistable behavior, which is closely related to the system known as absorptive optical bistability and cooperative resonance fluorescence. However the master equation has always a unique steady state, which is an apparent contradiction. It is known from advanced theoretical analysis that strong quantum coherences/collective behavior lifts this bistability and allows tunneling between the two states predicted by rate equation theory. Therefore it is to be expected that coherent effects play a dominant role in this setup.

The influence of the incoherent drive of the two-level laser was found to result in strong dephasing of the inter two-level system coherences and thus leads to individual behavior. In Chapter 4 the collective Dicke basis was introduced and it was seen that this collectivity has a strong influence on the light matter interaction strength: The interaction strength of the superradiant states with a cavity mode scales with  $\propto N^2$  while some of the subradiant states are dark, or rather do not couple to the cavity at all. If the two-level systems interact individually with the cavity mode the coupling scales strictly like  $\propto N$ .

While the closed system is completely described by the superradiant subspace which has dimension  $N + 1$  the individual system bath interactions like spontaneous emission, pure dephasing and incoherent driving were found to break the  $J^2$  symmetry of the Dicke Hamiltonian and thus does not allow a treatment in the symmetric Dicke states. This observation lead to the formu-

lation of the symmetrized Liouville space states and the observation that the density matrix is block diagonal in the Dicke basis in Chapter 5. In this chapter collective effects and especially the population of the subradiant and dark Dicke states are investigated. Therefore, instead of driving the two-level systems incoherently, the systems are now driven coherently via an external classical laser, which favors collective behavior. Driving is necessary since subradiant states are excited states, see Fig. 7.1 (b).

In a frame rotating at the external laser frequency, using the rotating wave approximation the system Hamiltonian reads

$$H = \hbar\Delta_0 b^\dagger b + \hbar\Delta_1 J_{11} + \hbar g(J_{10}b + J_{01}b^\dagger) + \hbar E(J_{10} + J_{01}), \quad (7.0.1)$$

where  $\Delta_0$ ,  $\Delta_1$  are the mode and TLS detuning,  $g$  is the TLS-mode coupling,  $E$  is the optical driving. Both cavity and TLS are subject to loss and dephasing, using Lindblad formalism [13]. The master equation reads

$$\partial_t \rho = \mathcal{L}\rho = \frac{i}{\hbar}[\rho, H] + \mathcal{D}_{de} + \mathcal{D}_{pd} + \mathcal{D}_{ph}. \quad (7.0.2)$$

The Lindblad dissipators describe decay processes like individual radiative and non-radiative decay

$$\mathcal{D}_{de} = \gamma/2 \sum_i (2\sigma_{01}^i \rho \sigma_{10}^i - \sigma_{11}^i \rho - \rho \sigma_{11}^i), \quad (7.0.3)$$

pure dephasing

$$\mathcal{D}_{pd} = \delta/2 \sum_i (\sigma_z^i \rho \sigma_z^i - \rho) \quad (7.0.4)$$

with  $\sigma_z^i = \sigma_{11}^i - \sigma_{00}^i$  and cavity decay

$$\mathcal{D}_{ph} = \kappa/2(2b\rho b^\dagger - b^\dagger b\rho - \rho b^\dagger b), \quad (7.0.5)$$

see Fig. 7.1 (a). All contributions to the master equation except  $\mathcal{D}_{de}$  and  $\mathcal{D}_{pd}$  commute with  $J^2$  and are thus total spin preserving, (Fig. 7.1 (b)).

Subradiance is a collective effect and the collective processes in the system, namely the cavity – two-level system interaction and the external semi-classical drive lead to such collective behavior. However these two processes do not couple different Dicke subspaces, thus only considering these two processes would confine the system to the superradiant subspace, as stated above. The individualization introduced through e.g. individual spontaneous emission couples the different Dicke subspaces but leads to individualization. It was found in Section 5.5.3 that two-level systems decaying through individual spontaneous emission are accurately described without any quantum coherences/off-diagonal elements (Eq. (5.5.17)). If the two-level systems behave completely individual there will also be no subradiant behavior in the system. Thus in order to observe genuine Dicke subradiant behavior an interplay between collectivity and individualization is necessary.

Investigating the population in all the Dicke basis states requires the computation of the whole density matrix, especially the off-diagonal elements are important (compare to the discussion in Chapter 4, Section 5.6 and the explicit expressions of the Dicke state projectors in Appendix B.4). Thus the information about the Dicke state occupations is not accessible to a simple rate equation theory.

Being able to practically treat collective and individual processes simultaneously while giving access to the full density matrix is exactly the strength of the permutation symmetric method. The numerical results of this chapter could not have been computed using a brute force solution, even the use of an adaptive step width Runge-Kutta together with the permutation symmetric

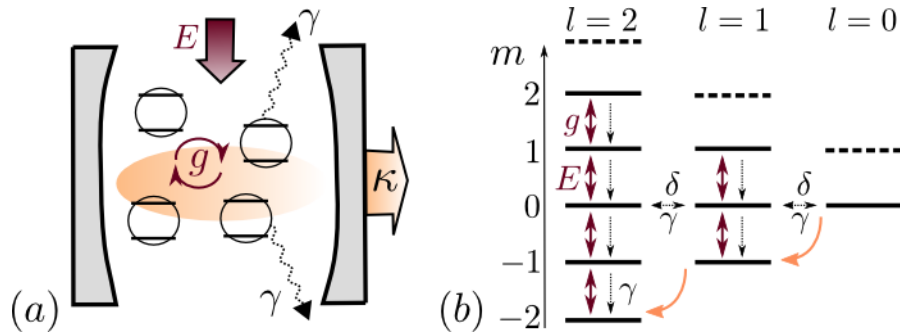


**Figure 7.1 – Illustrating the open Dicke model** (a) Schematic representation of the system. (b) Dicke states for  $N = 4$ . The lowest state in each  $l$  subspace is dark – the lowest state in the superradiant  $l_{max} = N/2$  subspace is the ground state. The interactions are depicted: Hamiltonian part (purple, thick), dissipators  $\mathcal{D}_{de}$  and  $\mathcal{D}_{pd}$  (black, thin) and dark state cascade (orange, curved). Dashed lines indicate the additional states for  $N = 5$  (with different values of  $m, l$ ).

method would make the present discussion next to impossible. The combination of fast time scales through superradiant effects and slow time scales introduced through the subradiant effects makes direct time integration very unfavorable. Thus the present discussion provides an excellent testing ground for the steady state solvers available through PsiQuaSP.

The chapter is organized as follows: First in Section 7.1 a short review of the physics of the Dicke model is given. In Section 7.2 the rate equation theory will be derived and the emergence of the bistable behavior will be explained. Furthermore the connections to optical bistability and cooperative resonance fluorescence will be explained. In Section 7.3 the superradiant to subradiant phase transition is introduced and its manifestation in experimentally accessible quantities is discussed. Thereafter in Section 7.4 the ground state relaxation properties of the system are investigated, which leads to the formation of dark state cascades. Finally in Section 7.5 the findings of this chapter are summarized and implications and deduced research questions are discussed.

## 7.1 Dicke model physics

The open (and closed) system Dicke model has been a work horse in quantum optics and beyond for decades [25, 43, 18, 19, 23, 158, 159, 160, 85, 161, 162, 163, 22, 164, 165, 166, 167, 17, 168, 169, 78, 102]. Not only is the Dicke model the theoretical foundation for lasers as discussed in the previous chapter but it also explains effects such as optical bistability, cooperative resonance fluorescence, super- and subradiance. These effects are connected to theoretical concepts and applications such as quantum light generation, (multipartite) entanglement and phase transitions.

In recent years superradiance has attracted a lot of interest [161, 22, 168, 169, 170] since it is an experimentally accessible effect of truly collective behavior and it was believed for a long time that there is an intrinsic connection between superradiance and entanglement: The superradiant subspace is spanned by the symmetric  $N$  particle generalizations of the Bell states, these states are entangled and are called  $W$ -states in the entanglement community [171, 172]. However it was found recently that there is in fact no connection between superradiance and entanglement, even though the process lives in a space whose basis states are entangled states the whole density matrix is separable [168]. Generally a mixed  $N$ -partite system is said to be separable (entangled) if it (cannot) be written as a sum over direct products of possibly mixed

single system density matrices [80, 81]

$$\rho = \sum_n p_n \rho_n^{(1)} \otimes \rho_n^{(2)} \otimes \cdots \otimes \rho_n^{(N)}. \quad (7.1.1)$$

Superradiance has been demonstrated in a large variety of material platforms since it is a spontaneous process that forms by itself: Preparing  $N$  two-level quantum emitters in a fully excited state results in a spontaneous, highly directed superradiant burst provided that the two-level emitters interact collectively to their electromagnetic surrounding. This can either be achieved by confining a free space ensemble of two-level quantum emitters in a spatial volume of  $(\lambda/2)^3$ , with  $\lambda$  being the wavelength of the emitted light, or by placing the emitters in a bad cavity ( $\kappa \gg g$ ). In fact the effect also occurs in classical acoustic, mechanical systems and can be explained by phase matching [173].

Contrary to superradiance, subradiance is being investigated for its prospects to store quantum information: As seen in Chapter 4 some of the subradiant states are dark and thus provide excellent candidates to store a quantum state or rather provide long lived coherent excitations [169, 170]. However since the subradiant states do not or only weakly couple to the external radiation field and therefore also generally need a long time to be populated this phenomenon has remained more elusive.

The Hamiltonian Eq. (7.0.1) already is formulated in the rotating-wave approximation (RWA). This implies that it is only valid for  $g \lesssim 0.1\sqrt{\omega\omega_1}$ . Including the non-RWA terms results in the full Dicke Hamiltonian

$$H = \hbar\omega b^\dagger b + \hbar\omega_1 J_{11} + \hbar g(J_{10} + J_{01})(b^\dagger + b), \quad (7.1.2)$$

where also the rotating frame is no longer applicable<sup>1</sup>. For ultra-strong coupling this Hamiltonian undergoes a quantum phase transition at the critical coupling strength  $4Ng^2 = \omega\omega_1$ : The Hamiltonian gap closes and the ground state of the system changes to a state with non-zero mean photon number. Therefore this phase transition is often called the superradiant phase transition [18, 85]. However there is an active debate where and if it is actually possible to observe this phase transition in quantum optical setups [105, 106].

In this chapter/thesis only moderate coupling strengths are considered and therefore it is possible to treat the Dicke Hamiltonian in the RWA, like in Eq. (7.0.1).

## 7.2 Bistable effects in quantum optics

As stated above the open Dicke model gives birth to effects like optical bistability and cooperative resonance fluorescence. These two setups are closely related to the system studied in this chapter. This section starts with a rate equation/low order cluster expansion theory derivation, starting from the master equation Eq. (7.0.2). This will serve as an introduction to the notion of bistability in quantum optics. However the focus of the discussion here lies on where the rate equation theory breaks down, where it produces results that are in obvious contradiction to the full quantum theory. It is this regime where quantum correlations are expected to be strong and should dominate the behavior of the system [14]. Afterwards a short review of cooperative resonance fluorescence and optical bistability is given and the similarities and differences to the investigated effects in this chapter are discussed.

The derivation of the rate equation theory starts from the time derivatives of the expectation values of the elementary polarization operators  $b$ ,  $J_{01}$  and the collective excited state projector

<sup>1</sup>Unless one wishes to work with an explicitly time dependent Hamiltonian.

$J_{11}$ <sup>2</sup>. These expectation values couple to the higher order correlations  $\langle bJ_{11} \rangle$  and  $\langle bJ_{10} \rangle$ , which again can be factorized

$$\langle bJ_{11} \rangle \rightarrow \langle b \rangle \langle J_{11} \rangle, \quad \langle bJ_{10} \rangle \rightarrow \langle b \rangle \langle J_{10} \rangle, \quad (7.2.1)$$

to give a closed set of equations of motion. On resonance ( $\Delta_0 = \Delta_1 = 0$ ) one can derive an equation that relates the input power  $\propto E^2$  to the mean, two-level system excitation number  $n = \langle J_{11} \rangle$

$$\epsilon = -\frac{n}{2n - N} (1 - 2C(2n - N) + \frac{1}{2}C^2(2n - N)^2), \quad (7.2.2)$$

with

$$\epsilon = \frac{4E^2}{\gamma(\gamma + \delta)}, \quad C = \frac{4g^2}{\kappa(\gamma + \delta)}. \quad (7.2.3)$$

The parameter  $C$  is often called cooperativity [174]. If it is large enough the system behaves bistable. The interesting part in Eq. (7.2.2) is that the right hand side is a rational function, including a second order polynomial and a first order pole at  $n = N/2$ , whereas the left hand side is a constant that is fixed by external parameters. Thus for a given external field strength  $E$  there may be multiple solutions to this equation. This observation serves as the theoretical origin of the phenomenon called optical bi- and multistability [21, 175] and has attracted considerable interest over the last couple of decades: Bistability and multistability imply that depending on the initial state the system evolves into different steady states. In other words the steady state of the system contains information about the initial state which has sparked vivid discussions around the question of whether this could be used to store quantum information. This phenomenon is closely related to or rather the origin of the notion of dissipative phase transitions (see below) [73]. Also the bistable behavior can be exploited to build all optical transistor and transmission devices or rather optical logical devices [176, 177]. The field of all-optical logical devices is currently particularly relevant for telecommunication applications as it is believed that such devices could result in an urgently needed reduction of the energy consumption of the internet [178].

Particularly striking is the observation that the original master equation always has a unique, defined steady state. The fact that both the cavity and the two-level systems are subject to (individual) spontaneous emission is a sufficient criterion for a unique steady state [69, 72]. Thus already at this level, without having computed anything, there is an apparent contradiction between rate equation theory and the full quantum solution, as opposed to laser theory.

The apparent contradiction between bistable rate equation prediction and unique steady state of the quantum solution and the actual experimental observations of bistabilities was one of the major research questions centered around bistable systems in quantum optics. This problem was resolved when it was realized that in these systems the Liouvillian gap can become very small and that it may even close in the thermodynamic, infinite system size limit [179, 97, 180]. Thus in the infinite system size limit the contradiction is lifted, however in the small or mesoscopic range investigated here this contradiction prevails.

In Fig. 7.2 the rate equation theory expectation is compared to the number state distributions from the full quantum solution of PsiQuaSP. The rate equation predicts the mean values of the distribution, however a distribution always has a unique mean value. In the low and high driving limit the rate equation accurately predicts the mean value however at the bistable, phase transition point the rate equation theory fails, at least in the small system limit: In the bistable

<sup>2</sup>Here the polarizations  $\langle b \rangle$  and  $\langle J_{10} \rangle$  have to be/can be included since the semiclassical optical pump drives these polarizations, contrary to the laser example of the previous chapter. There all these polarizations are strictly zero. The semi-classical pump breaks the  $U(1)$  symmetry, that leads to the  $\propto N^2$  scaling of the two-level system degrees of freedom, see Chapter 9 for details.

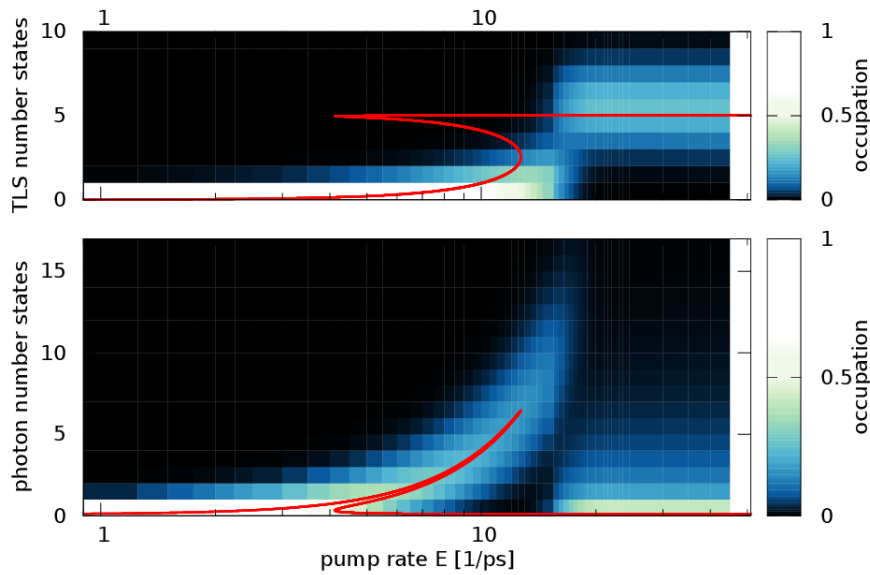


**Figure 7.2 – Rate equation vs full quantum solution:** The distributions are the full quantum solutions computed by PsiQuaSP and the red line represents the rate equation solution. Far away from the switching, bistable range the rate equation predictions are somewhat accurate, however in the range  $5 - 20 \text{ ps}^{-1}$  the rate equation theory clearly fails.

range the rate equation actually has three solutions but it can be shown that the "middle" solution is always unstable, therefore only the upper and lower most solutions represent the actual bistability. At the point where the distribution of the full quantum solution suddenly switches – the phase transition point – it actually bears two maxima each in the photon number states as well as in the two-level system number states. The doubly peaked photon distribution has been identified to be closely related to bistability: In the large system limit the positions of these maxima converge towards the two stable solutions of the rate equation theory and the position of the minimum between the two maxima converges towards the unstable rate equation solution [181]. This is highly reminiscent of the observation in quantum field theory that the classical trajectory of a particle is just the quantum trajectory of highest probability [182]. Here there are no trajectories – only steady states, but still the stable classical solution coincides with the quantum solution of highest probability and the unstable solution corresponds to the local minimum – the extremal points of the distribution converge towards the classical results and the curvature of the distribution at these extremal points determines the stability of the corresponding classical solution<sup>3</sup>.

The related experimental observations of bistabilities in these systems can be understood by realizing that the typical time scale in which the system is measured can become short to the steady state convergence time and thus the experimental observations of bistabilities are in fact transient effects. The actual time dependence of the bistable behavior in an experiment has only been measured and calculated recently [183, 184].

The system defined by Eqs. (7.0.2) and (7.2.2) is closely related to absorptive optical bistability and cooperative resonance fluorescence. Historically these two phenomena were the first physical effects that allowed to study cooperative/collective effects in the open Dicke model theoretically

<sup>3</sup>Here a discrete probability distribution is considered, which obviously has no curvature. But going to larger system sizes the discrete distribution can be approximated by a continuous distribution, which in fact would be the phase space formulation of the problem. This is also similar to solid state physics where discrete sums over many summands are approximated by continuous functions.

as well as experimentally. The discussion of these effects were also the main driving force of the development of the quantum optical phase space methods in the 1970's and 80's that were originally developed around laser theory, but needed to be improved to describe the strong collective effects in these systems<sup>4</sup>. The phase space methods also serve as the many emitter counterpart of the permutation symmetric method introduced in Chapter 5.

The notion of optical bistability and cooperative resonance fluorescence was coined by the seminal papers by Bonifacio and Lugiato [21, 175]. They derived a semi-classical rate equation theory based on physical intuition rather than a microscopic Hamiltonian and observed bistable behavior between different branches – a collective and an individual branch.

In the bad cavity (short photon lifetime,  $\kappa \gg g$ ) limit the setup considered in this chapter is equal to cooperative resonance fluorescence setup: In the bad cavity limit it is possible to adiabatically eliminate the cavity mode which results in the master equation (on resonance  $\Delta_0 = \Delta_1 = 0$ ) [19, 97]

$$\begin{aligned} \dot{\rho} = & + iE [\rho, J_{10} + J_{01}] + \frac{g^2}{\kappa} (2J_{01}\rho J_{10} - J_{10}J_{01}\rho - \rho J_{10}J_{01}) \\ & + \frac{\gamma}{2} \sum_i (2\sigma_{01}^i \rho \sigma_{10}^i - \sigma_{11}^i \rho - \rho \sigma_{11}^i). \end{aligned} \quad (7.2.4)$$

Here  $E$  is still the coherent emitter driving strength,  $g$  is the cavity coupling strength,  $\kappa$  is the cavity photon decay rate and  $\gamma$  is the individual decay rate of the two-level systems. This is a master equation that describes two competing physical decay processes: collective and individual decay. For low driving strengths the system behaves collective and for high driving strength the system behaves individual. In the region between these two branches, rate equation theory predicts a bistable behavior. In absorptive optical bistability usually the cavity is driven by an external laser instead of the two-level systems. Here usually the two-level systems are adiabatically eliminated, which corresponds to the good cavity limit<sup>5</sup>. This system also splits in two branches for low and high driving strengths with a bistable switching region predicted by rate equation theory. Generally these two setups are very similar and were investigated in the context of the mentioned bi-, multistability, cooperativity, squeezing and quantum light generation (anti-bunching). Since the phase space methods allow analytic treatments of the steady state properties almost all of these works focus on steady state behavior and almost no work has been done on explicit transient dynamics. Furthermore, even though these systems were studied in the context of collective behavior there are – to the best of my knowledge – no prior studies investigating the population of the various subradiant Dicke states in these systems. There have been  $J^2$ , total spin preserving studies that essentially studied the superradiant effects albeit not using this nomenclature [19, 23, 159, 160].

---

<sup>4</sup>In the early days of the phase space methods it was customary to expand the density matrix *diagonally* in photonic and atomic coherent states, see e.g. Ref. [19]. This however leads to a non-positive semidefinite diffusion matrix in the associated Fokker-Planck equations and thus sometimes to unphysical behavior. This was resolved by expanding the density matrix in a non-diagonal way in the coherent state, which is named generalized or positive P representation [104, 4, 32]. From a modern perspective it seems hardly surprising that a system that bears strong quantum correlations, encoded in the off-diagonal elements of the density matrix, needs a full expansion of the density matrix in order to give physically meaningful results.

<sup>5</sup>There are some works that treat optical bistability without good or bad cavity limit e.g. Ref. [185]. These works rely on the positive  $P$  representation in the high emitter number limit, which essentially amounts to a weak quantum correlation limit. In this chapter the strong correlation limit is investigated.

### 7.3 Superradiant to subradiant phase transition

In this section the population of subradiant states in the system through individual decay and pure dephasing processes is investigated – both processes do not conserve the total spin. Counterintuitively, the cavity lifetime determines the population of the subradiant states, even though the cavity decay Liouvillian does not break the  $J^2$  symmetry and thus does not couple different Dicke subspaces: Increasing the cavity lifetime changes the nature of the non-equilibrium phase transition discussed in the previous section. In the bad cavity, cooperative resonance fluorescence limit the subradiant states are always suppressed by quantum coherence, essentially the quantum correlations are pushing the system into the superradiant subspace. Increasing the cavity lifetime completely changes this behavior, it leads to an amplification of these subradiant states above the phase transition. The individual spontaneous emission process is a necessary requirement for the population of subradiant Dicke states, however the associated decay rate has no influence on the population behavior of the subradiant states in realistic parameter regimes. The coherences of the subradiant states are only formed through the cavity degrees of freedom. The observed effect is thus a cavity assisted generation of subradiant quantum coherences.

This effect is accompanied by clear changes in experimentally accessible signatures. Furthermore the system is found to exhibit genuine multi-partite entanglement below the transition. Switching off the external driving, the subsequent relaxation into the ground state forms a long-lived cascade of dark Dicke states. This results in a simple, deterministic protocol for dark state preparation with populations close to unity under the influence of dephasing. This could be useful for storing quantum information. The results presented here were published in M. Gegg, A. Carmele, A. Knorr, M. Richter arXiv:1705.02889 (2017).

As explained in Chapter 4 the total spin  $l(l+1)$  is the eigenvalue of the Casimir operator

$$J^2 = (J_{10}J_{01} + J_{01}J_{10})/2 + J_z, \quad (7.3.1)$$

with  $J_z = 1/2 \sum_i \sigma_z^i$ . The  $J^2$  and  $J_z$  eigenvalues determine the coupling strength of the multi TLS (Dicke) state to an optical mode, the collective dipole transition element. This coupling strength distinguishes between superradiance and subradiance. For superradiant states the dipole element scales superlinear in  $N$ , while for subradiant states the scaling is sublinear in  $N$  and some subradiant states are dark [28]. Dark means that the dipole transition element vanishes, meaning these states cannot decay e.g. by creating a cavity photon. However this is only true for collective,  $J^2$  symmetric interactions, these states still decay into other states via the individual,  $J^2$  symmetry breaking decay and dephasing processes  $\mathcal{D}_{de}$  and  $\mathcal{D}_{pd}$ , c.f. Fig. 7.1 (b). Generally the spin preserving contributions in the master equation generate quantum correlations leading to collective TLS behaviour (such as super- and subradiance) and the nonpreserving terms destroy correlations leading to individualization. However only the spin nonpreserving contributions introduce coupling between superradiant and subradiant states, thus in order to prepare subradiant states an interplay of collectivity and individualization is necessary. Throughout this discussion  $l_{max} = N/2$  will refer to the superradiant subspace and  $l_{min} = 0, 1/2$  will refer to the most subradiant subspace.

As stated above, in the bad cavity limit ( $\kappa \gg g$ ) Eq. (7.0.2) corresponds to the cooperative resonance fluorescence setup [19, 23]. The system exhibits a non-equilibrium phase transition for increasing  $E$  for both total spin preserving and nonpreserving setups [19]. In the following the behavior of the system at moderate cavity lifetimes  $\kappa \sim g$  will be investigated, the intermediate range between good and bad cavity limit. The system then represents the intermediate regime between cooperative resonance fluorescence and absorptive optical bistability setup [176] (instead of driving the TLS, in optical bistability the cavity is driven, opposed to Fig. 7.1 (a)).

### 7.3.1 Collectivity measure

Investigating super- and subradiant states requires a suitable measure. Unfortunately computing the respective Dicke state populations is not sufficient for investigating collective effects, if dephasing is present: Dicke states  $|l, m\rangle$  are eigenstates of  $J^2$  and  $J_z$  with corresponding quantum numbers  $l(l+1)$ ,  $0 \leq l \leq N/2$  and  $|m| \leq l$ .  $l_{max} = N/2$  defines the superradiant subspace and  $l_{min} = 0, 1/2$  defines the (most) subradiant subspace, see Fig. 7.1 (b). As an example consider the  $N = 4$  Dicke states: The superradiant subspace consists of five states and there are three  $l$  subspaces in total with quantum numbers  $l = 2, 1, 0$ . As explained in Section 5.6 and Appendix B.4 the Dicke state projectors can be expressed in the symmetrized Liouville basis states  $\hat{\mathcal{P}}[n, k, l]$ : The superradiant subspace reads

$$\begin{aligned}
|2, -2\rangle\langle 2, -2| &= \frac{1}{1} \hat{\mathcal{P}}[0, 0, 0], \\
|2, -1\rangle\langle 2, -1| &= \frac{1}{4} (\hat{\mathcal{P}}[1, 0, 0] + \hat{\mathcal{P}}[0, 1, 1]), \\
|2, 0\rangle\langle 2, 0| &= \frac{1}{6} (\hat{\mathcal{P}}[2, 0, 0] + \hat{\mathcal{P}}[1, 1, 1] + \hat{\mathcal{P}}[0, 2, 2]), \\
|2, 1\rangle\langle 2, 1| &= \frac{1}{4} (\hat{\mathcal{P}}[3, 0, 0] + \hat{\mathcal{P}}[2, 1, 1]), \\
|2, 2\rangle\langle 2, 2| &= \frac{1}{1} \hat{\mathcal{P}}[4, 0, 0].
\end{aligned} \tag{7.3.2}$$

The other two subspaces are given by

$$\begin{aligned}
D_1|1, -1\rangle\langle 1, -1| &= \frac{1}{4} (3\hat{\mathcal{P}}[1, 0, 0] - \hat{\mathcal{P}}[0, 1, 1]), \\
D_1|1, 0\rangle\langle 1, 0| &= \frac{1}{2} (\hat{\mathcal{P}}[2, 0, 0] - \hat{\mathcal{P}}[0, 2, 2]), \\
D_1|1, 1\rangle\langle 1, 1| &= \frac{1}{4} (3\hat{\mathcal{P}}[3, 0, 0] - \hat{\mathcal{P}}[2, 1, 1]), \\
D_0|0, 0\rangle\langle 0, 0| &= \frac{1}{6} (2\hat{\mathcal{P}}[2, 0, 0] + 2\hat{\mathcal{P}}[1, 1, 1] - \hat{\mathcal{P}}[0, 2, 2]).
\end{aligned} \tag{7.3.3}$$

$D_0$  and  $D_1$  are the degeneracies of the respective Dicke subspaces given by Eq. (4.1.18). Since the processes in the master equation do not discriminate between the different degenerate Dicke states, this degeneracy just enters as a prefactor here.

Calculating the population of the Dicke states then amounts to computing the expectation values

$$\text{tr}[|l, m\rangle\langle l, m|\rho] = \langle l, m|\rho\rangle \equiv p(l, m) \tag{7.3.4}$$

Thus expressed in the permutation symmetric density matrix elements  $\mathcal{P}[n, k, l]$  these populations are generally given by an expression like

$$p(l, m) = a_0(l, m)\mathcal{P}[n, 0, 0] \pm a_1(l, m)\mathcal{P}[n-1, 1, 1] \dots, \tag{7.3.5}$$

with  $n = m + N/2$ , where the prefactors  $a_k(l, m)$  are rational numbers depending on the two quantum numbers  $l$  and  $m$ .

In the presence of dephasing the elements  $\mathcal{P}[n, k, k]$  for  $k \neq 0$  (representing quantum correlations/coherences) experience dephasing. If the dephasing is strong enough it will completely suppress the quantum correlations, i.e.  $\mathcal{P}[n, k, k] = 0$  for  $k \neq 0$ . This situation then corresponds to a completely incoherent mixture of TLS occupations. For varying numbers of TLS,  $\mathcal{P}[n, 0, 0]$

distributions allow a large variety of populations in super- and subradiant states even if quantum coherences are absent. Generally – when spin non-conserving terms are included – the superradiant subspace population decreases, since for large  $N$  the superradiant subspace is very small compared to the full Hilbert space ( $N + 1$  vs.  $2^N$ ). However without quantum coherences ( $\mathcal{P}[n, k, k]$ ,  $k \neq 0$ ) in the individual TLS basis the label super- and subradiance becomes meaningless, since the quantum coherences are the signatures of the collectivity of the Dicke states and reflect the redistribution of oscillator strength through collective effects. In other words, in general the study of quantum coherent effects between distinct quantum emitters requires explicitly looking at the offdiagonal elements of the density matrix in the basis of the individual quantum emitters.

Thus – in the open Dicke model –  $\mathcal{P}[n - k, k, k]$  are the key quantities that distinguish a super- or subradiant state from a classical, incoherent mixture of TLS population ( $\mathcal{P}[i, j, k] = 0$  for  $j, k \neq 0$ ). Or in other words the  $\mathcal{P}[n - k, k, k]$  distinguish between collective and individual behavior. The decay process  $\mathcal{D}_{de}$  and the pure dephasing  $\mathcal{D}_{pd}$  act individually on every TLS and thus destroy the collectivity, resulting in incoherent mixtures.

To quantify the effect of collectivity and distinguish between collective and individual behavior we introduce the ratio between the full Dicke subspace population and its incoherent part [20]

$$R(l) = \frac{\sum_m p(l, m)}{\sum_m a_0(l, m) \mathcal{P}[m + N/2, 0, 0]}, \quad (7.3.6)$$

as a collectivity measure.  $\mathcal{P}[i, k, k] \sim 0$ ,  $k \neq 0$  results in  $R(l) = 1$ : The influence of quantum correlations between the individual TLS on the subspace population is zero or negligible – the TLS act *individually*.  $\mathcal{P}[i, k, k] \neq 0$ ,  $k \neq 0$  results in  $R(l) < 1/R(l) > 1$ : Quantum correlations *suppress/increase* the respective subspace occupation – the TLS act *collectively*.  $R(l)$  provides a reality check, since in any experiment dephasing is present and isolated Dicke subspaces (or states) will likely not occur.

In the entire chapter the parameters for the individual decay lifetime and the emitter cavity coupling are fixed at  $\gamma = 1.0 \text{ ns}^{-1}$  and  $g = 3.3 \text{ meV}$ . At optical frequencies this is well outside the ultra-strong coupling regime, the parameters are well inside the validity range of the RWA and the presented effect is not related to the superradiant phase transition known from the closed Dicke model [85].

There are two  $J^2$  symmetry breaking effects in this setup: The individual spontaneous decay  $\mathcal{D}_{de}(\rho)$  and the pure dephasing  $\mathcal{D}_{pd}(\rho)$ . First only the influence of the spontaneous decay is investigated and the influence of pure dephasing is investigated later. Including small pure dephasing preserves all effects.

### 7.3.2 Nature of the phase transition

In the steady state the most basic feature of the nonequilibrium phase transition is the change from the ground state to a half excited TLS state with increasing external driving field (Fig. 7.3 (a)). In the bad cavity limit this behavior is well studied in the context of cooperative resonance fluorescence [19]. Increasing the cavity quality (decreasing the ratio between cavity decay rate and TLS-cavity coupling strength  $\kappa/g$ ) makes the transition sharper but the overall effect does not change much. Contrary a drastic change is seen in the in the behavior of the collectivity measure for the superradiant subspace  $R(l_{max} = N/2)$ , Fig. 7.3 (b). While in the bad cavity limit the superradiant subspace population is always increased by collective effects ( $R(l_{max}) \geq 1$ ), an increased suppression ( $R(l_{max}) < 1$ ) of the superradiant subspace occurs for increasing cavity lifetime/quality. This is accompanied by a drastic increase of coherent cavity photons below and

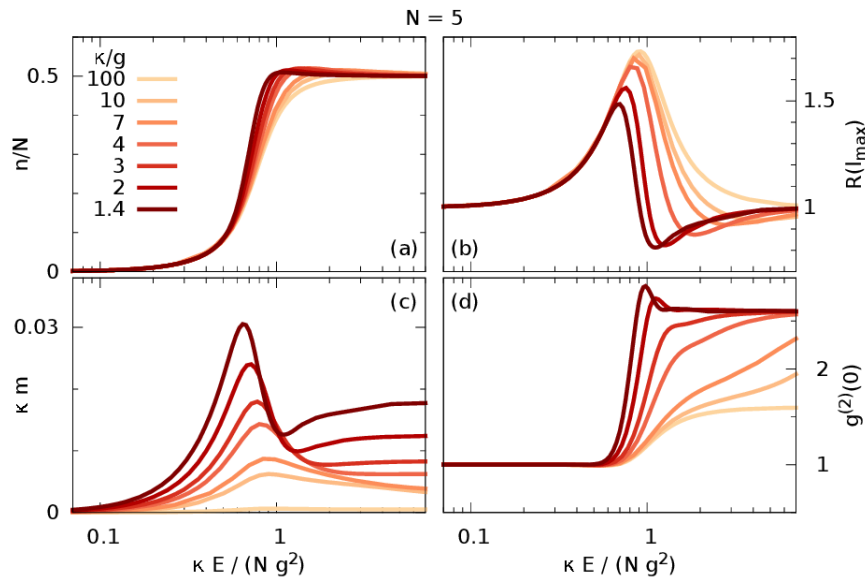


**Figure 7.3 – Leaving the bad cavity limit:** Variation of the external pumping strength for different ratios  $\kappa/g$ : (a) the normalized TLS excitation number  $n/N = \langle J_{11} \rangle / N$ , (b) the relative superradiant subspace occupation  $R(l_{max} = N/2)$ , (c) the cavity output rate  $\kappa m = \kappa \langle b^\dagger b \rangle$  and (d) the photonic second order correlation function  $g^{(2)}(0)$ : Drastic qualitative change for  $\kappa/g$  approaching unity.

a pronounced bunching at moderate photon numbers above the phase transition (Fig. 7.3 (c) and (d)). The maximum in the second order photon correlation function indicates the transition from increased to suppressed superradiant subspace occupation. Please note that the cavity decay does not lead to an effective dephasing/individualization contribution for the TLS (it preserves  $J^2$  symmetry), thus the population of subradiant states through different cavity lifetimes is a highly nontrivial effect.

Above the phase transition collectivity favors the most subradiant subspace  $l_{min}$ : The dependence of  $R(l_{max})$  on the number of TLS  $N$ , Fig. 7.4 (a), shows a growing collective change in population of the superradiant subspace for increasing  $N$ . Both the increase below the phase transition and the suppression above the phase transition increase. In Fig. 7.4 (b) the ratio  $R(l_{max} - 2)$  is plotted which exists only for  $N \geq 4$  – it switches from complete collective suppression below to collective increase above the transition. However the collective increase in population decreases for increasing  $N$ . At first glance it seems that the collective increase in subradiant subspaces drops for higher emitter numbers. This is however not the case: For  $N = 4, 5$  there are three different  $l$  subspaces:  $l_{max}$ ,  $l_{max} - 1$  and  $l_{max} - 2$ . Thus for  $N = 4, 5$  the subspace  $l_{max} - 2$  corresponds to the most subradiant subspace i.e.  $N = 4$ :  $l_{min} = 4/2 - 2 = 0$  and  $N = 5$ :  $l_{min} = 1/2$ . In these two cases the collective increase in population is strongest. For larger  $N$  subspaces with smaller  $l$  exist, e.g.  $N = 6$ :  $l_{min} = l_{max} - 3$ . Looking at  $R(0)$  (only defined for even  $N$ , always corresponds to the most subradiant subspace), Fig. 7.4 (c), it appears that the increase due to collective effects in fact increases with  $N$ , however always only in the most subradiant subspace. Thus the collective increase is always most pronounced in the most subradiant subspace ( $l_{min}$ ) above the phase transition. Remarkably, below the phase transition the subradiant subspaces are completely suppressed, c.f. Figs. 7.4 (b), (c). In the bad cavity limit this corresponds to the collective branch known from cooperative resonance fluorescence (explained above). This discussion shows that this collective branch can be attributed to superradiant behavior since subradiant subspaces are completely suppressed. In an incoherent

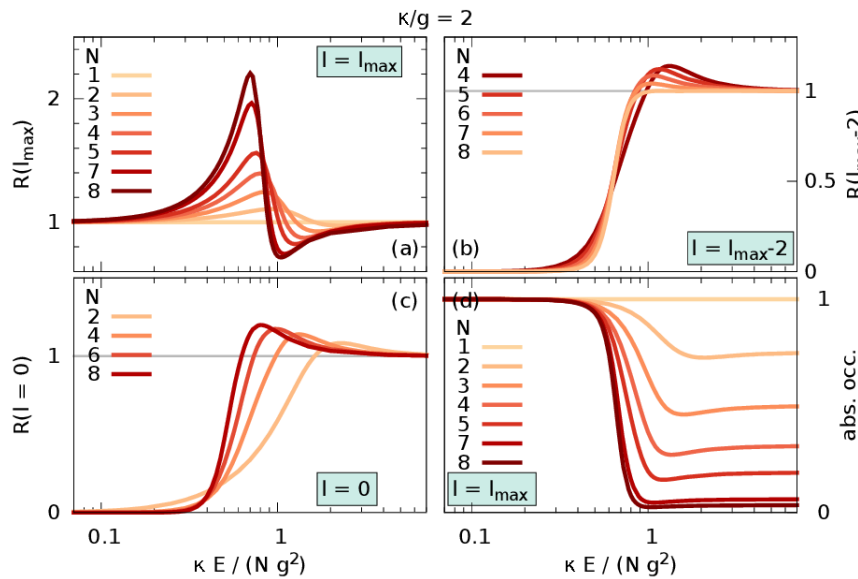


**Figure 7.4 – Increasing the system size:** Relative Dicke subspace occupation for varying  $N$ : (a) the superradiant subspace  $l = N/2$ , (b)  $l = N/2 - 2$ , (c)  $l = 0$ . These states have no interactions due to the Hamiltonian. They only couple to states with  $l > 0$  through decay and dephasing. (d) Absolute occupation in the superradiant subspace: Approaching zero above the phase transition for  $N \rightarrow \infty$ , even without correlations.

setting, like for example thermal distributions, all these curves would be strictly fixed at one, no increase and no suppression. This means that subradiant states are in fact populated but the populations are such that all quantum coherent effects completely cancel each other.

The total occupation in the superradiant subspace goes to zero above the phase transition for  $N \rightarrow \infty$ , Fig. 7.4 (d). Naively we could associate this with subradiance. However for  $E \rightarrow \infty$  the TLS are in a completely incoherent, equipartitioned state [186]. This can be seen from the fact that for high pump rates the  $R(l)$  curves of all subspaces approach unity, which corresponds to a completely incoherent mixture. In this limit the superradiant subspace is only depopulated since this subspace becomes very small compared to the full Hilbert (Liouville) space for large  $N$ . This is clearly not a collective effect. This illustrates that (in the steady state) it is impossible to distinguish between collective and individual behavior by using Dicke state occupations alone, which serves as a motivation for the collectivity measure. However by looking at both the absolute and relative populations it is possible to conclude that in the good cavity and large  $N$  limit the system changes from a predominantly superradiant to a predominantly subradiant phase at the transition, where both phases exhibit genuine collective behavior. This constitutes the main result of this discussion.

In Fig. 7.5 the scaling of experimentally more accessible quantities with the number of individual TLS  $N$  is presented: The normalized TLS excitation develops a kink for increasing  $N$ , indicating a second-order transition, Fig. 7.5 (a). The normalized Liouvillian gap  $|\lambda_1|/\gamma$ , which corresponds to the slowest time scale in the system to reach steady state (see Section 3.4), decreases around the phase transition for increasing  $N$ , Fig. 7.5 (b). It might even vanish for  $N \rightarrow \infty$ , creating a second steady state. The intracavity mean photon number shows the formation of a local minimum at the transition and an increase in the peak intensity, Fig. 7.5 (c). Also bunching ( $g^{(2)}(0) > 1$ ) increases for increasing  $N$ , Fig. 7.5 (d). Overall the transition becomes sharper and more pronounced for increasing  $N$  and decreasing  $\kappa/g$ , since these parameters increase the system size. This displays a typical property of phase transitions, which are well defined only

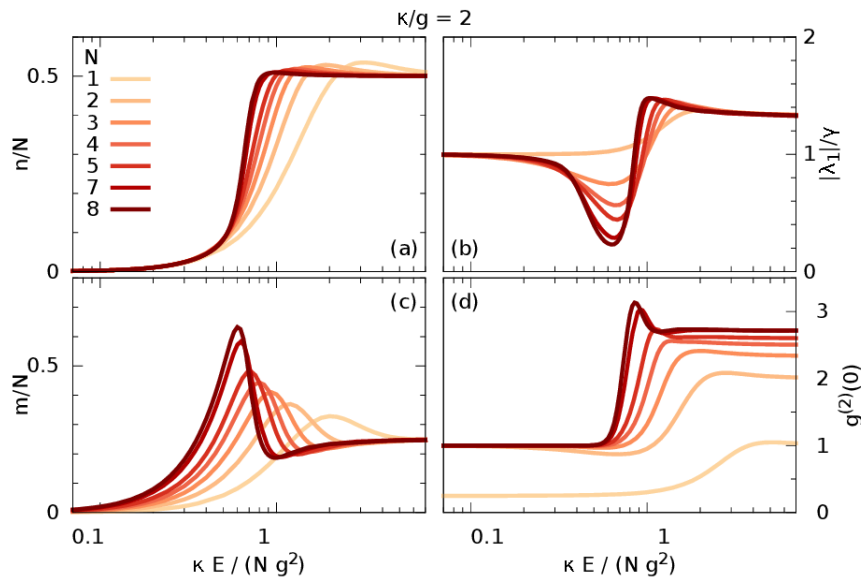


**Figure 7.5 – Experimental signatures for varying  $N$ :** (a) the normalized TLS excitation number  $n/N = \langle J_{11} \rangle / N$ , (b) the renormalized Liouvillian gap  $|\lambda_1|/\gamma$ , (c) the rescaled intracavity photon number  $m/N = \langle b^\dagger b \rangle / N$  and (d) the second order correlation  $g^{(2)}(0)$ .

in the thermodynamic limit (infinite system size) and blur for small system sizes [19, 84, 187]. The presence of individual spontaneous decay  $\mathcal{D}_{de}(\rho)$  is a necessary condition for the population of subradiant states, as it is the only parameter in the present discussion that breaks the  $J^2$  symmetry. Therefore one would intuitively expect a strong dependence of the population behavior of the subradiant states on the spontaneous decay parameter  $\gamma$ . This however is not the case, see Fig. 7.6: Both the normalized mean excitation as well as the relative subradiant subspace population  $R(1/2)$  hardly depend on  $\gamma$  at all in realistic parameter ranges. Only in the limit of (unrealistically) short lifetimes  $\gamma \sim 10$  ps there is an observable dependence in the bad cavity limit and even in that limit the qualitative behavior of the relative population  $R(1/2)$  does not change at all. In the moderate cavity quality range there is practically no detectable influence of this parameter. Please note that if the spontaneous decay rate  $\gamma$  would be artificially set to zero, the relative subradiant subspace occupation  $R(1/2)$  would strictly remain zero at all driving strengths. The reason why a stronger individualization leads to a population of subradiant states at higher pump powers is due to the fact that the subradiant states are excited states and the pump needs to overcome the spontaneous decay in order to be able to populate these excited states.

This means that the only process in the master equation that enables population in subradiant states has no influence on the related subradiant coherences. The only parameter in the system that determines the subradiant coherences is the cavity quality  $\kappa/g$ . This means that the present process is a cavity assisted generation of subradiant coherences, even though both cavity related parameters  $g$  and  $\kappa$  do not break the  $J^2$  symmetry and therefore do not couple different Dicke subspaces. Furthermore for even  $N$  the most subradiant states are all dark (associated to  $R(0)$ , see Fig. 7.4 (c)), there are no bright states in this subspace, meaning that the entire subspace does not couple to the cavity at all. But still the cavity quality factor determines its relative population.

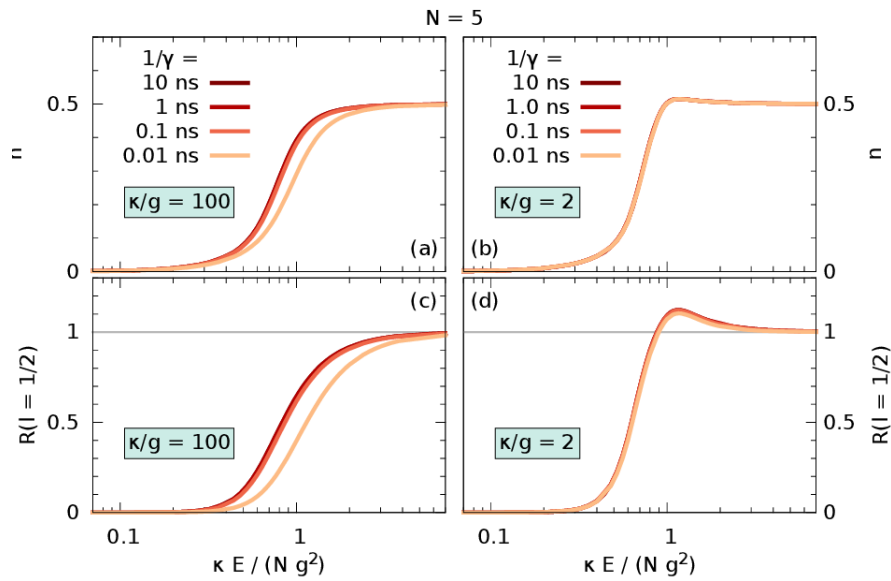


**Figure 7.6 – Dependence on the spontaneous decay rate:**  $N = 5$  (a) and (b) the normalized TLS excitation number  $n/N = \langle J_{11} \rangle / N$ . (c) and (d) the relative most subradiant subspace occupation  $R(1/2)$ . (a) and (c) are in the bad cavity limit – (b) and (d) have a moderate cavity quality. In the typical range of lifetimes of quantum emitters 0.1 – 10 ns there is no visible effect at all.

### 7.3.3 Robustness test and entanglement properties

So far all results were presented without including pure dephasing. Now the robustness of the collective effects at the phase transition against pure dephasing is investigated: In Fig. 7.7 (a) the collective behavior of the relative Dicke subspace population is reduced for increasing  $\delta$ . However the effect of clear distinction of superradiant state below and subradiant state above phase transition is preserved for  $\delta \sim \gamma$ . The general trend of the total Dicke subspace occupation is not affected by pure dephasing, as in Fig. 7.4 (d). This finding is only concerned with the steady state properties in the system. The qualitative dynamical behavior remains the same, as will be seen in the next section.

In the spin preserving setup the TLS are entangled via spin squeezing below the phase transition [22]. Spin squeezing is a concept originating from quantum metrology, where it was developed around the idea that squeezed atomic coherent states could be used for measurement precision below the shot noise limit, but also has attracted a lot of attention as an entanglement witness [188, 189, 190, 191]. An entanglement witness is just a qualitative measure whether a system is excited (or not), it does not provide a quantitative measure of the entanglement strength. Here we employ the spin squeezing inequalities introduced by Tóth *et al.* that are explicitly derived as an entanglement witness for many two- (and multi-) level system setups [79, 80]. The spin preserving case does not contain any subradiant states/effects and cannot model the effects of pure dephasing. The spin preserving and nonpreserving scenarios are two limits of the same physical system [192, 4]. Thus an investigation of entanglement in our setup and its preservation under dephasing is desirable: We find that the spin squeezing inequalities (SSI) by Tóth *et al.* detect entanglement below the phase transition for  $\delta < \gamma$ , see Fig. 7.7 (b): The quantity plotted

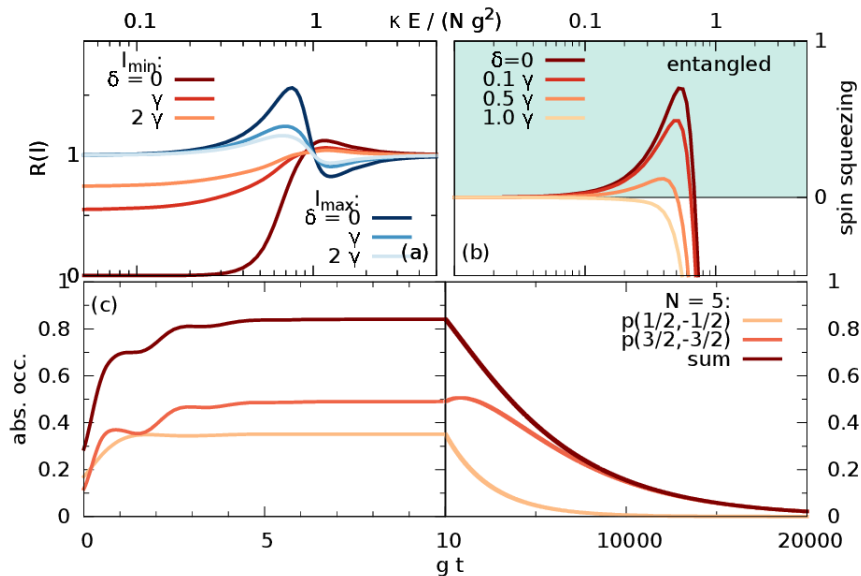


**Figure 7.7 – Robustness, entanglement and dark state cascades** (a) The ratio  $R(l)$  for  $N = 5$  for  $l = l_{min}, l_{max}$  and varying  $\delta$ : The clear switching at the phase transition survives for  $\delta \sim \gamma$ . (b) Entanglement via spin squeezing inequalities: entanglement below the transition for  $\delta < \gamma$ . (c) Driving the system to the maximum subradiance point with subsequent relaxation to the ground state  $N = 5, \delta = 0$ : A cascade of dark states is generated. Total dark state occupation close to unity.

there corresponds to one of the seven inequalities derived by Tóth *et al.*

$$\underbrace{\langle J_y^2 \rangle + \langle J_z^2 \rangle - \frac{N}{2} - (N-1)(\Delta J_x)^2}_{=: A} \leq 0, \quad (7.3.7)$$

and the two-level systems are not in a separable state as soon as the inequality is violated.  $A$  is the quantity plotted in Fig. 7.7 (b). Hence the entanglement detected in the spin preserving setup is still present for spin nonpreserving setups. For more information on the spin squeezing inequalities by Tóth *et al.* please refer to Appendix C.

## 7.4 Dark state cascades

Super- and subradiance are concepts related to time evolution and so far only steady state values were presented: Now, the system is driven to the steady state with maximum  $R(l_{min})$  (see Fig. 7.4 (b) and (c)) and then the driving field is switched off. The system relaxes into the ground state and we observe that a cascade of dark states is generated, Fig. 7.7 (c):  $p(1/2, -1/2)$  and  $p(3/2, -3/2)$  are the populations in the lowest states of the smallest  $l = l_{min}$  and intermediate  $l_{max} > l > l_{min}$  subspace, c.f. Fig. 7.1 (b). Both states are dark. They are populated on time scales of the inverse TLS-photon coupling constant  $g^{-1}$ , because the higher energy bright states of the associated  $l$  subspaces decay via the emission of cavity photons. This implies that for even  $N$  the single, most subradiant state population  $p(0, 0)$  does not experience fast initial population since there are no other, higher energy bright state in this  $l = 0$  subspace, see Fig. 7.1 b). The cavity photons subsequently leave the cavity through the cavity decay. After the initial fast population of the  $|l, -l\rangle$  states due to the TLS cavity interaction the dynamics are governed by spontaneous emission. The overall dark state population subsequently decays on

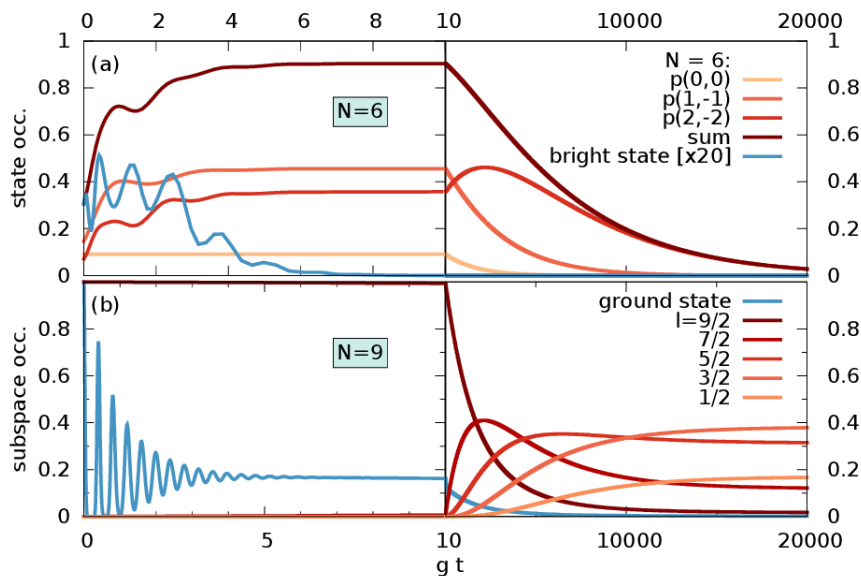


**Figure 7.8 – Depopulation vs. population dynamics:** (a) The dark state cascade for  $N = 6$ . As expected the total dark state population is larger than for  $N = 5$ , see Fig 7.7 (c). There is a single dark state in this setup  $p(0,0)$ , which has no higher energy states in the same subspace, thus it does not experience any fast, initial population dynamics. (b) The population dynamics of the different Dicke subspaces  $N = 9$ . The dynamics of the total subspace occupation is completely governed by the slow time scale  $\gamma$  stemming from the individual decay process. The cascade is inverted, first all systems are in the  $l_{max}$  subspace, then the  $l_{max} - 1$  subspace is populated and so forth. The dynamics of the ground state still bears the fast initial dynamics, which are here governed by the driving  $E$  rather than the coupling  $g$ .

the slower time scale  $\gamma^{-1} = 5000g^{-1}$  towards the ground state of the TLS ( $|5/2, -5/2\rangle$ ). For  $N = 5$  decay follows the Dicke state cascade

$$p(1/2, -1/2) \rightarrow p(3/2, -3/2) \rightarrow p(5/2, -5/2) \quad (7.4.1)$$

In general for different  $N$ : All  $m > -l$  states relax to the  $m = -l$  states on time scales of the inverse TLS-photon coupling constant  $g^{-1}$  which is orders of magnitude faster than the decay time  $\gamma^{-1}$ . Subsequently the dark states  $|l, -l\rangle$  relax in a cascade to the lower energy, dark states  $|l+1, -l-1\rangle$  with minimal  $l$  on time scales of  $\gamma^{-1}$  towards the ground state  $|l_{max}, -l_{max}\rangle$ , Fig. 7.1 (b):

$$p(l_{min}, -l_{min}) \rightarrow p(l_{min} + 1, -l_{min} - 1) \rightarrow \dots \rightarrow p(l_{max}, -l_{max}) \quad (7.4.2)$$

Please note that the overall occupation in subradiant dark states reaches values close to unity: The total population of the superradiant subspace tends to zero for large  $N$ , thus for large  $N$  all occupation is first quickly transferred into the dark Dicke states before slowly decaying towards the ground state. Increasing the number of TLS also increases the dark state occupation during ground state relaxation. Subradiant correlations are clearly dominant here, since without these correlations the excitation in the TLS would still decay via the TLS cavity interaction Hamiltonian. This could be exploited for a controlled generation of subradiant states.

This discussion implies that for even numbers in  $N$  the most subradiant state  $p(0,0)$  should not experience any initial fast dynamics since there are no higher energy bright states in this subspace that could decay into this state, see Fig. 7.1 (b). In fact looking at the dark state

cascade for  $N = 6$  in Fig. 7.8 (a) confirms this. Also the overall occupation in dark states reaches higher values, as expected from the considerations above. For comparison also the time dynamics of a bright state population is shown  $p(3, -2)$ . This state is the first excited state in the superradiant subspace and it completely decays on time scales of  $g^{-1}$ .

In Fig. 7.8 (b) the population dynamics of the system is shown. Here the system starts in the ground state and the driving field is switched on. The shown populations are the total subspace populations

$$P(l) = \sum_m p(l, m) \quad (7.4.3)$$

as in Fig. 7.4 (d). Since the population of the total Dicke subspace can only be changed by the individual decay process  $\mathcal{D}_{de}(\rho)$  the dynamics of the subspace occupations are governed by the spontaneous decay rate  $\gamma$ . For comparison the population in the ground state  $p(9/2, -9/2)$  is plotted, it shows fast initial dynamics since it couples to the higher energy superradiant states through the driving and the emitter cavity coupling. The slow time dynamics are then again governed by the slow  $\gamma$ .

The only requirement for the dark state cascade and the slow Dicke subspace population to occur is individualization: These effects also occur in the bad cavity limit and for strong pure dephasing (also for  $\delta \gg \gamma$ ). The only difference is that the total transient populations are lower but still approach unity for  $N \rightarrow \infty$ : Subradiant states are always populated in the presence of external driving as long as individualization is present and the superradiant subspace becomes very small to the total Hilbert/Liouville space for large  $N$ . Thus the system will have an increasing population in subradiant states for large  $N$  also in the bad cavity and strong dephasing limit. In the case of strong pure dephasing the slow time scale becomes faster (coherence time). However the effect of favoring subradiant states and the distinction between incoherent/thermal/individual versus quantum coherent/collective two-level system behavior *in the steady state* relies on the moderate cavity quality and the low pure dephasing. For the same reason the effect should also be stable against small disorder: As long as the disorder is small compared to the collective coupling  $g$  the fast time dynamics will be governed by collective dynamics that only couple states of the same Dicke subspace and the individualization introduced by the disorder will dominate only in the long time behavior.

Experimental systems for observing the effects presented in this paper have to meet certain requirements: The pure dephasing of the TLS coherences should be small compared to the decay rate, i.e.  $\delta \sim \gamma$ . This can be realized with e.g. Rydberg ensembles [170, 193, 194] or with NV centers [195] and quantum dots [196] at low temperatures. Also a small inhomogeneous broadening is required, since it would likely blur the presented effect. For quantum dots this is more challenging than for NV centers and Rydberg ensembles. Generally, the decay rate  $\gamma$  is not a crucial parameter but the ratio between decay and pure dephasing. If pure dephasing is too large the steady state effects are blurred, in the ground state relaxation subradiant state occupation is decreased and coherence times are shorter. However the dark state cascade effect is stable even against larger pure dephasing  $\delta > \gamma$ .

The parameters used in this study are realistic for NV centers, quantum dots and Rydberg atoms and the behavior is stable over a wide parameter range.

## 7.5 Conclusion

The investigations in this chapter were concerned around the collective effects in the open Dicke model. Contrary to the closed system, which completely lives in the superradiant subspace the presence of individual decay and pure dephasing allows the system to populate subradiant states. In order to investigate the population in the subradiant states the system is driven by an external

cw laser. It was found that this system is closely connected to two standard setups of quantum optics, namely cooperative resonance fluorescence and absorptive optical bistability. The rate equation theory predicts bistable behavior which is in contradiction to the full quantum solution that always exhibits a unique steady state. This contradiction is relieved when considering the large system size or thermodynamic limit, but this observation already hints at the importance of quantum correlations in this setup. Since the strength of the permutation symmetric method is the ability to compute the full non-approximate density matrix this serves as an ideal testing ground for the capabilities of this method. Furthermore this discussion also serves as an ideal testing ground for the solvers PETSc and SLEPc solvers available in PsiQuaSP: The population dynamics in Fig. 7.8 b) for  $N = 9$  were calculated in parallel on four cpus, using the permutation symmetric method and an adaptive time step Runge-Kutta and the whole calculation took roughly 2 months. This corresponds to a single point in the steady state plots. For  $N = 5$  at  $\kappa \sim g$  the explicit time integration still takes roughly two weeks on four cpus. Using the SLEPc Krylov-Schur algorithm and the shift and invert spectral transformation as explained in Appendix A.6 *the entire curve* in the steady state plot can be computed over night on four cpus. The investigation of the population of the subradiant states revealed that the non-equilibrium phase transition known from cooperative resonance fluorescence experiences a stark qualitative change when leaving the bad cavity limit. This results in a new type of phase transition altogether. In this new phase transition the system undergoes a change from a steady state superradiant into a steady state subradiant state. Counterintuitively, the crucial parameter for this process is the cavity quality factor and not the individual spontaneous decay rate. This has not been reported before, in fact the results in this chapter provide the first study investigating the steady state population dynamics of subradiant states.

The transient dynamics of the system show that there is a pronounced separation of time scales in the system. The collective effects dominate the fast dynamics and the individual effects like spontaneous decay and pure dephasing dominate the slow dynamics. These time scales are separated by factors of  $g/\gamma = 10^3 - 10^4$  for common parameters in quantum optical setups. Also separation factors of up to  $10^5$  or more are conceivable – the decay time of  $\gamma^{-1} = 1$  ns is can be easily chosen longer and the emitter cavity coupling strength of  $\hbar g = 3.3$  meV is also very moderate and could be chosen larger.

# 8

## Quantum dots on a thin metal film

So far most of the discussion in this thesis was concerned with many identical emitters that interact with electromagnetic vacuum modes. Aside from collective effects in conventional quantum optical setups the field of quantum optics in media is receiving increasing attention in recent years, sparked by the advances in nanofabrication tools and the ever ongoing quest for miniaturization. As stated in Chapter 2 metal nanostructures provide a promising material platform in this field.

Generally metal nanostructures and metal interfaces have strong influence on the photonic environment due to near field enhancements at the metal interface – in short the nanosized counterpart of the antenna effect. This allows to strongly alter the emission properties of quantum emitters due to e.g. the Purcell effect, which is based on mode confinement and resonance. However the influence of the metal nanostructures on the optical properties is more complex than just mode confinement, the influence is threefold: First, the excitation rate of the quantum emitter placed in the hotspot of a metal nanostructure is increased since the metal nanostructure acts like a nanolens that focuses the field of e.g. the excitation laser onto the quantum emitter. Second, for the same reason also the emission rate is increased. Third, not all of the energy that is emitted from the quantum emitter is observable in the far field (usually only a fraction), since plasmonic structures usually have high non-radiative losses. All these effects together provide a rich playground for altering and tuning the optical properties of plasmonic hybrid systems.

The geometry of a metal interface has a very strong, non-monotonous and spatially dependent effect on the optical properties of an emitter placed in its vicinity or rather the whole hybrid system. There is a huge difference whether the quantum emitter is located in a node or a antinode of the plasmonic near field. This makes control in the fabrication of these systems very challenging: Small deviations in the fabrication/setup can lead to dramatically different optical properties. This hinders a controlled fabrication of devices with defined optical properties.

Plasmonic materials are usually gold and silver and spatial arrangements in which these metals

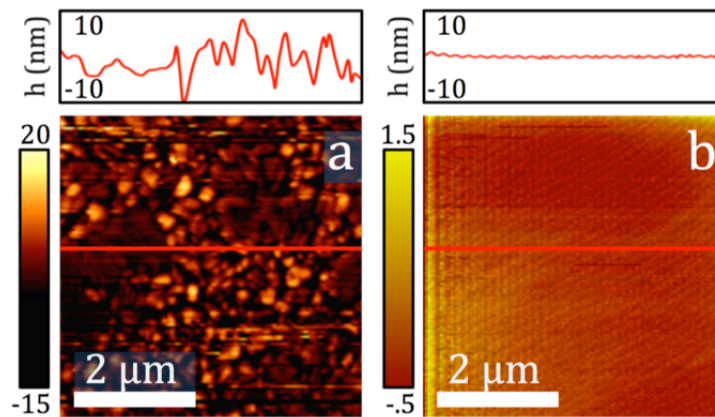


**Figure 8.1 – AFM scans of the two different metal films:** The thermal film has a highly random surface roughness of  $\sim 10$  nm, obstructing the preparation of controlled metal - quantum emitter hybrids. Contrary the epitaxial film has a surface roughness below the AFM detection limit of  $\sim 0.4$  nm. Figure taken from Ref. [199].

are fabricated for plasmonic purposes can be split in two general categories: Various forms of metal nanoparticles – on substrate, in solution, grown, etched, etc. – and metal films or surfaces. For a long time, the state of the art for growing metal films was thermal vapor deposition [58]. However this approach leads to random surface corrugations, obstructing the quality of the surface and again introducing randomness in the fabrication process and thus the optical properties of derived hybrid systems. This was changed recently when it was shown that epitaxially grown silver (Ag) films provide superior plasmonic properties [197, 198]. These silver films have a surface roughness below the detection limit of standard atomic force microscopes, as opposed to the thermally deposited Ag films, see Fig 8.1.

Tom Hartsfield from Xiaoqin (Elaine) Li’s group has measured the distribution of lifetimes of giant core-shell quantum dots on an epitaxial Ag film and compared them to the lifetimes of these quantum dots on a standard thermally deposited Ag film. He found that the reduction in lifetime is much more pronounced for the epitaxial film than for the thermal film and that the distribution of lifetimes is much narrower, see Fig. 8.2. The measurements were performed on single quantum dots, which was confirmed using  $g^{(2)}$  function measurements. The experimental distributions stem from measuring 30 individual quantum dots per substrate [199]. Thus the epitaxial Ag film based hybrid systems provide a highly increased reproducibility and control over the optical properties.

In order to explain their experimental findings we adopted the treatments of Hughes *et al.* [200, 201] for single emitter – plasmon systems in the low excitation limit. They applied the formalism of Welsch *et al.* (see Section 2.2.2) to practical calculations on metal nanoparticle quantum – emitter hybrid systems. The results presented in this Chapter were published in Tom Hartsfield, Michael Gegg, *et al.* ACS Photonics 3, 1085 (2016) [199].

The Chapter is organized as follows: In Section 8.1 the spectral response for a weakly excited quantum emitter – dissipative mode hybrid is derived. Based on this a simple model system that catches the essential parts of the randomness of the thermal Ag film is developed in Section 8.2, which successfully explains the experimental findings.

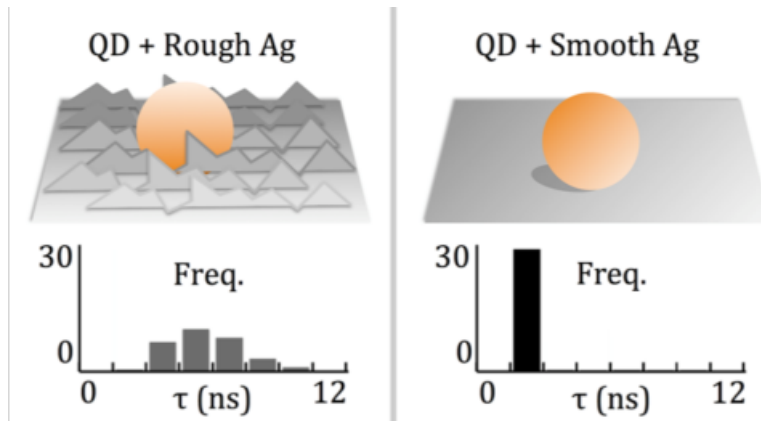


**Figure 8.2 – System sketch and lifetime distribution:** The rough, thermal Ag film leads to a broad, smeared out lifetime distribution of the randomly distributed quantum dots. The smooth, epitaxial Ag film leads to a very defined and narrow distribution. Figure taken from Ref. [199].

## 8.1 Spectral response

Before modeling the surface roughness the spectral response of a single quantum dot coupled to a dissipative mode continuum needs to be derived. For this purpose the formalism of Welsch *et al.* is used, which was introduced in Section 2.2.2. The following treatment is an adaptation of the discussion of Hughes *et al.* in Ref. [200, 201].

The Hamiltonian of the coupled quantum dot dissipative mode setup reads

$$H = \hbar\omega_d\sigma_{11} + \int d^3\mathbf{r} \int_0^\infty d\omega_l \hbar\omega_l \hat{\mathbf{f}}^\dagger(\mathbf{r}, \omega_l) \hat{\mathbf{f}}(\mathbf{r}, \omega_l) - (\sigma_{10} + \sigma_{01}) \mathbf{d} \cdot \hat{\mathbf{E}}(r_d), \quad (8.1.1)$$

where the quantum dot is treated by a two-level system with excitation energy  $\hbar\omega_d$  and  $\hat{\mathbf{E}}(r_d)$  is the electric field operator at the position of the quantum dot. This amounts to a point dipole approximation, thus neglecting the spatial dimensions of the quantum dot.

The spectral response is the Fourier transform of the temporal dynamics of the system, thus the start of the derivation are the Heisenberg equations of motion of the operators  $\sigma_{01}$  and  $\hat{\mathbf{f}}(\mathbf{r}, \omega)$ <sup>1</sup>. The two-level system operator yields

$$\partial_t \sigma_{01} = \frac{i}{\hbar} [H, \sigma_{01}] = -i\omega_d \sigma_{01} - \frac{i}{\hbar} \sigma_z \mathbf{d} \cdot \hat{\mathbf{E}}(r_d), \quad (8.1.2)$$

with  $\sigma_z = \sigma_{11} - \sigma_{00}$ . In the low excitation limit one can use the one photon correlation approximation  $\sigma_z = -1$  [200, 201], resulting in

$$\partial_t \sigma_{01} = \frac{i}{\hbar} [H, \sigma_{01}] = -i\omega_d \sigma_{01} + \frac{i}{\hbar} \mathbf{d} \cdot \hat{\mathbf{E}}(r_d). \quad (8.1.3)$$

The equation of motion for the bosonic operator  $\hat{\mathbf{f}}(\mathbf{r}, \omega)$  reads

$$\partial_t \hat{\mathbf{f}}(\mathbf{r}, \omega) = -i\omega \hat{\mathbf{f}}(\mathbf{r}, \omega) - (\sigma_{10} + \sigma_{01}) \frac{\omega^2}{c^2} \sqrt{\frac{\epsilon_I(\mathbf{r}, \omega)}{\hbar\pi\epsilon_0}} (\mathbf{G}^*(\mathbf{r}, \mathbf{r}_d, \omega) \cdot \mathbf{d}), \quad (8.1.4)$$

<sup>1</sup>Writing these operators in brackets  $\langle \dots \rangle$  would be equivalent to a Schrödinger picture expansion, which is used in all the rest of this thesis. However the density matrix is not well defined at this level of theory, thus the Heisenberg picture is the proper choice. Resolving this problem is a matter of current research [67].

where the complex conjugate of the dyadic Green' function  $\mathbf{G}^*(\mathbf{r}, \mathbf{r}_d, \omega)$  originates from the fact that  $\hat{\mathbf{f}}(\mathbf{r}, \omega)$  does not commute with  $\hat{\mathbf{E}}^{(+)}(\mathbf{r}, \omega) \propto \hat{\mathbf{f}}^\dagger(\mathbf{r}, \omega)$ .

Since the explicit form of the  $\hat{\mathbf{f}}(\mathbf{r}, \omega)$  is not known or rather the construction of Fock states based on these operators is difficult the aim is to eliminate these operators from the equations [67]. Thus the aim is to arrive at expressions for the spectral response of the system only in terms of the two-level system operators  $\sigma_{10}, \dots$ , the dyadic Green's function  $\mathbf{G}(\mathbf{r}, \mathbf{r}_d, \omega)$  and material properties such as  $\epsilon(\mathbf{r}, \omega)$ . The whole derivation involves a couple of Laplace/Fourier transforms, Kramers-Kronig and complex contour integrals and is omitted here since it only involves textbook complex analysis techniques.

The resulting Laplace transform of the electric field operator reads

$$\hat{\mathbf{E}}(\mathbf{r}, \omega) = \frac{1}{\epsilon_0} \frac{\omega^2}{c^2} \mathbf{d} \cdot \mathbf{G}(\mathbf{r}, \mathbf{r}', \omega) (\sigma_{10}(\omega) + \sigma_{01}(\omega)) \quad (8.1.5)$$

where  $\sigma_{10}(\omega) + \sigma_{01}(\omega)$  is the Laplace transform of the two-level system operators, which is given by

$$\sigma_{10}(\omega) + \sigma_{01}(\omega) = i \frac{\sigma_{10}(t=0)(\omega + \omega_d) + \sigma_{01}(t=0)(\omega - \omega_d)}{\omega_d^2 - \omega^2 - 2\omega_d \frac{\omega^2}{c^2} \mathbf{d} \cdot \mathbf{G}(\mathbf{r}_d, \mathbf{r}_d, \omega) \cdot \mathbf{d} / (\hbar \epsilon_0)}. \quad (8.1.6)$$

The spectrum of the hybrid system is given through

$$S(\mathbf{r}, \omega) = \langle (\hat{\mathbf{E}}(\mathbf{r}, \omega))^\dagger \hat{\mathbf{E}}(\mathbf{r}, \omega) \rangle = \left| \frac{\omega^2}{\epsilon_0 c^2} \frac{\mathbf{d}^T \cdot \mathbf{G}(\mathbf{r}, \mathbf{r}_d, \omega) (\omega - \omega_d)}{\omega_d^2 - \omega^2 - 2\omega_d \frac{\omega^2}{c^2} \mathbf{d} \cdot \mathbf{G}(\mathbf{r}_d, \mathbf{r}_d, \omega) \cdot \mathbf{d} / (\hbar \epsilon_0)} \right|^2, \quad (8.1.7)$$

with the assumption that the quantum dot is initially excited, thus only the  $\sigma_{10}(t=0)\sigma_{01}(t=0) = \sigma_{11}(t=0)$  term survives. This expression does not contain any operators or unknown quantities anymore. Therefore this expression can be used to calculate the spectral response of the hybrid system.

## 8.2 Modeling the surface roughness

The idea behind the theoretical explanation of the optical response of the quantum dots on the smooth and the rough Ag films is that the roughness of the thermal Ag film supports localized surface plasmon modes that can be modeled by metal nanoparticles. The two different metal films are both coated with a thin dielectric  $\text{Al}_2\text{O}_3$  layer of  $\sim 3$  nm thickness and the quantum dots are directly placed on that dielectric layer. Thus the distance between quantum dot and the surface should be more or less constant. The broad distribution of the lifetimes then stems from the fact that the surface corrugations of the rough film are random in their spatial dimension and should therefore be modeled as an ensemble of metal nanoparticles with random diameter. Since the quantum dot – metal nanoparticle interaction strength decays fast with increasing distance it is possible to neglect contributions from surface corrugations that are further away. Therefore the rough surface can be treated as a single metal nanoparticle. On the other hand the smooth surface should be represented by the infinite diameter limit. This is a rough model that is intended to incorporate the dominant contributions and to qualitatively explain the experimental findings. Since precise information on the actual geometry of the surface – quantum dot hybrid system is not available this is the proper choice of method.

Based on these model considerations the aim is to calculate the spectral response of the metal nanoparticle – quantum dot system using Eq. (8.1.7). Lifetimes are obtained by numerically Fourier transforming these spectra and fitting the resulting decay dynamics with a mono-exponential function. This is an approximate approach, neglecting e.g. Fano lineshape effects (see below). The lifetimes are calculated for varying metal nanoparticle diameters. The smooth

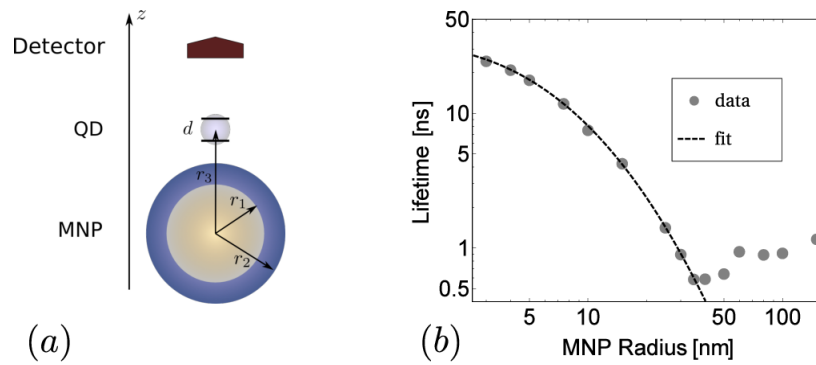


**Figure 8.3 – Model system and lifetime dependence:** (a) The employed model for the surface roughness: A single quantum dot interacting with a coated metal nanoparticle. The whole setup is aligned along the  $z$  axis, which simplifies the calculation of the Green's functions. (b) The dependence of the quantum dot lifetime on the metal nanoparticle diameter. For small radii the behavior is monotonous. For large radii the behavior is more erratic but also converges to a constant value. The data stems from fitting the numerical Fourier transform of the spectrum with a single exponential decay.

silver decay time is then associated with the infinite radius limit of the resulting curve. The distribution of lifetimes on the rough film is explained by assuming an ensemble metal nanoparticles with Gaussian distributed radii and calculating the resulting distribution of lifetimes. The coated metal nanoparticle represents a spherically symmetric layered material. The dyadic Green's function for such an arbitrary spherically symmetric layered material was derived by Li *et al.* [64]. The theoretical model shown in Fig. 8.3 consists of three layers: (1) the surrounding vacuum (or air) containing both the detector and the quantum dot, (2) the dielectric coating and (3) the metal nanoparticle. Green's functions of layered materials can be split into a free space and a scattered (medium) part

$$\mathbf{G}(\mathbf{r}, \mathbf{r}', \omega) = \mathbf{G}_0(\mathbf{r}, \mathbf{r}', \omega) + \mathbf{G}_s(\mathbf{r}, \mathbf{r}', \omega), \quad (8.2.1)$$

if both spatial arguments  $\mathbf{r}$  and  $\mathbf{r}'$  are located in the same layer, which is justified in the present case. Therefore for calculating the spectral response of the metal nanoparticle – quantum dot setup the free space part of the dyadic Green's function can be omitted [200, 201]. The only remaining contribution that needs to be evaluated is the scattered part of the Green's function in layer (1)  $\mathbf{G}_s^{11}(\mathbf{r}, \mathbf{r}', \omega)$ . The expression for this Green's function is given by [64]

$$\mathbf{G}_s^{11}(\mathbf{r}, \mathbf{r}', \omega) = \frac{ik_1}{4\pi} \sum_{n=1}^{\infty} \sum_{m=0}^n (2 - \delta_{m0}) \frac{2n+1}{n(n+1)} \frac{(n-m)!}{(n+m)!} \cdot \left[ B_M^{11} \mathbf{M}_{mn}^{e,o}(k_1 \mathbf{r}) \mathbf{M}_{mn}^{e,o}(k_1 \mathbf{r}') + B_N^{11} \mathbf{N}_{mn}^{e,o}(k_1 \mathbf{r}) \mathbf{N}_{mn}^{e,o}(k_1 \mathbf{r}') \right]. \quad (8.2.2)$$

The  $\mathbf{M}_{mn}^{e,o}$  and  $\mathbf{N}_{mn}^{e,o}$  are called vector wave functions and can be understood as vector valued spherical harmonics: They are orthogonal to each other and provide a suitable basis for the expansion of the spherically symmetric Green's function [64]. The full expressions for these vector wave functions are complicated, but with the symmetry assumptions used here they

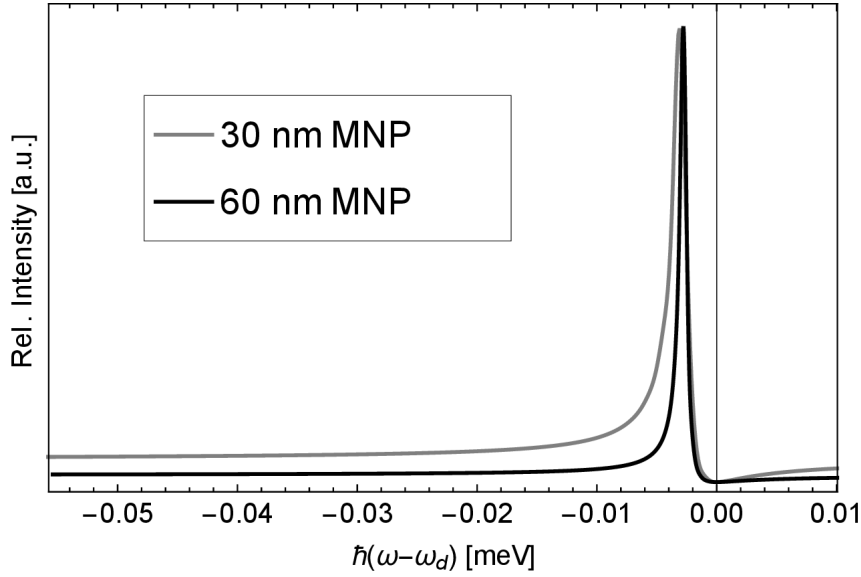


**Figure 8.4 – Fano lineshapes in the hybrid system:** Rescaled spectral response Eq. (8.1.7) of the hybrid system close to the quantum dot resonance. Destructive interference directly at the resonance.

simplify considerably and read

$$\begin{aligned}
 \mathbf{M}_{mn}^e(k\mathbf{r}) &= -h_n^{(1)}(kr) \frac{dP_n^m(\cos\theta)}{d\theta} \Big|_{\cos\theta=0} \hat{\phi} \\
 \mathbf{M}_{mn}^o(k\mathbf{r}) &= 0 \\
 \mathbf{N}_{mn}^e(k\mathbf{r}) &= \frac{n(n+1)}{kr} h_n^{(1)} P_n^m(0) \hat{r} \\
 \mathbf{N}_{mn}^o(k\mathbf{r}) &= \frac{m}{kr} \frac{d[rh_n^{(1)}(kr)]}{dr} P_n^m(0) \hat{\phi},
 \end{aligned} \tag{8.2.3}$$

where the  $h_n^{(1)}(kr)$  are the spherical Hankel functions of the first type and the  $P_n^m(x)$  are the Legendre polynomials.  $\hat{r}$ ,  $\hat{\phi}$  (and  $\hat{\theta}$ ) are the unit vectors in spherical coordinates. The  $\omega$  dependence enters Eq. (8.2.2) through the wave number values  $k_i$

$$k_i = \frac{\omega}{c} \sqrt{\mu_i(\omega)\epsilon_i(\omega)} \sim \frac{\omega}{c} \sqrt{\epsilon_i(\omega)} = \begin{cases} \frac{\omega}{c} \sqrt{\epsilon_i} = \text{const} \cdot \frac{\omega}{c}, & \text{for } i = 1, 2 \\ \frac{\omega}{c} \sqrt{\epsilon(\omega)}, & \text{for } i = 3. \end{cases} \tag{8.2.4}$$

again assuming the setup to be non-magnetic. The  $B_{M,N}^{11}$  are scattering coefficients, which depend on the radii of the different spherical layers  $r_i$  and the wave numbers  $k_i$  of the inner layers,  $\omega$  and  $n$

$$B_{M,N}^{11} = B_{M,N}^{11}(r_2, r_3, k_2, k_3, \omega, n). \tag{8.2.5}$$

The explicit expressions of these scattering coefficients are complicated and are therefore omitted here, their function is to account for the geometry and dielectric properties of the internal layers. Their explicit form can be found in Ref. [64]. The relative dielectric constant of the coating layer  $\text{Al}_2\text{O}_3$  at optical frequencies is assumed to be constant over the relevant spectral range and can be calculated from the refractive index  $\epsilon_2 = n^2 \sim 3.11$ , assuming that magnetic effects can be neglected [202, 203]. The dielectric function of the metal is obtained from experimental data, which is in contrast to the treatment of Li *et al.* in Ref. [64] who used a Drude model

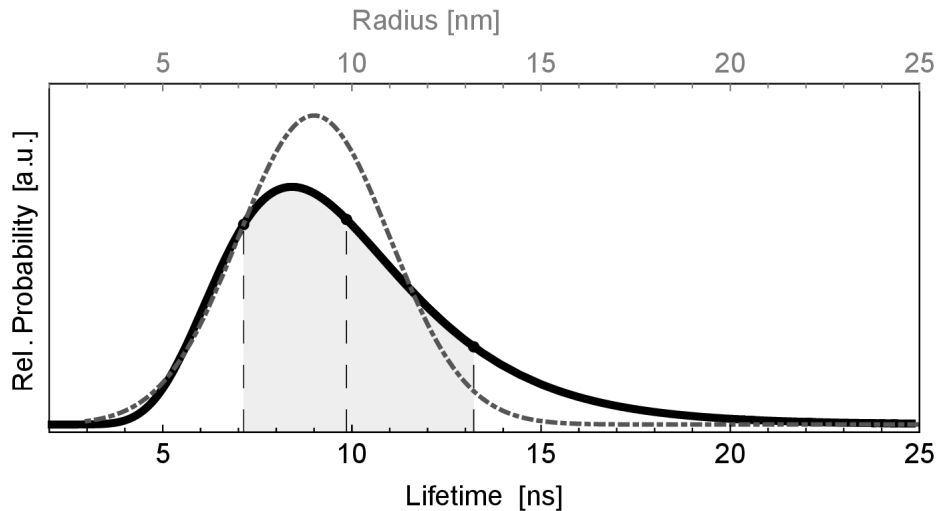


**Figure 8.5 – Gaussian radii distribution results in asymmetric lifetime distribution:** Assuming a Gaussian distribution of surface roughness radii leads to the same asymmetry of the observed lifetimes that was observed in the experiment.

ansatz. The data on the refractive index of the silver nanoparticles can be either taken from the standard reference of Johnson and Christie [58] which used thermal Ag, or from the data available on the refractive index of the epitaxial Ag films from Ref. [198]. Even though the epitaxial film has superior plasmonic properties resulting in e.g. elongated plasmon-polariton propagation lengths [198] the choice of data has no obvious effect on the calculated lifetimes. This further indicates that the lifetime distribution is a geometric effect.

The infinite sum in Eq. (8.2.2) is numerically evaluated up to convergence using Mathematica. Please note that omitting the coating layer results in much simpler expressions for the dyadic Green's function, however it is only possible to reproduce the experimental results when including this layer. The coating layer shifts the elementary plasmon resonance  $\sim 3$  eV closer to the quantum dot resonance  $\sim 2$  eV and also results in further surface effects at the dielectric/air interface where the quantum dot is located. Both these effects have a strong influence on the spectral response of the hybrid system.

The lifetime of the quantum dot as a function of the metal nanoparticle radius in Fig. 8.3 (b) shows a monotonous dependency for small radii and a more erratic but saturated behavior for larger radii. The large radius limit is  $\sim 1$  ns, which is remarkably close to the experimentally observed 0.6 ns. In order to model the surface roughness a Gaussian distribution of metal nanoparticle radii  $d(r)$  is assumed. For calculating the resulting distribution of lifetimes the monotonous range of the data in Fig. 8.3 (b) is fitted with an order 4 polynomial  $r = f(t)$  and the distribution is then given by

$$\tilde{d}(t) = d(f(t))\partial_t f(t). \quad (8.2.6)$$

The functions for  $d(r)$  and  $\tilde{d}(t)$  are plotted in Fig. 8.5. The mean and variance of the distribution are rough estimates based on the AFM data. Nonetheless the qualitative observation of an asymmetrical distribution of lifetimes can be reproduced. Also the absolute mean value of the lifetimes is  $\sim 10$  ns compared to a measured mean lifetime of  $\sim 6$  ns represents a quite satisfactory agreement. The calculation seems to systematically overestimate the lifetimes, but the agreement is striking considering the roughness of the employed model and the many unknowns.

### 8.3 Conclusion

In this chapter the dissipative mode approach by Welsch *et al.* was successfully employed to describe the experimental findings on the optical properties of quantum dots close to two different silver surfaces. Even though the model assumptions for treating the surface roughness are simplistic, the theory still catches the qualitative findings of the experiment and even reproduces the absolute values closely.

Furthermore the theoretical treatment allows to make comments on how the optical properties of the quantum dots on the smooth metal film could be further tuned: Increasing/decreasing the thickness of the spacing/coating layer should increase/decrease the lifetime of the quantum dots since the quantum dots have more overlap with the evanescent modes of the surface. Also increasing the dielectric constant of the coating layer should reduce the lifetime since it brings the plasmon resonance closer to the quantum dot resonance. However the different measured optical properties of the rough and the smooth silver films have no observable influence on the dynamics of the hybrid, which is probably due to the strong detuning of the plasmonic and the quantum dot resonance.

# 9 Further usages of PsiQuaSP

In this chapter some additional usages of PsiQuaSP are presented. The general theory of permutation symmetric Liouville space operators and the corresponding symmetrized states allow for a large flexibility in constructing master equations. Furthermore the very general framework provided by PETSc allows to include additional packages that can be exploited. In this chapter two features of PsiQuaSP are presented that are not obvious. The first feature is the ability to treat non-identical systems and the second feature is a very general graph theory based optimization technique.

## 9.1 Nonidentical systems

Even though PsiQuaSP and the permutation symmetric method were designed to treat identical systems, it can also be used to treat non-identical, distinguishable systems and disorder. In principle this includes systems such as spin-chains with nearest neighbor (and all other conceivable) interactions, distance dependent processes like direct dipole-dipole coupling or Förster transfer and chiral, directional waveguide, cascaded QED setups involving multi-level systems. Also the many emitter case of the plasmonic setups discussed in Chapter 8 could be treated this way: The strong distance, position dependence of the plasmonic near fields breaks the permutation symmetry, therefore the quantum dots or generic quantum emitters need to be treated as distinguishable particles. In the following the general approach for treating such systems will be outlined.

In order to treat all these setups the whole many multi-level system part is treated as a single multi-level system, of considerably larger size: This in principle recovers the exponential complexity of the direct product state basis found in Chapter 4. However the techniques developed in this thesis, especially the sketches, will prove helpful when treating complex systems like that

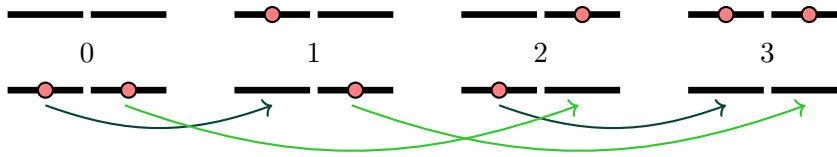


**Figure 9.1 – Two non-identical two-level systems:** The direct product basis of two two-level systems has  $2^2 = 4$  states. Labeling these states with  $0, 1, \dots$  and looking at the actions of the elementary flip operators makes this system compatible with the permutation symmetric approach and PsiQuaSP.

and allow to identify reductions in complexity.

In Fig. 9.1 the direct product basis for a set of two two-level systems is shown, which has Hilbert space dimension 4. The states are labeled from 0 to 3 and the elementary flip operators for the individual two-level system  $\sigma_{10}^i$  and  $\sigma_{01}^i$  can be read off Fig. 9.1:

$$\begin{aligned} \sigma_{10}^1 &= J_{10} + J_{32}, & \sigma_{01}^1 &= J_{01} + J_{23}, \\ \sigma_{10}^2 &= J_{20} + J_{31}, & \sigma_{01}^2 &= J_{02} + J_{13}. \end{aligned} \quad (9.1.1)$$

The  $J_{\dots}$  operators are again constructed from the  $\Gamma$  matrices as explained in the Sections 5.5.2 and A.4: In PsiQuaSP one defines a function for each of the elementary operators acting from the left and acting from the right  $\sigma_{\dots}^i \rho$ ,  $\rho \sigma_{\dots}^i$  and then use PETSc matrix product and addition tools to construct more complicated Liouvillians. For example constructing a disordered version of the Dicke model for two two-level systems

$$\begin{aligned} H &= \hbar \omega b^\dagger b + \hbar \sum_i \omega_i \sigma_{11}^i + \hbar \sum_i g_i (\sigma_{10}^i b + \sigma_{01}^i b^\dagger) \\ \mathcal{D}_{sp}(\rho) &= \sum_i \frac{\gamma_i}{2} (2\sigma_{01}^i \rho \sigma_{10}^i - \sigma_{11}^i \rho - \rho \sigma_{11}^i) \\ \mathcal{D}_{ph}(\rho) &= \frac{\kappa}{2} (2b \rho b^\dagger - b^\dagger b \rho - \rho b^\dagger b) \end{aligned} \quad (9.1.2)$$

results in the sketches Fig. 9.2: Again the spontaneous emission sketch only connects densities to densities and dephases the off-diagonal elements. Please note that for a single multi-level system the sketches and the density matrix are identical: Replacing the  $n_{\dots}$  in the bubbles with  $\rho_{\dots}$  is equivalent and recovers the density matrix. The cavity – emitter coupling looks a bit more complicated, but the construction of these operators can be automatized. For three two-level systems the direct product basis and the flip operators are shown in Fig. 9.3, which is represented by a single 8 level system in PsiQuaSP. Generally a set of  $N$  distinguishable  $d$ -level systems is described by  $d^N$  Hilbert space basis states and therefore such a system is treated as a  $d^N$ -level system in PsiQuaSP.

Drawing these sketches for systems more complicated than three two-level systems is a daunting task and it is not recommended to do so. The two examples presented here only serve as a proof of principle and also as a visualization of possible decouplings and therefore the possible reduction in degrees of freedom. The construction of the elementary single spin operators  $\sigma_{\dots}^i$  from the "collective" operators  $J_{\dots}$  can be done algorithmically and also the exploitation of possible decouplings can be automated as will be seen in the next section.

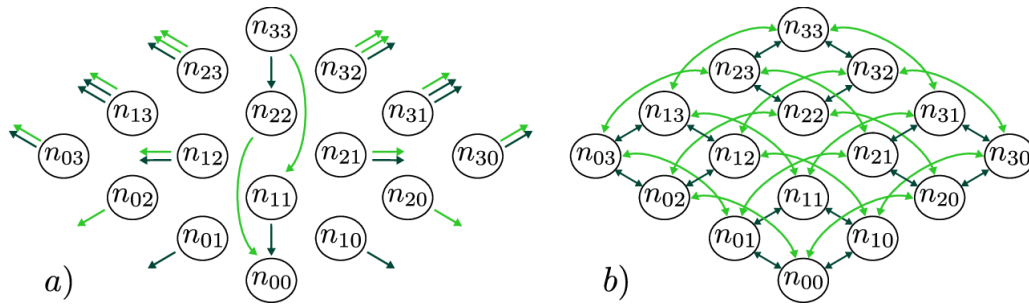


**Figure 9.2 – Sketches for two non-identical two-level systems:** The sketches for the two two-level systems form Fig. 9.1. a) The spontaneous emission Liouvillian and b) the emitter – cavity coupling Liouvillian (same color coding as Fig. 9.1). At this level there is no decoupling of off-diagonal degrees of freedom.

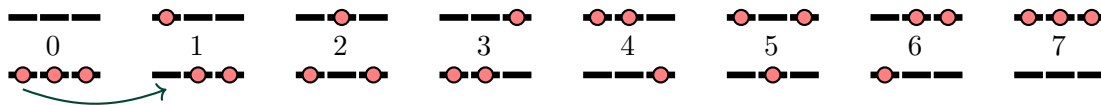


**Figure 9.3 – Three non-identical two-level systems:** The direct product basis of two two-level systems has  $2^3 = 8$  states. These states are again labeled with numbers 0, 1, ... and the actions of the elementary flip operators can be drawn.

## 9.2 Graph theory based optimization

In this Section graph theory is used to reduce the complexity of numerically solving a master equation. The approach is generally applicable for any master equation, however it does not always lead to improved performance. The approach presented in this section was inspired by the discussion of Schirmer and Wang [72] and the partitioning techniques provided by the PETSc library, especially the ParMETIS package.

### 9.2.1 Graph theory and partitioning in a nutshell

Any matrix  $A$  can be represented by a graph [204]. Each dimension of the matrix (or each diagonal element) is represented by a vertex in the graph and the off-diagonal elements are represented by the edges, connecting these vertices. Generally for the discussion in this section the diagonal entries are not considered and the actual values of the entries are unimportant. The matrix  $A$  is called the adjacency matrix of the graph, see Fig. 9.4.

Graph theory is used for optimizing parallel performance: When computing e.g. a matrix vector multiplication in distributed memory parallelization, the matrix and the vector are split into groups of rows and each group of rows is stored at and treated by a different processor. This grouping is usually called partitioning. All vector elements stored on a single processor are called the local elements and all other elements, stored on the other processors are called the non-local elements. When computing the matrix vector product the entries of the matrix that connect only local elements can be treated on the processor independent of the other processors, however the elements that connect to nonlocal elements require interprocess communication: The nonlocal elements need to be communicated from one processor to the next in order to compute the matrix vector product. This interprocess communication makes parallelization inefficient. In order to overcome this problem or at least optimize the parallel performance there are a lot of packages that aim to minimize this interprocess communication, or rather the number of non-local matrix elements. One of these packages available through PETSc is ParMETIS [136].

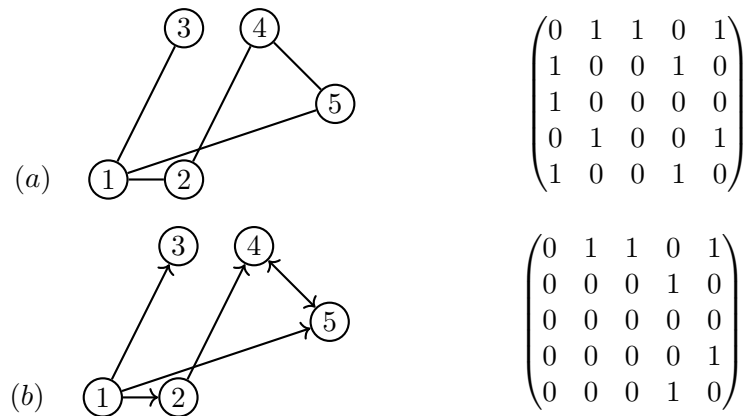


**Figure 9.4 – Graph and adjacency matrix:** The nodes of a graph are called vertices and the connections between the vertices are called edges. The adjacency matrix  $A$  of a graph of  $v$  vertices is a  $v \times v$  matrix, where the nonzero elements  $A_{ij}$  represent the edges between the vertices. For simplicity all nonzero elements are equal to 1 here, but this is not a requirement for a graph, the edges then simply have weights. There are simple, undirected graphs represented by symmetric matrices (a) and directed graphs represented by asymmetrical matrices (b).

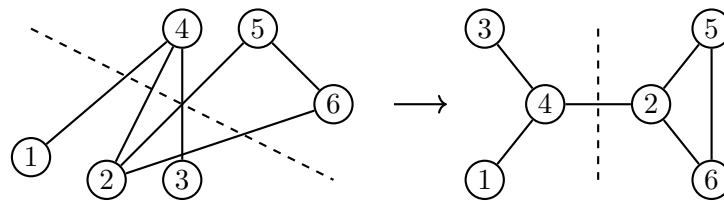


**Figure 9.5 – Graph partitioning:** Partitioning a graph across two processors may lead to an unnecessary number of edge cuts, which lead to interprocess communication. Graph partitioning packages such as ParMETIS repartition graphs in order to reduce the number of edge cuts. Here in the left partitioning the vertices 1, 2, 3 are stored on the first processor and the vertices 4, 5, 6 are stored on the second processor leading to 5 edge cuts. The optimized partitioning on the right hand side only has a single edge cut and thus has superior parallel performance.

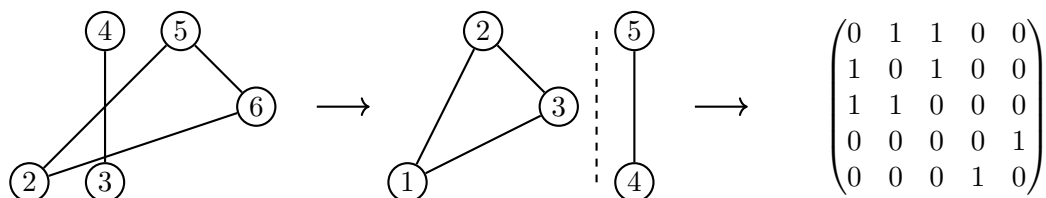


**Figure 9.6 – Disconnected Graph and block-diagonal adjacency matrix:** A graph whose vertices are not all connected is called a disconnected graph. Relabeling the vertex numbers results in a block-diagonal adjacency matrix. This allows an optimal parallelization/partitioning without any edge cuts.

These packages treat the matrix as a graph and try to find a partitioning that reduces the number of edge cuts, the number of edges that connect the different partitions, see Fig. 9.5. This is equivalent to minimizing the number of matrix elements that connect non-local elements and is therefore equivalent to a reduction in interprocess communication. The use of graph theory is beneficial since it provides a more intuitive approach to this optimization procedure which helps in the design of appropriate algorithms.

If there is a partitioning in which the matrix is block diagonal, or rather the number of edge cuts is zero, meaning there are no entries in the matrix that connect non-local elements, the matrix vector multiplication can be computed on each processor completely independent of the other processors, see Fig. 9.6. This would then lead to an optimal speedup in computing time: Computing the matrix vector product in parallel on  $n$  processors leads to a speedup of factor  $n$  only if the matrix is block diagonal across these  $n$  processors.

Even if there is no block diagonal form of the matrix, optimizing the partitioning of any master equation in PsiQuaSP may still lead to significantly improved parallel performance.

### 9.2.2 Reduction of degrees of freedom

PsiQuaSP uses a vectorized version of the master equation

$$\dot{\rho} = \mathcal{L}\rho \quad (9.2.1)$$

thus the Liouvillian is represented by a matrix, see Appendix B.2 for details on the vectorized representation. Generally the Liouvillian matrix is non-hermitian and even the distribution of entries is not symmetrical, therefore the representing graph would be directed<sup>1</sup>. For partitioning purposes it is however beneficial to work with a symmetric matrix, therefore the matrix

$$\text{SYM} = \mathcal{L} + \mathcal{L}^\dagger \quad (9.2.2)$$

will be used. This new matrix does not introduce new couplings between elements, it merely adds the elements that result in a symmetric distribution of entries, compare Figs. 9.4 (a) and (b). It will also not be used for calculations, the only purpose is to use it for the graph partitioning.

If there exists a partitioning of this matrix that is block diagonal this has two consequences: (i) If there are  $n$  partitions that contain density degrees of freedom the master equation has at least  $n$  linearly independent steady states and (ii) partitions that do not contain density degrees of freedom can be omitted from the dynamics.

Statement (i) stems from the observation that the blocks are non-interacting therefore if the system is prepared inside of one partition it will never leave this partition [72], which is equivalent to the discussion in Section 3.4. This implies that each normalized, linear superposition of the steady states is again a valid steady state. This is similar to the decoupling of the Dicke subspaces in a  $J^2$  symmetric master equation. Only considering collective decay in a set of identical two-level systems, i.e.

$$\dot{\rho} = \frac{\gamma}{2}(J_{01}\rho J_{10} - J_{10}J_{01}\rho - \rho J_{10}J_{01}) \quad (9.2.3)$$

means that each mixture in the dark  $|l, -l\rangle$  Dicke states is a valid steady state (compare to Chapters 4 and 7). Therefore the number of different Dicke subspaces defined by the number

<sup>1</sup>Essentially the sketch representation for the permutation symmetric method is also just a graph. In fact it turns out that only the unidirectional arrows introduced through spontaneous decay are the arrows responsible for the Liouvillian matrix being a directed graph. Since the sketches also have a close connection to the Lie algebras there might be some connections between Lie algebras and graph theory hidden in the methodology presented in this thesis.

of distinct values of total pseudo spin quantum number  $l$  and the dimension of the null space of this Liouvillian are the same. If the state is prepared in one of the disconnected Liouville subspaces (or generally a subset of these subspaces) then all the other subspaces can be omitted and graph partitioning provides an easy tool to do so.

Statement (ii) is similar to the discussion around the sketches and the additional symmetries in Section 5.4.3: Disconnected coherence degrees of freedom, or rather, disconnected off-diagonal density matrix elements only experience dephasing but no driving. Therefore in the steady state they will be zero and can be neglected. However the graph theory based method is much more general and powerful than the sketch representation. One example where this approach has merit is as follows: In Chapter 6 the cQED lasers were discussed: For instance the two-level laser master equation reads

$$\dot{\rho} = \frac{i}{\hbar}[\rho, H] + \frac{P}{2}\mathcal{D}_{0\rightarrow 1}(\rho) + \frac{\gamma}{2}\mathcal{D}_{1\rightarrow 0}(\rho) + \frac{\kappa}{2}\mathcal{D}_{ph}(\rho) \quad (9.2.4)$$

with

$$\begin{aligned} H &= \hbar\Delta_0 b^\dagger b + \hbar\Delta_1 J_{11} + \hbar g(J_{10}b + J_{01}b^\dagger) \\ \mathcal{D}_{0\rightarrow 1} &= \sum_i (2\sigma_{10}^i \rho \sigma_{01}^i - \sigma_{00}^i \rho - \rho \sigma_{00}^i) \\ \mathcal{D}_{1\rightarrow 0} &= \sum_i (2\sigma_{01}^i \rho \sigma_{10}^i - \sigma_{11}^i \rho - \rho \sigma_{11}^i) \\ \mathcal{D}_{ph}(\rho) &= (2b\rho b^\dagger - b^\dagger b\rho - \rho b^\dagger b). \end{aligned}$$

It was pointed out by Xu and Holland [205] that this equation bears an additional  $U(1)$  symmetry. Replacing the operators  $b, b^\dagger$  and  $\sigma_{01}, \sigma_{10}$  by

$$b \rightarrow b e^{i\phi}, \quad b^\dagger \rightarrow b^\dagger e^{-i\phi}, \quad \sigma_{01} \rightarrow \sigma_{01} e^{i\phi}, \quad \sigma_{10} \rightarrow \sigma_{10} e^{-i\phi}, \quad (9.2.5)$$

leaves the master equation invariant. This results in a predetermined relation between the off-diagonal elements of the density matrix

$$tr[\hat{\mathcal{P}}[n_{11}, n_{10}, n_{01}][m_l]\langle m_r | \rho] = \mathcal{P}[n_{11}, n_{10}, n_{01}; m_l, m_r] \quad (9.2.6)$$

Looking explicitly at the equations of motion one can derive that the following equality holds

$$n_{01} - n_{10} = m_l - m_r. \quad (9.2.7)$$

All contributions in the master equation except the Dicke interaction Hamiltonian leave the off-diagonal elements unchanged, i.e.

$$\partial_t \mathcal{P}[n_{11}, n_{10}, n_{01}; m_l, m_r] \propto \mathcal{P}[n_{11} \pm x, n_{10}, n_{01}; m_l \pm y, m_r \pm y]. \quad (9.2.8)$$

Only the Dicke interaction Hamiltonian introduces coupling of diagonal density matrix elements to off-diagonal elements, but the action of the Dicke interaction Hamiltonian leaves the relation Eq. (9.2.7) unchanged. This means that one degree of freedom in this equation is predetermined and can thus be eliminated, e.g.

$$n_{01} = m_l - m_r + n_{10}. \quad (9.2.9)$$

and the system is completely described by a new quantity

$$\mathcal{P}[n_{11}, n_{10}, n_{01} = m_l - m_r + n_{10}; m_l, m_r] = \mathcal{P}[n_{11}, n_{10}; m_l, m_r], \quad (9.2.10)$$

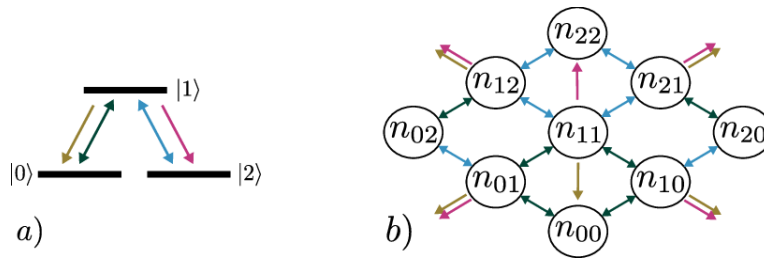


**Figure 9.7 – Example system for graph theory based optimization:** (a) Level scheme and (b) sketch. The sketch representation does not reveal the  $U(1)$  symmetric decoupling.

which only scales like  $N^2$  in the two-level system degrees of freedom.

Observing this symmetry in this master equation, deriving the relations Eqs. (9.2.7), (9.2.9) and programming an interface that treats the eliminated degree of freedom  $n_{01}$  is possible, but is limited to this specific single problem. Also if more mode degrees of freedom are considered than the total number  $N$  of two-level systems it will be beneficial to eliminate  $m_l$  or  $m_r$  instead. Furthermore the symmetry also appears in more complicated setups, like multi three- and four-level system setups coupled to bosonic modes using the Dicke interaction Hamiltonian – it only requires the RWA (without the RWA in the Dicke interaction this symmetry does not hold). Explicitly deriving the equivalent relations for the off-diagonal elements is not so simple for these systems when additional interaction Hamiltonians are present. However the graph theory based method outlined above can detect and harvest this symmetry in *any* master equation. Also other, less obvious symmetries for instance in non-identical setups can be detected.

In the PsiQuaSP library the usage of this method is illustrated in the `ex5` example in the `example` folder: There a set of  $\Lambda$ -systems where one transition couples to a bosonic mode and the other transition is driven by an external laser is considered, see Fig. 9.7. In an appropriate rotating frame the Hamiltonian reads

$$H = \hbar\Delta_0 b^\dagger b + \hbar\Delta_1 J_{22} + \hbar g(J_{01} b^\dagger + J_{10} b) + \hbar E(J_{21} + J_{12}), \quad (9.2.11)$$

where  $\Delta_0$  is the detuning between the  $0 - 1$  transition and the cavity mode and  $\Delta_1$  is the detuning between the  $1 - 2$  transition and the driving laser. Open system contributions are e.g. spontaneous emission and a finite photon lifetime

$$\begin{aligned} \mathcal{D}_1(\rho) &= \frac{\gamma}{2} \sum_i (2\sigma_{01}^i \rho \sigma_{10}^i - \sigma_{11}^i \rho - \rho \sigma_{11}^i), & \mathcal{D}_2(\rho) &= \frac{\gamma'}{2} \sum_i (2\sigma_{21}^i \rho \sigma_{12}^i - \sigma_{11}^i \rho - \rho \sigma_{11}^i), \\ \mathcal{D}_3(\rho) &= \frac{\kappa}{2} (2b\rho b^\dagger - b^\dagger b\rho - \rho b^\dagger b). \end{aligned} \quad (9.2.12)$$

This master equation bears the  $U(1)$  symmetry and ParMETIS is used to reduce the complexity of the solution from  $N^8$  to  $\sim N^7$ , the same reduction found above. The total number of needed density matrix elements is shown in Fig. 9.8. There is no need to derive any relations, the method can just be applied as is to any master equation. Please note that also this approach is not an approximation, it simply provides a unified interface to exploit decoupling of degrees of freedom in quantum master equations. Another example where the graph theory based reduction is beneficial is when non-identical systems are considered as in the last section: The PsiQuaSP user sets all degrees of freedom that correspond to the  $N$   $d$ -level systems (the  $d^N$ -level system), algorithmically builds the elementary  $\sigma_{\dots}^i$  matrices and then uses graph partitioning to find possible disconnected regions. This approach allows for a fully automatized optimization of the non-identical master equations of the last section and is achieved with minor programming effort.

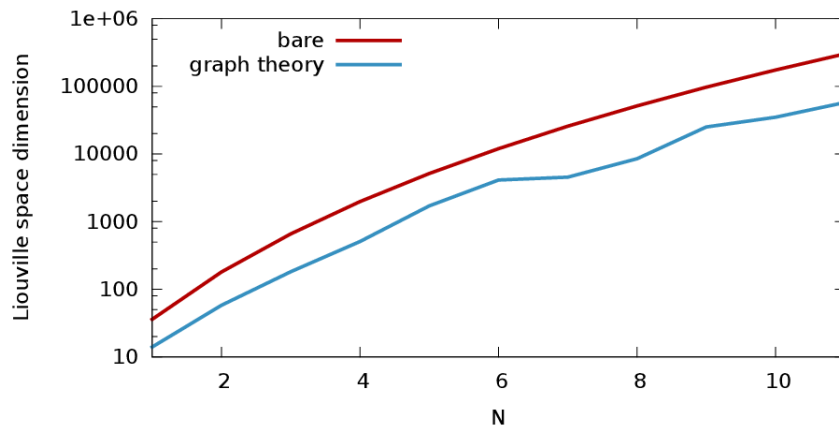


**Figure 9.8 – Graph theory based reduction of degrees of freedom:** The Liouville space dimension before and after graph theory based optimization for a multi  $\Lambda$ -system master equation.

However if there is no decoupling of degrees of freedom then there will also be no reduction in the degrees of freedom.

Overall the graph theory based method described in this section is a highly non-standard tool in a quantum master equation setting. In 2016 Shi *et al.* were using graph theory to investigate possibilities in quantum networks on a completely analytic level [206]. To my knowledge there are no studies having used graph theory based optimization schemes as a numerical recipe for quantum master equations.

### 9.3 Conclusion

In this chapter two non-obvious features of the PsiQuaSP library were introduced that have a very broad application range. First the method for treating non-identical systems was outlined. Using this approach in principle every conceivable master equation can be implemented using a number state representation (there is so far no support for coherent states). This ranges from disorder in quantum optical systems, distance dependent interactions like direct dipole-dipole coupling or Förster transfer and chiral/cascaded waveguide cQED to systems that are actually outside of quantum optics or quantum information such as spin chains with system bath interaction. Especially the application of coupling multiple emitters to the strongly distance dependent dispersive modes arising in the Welsch formalism used in Chapter 8 could prove interesting. However all these systems again live at first in a fully exponential Hilbert/Liouville space. The second feature – the graph theory based method – provides a general framework to detect arbitrary decoupling in the equations of motion, including the decoupling that cannot even be seen in the sketch representation.

Overall the discussion presented in this chapter dramatically widens the application range of the PsiQuaSP library and the graph theory based optimization schemes provides a major computational asset.

## IV Epilogue



# 10 Summary and Outlook

In this thesis a general formalism for the open system description of indistinguishable quantum emitters for quantum optical and quantum information setups was introduced. The requirement of indistinguishability was utilized to reduce the exponential size of the associated Liouville space to a polynomial size. This is equivalent to restricting the dynamics to the fully symmetrical Liouville multiplet states. The formalism was derived by directly investigating the occurring equations of motion and was subsequently generalized to a concise mathematical form that allows to utilize the full power of this method. The graphical representation of the formalism greatly facilitates the usage and allows for a simple translation of quantum master equations into numerical code using our library `PisQuaSP`. Furthermore this representation and the resulting sketches proved to be a valuable tool also in more abstract and formal treatments, especially when considering Lie algebraic bosonization methods. The library `PisQuaSP` provides a unified platform to compute the steady state behavior and time dynamics of arbitrary quantum master equations based on a number state representation. This includes a large variety of systems, also those that are not related to indistinguishable emitters.

The connection of the Lie algebraic concepts of spin multiplets and Casimir operators to the general case of identical multi-level quantum emitters in quantum optics was reviewed. It was shown that there is a close intrinsic connection to the symmetrized Liouville space basis states of the introduced formalism. Not only are these considerations of general mathematical interest, they can be utilized for density matrix diagonalization of large sets of correlated multi-level systems, which provides a major methodological advance in the field.

The developed tools were applied to two main scenarios: cQED lasers and collective effects in the open Dicke model. The discussion of cQED lasers showed that strong correlations prevail in the sub-threshold regime and that also multi-level gain setups are not suitable to overcome the intrinsic losses in the spaser setup.

The study of collective effects in the open Dicke model resulted in the prediction of a new type

of phase transition in this decade old problem – the superradiant to subradiant phase transition. It represents a cavity assisted generation of subradiant and dark state coherences in the steady state behavior. This is especially surprising since the subradiant and dark states have only small or no coupling to the cavity degrees of freedom. Contrary the essential parameter coupling dark states to bright states – the spontaneous decay rate  $\gamma$  – was found to have little or no influence on the behavior of the system. This new phase transition can be exploited for the deterministic preparation of dark states in the steady state. Furthermore in the ground state relaxation of the system a cascade of dark states was found, that is stable against dephasing and all other parameters in the system. The only requirement is the existence of individualization and a process that drives the system into an excited steady state. Therefore the dark state cascade should be a very general process in many types of setups comprised of (approximately) identical two-level quantum emitters. The presented discussion on the open Dicke model represents the first study investigating subradiant effects under realistic system bath interactions or rather utilizing an open system quantum master equation theory. Since subradiant states have been recently discussed for their prospects to store quantum information this discussion is an important contribution to the current discussions in this field.

The permutation symmetric formalism is also suited to study another phase transition in this system – the superradiant phase transition – which has been investigated for decades and is highly disputed up to today. Especially the behavior of this closed system quantum phase transition under the influence of dissipation and dephasing is a matter of utmost current research interest. In addition it would be interesting to apply the method and the library to other known effects in quantum optics in the few particle and strong correlation limit – for instance absorptive optical bistability. Also investigating collectivity in multi-level system setups like coherent population trapping and stimulated adiabatic Raman passage under the influence of dissipation and decay could reveal interesting new collective, quantum coherent effects. Overall there is a vast range of application for the formalism and the library.

In another study the effect of thin metal films on the lifetime dynamics of single quantum dots was investigated. In this joint experimental and theoretical study the drastic change and enhanced reproducibility of the samples using a new type of metal film could be explained using an advanced theoretical formalism for dissipative quantized optical modes. The theory essentially represents a non-perturbative treatment of the strong system bath interactions arising in plasmonic structures.

The possibility of treating non-identical systems in PsiQuaSP makes the library also an ideal tool to investigate many emitter physics in this field of plasmonics and general dissipative quantum optical setups in media: In the field of dissipative modes including non-perturbative system bath interaction recent progress has been made towards a full density matrix formulation of the problem. The theory predicts non-orthonormal bosonic Fock states leading to mode-mode coupling effects. This allows to study completely new physics in dissipative quantum optics away from the low excitation limit, including driving. The introduced library PsiQuaSP provides an ideal framework to directly translate these new master equations into numerical code and to investigate effects of single emitters, identical sets of emitters and non-identical emitters in this new, exciting field of quantum optics. Other promising application ranges of PsiQuaSP are cascaded or chiral cQED setups and collectivity in phonon lasers and laser cooling.

To summarize a new formalism was introduced that has a wide application range in quantum optics and quantum information setups. The formalism was cast into an easy to use computer library that provides efficient, scalable and flexible code. This framework was utilized to study different quantum optical setups in a completely new way, which lead to the prediction of a new type of quantum coherent phase transition. The range of application of the method and the library far exceeds the original expectations and will prove valuable in future investigations.

# 11 Acknowledgements

I wish to thank Prof. Andreas Knorr and Dr. Marten Richter for giving me the opportunity to work on this topic and supporting my research. The many discussions with them shaped and influenced the presented work to a great extent. I especially thank Dr. Marten Richter for the important guidance in the development of the PsiQuaSP library.

I thank Prof. Jan Wiersig for being the second Gutachter of my thesis and Prof. Birgit Kangießer for taking over the job of the Prüfungsvorsitz.

Furthermore I wish to thank Prof. Mackillo Kira for letting me stay in his research group at the University of Michigan in the beginning of 2017, for teaching me some aspects of actual semiconductor cluster expansion and his inspirations that lead to the support of non-identical systems in the PsiQuaSP library. I also thank Dr. Imran Mirza of the University of Michigan for many inspiring discussions. I want to thank the School of Nanophotonics of the SFB 787 for paying for the expenses of this trip and many other trips to conferences around the world and overall the DFG for the financial support.

Special thanks goes to Dr. Alexander Carmele for the many valuable discussions around the open Dicke model, dark states and quantum coherent phenomena.

I thank all of the current and past members of the AG Knorr for being my colleagues, discussion partners, sources of inspiration and for all the nice moments at lunch, (coffee) breaks, symposia, workshops and conferences. Especially thank Nicolas Naumann, Leon Droenner and Sandra Kuhn for being my office (and gossip) mates and all the people from the mensa group for the daily enjoyable lunch breaks: Malte Selig, Florian Wendler, Torben Winzer, Gunnar Berghäuser, Markus Krecik, Sven Hein, Manuel Kraft and Shahab Azizabadi. I thank Malte

Selig for organizing the short but enjoyable AG Knorr table tennis league with me.

For proofreading my thesis and their valuable input I thank Leon Droenner, Nicolas Naumann, Sandra Kuhn, Sebastian Franke, Alexander Carmele, Judith Specht and David Meidinger. Also for helping with benchmarking the PsiQuaSP library I want to thank Christopher Wächtler and Leon Droenner.

I thank Marten Richter and Peter Orłowski for the technical support, the well managed computer cluster and also for providing access to ancient technologies such as CD-ROM writers and laptops with VGA connector.

I especially want to thank my girlfriend Lisa for her emotional support and her coping with all the dreary physics talk and actually listening, even though not being related to science at all. I also want to thank my family, friends and flatmates for making my life aside research enjoyable.

# B Properties of the symmetrized Liouville space basis

## B.1 Scaling

The number of basis matrices  $m + 1$  of the single  $(d + 1)$ -level system  $|k\rangle\langle l|$  is

$$m + 1 = (d + 1)^2, \quad (\text{B.1.1})$$

where  $m$  of these matrices form a representation of the  $SU(d + 1)$  group, since trace conservation (always demanded for special unitary groups) eliminates one of these matrices. Let us denote the corresponding single spin matrices by  $\sigma_i$ ,  $i \in \{0, \dots, m\}$  and the corresponding  $N$  spin basis matrix in the "set-free" notation as

$$\bigotimes_{i=0}^m \sigma_i^{\otimes n_i}. \quad (\text{B.1.2})$$

The total number of degrees of freedom  $Z$  of the collective  $N$  spin system obeying a permutation symmetric Lindblad equation is determined by the expression

$$\sum_{i=0}^m n_i = N. \quad (\text{B.1.3})$$

It turns out that  $Z$  is given by

$$Z(m) = \binom{N + m}{N}, \quad (\text{B.1.4})$$

which will be proven in the following using mathematical induction. For this purpose it is useful to rewrite Eq. (B.1.3)

$$\sum_{i=0}^m n_i = N \rightarrow \sum_{i=0}^{m-1} n_i = N - n_m, \quad (\text{B.1.5})$$

where now the rhs has  $N + 1$  possibilities of being fulfilled:  $0 \leq N - n_m \leq N$  and  $Z(m)$  is then given by the sum over all these contributions, which would result in

$$Z(m) = \sum_{k=0}^N \binom{k+m-1}{k}, \quad (\text{B.1.6})$$

if Eq. (B.1.4) is valid. Hence if by showing that

$$\sum_{k=0}^N \binom{k+m-1}{k} = \binom{N+m}{N} \quad (\text{B.1.7})$$

for all  $m > 1$  and acknowledging that it produces the correct result for  $m = 1$

$$\begin{aligned} \sum_{k=0}^N \binom{k}{k} &= \sum_{k=0}^N 1 = N + 1 \\ \binom{N+1}{N} &= N + 1 \end{aligned} \quad (\text{B.1.8})$$

it holds for all  $m$ . This is possible by induction:

**Inductive basis:** Eq. (B.1.8)

**Inductive hypothesis:**  $m = p$

$$\sum_{k=0}^N \binom{p-1+k}{k} = \binom{N+p}{N} \quad (\text{B.1.9})$$

**Inductive step:**  $m = p + 1$

$$\sum_{k=0}^N \binom{p+k}{k} = \sum_{k=0}^N \binom{p+k}{p} \quad (\text{B.1.10})$$

$$= \sum_{k=0}^N \binom{p-1+k}{k} + \sum_{k=1}^N \binom{p+k-1}{k-1} \quad (\text{B.1.11})$$

$$= \binom{N+p}{N} + \sum_{k=0}^{N-1} \binom{p+k}{k} \quad (\text{B.1.12})$$

$$= \binom{N+p}{N} + \binom{N+p}{N-1} \quad (\text{B.1.13})$$

$$= \binom{N+p+1}{N} \quad \text{q.e.d} \quad (\text{B.1.14})$$

## B.2 Properties of the symmetrized Liouville space basis states

For the following discussion it is useful to introduce a vectorized representation of the symmetrized Liouville space states  $\hat{\mathcal{P}}$ :

$$\hat{\mathcal{P}}[\{n_{kl}\}] \equiv |\{n_{kl}\}\rangle \quad (\text{B.2.1})$$

**Orthogonality:** These basis states are orthogonal according to the Hilbert-Schmidt inner product

$$\begin{aligned}
\langle \{n'_{kl}\} | \{n_{kl}\} \rangle &= \text{tr}[\hat{\mathcal{P}}^\dagger[\{n'_{kl}\}]\hat{\mathcal{P}}[\{n_{kl}\}]] \\
&= \text{tr}\left[\left(\mathcal{S} \bigotimes_{k,l}^d \sigma_{kl}^{\otimes n'_{kl}}\right)^\dagger \mathcal{S} \bigotimes_{k,l}^d \sigma_{kl}^{\otimes n_{kl}}\right] \\
&= \text{tr}\left[\mathcal{S} \bigotimes_{k,l}^d \sigma_{lk}^{\otimes n'_{kl}} \mathcal{S} \bigotimes_{k,l}^d \sigma_{kl}^{\otimes n_{kl}}\right] \\
&= \delta_{\{n'_{kl}\}, \{n_{kl}\}} \binom{N}{\{n_{kl}\}}. \tag{B.2.2}
\end{aligned}$$

This can be understood as follows: The product can only be nonzero if  $\{n'_{kl}\} = \{n_{kl}\}$  since otherwise the resulting states would not correspond to a diagonal entry, for instance

$$\sigma_{xy}^1 \sigma_{xy}^2 \cdots \sigma_{xy}^n \cdot \sigma_{yx}^1 \sigma_{yx}^2 \cdots \sigma_{yx}^{n-1} \sigma_{yz}^n = \sigma_{xx}^1 \cdots \sigma_{xx}^{n-1} \sigma_{xz}^n, \tag{B.2.3}$$

here the last spin is represented by an off-diagonal state and thus in the trace operation this state yields zero. Since every product state appears exactly once in the symmetrized state it follows that there will be a multinomial number of diagonal states resulting from the product, which gives a 1 in the trace operation and the sum over all contributions gives the multinomial.

**Identities and projectors:** The Hilbert space identity in the  $\hat{\mathcal{P}}$  representation is given by

$$I_H = \sum_{\{n_{kk}\}} \hat{\mathcal{P}}[\{n_{kk}\}] = \sum_{\{n_{kk}\}} \mathcal{S} \bigotimes_k^d \sigma_{kk}^{\otimes n_{kk}}, \tag{B.2.4}$$

where the sum runs over all possible sets of  $\{n_{kk}\} = \{n_{dd}, n_{(d-1)(d-1)} \cdots n_{00}\}$ , without any flip operator contributions. The Liouville space identity is given by

$$I_L = \sum_{\{n_{kl}\}} \binom{N}{\{n_{kl}\}}^{-1} |\{n_{kl}\}\rangle \langle \{n_{kl}\}|. \tag{B.2.5}$$

Since the  $\hat{\mathcal{P}}$  are not normalized there is also a projector, which is not equal to the identity

$$P_L = \sum_{\{n_{kl}\}} |\{n_{kl}\}\rangle \langle \{n_{kl}\}|. \tag{B.2.6}$$

**Vectorized representation:** PsiQuaSP uses an expansion of the density matrix based on the Hilbert-Schmidt inner product

$$\mathcal{P}[\{n_{ij}\}] = \text{tr}[\hat{\mathcal{P}}[\{n_{ij}\}]\rho] \tag{B.2.7}$$

The actions of any operators  $A, B$  on the density matrix is thus handled by PsiQuaSP like

$$A\rho B \rightarrow \text{tr}[\hat{\mathcal{P}}[\{n_{ij}\}]A\rho B] = \text{tr}[B\hat{\mathcal{P}}[\{n_{ij}\}]A\rho] = \text{tr}[\hat{\mathcal{P}}[\{n'_{ij}\}]\rho] \tag{B.2.8}$$

The vectorization of a matrix  $A = (a_1, a_2 \dots)$ , where  $a_i$  are the column vectors, is defined as

$$|A\rangle \equiv \text{vec}(A) = \begin{pmatrix} a_1 \\ a_2 \\ \vdots \end{pmatrix} \tag{B.2.9}$$

Considering the matrix equation

$$AXB = C \quad (\text{B.2.10})$$

the following identity holds [207]

$$(B^T \otimes A)|X\rangle = |C\rangle. \quad (\text{B.2.11})$$

This is formally equivalent to the  $R, L$  algebra used in the main text. The  $R, L$  algebra is useful for abstract mathematical calculations, however Eq. (B.2.11) gives a representation of the *actual* matrices that are set by PsiQuaSP. Two properties of the direct product are interesting for this equation: The matrix product and the hermitian transpose:

$$\begin{aligned} (A \otimes B)(C \otimes D) &= (AC \otimes BD) \\ (A \otimes B)^\dagger &= (A^\dagger \otimes B^\dagger). \end{aligned} \quad (\text{B.2.12})$$

The second identity could be utilized to construct something like  $J_{xy}^L$  from  $J_{yx}^L$  using the hermitian transpose operation `MathHermitianTranspose(...)` of PETSc. Unfortunately it turns out that the unnormalized states  $\hat{\mathcal{P}}$  do not allow this relation (see below).

This can be used to vectorize the master equation

$$\dot{\rho} = A\rho B \rightarrow |\dot{\rho}\rangle = (B^T \otimes A)|\rho\rangle \quad (\text{B.2.13})$$

Then the  $\hat{\mathcal{P}}$  representation of the master equation  $\dot{\rho} = A\rho B$  becomes

$$\begin{aligned} |\dot{\rho}\rangle &= \sum_{\{n_{kl}\}} |\{n_{kl}\}\rangle \langle \{n_{kl}\} | \dot{\rho} \rangle \\ &= \sum_{\{n_{kl}\}} |\{n_{kl}\}\rangle \langle \{n_{kl}\} | (B^T \otimes A) |\rho\rangle \\ &= \sum_{\{n_{kl}\}} |\{n_{kl}\}\rangle \langle \{n_{kl}\} | (B^T \otimes A) \sum_{\{m_{kl}\}} \left( \binom{N}{\{m_{kl}\}} \right)^{-1} |\{m_{kl}\}\rangle \langle \{m_{kl}\} | \rho \rangle \\ &= \sum_{\{n_{kl}\}} \sum_{\{m_{kl}\}} \left( \binom{N}{\{m_{kl}\}} \right)^{-1} \langle \{n_{kl}\} | (B^T \otimes A) | \{m_{kl}\}\rangle |\{n_{kl}\}\rangle \langle \{m_{kl}\} | \rho \rangle \\ &= \sum_{\{n_{kl}\}} \sum_{\{m_{kl}\}} \underbrace{\left( \binom{N}{\{m_{kl}\}} \right)^{-1} \text{tr}[B\hat{\mathcal{P}}^\dagger[\{n_{kl}\}]A\hat{\mathcal{P}}[\{m_{kl}\}]]}_{(B^T \otimes A)_{\{m_{kl}\}}^{\{n_{kl}\}}} |\{n_{kl}\}\rangle \langle \{m_{kl}\} | \rho \rangle \end{aligned}$$

Hence the elements of the matrices in PsiQuaSP are the  $(B^T \otimes A)_{\{m_{kl}\}}^{\{n_{kl}\}}$ . Looking at

$$\left( (B^T \otimes A)_{\{m_{kl}\}}^{\{n_{kl}\}} \right)^\dagger = \left( \binom{N}{\{m_{kl}\}} \right)^{-1} \text{tr}[B^\dagger \hat{\mathcal{P}}^\dagger[\{m_{kl}\}]A^\dagger \hat{\mathcal{P}}[\{n_{kl}\}]] \quad (\text{B.2.14})$$

and

$$\left( (B^T \otimes A)^\dagger \right)_{\{n_{kl}\}}^{\{m_{kl}\}} = \left( \binom{N}{\{n_{kl}\}} \right)^{-1} \text{tr}[B^\dagger \hat{\mathcal{P}}^\dagger[\{m_{kl}\}]A^\dagger \hat{\mathcal{P}}[\{n_{kl}\}]] \quad (\text{B.2.15})$$

it is clear that the two elements are not equivalent due to the normalization. Introducing a normalization for  $\hat{\mathcal{P}}$  according to the Hilbert-Schmidt inner product

$$\tilde{\mathcal{P}}[\{n_{kl}\}] = \left( \binom{N}{\{n_{kl}\}} \right)^{-\frac{1}{2}} \mathcal{S} \bigotimes_{k,l}^d \sigma_{kl}^{\otimes n_{kl}} \quad (\text{B.2.16})$$

for the construction of the projector  $P_L$  would result in  $\tilde{P}_L = I_L$  and thus

$$\left( (B^T \otimes A)^\sim \right)_{\{m_{kl}\}}^{\{n_{kl}\}} = \text{tr} [B \tilde{\mathcal{P}}^\dagger[\{n_{kl}\}] A \tilde{\mathcal{P}}[\{m_{kl}\}]] \quad (\text{B.2.17})$$

but would again lead to a less stable numerical code. Therefore in PsiQuaSP this is not used.

### B.3 Permutation symmetric Liouville space operators $\Gamma$

In this section the properties of the permutation symmetric Liouville space operators

$$\Gamma_{mm}^{nn} \hat{\mathcal{P}}[\{n_{kl}\}] = \sum_i \sigma_{mm}^i \hat{\mathcal{P}}[\{n_{kl}\}] \sigma_{nn}^i, \quad (\text{B.3.1})$$

and

$$\Gamma_{mn}^{op} \hat{\mathcal{P}}[\{n_{kl}\}] \equiv \sum_i \sigma_{mn}^i \hat{\mathcal{P}}[\{n_{kl}\}] \sigma_{op}^i, \quad (\text{B.3.2})$$

are derived.

The  $\Gamma_{mm}^{nn}$  operator commutes with the  $\mathcal{S}$  operator, since it leaves each state in the sum unchanged

$$\begin{aligned} \Gamma_{mm}^{nn} \hat{\mathcal{P}}[\{n_{kl}\}] &= \sum_i \sigma_{mm}^i \hat{\mathcal{P}}[\{n_{kl}\}] \sigma_{nn}^i, \\ &= \sum_i \sigma_{mm}^i \mathcal{S} \bigotimes_{k,l}^d \sigma_{kl}^{\otimes n_{kl}} \sigma_{nn}^i, \\ &= \sum_i \sigma_{mm}^i \mathcal{S} \dots \sigma_{mn}^{\otimes n_{mn}} \dots \sigma_{nn}^i, \\ &= \mathcal{S} \dots \left( \sum_i \sigma_{mm}^i \sigma_{mn}^{\otimes n_{mn}} \sigma_{nn}^i \right) \dots, \\ &= n_{mn} \mathcal{S} \dots \sigma_{mn}^{\otimes n_{mn}} \dots, \\ &= n_{mn} \hat{\mathcal{P}}[\{n_{kl}\}]. \end{aligned} \quad (\text{B.3.3})$$

The  $\Gamma_{mn}^{op}$  operator does not commute with the  $\mathcal{S}$  operator, since it changes the state. Therefore it is advantageous to introduce the commutation relations first:

$$\begin{aligned} [\Gamma_{mn}^{op}, \Gamma_{nn}^{oo}] &= \sum_{i,j} \sigma_{mn}^i \sigma_{nn}^j \dots \sigma_{oo}^j \sigma_{op}^i - \sum_{i,j} \sigma_{nn}^i \sigma_{mn}^j \dots \sigma_{op}^j \sigma_{oo}^i \\ &= \sum_i \underbrace{\sigma_{mn}^i \sigma_{nn}^i}_{=\sigma_{mn}^i} \dots \underbrace{\sigma_{oo}^i \sigma_{op}^i}_{=\sigma_{op}^i} - \sum_i \underbrace{\sigma_{nn}^i \sigma_{mn}^i}_{=0} \dots \underbrace{\sigma_{op}^i \sigma_{oo}^i}_{=0} \\ &= \sum_i \sigma_{mn}^i \dots \sigma_{op}^i \\ &= \Gamma_{mn}^{op}. \end{aligned} \quad (\text{B.3.4})$$

In the step from the first to the second line I used the fact that spin matrices of different spins commute and therefore cancel each other out in the commutation relation. From this it is clear that

$$[\Gamma_{mn}^{op}, \Gamma_{mm}^{pp}] = -\Gamma_{mn}^{op}. \quad (\text{B.3.5})$$

The derivation of the other commutation relations is completely analogous. With this it is easy to show that the states produced through the action of  $\Gamma_{mn}^{op}$  are again eigenstates of  $\Gamma_{nn}^{oo}$

$$\Gamma_{nn}^{oo} \Gamma_{mn}^{op} \hat{\mathcal{P}}[\{n_{kl}\}] = \Gamma_{mn}^{op} (\Gamma_{nn}^{oo} - 1) \hat{\mathcal{P}}[\{n_{kl}\}] = (n_{no} - 1) \Gamma_{mn}^{op} \hat{\mathcal{P}}[\{n_{kl}\}] \quad (\text{B.3.6})$$

and  $\Gamma_{mm}^{pp}$

$$\Gamma_{mm}^{pp}\Gamma_{mn}^{op}\hat{\mathcal{P}}[\{n_{kl}\}] = \Gamma_{mn}^{op}(\Gamma_{nn}^{oo} + 1)\hat{\mathcal{P}}[\{n_{kl}\}] = (n_{mp} + 1)\Gamma_{mn}^{op}\hat{\mathcal{P}}[\{n_{kl}\}] \quad (\text{B.3.7})$$

but with different eigenvalues. Looking at

$$\begin{aligned} \langle \{n_{kl}\} | \Gamma_{mn}^{op} \Gamma_{nm}^{po} | \{n_{kl}\} \rangle &= \sum_{i,j} \text{tr}[\hat{\mathcal{P}}^\dagger[\{n_{kl}\}]\sigma_{mn}^i\sigma_{nm}^j\hat{\mathcal{P}}[\{n_{kl}\}]\sigma_{po}^j\sigma_{op}^i] \\ &= \underbrace{\sum_i \text{tr}[\hat{\mathcal{P}}^\dagger[\{n_{kl}\}]\sigma_{mm}^i\hat{\mathcal{P}}[\{n_{kl}\}]\sigma_{pp}^i]}_{n_{mp}\text{tr}[\hat{\mathcal{P}}^\dagger\hat{\mathcal{P}}]} + \underbrace{\sum_{i \neq j} \text{tr}[\hat{\mathcal{P}}^\dagger[\{n_{kl}\}]\sigma_{mn}^i\sigma_{nm}^j\hat{\mathcal{P}}[\{n_{kl}\}]\sigma_{po}^j\sigma_{op}^i]}_{n_{mp}n_{no}\text{tr}[\hat{\mathcal{P}}^\dagger\hat{\mathcal{P}}]} \\ &= n_{mp}(n_{no} + 1)\text{tr}[\hat{\mathcal{P}}^\dagger\hat{\mathcal{P}}] \\ &= n_{mp}(n_{no} + 1)\frac{N!}{\dots n_{mp}!\dots n_{no}!\dots} \\ &= (n_{no} + 1)^2\frac{N!}{\dots (n_{mp} - 1)!\dots (n_{no} + 1)!\dots} \\ &= (n_{no} + 1)^2\langle \dots n_{mp} - 1 \dots n_{no} + 1 \dots | \dots n_{mp} - 1 \dots n_{no} + 1 \dots \rangle. \end{aligned} \quad (\text{B.3.8})$$

## B.4 Block diagonal representation of the density matrix in $su(d)$ multiplets

### B.4.1 Two-level systems

Not only is it generally interesting from a theoretical viewpoint how these representations are connected, since the symmetry breaking was the motivation for the whole discussion, but Dicke super- and subradiance are active research fields that are related to multipartite entanglement and quantum information storage. For this purpose it is important to have a comprehensible theoretical approach that allows to study realistic dephasing effects in these systems. The link between the two representations was first introduced by Xu and Holland [110] using the basis representation of Hartmann [107]. I transferred their findings on the representation used in this work.

The symmetric, superradiant Dicke states can be easily constructed from the ground state

$$|l, m\rangle = \left( \frac{(l-m)!}{(2l)!(l+m)!} \right) J_{10}^{(m+l)} |l, -l\rangle \stackrel{l=N/2}{=} \left( \frac{(\frac{N}{2}-m)!}{N!(\frac{N}{2}+m)!} \right) J_{10}^{(m+\frac{N}{2})} |0\rangle_N, \quad (\text{B.4.1})$$

where  $|0\rangle_N$  is just the normal  $N$  two-level system ground state Eq. (4.1.4). The two-level system symmetrized Liouville space basis states are given by

$$\hat{\mathcal{P}}[n_{11}, n_{10}, n_{01}] = \mathcal{S}\sigma_{11}^{\otimes n_{11}}\sigma_{10}^{\otimes n_{10}}\sigma_{01}^{\otimes n_{01}}\sigma_{00}^{\otimes n_{00}}. \quad (\text{B.4.2})$$

The ground state projector is

$$|0\rangle_N\langle 0|_N = \hat{\mathcal{P}}[0, 0, 0] = \sigma_{00}^{\otimes N}. \quad (\text{B.4.3})$$

Using these expressions we can define arbitrary Liouville space basis states based on the *symmetric, superradiant* Dicke states

$$|\frac{N}{2}, m\rangle\langle \frac{N}{2}, n| = \left( \frac{(\frac{N}{2}-m)!}{N!(\frac{N}{2}+m)!} \cdot \frac{(\frac{N}{2}-n)!}{N!(\frac{N}{2}+n)!} \right) J_{10}^{(m+\frac{N}{2})}\hat{\mathcal{P}}[0, 0, 0]J_{01}^{(n+\frac{N}{2})}. \quad (\text{B.4.4})$$

This complicated looking expression greatly simplifies when looking at the diagonal entries  $|\frac{N}{2}, m\rangle\langle\frac{N}{2}, m|$ , with  $m = n - N/2$

$$|\frac{N}{2}, n - \frac{N}{2}\rangle\langle\frac{N}{2}, n - \frac{N}{2}| = \binom{N}{n}^{-1} \sum_{k=0}^{max} \hat{\mathcal{P}}[n - k, k, k], \quad max = min(n, N - n). \quad (\text{B.4.5})$$

Explicitly writing this down for e.g.  $N = 4$  results in

$$\begin{aligned} |2, -2\rangle\langle 2, -2| &= \frac{1}{1} \hat{\mathcal{P}}[0, 0, 0], \\ |2, -1\rangle\langle 2, -1| &= \frac{1}{4}(\hat{\mathcal{P}}[1, 0, 0] + \hat{\mathcal{P}}[0, 1, 1]), \\ |2, 0\rangle\langle 2, 0| &= \frac{1}{6}(\hat{\mathcal{P}}[2, 0, 0] + \hat{\mathcal{P}}[1, 1, 1] + \hat{\mathcal{P}}[0, 2, 2]), \\ |2, 1\rangle\langle 2, 1| &= \frac{1}{4}(\hat{\mathcal{P}}[3, 0, 0] + \hat{\mathcal{P}}[2, 1, 1]), \\ |2, 2\rangle\langle 2, 2| &= \frac{1}{1} \hat{\mathcal{P}}[4, 0, 0]. \end{aligned} \quad (\text{B.4.6})$$

Thus the projectors onto the superradiant states are just simple sums over the symmetrized basis states, normalized with an inverse binomial. Since the inclusion of individual decay and dephasing breaks the  $J^2$  symmetry, the symmetric Dicke subspace is not sufficient, i.e. the system may populate subradiant subspaces ( $l < N/2$ ). In order to construct a representation of the other  $l$  subspaces it suffices to have a single state in the respective subspace, since all other states can again be constructed by applying the raising and lowering operators, see Eq. (B.4.4) and (4.1.13). Dicke states are permutation symmetric states, the superradiant Dicke projectors were found to have a simple representation in the  $\hat{\mathcal{P}}$  representation. Therefore the other Dicke projectors  $|l, m\rangle\langle l, m|$  should be expressible as linear superposition of symmetrized Liouville space states too:

$$|l, n - l\rangle\langle l, n - l| = a_0(l, n)\hat{\mathcal{P}}[n, 0, 0] + a_1(l, n)\hat{\mathcal{P}}[n - 1, 1, 1] + \dots \quad (\text{B.4.7})$$

The difficulty then lies in finding the coefficients  $a_k(l, n)$ . This can be done by looking at the Hilbert space identity [110]

$$\sum_{l, n} D_l |l, n - l\rangle\langle l, n - l| \stackrel{!}{=} \sum_n \hat{\mathcal{P}}[n, 0, 0], \quad (\text{B.4.8})$$

where the degeneracy  $D_l$  of the Dicke states has to be included, Eq. (4.1.18). Hence all elements  $\hat{\mathcal{P}}[n - k, k, k]$ , with  $k \neq 0$  have to cancel out. The  $\hat{\mathcal{P}}[n - k, k, k]$  only enter the expressions of Dicke state projectors of matching excitation, therefore they have to cancel when summing the Dicke projectors over all matching excitations:

$$\sum_l D_l |l, n - l\rangle\langle l, n - l| \stackrel{!}{=} \hat{\mathcal{P}}[n, 0, 0]. \quad (\text{B.4.9})$$

With this we can construct the  $l = 1$  subspace of the  $N = 4$  example above: The ground state projector in the  $l = 1$  subspace is  $|1, -1\rangle\langle 1, -1|$  and from Eq. (B.4.8) follows

$$|2, -1\rangle\langle 2, -1| + D_1 |1, -1\rangle\langle 1, -1| = \hat{\mathcal{P}}[1, 0, 0], \quad (\text{B.4.10})$$

since these Dicke projectors are the only ones with a single excitation. It follows that

$$\begin{aligned} D_1 |1, -1\rangle\langle 1, -1| &= \hat{\mathcal{P}}[1, 0, 0] - |2, -1\rangle\langle 2, -1| \\ &= \frac{1}{4}(3\hat{\mathcal{P}}[1, 0, 0] - \hat{\mathcal{P}}[0, 1, 1]). \end{aligned} \quad (\text{B.4.11})$$

From this projector the whole  $l = 1$  Liouville subspace can be constructed by applying the raising operators from the left and the right. Further computing the  $l = 0$  subspace is done by

$$|2, 0\rangle\langle 2, 0| + D_1|1, 0\rangle\langle 1, 0| + D_0|0, 0\rangle\langle 0, 0| = \hat{\mathcal{P}}[2, 0, 0]. \quad (\text{B.4.12})$$

Since this is a single (albeit degenerate) state, there is no need to apply raising operators here. All Dicke state projectors for  $N = 4$  are thus given by Eq. (B.4.6) and

$$\begin{aligned} D_1|1, -1\rangle\langle 1, -1| &= \frac{1}{4}(3\hat{\mathcal{P}}[1, 0, 0] - \hat{\mathcal{P}}[0, 1, 1]), \\ D_1|1, 0\rangle\langle 1, 0| &= \frac{1}{2}(\hat{\mathcal{P}}[2, 0, 0] - \hat{\mathcal{P}}[0, 2, 2]), \\ D_1|1, 1\rangle\langle 1, 1| &= \frac{1}{4}(3\hat{\mathcal{P}}[3, 0, 0] - \hat{\mathcal{P}}[2, 1, 1]), \\ D_0|0, 0\rangle\langle 0, 0| &= \frac{1}{6}(2\hat{\mathcal{P}}[2, 0, 0] + 2\hat{\mathcal{P}}[1, 1, 1] - \hat{\mathcal{P}}[0, 2, 2]). \end{aligned} \quad (\text{B.4.13})$$

Hence the subradiant Dicke state projectors are given by more complicated, partially antisymmetric superpositions of symmetrized Liouville space states  $\hat{\mathcal{P}}$ . The values of the degeneracies  $D_l$  can be computed (Eq. (4.1.18)), but it is unimportant here, since the actions of the permutation symmetric master equation do not discriminate between different degenerate Dicke states.

Interactions with the environment destroy entanglement and Dicke states are entangled states. With this in mind it is illustrative to look at the action of e.g. the pure dephasing Liouvillian Eq. (5.3.25) on a superradiant projector Eq. (B.4.5)

$$\partial_t \left| \left\langle \frac{N}{2}, n - \frac{N}{2} \right\rangle \left\langle \frac{N}{2}, n - \frac{N}{2} \right| \right\rangle_{\mathcal{D}_{pd}} \propto -2\gamma' \sum_{k=0}^m k \mathcal{P}[n - k, k, k]. \quad (\text{B.4.14})$$

It becomes clear that the nondiagonal contributions to the Dicke state population are affected by dephasing. This constitutes clear view on how the entanglement of a Dicke state is suppressed in the presence of environmental interactions. Different contributions to the entanglement decay on different time scales, just depending on how far away from the main diagonal the corresponding density matrix entry is. The decay rate is  $2k\gamma'$ , where  $2k$  is the number specifying how far away from the main diagonal the entry is.

The representation of the density matrix in the Dicke bases outlined in this section is block-diagonal

$$\rho = \begin{pmatrix} \rho_{l=N/2} & 0 & 0 & \dots \\ 0 & \rho_{N/2-1} & 0 & \dots \\ 0 & 0 & \rho_{N/2-2} & \dots \\ \vdots & \vdots & \vdots & \ddots \end{pmatrix}, \quad (\text{B.4.15})$$

where each subblock has dimension  $(2l + 1)^2$ .

### B.4.2 Multi-level systems

Here the block diagonal representation for multi-level systems is outlined, the following discussion is not a complete proof, but it becomes apparent that this property should hold for multi-level systems:

Multiplets of  $su(N)$  are best represented by Young tableaux: For each multi-level system one draws a box

$$\square \quad (\text{B.4.16})$$



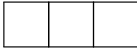
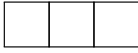
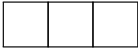
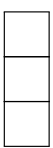
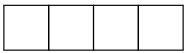
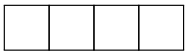
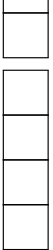
needs to be shown is that the squares of these numbers added up are equal to the number of possible symmetrized Liouville space states: Since all the states, multiplet states and symmetrized Liouville space states are orthogonal, it means that if we have the same number of elements they span a space of equal size, where the dimension of that space is equal to the number of basis elements. Furthermore, the multiplet states form a basis in Hilbert space and a basis transform is given by a orthogonal matrix  $Q$  with the property

$$Q^\dagger Q = I \tag{B.4.23}$$

where  $I$  is the identity: It follows

$$Q^\dagger I Q = I, \tag{B.4.24}$$

meaning that the Hilbert space identity is invariant to the basis transform. This is equivalent to the condition of the last section Eq. (B.4.8) and implies that the projectors on the multiplet states and the symmetrized Liouville space states live in the same space and therefore if the dimension of both representations is identical then they are completely equivalent. Therefore, in each multiplet subspace of dimension  $u$  we can construct  $u^2$  Liouville basis states and if the sum over all these Liouville space states is equal to the number of symmetrized Liouville space basis states these representations are equivalent and the density matrix can in fact be expressed in block diagonal form of dimension Eq. (B.4.20), which is at most polynomial in  $N$ .

$N$	$su(2)$	$u^2$	$su(3)$	$u^2$	$su(4)$	$u^2$
1	 $\rightarrow 2$	4	 $\rightarrow 3$	9	 $\rightarrow 4$	16
2	 $\rightarrow 3$	9	 $\rightarrow 6$	36	 $\rightarrow 10$	100
	 $\rightarrow 1$	1	 $\rightarrow 3$	9	 $\rightarrow 6$	36
3	 $\rightarrow 4$	16	 $\rightarrow 10$	100	 $\rightarrow 20$	400
	 $\rightarrow 2$	4	 $\rightarrow 8$	64	 $\rightarrow 20$	400
				 $\rightarrow 1$	1	 $\rightarrow 4 \ 16$
4	 $\rightarrow 5$	25	 $\rightarrow 15$	225	 $\rightarrow 35$	1225
	 $\rightarrow 3$	9	 $\rightarrow 15$	225	 $\rightarrow 45$	2025
	 $\rightarrow 1$	1	 $\rightarrow 6$	36	 $\rightarrow 20$	400
			 $\rightarrow 3$	9	 $\rightarrow 15$	225
					 $\rightarrow 1$	1
	$D_s$	sum	$D_s$	sum	$D_s$	sum
1	4	4	9	9	16	16
2	10	10	45	45	136	136
3	20	20	165	165	816	816
4	35	35	495	495	3876	3876

**Table B.1 – Young tableaux:** The number of boxes is equal to the number of multi-level systems. The numbers behind the arrows are equal to the number of different states that are represented by such a Young tableau, i.e. the dimension of the multiplet subspace  $u$ .  $u^2$  corresponds to the dimension of the Liouville space spanned by these multiplets. Apparently the sum over these Liouville blocks is equal to the number of symmetrized basis states  $D_s$  also for  $su(> 2)$ . For  $su(2)$  these numbers correspond to the dimensions of the Dicke subspaces.



## C Spin squeezing inequalities

In Chapter 7 the spin squeezing inequalities (SSI) introduced by Tóth *et al.* [79, 80] are employed as an entanglement measure. Tóth *et al.* derived seven inequalities that are satisfied by any separable  $N$ -qubit state, hence the violation of any of these inequalities implies entanglement. Four of the seven inequalities detect entanglement in our setup, but the violation of two equations is equivalent: the coherent driving field introduces a time dependent phase factor caused by local unitary transformations which do not affect entanglement [208] but cause the violation of the SSI to oscillate back and forth between the two associated inequalities (between (C.0.1), (C.0.2) and between (C.0.3), (C.0.4)). The four SSI that detect entanglement in our setup are

$$\langle J_y^2 \rangle + \langle J_z^2 \rangle - \frac{N}{2} - (N-1)(\Delta J_x)^2 \leq 0, \quad (\text{C.0.1})$$

$$\langle J_x^2 \rangle + \langle J_z^2 \rangle - \frac{N}{2} - (N-1)(\Delta J_y)^2 \leq 0, \quad (\text{C.0.2})$$

$$\langle J_x^2 \rangle + \frac{N(N-2)}{4} - (N-1) \left[ (\Delta J_y)^2 + (\Delta J_z)^2 \right] \leq 0, \quad (\text{C.0.3})$$

$$\langle J_y^2 \rangle + \frac{N(N-2)}{4} - (N-1) \left[ (\Delta J_x)^2 + (\Delta J_z)^2 \right] \leq 0, \quad (\text{C.0.4})$$

where the variances are defined as  $(\Delta A)^2 = \langle A^2 \rangle - \langle A \rangle^2$ . In order to simplify the discussion we only show one SSI in our plot:

$$\underbrace{\langle J_y^2 \rangle + \langle J_z^2 \rangle - \frac{N}{2} - (N-1)(\Delta J_x)^2}_{=:A} \leq 0, \quad (\text{C.0.5})$$

hence  $A$  is the quantity plotted in Fig. 5 (b). Since strictly speaking the quantities  $\langle J_y^2 \rangle$  and  $\langle J_x^2 \rangle$  do not have a defined steady state, but oscillate with the phase factor mentioned above, we set  $t = 0$  and thus set the phase factor to unity throughout the plot in Fig. 5 (d). Since, as stated above, the local unitary transformations causing the oscillation do not affect the entanglement,

this is a valid approach. In the following the local unitary transformation is explained:

On resonance the Hamiltonian of the system in a frame rotating at the external laser frequency  $\omega_l$  reads

$$H = g(J_{10}b + J_{01}b^\dagger) + E(J_{10} + J_{01}). \quad (\text{C.0.6})$$

The corresponding master equation for the setup considered in this work is

$$\partial_t \rho = \mathcal{L}\rho = \frac{i}{\hbar}[\rho, H] + \mathcal{D}_{de} + \mathcal{D}_{pd} + \mathcal{D}_{ph}, \quad (\text{C.0.7})$$

where  $\rho$  is the rotating frame density matrix. The transformation between normal frame and rotating frame is given by

$$\rho_n = e^{-\frac{i}{\hbar}H_{\text{rot}}t} \rho e^{\frac{i}{\hbar}H_{\text{rot}}t}, \quad (\text{C.0.8})$$

with the normal frame density matrix  $\rho_n$  and the Hamiltonian

$$H_{\text{rot}} = \hbar\omega_l(b^\dagger b + J_{11}). \quad (\text{C.0.9})$$

The Hamiltonian acts locally on the density matrix, in the sense that each TLS experiences an individual unitary transformation, i.e.

$$e^{J_{11}} = \prod_{i=1}^N e^{\sigma_{i1}^i}. \quad (\text{C.0.10})$$

Such a transformation leaves the quantum correlations invariant [208]. Nonetheless some quantities arising in the SSI experience a time dependency through this transformation. In fact only the rotating frame density matrix has a stationary steady state, the normal frame density matrix  $\rho_n$  exhibits an oscillating steady state, where diagonal entries are stationary and offdiagonal entries oscillate with a phase of multiples of  $\omega_l$ .

The quantities  $\langle J_{x,y}^2 \rangle$  and  $(\Delta J_{x,y})^2$  are explicitly time dependent in the normal frame. By adding Eqs. (C.0.1), (C.0.2) and (C.0.3), (C.0.4) respectively, one can derive time independent inequalities, which however do not detect entanglement in our setup.

## C.1 General remarks

The spin-squeezing inequalities provide a possibility of detecting entanglement without needing to perform a density matrix diagonalization [79, 80]. However they only provide a qualitative answer and are thus an entanglement witness. Since the density operator of a  $N$ -TLS system for  $N > 4$  is practically impossible to measure experimentally, the use of entanglement witnesses for larger systems should also be regarded the proper theoretical choice.

A (possibly mixed) state  $\rho$  of a  $N$ -TLS system is said to be entangled if it cannot be written as [80]

$$\rho = \sum_n p_n \rho_n^{(1)} \otimes \rho_n^{(2)} \otimes \cdots \otimes \rho_n^{(N)}, \quad (\text{C.1.1})$$

with

$$\sum_n p_n = 1, \quad (\text{C.1.2})$$

where the  $\rho_n^{(i)}$  are (not necessarily pure) single TLS density matrices for TLS  $i$ .

I use the optimal spin-squeezing inequalities introduced by Tóth et al. [79, 80]. These inequalities are inequalities in the collective spin operator expectation values  $\langle J_k \rangle$  and  $\langle J_k^2 \rangle$  with  $k \in \{x, y, z\}$  or rather in  $\langle J_k^2 \rangle$  and the spin variances

$$(\Delta J_m)^2 = \langle J_m^2 \rangle - \langle J_m \rangle^2. \quad (\text{C.1.3})$$

The full set of inequalities is given by

$$\langle J_x^2 \rangle + \langle J_y^2 \rangle + \langle J_z^2 \rangle \leq \frac{N(N+2)}{4} \quad (\text{C.1.4a})$$

$$(\Delta J_x)^2 + (\Delta J_y)^2 + (\Delta J_z)^2 \geq \frac{N}{2} \quad (\text{C.1.4b})$$

$$(N-1)(\Delta J_k)^2 + \frac{N}{2} - \langle J_l^2 \rangle - \langle J_m^2 \rangle \geq 0 \quad (\text{C.1.4c})$$

$$(N-1)[(\Delta J_k)^2 + (\Delta J_l)^2] - \frac{N(N-2)}{4} - \langle J_m^2 \rangle \geq 0 \quad (\text{C.1.4d})$$

and they hold for separable states as in Eq. (C.1.1). In the last two inequalities  $k, l, m$  refer to any possible permutation of  $x, y, z$ .

These inequalities are optimal in the sense that they can detect all entanglement that can be detected with knowledge of  $\langle J_k \rangle$  and  $\langle J_k^2 \rangle$  or  $\langle J_k^2 \rangle$  and  $(\Delta J_m)^2$ . (Have not proven this myself thus far).

The authors claim that (C.1.4a) is valid for all quantum states and it is in fact identical to the definition of the total spin operator/quantum number of the Dicke basis states. In the following I will provide a proof of inequalities (C.1.4b),(C.1.4c),(C.1.4d), following Ref. 80.

## C.2 Definitions and necessary inequalities

In this section all equalities and inequalities needed for the proof are presented.

### Single spins

In order to derive inequalities for collective spin operator expectation values, it is useful to first look at expectation values for single spins. Please note that since the Pauli matrices are hermitian all expectation values of Pauli matrices are real.

#### Observation:

Defining  $\langle \sigma_x^i \rangle = x_i$ ,  $\langle \sigma_y^i \rangle = y_i$  and  $\langle \sigma_z^i \rangle = z_i$  we have for single TLS states  $\rho^{(i)}$

$$x_i^2 + y_i^2 + z_i^2 \leq 1, \quad (\text{C.2.1})$$

where the equal sign holds for pure states. This is just the definition of the Bloch sphere [28].

#### Observation:

Here the  $x, y, z$  spin matrices are used. They have the useful property that

$$\sigma_k^2 = 1, \quad \text{for } k = x, y, z. \quad (\text{C.2.2})$$

A direct consequence is that

$$\langle (\sigma_x^i)^2 \rangle = \langle (\sigma_y^i)^2 \rangle = \langle (\sigma_z^i)^2 \rangle = 1, \quad (\text{C.2.3})$$

for all states.

#### Observation:

Another important relation is

$$\left( \sum_i k_i \right)^2 \leq N \sum_i k_i^2, \quad (\text{C.2.4})$$

where  $k \in \{x, y, z\}$ .

**Proof:**

$$\left(\sum_i k_i\right)^2 = \sum_i k_i^2 + \sum_{i \neq j} k_i k_j \leq \sum_i k_i^2 + \frac{1}{2} \underbrace{\sum_{i \neq j} (k_i^2 + k_j^2)}_{2(N-1) \sum_i k_i^2} = N \sum_i k_i^2,$$

where in the second step the binomial inequality  $ab \leq (a^2 + b^2)/2$  is used, which is easily derived from the positivity of the second binomial formula, i.e.  $(a - b)^2 \geq 0$ .

### Normal expectation values

**Observation:**

Operator expectation values  $\langle A \rangle$  are convex in a state  $\rho = p\rho_1 + (1 - p)\rho_2$ , i.e.

$$\langle A \rangle_\rho = p\langle A \rangle_{\rho_1} + (1 - p)\langle A \rangle_{\rho_2}, \quad (\text{C.2.5})$$

which is easily seen by expanding  $\langle \dots \rangle = \text{tr}[\dots \rho]$ .

### Variances

**Observation:**

The variances of hermitian operators  $(\Delta A)^2$  are concave in a state  $\rho = p\rho_1 + (1 - p)\rho_2$ , i.e.

$$(\Delta A)_\rho^2 \geq p(\Delta A)_{\rho_1}^2 + (1 - p)(\Delta A)_{\rho_2}^2, \quad (\text{C.2.6})$$

**Proof:**

Starting by inserting the definition

$$\begin{aligned} (\Delta A)_\rho^2 &= \langle A^2 \rangle_\rho - \langle A \rangle_\rho^2 \\ &= \text{tr} \left[ A^2(p\rho_1 + (1 - p)\rho_2) \right] - \text{tr} \left[ A(p\rho_1 + (1 - p)\rho_2) \right]^2 \\ &= p\langle A^2 \rangle_{\rho_1} + (1 - p)\langle A^2 \rangle_{\rho_2} - \left( p\langle A \rangle_{\rho_1} + (1 - p)\langle A \rangle_{\rho_2} \right)^2 \\ &\stackrel{?}{\geq} p\langle A^2 \rangle_{\rho_1} + (1 - p)\langle A^2 \rangle_{\rho_2} - p\langle A \rangle_{\rho_1}^2 - (1 - p)\langle A \rangle_{\rho_2}^2. \end{aligned}$$

Hence we need to show that for three real numbers  $a, b$  and  $p$ , with  $p \in [0, 1]$  the inequality

$$(pa + (1 - p)b)^2 \leq pa^2 + (1 - p)b^2$$

holds. We start by expanding the left hand side

$$\begin{aligned} p^2 a^2 + 2p(1 - p)ab + (1 - p)^2 b^2 &\leq pa^2 + (1 - p)b^2 \\ p(p - 1)a^2 + 2p(1 - p)ab + p(p - 1)b^2 &\leq 0 \\ \underbrace{(-1)}_{<0} \cdot \underbrace{p(1 - p)}_{\geq 0} \cdot \underbrace{(a - b)^2}_{\geq 0} &\leq 0. \end{aligned}$$

q.e.d.

**Observation:**

For product states  $\rho = \rho(1) \otimes \rho(2) \otimes \dots \otimes \rho(N)$  the variance can be written as

$$(\Delta J_k)^2 = \frac{N}{4} - \frac{1}{4} \sum_i k_i^2, \quad (\text{C.2.7})$$

with  $k \in \{x, y, z\}$  and omitting the subscript  $\rho$ .

**Proof:**

By inserting the definitions

$$\begin{aligned} (\Delta J_k)^2 &= \frac{1}{4} \left( \underbrace{\sum_i \langle (\sigma_k^i)^2 \rangle}_{=\sum_i 1=N} + \underbrace{\sum_{i \neq j} \langle \sigma_k^i \sigma_k^j \rangle}_{=\sum_i \langle \sigma_k^i \rangle \langle \sigma_k^j \rangle = \sum_i k_i k_j} - \sum_i k_i^2 - \sum_{i \neq j} k_i k_j \right) \\ &= \frac{N}{4} - \frac{1}{4} \sum_i k_i^2 \end{aligned}$$

The terms  $\langle \sigma_k^i \sigma_k^j \rangle$  factorize precisely because  $\rho$  is a product state and then the  $\sum_{i \neq j}$  terms cancel each other. q.e.d.

### C.3 Proofs

Since the variance is concave (Observation (C.2.6)) and the observables convex (Observation (C.2.5)) it suffices to show that the inequalities (C.1.4b),(C.1.4c) and (C.1.4d) hold for product states: let  $\rho$  be a separable state, i.e.

$$\rho = \sum_n p_n \rho_n^{(1)} \otimes \rho_n^{(2)} \otimes \cdots \otimes \rho_n^{(N)}, \quad (\text{C.3.1})$$

then for e.g. for inequality (C.1.4b)

$$\begin{aligned} (\Delta J_x)_\rho^2 + (\Delta J_y)_\rho^2 + (\Delta J_z)_\rho^2 &\geq \sum_n p_n \left( (\Delta J_x)_{\rho_n}^2 + (\Delta J_y)_{\rho_n}^2 + (\Delta J_z)_{\rho_n}^2 \right), \quad \text{using Obs. (C.2.6)} \\ &\geq \sum_n p_n \frac{N}{2}, \quad \text{inserting Eq. (C.1.4b)} \\ &= \frac{N}{2}, \end{aligned}$$

i.e. if the inequality holds for product states then it also holds for arbitrary mixtures of product (separable) states.

**Inequality Eq. (C.1.4b)**

Using Observation (C.2.7)

$$\begin{aligned} (\Delta J_x)^2 + (\Delta J_y)^2 + (\Delta J_z)^2 &= \frac{3N}{4} - \frac{1}{4} \sum_i (x_i^2 + y_i^2 + z_i^2) \\ &\geq \frac{3N}{4} - \frac{1}{4} \sum_i 1 \\ &= \frac{N}{2}, \end{aligned}$$

where we have used Observation (C.2.1) in the second step. q.e.d.

**Inequality Eq. (C.1.4c)**

Inserting the definitions and using Observation (C.2.7)

$$\begin{aligned}
& (N-1)(\Delta J_k)^2 + \frac{N}{2} - \langle J_l^2 \rangle - \langle J_m^2 \rangle \\
&= (N-1)\left(\frac{N}{4} - \frac{1}{4} \sum_i k_i^2\right) + \frac{N}{2} - \underbrace{\frac{1}{4} \sum_i (\langle (\sigma_i^i)^2 \rangle + \langle (\sigma_m^i)^2 \rangle)}_{=\frac{N}{2}} - \frac{1}{4} \sum_{i \neq j} \underbrace{(\langle \sigma_i^i \sigma_l^j \rangle + \langle \sigma_m^i \sigma_m^j \rangle)}_{l_i l_j + m_i m_j} \\
&= (N-1)\left(\frac{N}{4} - \frac{1}{4} \sum_i k_i^2\right) - \frac{1}{4} \left[ \left(\sum_i l_i\right)^2 + \left(\sum_i m_i\right)^2 \right] + \frac{1}{4} \sum_i (l_i^2 + m_i^2) \\
&\geq (N-1)\left(\frac{N}{4} - \frac{1}{4} \sum_i k_i^2\right) - \frac{N}{4} \left[ \sum_i l_i^2 + \sum_i m_i^2 \right] + \frac{1}{4} \sum_i (l_i^2 + m_i^2), \quad \text{Obs. (C.2.4)} \\
&= \frac{N-1}{4} \left( N - \sum_i (k_i^2 + l_i^2 + m_i^2) \right) \\
&= \frac{N-1}{4} \left( \sum_i (1 - k_i^2 - l_i^2 - m_i^2) \right) \\
&\geq 0, \quad \text{Obs. (C.2.1)}
\end{aligned}$$

q.e.d.

**Inequality Eq. (C.1.4d)**

The proof for Eq. (C.1.4d) is very similar to Eq. (C.1.4c): Inserting the definitions and using Observation (C.2.7)

$$\begin{aligned}
& (N-1)[(\Delta J_k)^2 + (\Delta J_l)^2] - \frac{N(N-2)}{4} - \langle J_m^2 \rangle \\
&= (N-1)\left[\frac{N}{2} - \frac{1}{4} \sum_i (k_i^2 + l_i^2)\right] - \frac{N(N-2)}{4} - \frac{N}{4} - \frac{1}{4} \sum_{i \neq j} m_i m_j \\
&= (N-1)\left[\frac{N}{4} - \frac{1}{4} \sum_i (k_i^2 + l_i^2)\right] - \frac{1}{4} \left(\sum_i m_i\right)^2 + \frac{1}{4} \sum_i m_i^2 \\
&\geq (N-1)\left[\frac{N}{4} - \frac{1}{4} \sum_i (k_i^2 + l_i^2)\right] - \frac{N-1}{4} \sum_i m_i^2, \quad \text{Obs. (C.2.4)} \\
&= \frac{N-1}{4} \sum_i (1 - k_i^2 - l_i^2 - m_i^2) \\
&\geq 0, \quad \text{Obs. (C.2.1)}
\end{aligned}$$

q.e.d.

**C.4 Comments**

Following Tóth et al. [79, 80] we have shown that the spin squeezing inequalities hold for separable states (mixtures of product states). That implies that if a state violates these inequalities it cannot be a separable state and is thus entangled. Hence the spin squeezing inequalities serve as an entanglement witness.

## C.5 Different representation

As stated above, the preferred choice of (collective) spin operators is the  $J_{kl}$  representation since it is more useful for multi-level systems. The spin squeezing inequalities are formulated using the  $x, y, z$  definition for two-level systems. In order to numerically evaluate the spin squeezing inequalities either all necessary observables occurring in Eqs. (C.1.4) need to be implemented or one rewrites the inequalities in a form that is more accessible to the choice of collective operators in this thesis. Here a middle way is chosen, the  $J_x$  and  $J_y$  by  $J_{01}$  and  $J_{10}$  are replaced and  $J_z$  is kept in the expressions since there is a ready made `Observable` setup function for this in PsiQuaSP.

The spin squeezing inequalities in terms of the  $J_{kl}$  representation: The following simple replacement can be seen directly from the definitions

$$\begin{aligned} J_x &= \frac{1}{2}(J_{10} + J_{01}), \\ J_y &= \frac{i}{2}(J_{10} - J_{01}), \end{aligned} \quad (\text{C.5.1})$$

and for the sake of completeness

$$J_z = \frac{1}{2}(J_{11} - J_{00}).$$

Keeping the  $J_z$  operator the spin squeezing inequalities now using  $J_{01}$ ,  $J_{10}$  and  $J_z$  become for Eqs. (C.1.4a) and (C.1.4b)

$$\frac{1}{2}\langle J_{10}J_{01} \rangle + \frac{1}{2}\langle J_{01}J_{10} \rangle + \langle J_z^2 \rangle \leq \frac{N(N+2)}{4} \quad (\text{C.5.2a})$$

$$\frac{1}{2}(\langle J_{10}J_{01} \rangle - \langle J_{10} \rangle \langle J_{01} \rangle) + \frac{1}{2}(\langle J_{01}J_{10} \rangle - \langle J_{10} \rangle \langle J_{01} \rangle) + \langle J_z^2 \rangle - \langle J_z \rangle^2 \geq \frac{N}{2} \quad (\text{C.5.2b})$$

$$(N-1)\left(\langle J_z^2 \rangle - \langle J_z \rangle^2\right) + \frac{N}{2} - \frac{1}{2}\langle J_{10}J_{01} \rangle - \frac{1}{2}(\langle J_{01}J_{10} \rangle) \geq 0 \quad (\text{C.5.2ca})$$

$$\dots \quad (\text{C.5.2cb})$$

$$\frac{N-1}{2}[\langle J_{10}J_{01} \rangle + \langle J_{01}J_{10} \rangle - 2\langle J_{10} \rangle \langle J_{01} \rangle] - \frac{N(N-2)}{4} - \langle J_m^2 \rangle \geq 0 \quad (\text{C.5.2da})$$

$$\dots \quad (\text{C.5.2db})$$



# D Equations of motion for the laser examples

## D.1 Three-level systems

We start by giving the equations of motion associated to (5.4.23)

$$\dot{\rho}_I = \frac{i}{\hbar}[\rho_I, H_{10} + H_{20}] + \mathcal{D}[\sigma_{12}^k]\rho_I + \mathcal{D}[\sigma_{01}^k]\rho_I, \quad (\text{D.1.1})$$

which are given in terms the elements

$$\mathcal{P}[n_{22}, n_{21}, n_{20}, n_{12}, n_{11}, n_{10}, n_{02}, n_{01}; k, p], \quad (\text{D.1.2})$$

i.e. has the full complexity of a many three-level system problem, since all polarization degrees of freedom are coupled to density degrees of freedom, cf. Fig. 5.7. We will use the RWA for reasons of brevity. The contribution of the Hamiltonian

$$H_{10}^{\text{RWA}} = \hbar g_{10} \sum_k (a^\dagger \sigma_{01}^k + a \sigma_{10}^k) \quad (\text{D.1.3})$$

is given by

$$\begin{aligned}
& \partial_t \mathcal{P}[n_{22}, n_{21}, n_{20}, n_{12}, n_{11}, n_{10}, n_{02}, n_{01}; k, p] \Big|_{H_{10}^{\text{RWA}}} \\
= & ig_{10} \left[ (n_{10} + 1) \sqrt{k} \quad \mathcal{P}[\dots n_{10} + 1 \dots; k - 1, p] \right. \\
& + (n_{11} + 1) \sqrt{k} \quad \mathcal{P}[\dots n_{11} + 1 \dots n_{01} - 1; k - 1, p] \\
& + (n_{12} + 1) \sqrt{k} \quad \mathcal{P}[\dots n_{12} + 1 \dots n_{02} - 1 \dots; k - 1, p] \\
& + (n_{00} + 1) \sqrt{k+1} \quad \mathcal{P}[\dots n_{10} - 1 \dots; k + 1, p] \\
& + (n_{01} + 1) \sqrt{k+1} \quad \mathcal{P}[\dots n_{11} - 1 \dots n_{01} + 1; k + 1, p] \\
& + (n_{02} + 1) \sqrt{k+1} \quad \mathcal{P}[\dots n_{12} - 1 \dots n_{02} + 1 \dots; k + 1, p] \\
& - (n_{00} + 1) \sqrt{p+1} \quad \mathcal{P}[\dots n_{01} - 1; k, p + 1] \\
& - (n_{10} + 1) \sqrt{p+1} \quad \mathcal{P}[\dots n_{11} - 1, n_{10} + 1 \dots; k, p + 1] \\
& - (n_{20} + 1) \sqrt{p+1} \quad \mathcal{P}[\dots n_{21} - 1, n_{20} + 1 \dots; k, p + 1] \\
& - (n_{01} + 1) \sqrt{p} \quad \mathcal{P}[\dots n_{01} + 1; k, p - 1] \\
& - (n_{11} + 1) \sqrt{p} \quad \mathcal{P}[\dots n_{11} + 1, n_{10} - 1 \dots; k, p - 1] \\
& \left. - (n_{21} + 1) \sqrt{p} \quad \mathcal{P}[\dots n_{21} + 1, n_{20} - 1 \dots; k, p - 1] \right].
\end{aligned} \tag{D.1.4}$$

Here the pumping Hamiltonian will be assumed to be a semiclassical coherent pumping Hamiltonian, again using RWA

$$H_{20}^{\text{RWA}} = \hbar\mu \sum_k (E_t^* \sigma_{02}^k + E_t \sigma_{20}^k), \tag{D.1.5}$$

with

$$E_t = E_0 e^{-i\omega_{ext}t}, \tag{D.1.6}$$

where  $\omega_{ext}$  is the frequency and  $E_0$  the amplitude of the semiclassical driving field. This contribution is given by

$$\begin{aligned}
& \partial_t \mathcal{P}[n_{22}, n_{21}, n_{20}, n_{12}, n_{11}, n_{10}, n_{02}, n_{01}; k, p] \Big|_{H_{20}^{\text{RWA}}} \\
= & i\mu E_0 \left[ (n_{20} + 1) \mathcal{P}[\dots n_{20} + 1 \dots; k, p] \right. \\
& + (n_{21} + 1) \mathcal{P}[\dots n_{21} + 1 \dots n_{01} - 1; k, p] \\
& + (n_{22} + 1) \mathcal{P}[\dots n_{22} + 1 \dots n_{02} - 1 \dots; k, p] \\
& + (n_{00} + 1) \mathcal{P}[\dots n_{20} - 1 \dots; k, p] \\
& + (n_{01} + 1) \mathcal{P}[\dots n_{21} - 1 \dots n_{01} + 1; k, p] \\
& + (n_{02} + 1) \mathcal{P}[\dots n_{22} - 1 \dots n_{02} + 1 \dots; k, p] \\
& - (n_{00} + 1) \mathcal{P}[\dots n_{02} - 1 \dots; k, p] \\
& - (n_{10} + 1) \mathcal{P}[\dots n_{12} - 1 \dots n_{10} + 1 \dots; k, p] \\
& - (n_{20} + 1) \mathcal{P}[\dots n_{22} - 1 \dots n_{20} + 1 \dots; k, p] \\
& - (n_{02} + 1) \mathcal{P}[\dots n_{02} + 1 \dots; k, p] \\
& - (n_{12} + 1) \mathcal{P}[\dots n_{12} + 1 \dots n_{10} - 1 \dots; k, p] \\
& \left. - (n_{22} + 1) \mathcal{P}[n_{22} + 1 \dots n_{20} - 1 \dots; k, p] \right].
\end{aligned} \tag{D.1.7}$$

The two spontaneous emission contributions are

$$\begin{aligned}
& \partial_t \mathcal{P}[n_{22}, n_{21}, n_{20}, n_{12}, n_{11}, n_{10}, n_{02}, n_{01}; k, p] \Big|_{\mathcal{D}[\sigma_{12}^k]} \\
= & \frac{\gamma_{12}}{2} [2(n_{22} + 1)\mathcal{P}[n_{22} + 1 \dots n_{11} - 1 \dots; k, p] \\
& - (2n_{22} + n_{12} + n_{02} + n_{21} + n_{20})\mathcal{P}[\dots; k, p]]
\end{aligned} \tag{D.1.8}$$

and

$$\begin{aligned}
& \partial_t \mathcal{P}[n_{22}, n_{21}, n_{20}, n_{12}, n_{11}, n_{10}, n_{02}, n_{01}; k, p] \Big|_{\mathcal{D}[\sigma_{01}^k]} \\
= & \frac{\gamma_{01}}{2} [2(n_{11} + 1)\mathcal{P}[\dots n_{11} + 1 \dots; k, p] \\
& - (2n_{11} + n_{12} + n_{21} + n_{01} + n_{10})\mathcal{P}[\dots; k, p]]
\end{aligned} \tag{D.1.9}$$

The equations of motion for the second setup (5.4.25)

$$\begin{aligned}
\dot{\rho}_{II} = & \frac{i}{\hbar} [\rho_{II}, H_{10}] + \mathcal{D}[\sigma_{20}^k]\rho_{II} + \mathcal{D}[\sigma_{12}^k]\rho_{II} \\
& + \mathcal{D}[\sigma_{01}^k]\rho_{II}.
\end{aligned} \tag{D.1.10}$$

are given in terms of the elements

$$\mathcal{P}[n_{22}, n_{11}, n_{10}, n_{01}; k, p], \tag{D.1.11}$$

cf. Fig. 5.8. Again in the RWA, the contribution of the Hamiltonian  $H_{10}^{\text{RWA}}$  is given by

$$\begin{aligned}
& \partial_t \mathcal{P}[n_{22}, n_{11}, n_{10}, n_{01}; k, p] \Big|_{H_{10}^{\text{RWA}}} \\
= & ig_{10} [(n_{10} + 1) \sqrt{k} \mathcal{P}[\dots n_{10} + 1 \dots; k - 1, p] \\
& + (n_{11} + 1) \sqrt{k} \mathcal{P}[\dots n_{11} + 1 \dots n_{01} - 1; k - 1, p] \\
& + (n_{00} + 1) \sqrt{k + 1} \mathcal{P}[\dots n_{10} - 1 \dots; k + 1, p] \\
& + (n_{01} + 1) \sqrt{k + 1} \mathcal{P}[\dots n_{11} - 1 \dots n_{01} + 1; k + 1, p] \\
& - (n_{00} + 1) \sqrt{p + 1} \mathcal{P}[\dots n_{01} - 1; k, p + 1] \\
& - (n_{10} + 1) \sqrt{p + 1} \mathcal{P}[\dots n_{11} - 1, n_{10} + 1 \dots; k, p + 1] \\
& - (n_{01} + 1) \sqrt{p} \mathcal{P}[\dots n_{01} + 1; k, p - 1] \\
& - (n_{11} + 1) \sqrt{p} \mathcal{P}[\dots n_{11} + 1, n_{10} - 1 \dots; k, p - 1]].
\end{aligned} \tag{D.1.12}$$

The three dissipator contributions are

$$\begin{aligned}
& \partial_t \mathcal{P}[n_{22}, n_{11}, n_{10}, n_{01}; k, p] \Big|_{\mathcal{D}[\sigma_{20}^k]} \\
= & \frac{\gamma_{20}}{2} [2(n_{00} + 1)\mathcal{P}[n_{22} - 1 \dots; k, p] \\
& - (2n_{00} + n_{01} + n_{10})\mathcal{P}[\dots; k, p]],
\end{aligned} \tag{D.1.13}$$

$$\begin{aligned}
& \partial_t \mathcal{P}[n_{22}, n_{11}, n_{10}, n_{01}; k, p] \Big|_{\mathcal{D}[\sigma_{12}^k]} \\
= & \frac{\gamma_{12}}{2} [2(n_{22} + 1)\mathcal{P}[n_{22} + 1 \dots n_{11} - 1 \dots; k, p] \\
& - 2n_{22}\mathcal{P}[\dots; k, p]],
\end{aligned} \tag{D.1.14}$$

and

$$\begin{aligned}
& \partial_t \mathcal{P}[n_{22}, n_{11}, n_{10}, n_{01}; k, p] \Big|_{\mathcal{D}[\sigma_{01}^k]} \\
= & \frac{\gamma_{01}}{2} [2(n_{11} + 1) \mathcal{P}[\dots n_{11} + 1 \dots; k, p] \\
& - (2n_{11} + n_{01} + n_{10}) \mathcal{P}[\dots; k, p]]
\end{aligned} \tag{D.1.15}$$

## D.2 Four-level systems

The equations of motion for (5.4.29)

$$\begin{aligned}
\dot{\rho}_{III} = & \frac{i}{\hbar} [\rho_{III}, H_{30} + H_{21}] + \mathcal{D}[\sigma_{23}^k] \rho_{III} + \mathcal{D}[\sigma_{01}^k] \rho_{III} \\
& + \mathcal{D}[\sigma_{12}^k] \rho_{III},
\end{aligned} \tag{D.2.1}$$

are given in terms of the elements

$$\mathcal{P}[n_{33}, n_{30}, n_{22}, n_{21}, n_{12}, n_{11}, n_{03}; k, p], \tag{D.2.2}$$

cf. Fig 5.9. The contribution of the Hamiltonian

$$H_{21}^{\text{RWA}} = \hbar g_{21} \sum_k (a^\dagger \sigma_{12}^k + a \sigma_{21}^k) \tag{D.2.3}$$

is given by

$$\begin{aligned}
& \partial_t \mathcal{P}[n_{33}, n_{30}, n_{22}, n_{21}, n_{12}, n_{11}, n_{03}; k, p] \Big|_{H_{21}^{\text{RWA}}} \\
= & ig_{21} [ (n_{12} + 1) \sqrt{k+1} \mathcal{P}[\dots n_{22} - 1 \dots n_{12} + 1 \dots; k+1, p] \\
& + (n_{11} + 1) \sqrt{k+1} \mathcal{P}[\dots n_{21} - 1 \dots n_{11} + 1 \dots; k+1, p] \\
& + (n_{21} + 1) \sqrt{k} \mathcal{P}[\dots n_{21} + 1 \dots n_{11} - 1 \dots; k-1, p] \\
& + (n_{22} + 1) \sqrt{k} \mathcal{P}[\dots n_{22} + 1 \dots n_{12} - 1 \dots; k-1, p] \\
& - (n_{21} + 1) \sqrt{p+1} \mathcal{P}[\dots n_{22} - 1, n_{21} + 1 \dots; k, p+1] \\
& - (n_{11} + 1) \sqrt{p+1} \mathcal{P}[\dots n_{12} - 1, n_{11} + 1 \dots; k, p+1] \\
& - (n_{12} + 1) \sqrt{p} \mathcal{P}[\dots n_{12} + 1, n_{11} - 1 \dots; k, p-1] \\
& - (n_{22} + 1) \sqrt{p} \mathcal{P}[\dots n_{22} + 1, n_{21} - 1 \dots; k, p-1] ].
\end{aligned} \tag{D.2.4}$$

The contribution of the Hamiltonian

$$H_{30}^{\text{RWA}} = \hbar \mu \sum_k (E_t^* \sigma_{03}^k + E_t \sigma_{30}^k), \tag{D.2.5}$$

is given by

$$\begin{aligned}
& \partial_t \mathcal{P}[n_{33}, n_{30}, n_{22}, n_{21}, n_{12}, n_{11}, n_{03}; k, p] \Big|_{H_{30}^{\text{RWA}}} \\
= & i\mu E_0 \left[ (n_{03} + 1) \mathcal{P}[\dots n_{33} - 1 \dots n_{03} + 1 \dots; k, p] \right. \\
& + (n_{00} + 1) \mathcal{P}[\dots n_{30} - 1 \dots; k, p] \\
& + (n_{30} + 1) \mathcal{P}[\dots n_{30} + 1 \dots; k, p] \\
& + (n_{33} + 1) \mathcal{P}[\dots n_{33} + 1 \dots n_{03} - 1 \dots; k, p] \\
& - (n_{30} + 1) \mathcal{P}[\dots n_{33} - 1, n_{30} + 1 \dots; k, p] \\
& - (n_{00} + 1) \mathcal{P}[\dots n_{03} - 1 \dots; k, p] \\
& - (n_{03} + 1) \mathcal{P}[\dots n_{03} + 1 \dots; k, p] \\
& \left. - (n_{33} + 1) \mathcal{P}[\dots n_{33} + 1, n_{30} - 1 \dots; k, p] \right].
\end{aligned} \tag{D.2.6}$$

cf. Fig. 5.9. The three dissipator contributions are

$$\begin{aligned}
& \partial_t \mathcal{P}[n_{33}, n_{30}, n_{22}, n_{21}, n_{12}, n_{11}, n_{03}; k, p] \Big|_{\mathcal{D}[\sigma_{23}^k]} \\
= & \frac{\gamma_{23}}{2} \left[ 2(n_{33} + 1) \mathcal{P}[n_{33} + 1 \dots n_{22} - 1 \dots; k, p] \right. \\
& \left. - (2n_{33} + n_{03} + n_{30}) \mathcal{P}[\dots; k, p] \right],
\end{aligned} \tag{D.2.7}$$

$$\begin{aligned}
& \partial_t \mathcal{P}[n_{33}, n_{30}, n_{22}, n_{21}, n_{12}, n_{11}, n_{03}; k, p] \Big|_{\mathcal{D}[\sigma_{12}^k]} \\
= & \frac{\gamma_{12}}{2} \left[ 2(n_{22} + 1) \mathcal{P}[\dots n_{22} + 1 \dots n_{11} - 1 \dots; k, p] \right. \\
& \left. - (2n_{22} + n_{12} + n_{21}) \mathcal{P}[\dots; k, p] \right],
\end{aligned} \tag{D.2.8}$$

and

$$\begin{aligned}
& \partial_t \mathcal{P}[n_{33}, n_{30}, n_{22}, n_{21}, n_{12}, n_{11}, n_{03}; k, p] \Big|_{\mathcal{D}[\sigma_{01}^k]} \\
= & \frac{\gamma_{01}}{2} \left[ 2(n_{11} + 1) \mathcal{P}[\dots n_{11} + 1 \dots; k, p] \right. \\
& \left. - (2n_{11} + n_{12} + n_{21}) \mathcal{P}[\dots; k, p] \right].
\end{aligned} \tag{D.2.9}$$

The equations of motion for (5.4.30)

$$\begin{aligned}
\dot{\rho}_{IV} &= \frac{i}{\hbar} [\rho_{IV}, H_{21}] + \mathcal{D}[\sigma_{30}^k] \rho_{IV} + \mathcal{D}[\sigma_{23}^k] \rho_{IV} \\
&\quad + \mathcal{D}[\sigma_{01}^k] \rho_{IV} + \mathcal{D}[\sigma_{12}^k] \rho_{IV},
\end{aligned} \tag{D.2.10}$$

are given in terms of the elements

$$\mathcal{P}[n_{33}, n_{22}, n_{21}, n_{12}, n_{11}; k, p], \tag{D.2.11}$$

cf. Fig. 5.10. The  $H_{21}^{\text{RWA}}$ ,  $\mathcal{D}[\sigma_{12}^k]$ , and  $\mathcal{D}[\sigma_{01}^k]$  do not change. The pumping dissipator contribution is given by

$$\begin{aligned}
& \partial_t \mathcal{P}[n_{33}, n_{22}, n_{21}, n_{12}, n_{11}; k, p] \Big|_{\mathcal{D}[\sigma_{30}^k]} \\
= & \frac{\gamma_{30}}{2} \left[ 2(n_{00} + 1) \mathcal{P}[n_{33} - 1 \dots; k, p] \right. \\
& \left. - 2n_{00} \mathcal{P}[\dots; k, p] \right],
\end{aligned} \tag{D.2.12}$$

and the  $\mathcal{D}[\sigma_{23}^k]$  contribution changes slightly since we can neglect the coherences  $n_{03}$  and  $n_{30}$ .

$$\begin{aligned}
& \partial_t \mathcal{P}[n_{33}, n_{22}, n_{21}, n_{12}, n_{11}; k, p] \Big|_{\mathcal{D}[\sigma_{23}^k]} \\
= & \frac{\gamma_{23}}{2} [2(n_{33} + 1)\mathcal{P}[n_{33} + 1 \dots n_{22} - 1 \dots; k, p] \\
& - 2n_{33}\mathcal{P}[\dots; k, p]],
\end{aligned} \tag{D.2.13}$$

## **E** Possible Dissipators

Consider a general  $n$ -level systems with basis states  $|0\rangle_i, |1\rangle_i, \dots, |n\rangle_i$ , ordered in ascending energy eigenvalues. The spontaneous emission Liouvillian between level  $l$  and  $k$  (with  $l > k$  ensuring that it is a spontaneous emission process) is given by

$$\mathcal{D}[\sigma_{kl}^j] = \frac{\gamma_{kl}}{2} \sum_i (2\sigma_{kl}\rho\sigma_{lk} - \sigma_{kl}\sigma_{lk}\rho - \rho\sigma_{kl}\sigma_{lk}). \quad (\text{E.0.1})$$

Backwards, the incoherent driving Liouvillian between level  $l$  and level  $k$  (again with  $l > k$ ) is

$$\mathcal{D}[\sigma_{lk}^j] = \frac{\gamma_{lk}}{2} \sum_i (2\sigma_{lk}\rho\sigma_{kl} - \sigma_{lk}\sigma_{kl}\rho - \rho\sigma_{lk}\sigma_{kl}). \quad (\text{E.0.2})$$

Collective spontaneous emission contributions can be constructed with

$$\mathcal{D}[J_{kl}] = \frac{\Gamma_{kl}}{2} (J_{kl}\rho J_{lk} - J_{lk}J_{kl}\rho - \rho J_{lk}J_{kl}). \quad (\text{E.0.3})$$

Pure dephasing contributions between individual levels are modeled by

$$\mathcal{D}[\sigma_z^{lk}] = \gamma_z^{lk} \sum_i (\sigma_z^{lk} \rho \sigma_z^{lk} - \rho), \quad (\text{E.0.4})$$

where  $\sigma_z^{lk} = \sigma_{ll} - \sigma_{kk}$  is the inversion operator between level  $l$  and  $k$  ( $l > k$ ).



## Bibliography

- [1] Edwin T Jaynes and Frederick W Cummings. Comparison of quantum and semiclassical radiation theories with application to the beam maser. *Proc. IEEE*, 51:89, 1963.
- [2] Roy J Glauber. Coherent and incoherent states of the radiation field. *Phys. Rev.*, 131:2766, 1963.
- [3] FT Arecchi, Eric Courtens, Robert Gilmore, and Harry Thomas. Atomic coherent states in quantum optics. *Phys. Rev. A*, 6:2211, 1972.
- [4] H. J. Carmichael. *Statistical Methods in Quantum Optics I: Master Equations and Fokker-Planck Equations*. Springer, 2002.
- [5] Maximilian Schlosshauer. *Decoherence and the quantum-to-classical transition*. Springer, 2007.
- [6] Howard J Carmichael. *Statistical Methods in Quantum Optics 2: Non-Classical Fields*. Springer, 2009.
- [7] Steven R White. Density matrix formulation for quantum renormalization groups. *Phys. Rev. Lett.*, 69:2863, 1992.
- [8] Michael L Wall, Arghavan Safavi-Naini, and Ana Maria Rey. Simulating generic spin-boson models with matrix product states. *Phys. Rev. A*, 94:053637, 2016.
- [9] M. Kira and S. W. Koch. *Semiconductor quantum optics*. Cambridge University Press, Cambridge, 2012.
- [10] Harry J Lipkin, N Meshkov, and AJ Glick. Validity of many-body approximation methods for a solvable model:(i). exact solutions and perturbation theory. *Nucl. Phys.*, 62:188, 1965.

- 
- [11] J.J. Sakurai. *Modern Quantum Mechanics*. Addison-Wesley, 1994.
- [12] Michael Tavis and Frederick W Cummings. Exact solution for an n-molecule–radiation-field hamiltonian. *Phys. Rev.*, 170:379, 1968.
- [13] Heinz-Peter Breuer and Francesco Petruccione. *The theory of open quantum systems*. Oxford, 2002.
- [14] HJ Carmichael, JS Satchell, and Sarben Sarkar. Nonlinear analysis of quantum fluctuations in absorptive optical bistability. *Phys. Rev. A*, 34:3166, 1986.
- [15] M. O. Scully and M. S. Zubairy. *Quantum optics*. Cambridge, 1997.
- [16] H. A. M. Leymann, A. Foerster, F. Jahnke, J. Wiersig, and C. Gies. Sub- and superradiance in nanolasers. *Phys. Rev. Applied*, 4:044018, 2015.
- [17] Marten Richter, Michael Gegg, T. Sverre Theuerholz, and Andreas Knorr. Numerically exact solution of the many emitter–cavity laser problem: Application to the fully quantized spaser emission. *Phys. Rev. B*, 91:035306, 2015.
- [18] Y. K. Wang and F. T. Hioe. Phase transition in the dicke model of superradiance. *Phys. Rev. A*, 7:831, 1973.
- [19] D. F. Walls, P. D. Drummond, S. S. Hassan, and H. J. Carmichael. Non-equilibrium phase transitions in cooperative atomic systems. *Suppl. Prog. Theor. Phys.*, 64:307, 1978.
- [20] Michael Gegg, Alexander Carmele, Andreas Knorr, and Marten Richter. Superradiant to subradiant phase transition in the open system dicke model: Dark state cascades. *arXiv:1705.02889*, 2017.
- [21] R Bonifacio and LA Lugiato. Cooperative effects and bistability for resonance fluorescence. *Optics Communications*, 19:172, 1976.
- [22] Alejandro González-Tudela and Diego Porras. Mesoscopic entanglement induced by spontaneous emission in solid-state quantum optics. *Phys. Rev. Lett.*, 110:080502, 2013.
- [23] H. J. Carmichael. Analytical and numerical results for the steady state in cooperative resonance fluorescence. *J. Phys. B: At. Mol. Phys.*, 13:3551, 1980.
- [24] Sven M Hein, Franz Schulze, Alexander Carmele, and Andreas Knorr. Optical feedback-enhanced photon entanglement from a biexciton cascade. *Phys. Rev. Lett.*, 113:027401, 2014.
- [25] R. H. Dicke. Coherence in spontaneous radiation processes. *Phys. Rev.*, 93:99–110, 1954.
- [26] M. Gegg and M. Richter. PsiQuaSP – Permutation symmetry for identical Quantum Systems Package. <https://github.com/modmido/psiquasp>.
- [27] Michael Gegg and Marten Richter. Psiquasp – a library for efficient computation of symmetric open quantum systems. *arXiv:1707.01079*, 2017.
- [28] L. Mandel and E. Wolf. *Optical coherence and quantum optics*. Cambridge, 1995.
- [29] J Drenth Moras, B Strandberg, D Suc, and K Wilson. Semiconductor clusters, nanocrystals, and quantum dots. *Science*, 271:933, 1996.

- [30] Christian Kurtsiefer, Sonja Mayer, Patrick Zarda, and Harald Weinfurter. Stable solid-state source of single photons. *Phys. Rev. Lett.*, 85:290, 2000.
- [31] MV Gurudev Dutt, L Childress, L Jiang, E Togan, J Maze, F Jelezko, AS Zibrov, PR Hemmer, and MD Lukin. Quantum register based on individual electronic and nuclear spin qubits in diamond. *Science*, 316(5829), 2007.
- [32] Daniel F Walls and Gerard J Milburn. *Quantum optics*. Springer, 2007.
- [33] K. Bergmann, H. Theuer, and B. W. Shore. Coherent population transfer among quantum states of atoms and molecules. *Rev. Mod. Phys.*, 70:1003, 1998.
- [34] Oliver Benson, Charles Santori, Matthew Pelton, and Yoshihisa Yamamoto. Regulated and entangled photons from a single quantum dot. *Phys. Rev. Lett.*, 84:2513, 2000.
- [35] Ian Affleck and FDM Haldane. Critical theory of quantum spin chains. *Phys. Rev. B*, 36:5291, 1987.
- [36] Juan P Dehollain, Stephanie Simmons, Juha T Muhonen, Rachpon Kalra, Arne Laucht, Fay Hudson, Kohei M Itoh, David N Jamieson, Jeffrey C McCallum, Andrew S Dzurak, et al. Bell's inequality violation with spins in silicon. *Nature nanotechnology*, 2015.
- [37] Alloyed quantum dots. <http://www.sigmaaldrich.com/technical-documents/articles/materials-science/nanomaterials/quantum-dots.html>. Accessed: 2017-04-28.
- [38] Lachlan J. Rogers, Kay D. Jahnke, Mathias H. Metsch, Alp Sipahigil, Jan M. Binder, Tokuyuki Teraji, Hitoshi Sumiya, Junichi Isoya, Mikhail D. Lukin, Philip Hemmer, and Fedor Jelezko. All-optical initialization, readout, and coherent preparation of single silicon-vacancy spins in diamond. *Phys. Rev. Lett.*, 113:263602, 2014.
- [39] MA Noginov, G Zhu, AM Belgrave, Reuben Bakker, VM Shalaev, EE Narimanov, S Stout, E Herz, T Suteewong, and U Wiesner. Demonstration of a spaser-based nanolaser. *Nature*, 460:1110, 2009.
- [40] Oregon green. <https://www.thermofisher.com/order/catalog/product/010241>. Accessed: 2017-04-28.
- [41] Electron spins in solids. <http://www.quantuminfo.physik.rwth-aachen.de/cms/Quantuminfo/Forschung/Institut-fuer-Quantentechnologie/~eyea/Bluhm-SiGe/?lidx=1>. Accessed: 2017-04-28.
- [42] Walter Pfeifer. *The Lie Algebras  $su(N)$  – An introduction*. Birkhäuser, 2003.
- [43] Barry M Garraway. The dicke model in quantum optics: Dicke model revisited. *Philos Trans A Math Phys Eng Sci*, 369:1137–1155, 2011.
- [44] Allan W Snyder and John Love. *Optical waveguide theory*. Springer Science & Business Media, 2012.
- [45] S. A. Maier. *Plasmonics – fundamentals and applications*. Springer, 2007.
- [46] MS Tame, KR McEnery, SK Özdemir, J Lee, SA Maier, and MS Kim. Quantum plasmonics. *Nature Physics*, 9:329–340, 2013.

- [47] Jacob B Khurgin and Greg Sun. Landau damping – the ultimate limit of field confinement and enhancement in plasmonic structures. In *Quantum Plasmonics*, pages 303–322. Springer International Publishing, 2017.
- [48] WE Lamb. Anti-photon. *Appl. Phys. B*, 60(2), 1995.
- [49] Albert Einstein. Über einen die erzeugung und verwandlung des liches betreffenden heuristischen gesichtspunkt. *Annalen der physik*, 322:132, 1905.
- [50] S Reitzenstein, C Hofmann, A Gorbunov, M Strauß, SH Kwon, C Schneider, A Löffler, S Höfling, M Kamp, and A Forchel. Al as/ ga as micropillar cavities with quality factors exceeding 150.000. *Appl. Phys. Lett.*, 90:251109, 2007.
- [51] John D Joannopoulos, Steven G Johnson, Joshua N Winn, and Robert D Meade. *Photonic crystals: molding the flow of light*. Princeton, 2011.
- [52] K Lance Kelly, Eduardo Coronado, Lin Lin Zhao, and George C Schatz. The optical properties of metal nanoparticles: The influence of size, shape, and dielectric environment. *J. Phys. Chem. B*, 107:668, 2003.
- [53] David Schurig, JJ Mock, BJ Justice, Steven A Cummer, John B Pendry, AF Starr, and DR Smith. Metamaterial electromagnetic cloak at microwave frequencies. *Science*, 314:977, 2006.
- [54] Gerd Czycholl. *Theoretische Festkörperphysik*. Springer, 2008.
- [55] A Ridolfo, O Di Stefano, N Fina, R Saija, and S Savasta. Quantum plasmonics with quantum dot-metal nanoparticle molecules: influence of the fano effect on photon statistics. *Phys. Rev. Lett.*, 105(26):263601, 2010.
- [56] T Sverre Theuerholz, Alexander Carmele, Marten Richter, and Andreas Knorr. Influence of förster interaction on light emission statistics in hybrid systems. *Phys. Rev. B*, 87:245313, 2013.
- [57] Michael Gegg. Interaction of  $N$  two-level systems with a metal-nanoparticle. *Masterthesis (unpublished)*, 2014.
- [58] Peter B Johnson and R-W Christy. Optical constants of the noble metals. *Phys. Rev. B*, 6:4370, 1972.
- [59] David J Bergman and Mark I Stockman. Surface plasmon amplification by stimulated emission of radiation: quantum generation of coherent surface plasmons in nanosystems. *Phys. Rev. Lett.*, 90:027402, 2003.
- [60] Mark I Stockman. Spaser action, loss compensation, and stability in plasmonic systems with gain. *Phys. Rev. Lett.*, 106:156802, 2011.
- [61] Ho Trung Dung, Ludwig Knöll, and Dirk-Gunnar Welsch. Spontaneous decay in the presence of dispersing and absorbing bodies: General theory and application to a spherical cavity. *Phys. Rev. A*, 62:053804, 2000.
- [62] Ho Trung Dung, Stefan Yoshi Buhmann, Ludwig Knöll, Dirk-Gunnar Welsch, Stefan Scheel, and Jürgen Kästel. Electromagnetic-field quantization and spontaneous decay in left-handed media. *Phys. Rev. A*, 68:043816, 2003.

- 
- [63] L. D. Landau, J.S. Bell, M.J. Kearsley, L.P. Pitaevskii, E.M. Lifshitz, and J.B. Sykes. *Electrodynamics of continuous media*, volume 8. Elsevier, 2013.
- [64] Le-Wei Li, Pang-Shyan Kooi, Mook-Seng Leong, and Tat-Soon Yee. Electromagnetic dyadic green's function in spherically multilayered media. *IEEE Transactions on Microwave Theory and Techniques*, 42:2302, 1994.
- [65] Le-Wei Li, Pang-Shyan Kooi, Mook-Seng Leong, and Tat-Soon Yeo. On the eigenfunction expansion of dyadic green's function in planarly stratified media. *J. Electrom. Waves Appl.*, 8:663, 1994.
- [66] Personal discussions with Kurt Busch, Marten Richter and Andreas Knorr.
- [67] Personal discussions with Sebastian Franke.
- [68] U. Fano. Description of states in quantum mechanics by density matrix and operator techniques. *Rev. Mod. Phys.*, 29:74, 1957.
- [69] Angel Rivas and Susana F Huelga. *Open Quantum Systems*. Springer, 2012.
- [70] Goran Lindblad. On the generators of quantum dynamical semigroups. *Comm. Math. Phys.*, 48:119–130, 1976.
- [71] V. V. Albert and L. Jiang. Symmetries and conserved quantities in lindblad master equations. *Phys. Rev. A*, 89:022118, 2014.
- [72] SG Schirmer and Xiaoting Wang. Stabilizing open quantum systems by markovian reservoir engineering. *Phys. Rev. A*, 81:062306, 2010.
- [73] E. M. Kessler, G. Giedke, A. Imamoglu, S. F. Yelin, M. D. Lukin, and J. I. Cirac. Dissipative phase transition in a central spin system. *Phys. Rev. A*, 86:012116, 2012.
- [74] Hermann Haken. *Laser theory*. Springer, 2012.
- [75] N Skribanowitz, IP Herman, JC MacGillivray, and MS Feld. Observation of dicke superradiance in optically pumped hf gas. *Phys. Rev. Lett.*, 30:309, 1973.
- [76] Michel Gross and Serge Haroche. Superradiance: An essay on the theory of collective spontaneous emission. *Phys. Rep.*, 93:301, 1982.
- [77] Michael Scheibner, Thomas Schmidt, Lukas Worschech, Alfred Forchel, Gerd Bacher, Thorsten Passow, and Detlef Hommel. Superradiance of quantum dots. *Nat. Phys.*, 3:106, 2007.
- [78] Kankan Cong, Qi Zhang, Yongrui Wang, G Timothy Noe, Alexey Belyanin, and Junichiro Kono. Dicke superradiance in solids. *JOSA B*, 33:C80–C101, 2016.
- [79] Géza Tóth, Christian Knapp, Otfried Gühne, and Hans J. Briegel. Optimal spin squeezing inequalities detect bound entanglement in spin models. *Phys. Rev. Lett.*, 99:250405, 2007.
- [80] Géza Tóth, Christian Knapp, Otfried Gühne, and Hans J. Briegel. Spin squeezing and entanglement. *Phys. Rev. A*, 79:042334, 2009.
- [81] Ryszard Horodecki, Paweł Horodecki, Michał Horodecki, and Karol Horodecki. Quantum entanglement. *Rev. Mod. Phys.*, 81:865, 2009.

- [82] Philipp Hyllus, Wiesław Laskowski, Roland Krischek, Christian Schwemmer, Witlef Wieczorek, Harald Weinfurter, Luca Pezzé, and Augusto Smerzi. Fisher information and multiparticle entanglement. *Phys. Rev. A*, 85:022321, 2012.
- [83] H Eugene Stanley. *Phase transitions and critical phenomena*. Oxford, 1971.
- [84] Perry R. Rice and H. J. Carmichael. Photon statistics of a cavity-QED laser: A comment on the laser – phase-transition analogy. *Phys. Rev. A*, 50(5):4318–4329, Nov 1994.
- [85] Clive Emary and Tobias Brandes. Quantum chaos triggered by precursors of a quantum phase transition: The dicke model. *Phys. Rev. Lett.*, 90:044101, 2003.
- [86] Tony E Lee, Ching-Kit Chan, and Susanne F Yelin. Dissipative phase transitions: Independent versus collective decay and spin squeezing. *Phys. Rev. A*, 90:052109, 2014.
- [87] John Riordan. *An introduction to combinatorial analysis*. Wiley, 1958.
- [88] F. T. Arecchi, R. Gilmore, and D. M. Kim. Coherent states for  $r$ -level atoms. *LETT. NUOVO CIMENTO*, 6:219, 1973.
- [89] Mathias Hayn, Clive Emary, and Tobias Brandes. Phase transitions and dark-state physics in two-color superradiance. *Phys. Rev. A*, 84:053856, 2011.
- [90] T Holstein and Hl Primakoff. Field dependence of the intrinsic domain magnetization of a ferromagnet. *Phys. Rev.*, 58:1098, 1940.
- [91] Abraham Klein and E. R. Marshalek. Boson realizations of lie algebras with applications to nuclear physics. *Rev. Mod. Phys.*, 63:375, 1991.
- [92] MD Towler. Quantum monte carlo, or, how to solve the many-particle schrödinger equation accurately whilst retaining favourable scaling with system size. *Computational Methods for Large Systems: Electronic Structure Approaches for Biotechnology and Nanotechnology*, 2011.
- [93] Roger Temam. *Navier-stokes equations*, volume 2. North-Holland Amsterdam, 1984.
- [94] Jochen Gemmer, Mathias Michel, and Günter Mahler. In *Quantum Thermodynamics*. Springer, 2004.
- [95] Piet Brouwer. Lecture notes on theoretical solid state physics, 2013.
- [96] S. Sarkar and J. S. Satchell. Solution of master equations for small bistable systems. *Journal of Physics A: Mathematical and General*, 20:2147, 1987.
- [97] S. Sarkar and J. S. Satchell. Optical bistability with small numbers of atoms. *Europhys. Lett.*, 3:797, 1987.
- [98] Bradley A Chase and JM Geremia. Collective processes of an ensemble of spin-1/ 2 particles. *Phys. Rev. A*, 78:052101, 2008.
- [99] Ben Q Baragiola, Bradley A Chase, and JM Geremia. Collective uncertainty in partially polarized and partially decohered spin-1 2 systems. *Phys. Rev. A*, 81:032104, 2010.
- [100] Stephan Hartmann. Generalized dicke states. *arXiv*, 1201.1732v1, 2012.

- 
- [101] Michael Gegg and Marten Richter. Efficient and exact numerical approach for many multi-level systems in open system CQED. *New J. Phys.*, 18:043037, 2016.
- [102] Peter Kirton and Jonathan Keeling. Suppressing and restoring the dicke superradiance transition by dephasing and decay. *Phys. Rev. Lett.*, 118:123602, 2017.
- [103] D. Pagel, A. Alvermann, and H. Fehske. Nonclassical light from few emitters in a cavity. *Phys. Rev. A*, 91:043814, 2015.
- [104] PD Drummond and CW Gardiner. Generalised p-representations in quantum optics. *J. Phys. A*, 13:2353, 1980.
- [105] Pierre Nataf and Cristiano Ciuti. Is there a no-go theorem for superradiant quantum phase transitions in cavity and circuit qed? *arXiv preprint arXiv:1006.1801*, 2010.
- [106] Ricardo Puebla, Myung-Joong Hwang, Jorge Casanova, and Martin B. Plenio. Probing the dynamics of a superradiant quantum phase transition with a single trapped ion. *Phys. Rev. Lett.*, 118:073001, 2017.
- [107] Stephan Hartmann. Generalized Dicke States. *Quantum Inf. Comput.*, 16:1333, 2016.
- [108] GM D'Ariano, L Maccone, and M Painsi. Spin tomography. *J. Opt. B*, 5:77, 2003.
- [109] Géza Tóth, Witlef Wieczorek, David Gross, Roland Krischek, Christian Schwemmer, and Harald Weinfurter. Permutationally invariant quantum tomography. *Phys. Rev. Lett.*, 105:250403, 2010.
- [110] Minghui Xu, D. A. Tieri, and M. J. Holland. Simulating open quantum systems by applying  $\text{su}(4)$  to quantum master equations. *Phys. Rev. A*, 87:062101, 2013.
- [111] Minghui Xu and M. J. Holland. Conditional ramsey spectroscopy with synchronized atoms. *Phys. Rev. Lett.*, 114:103601, 2015.
- [112] Yuan Zhang and Volkhard May. Theory of molecule metal nano-particle interaction: Quantum description of plasmonic lasing. *J. Chem. Phys.*, 142:224702, 2015.
- [113] Nathan Shammah, Neill Lambert, Franco Nori, and Simone De Liberato. Superradiance with local phase-breaking effects. *arXiv:1704.07066*, 2017.
- [114] Birgit Krummheuer, Vollrath Martin Axt, and Tilmann Kuhn. Theory of pure dephasing and the resulting absorption line shape in semiconductor quantum dots. *Phys. Rev. B*, 65:195313, 2002.
- [115] Hermann Haken. *Laser Theory*. Springer, 1984.
- [116] Timur V. Tscherbul and Paul Brumer. Long-lived quasistationary coherences in a  $v$ -type system driven by incoherent light. *Phys. Rev. Lett.*, 113:113601, 2014.
- [117] Marlan O. Scully, Kimberly R. Chapin, Konstantin E. Dorfman, Moochan Barnabas Kim, and Anatoly Svidzinsky. Quantum heat engine power can be increased by noise-induced coherence. *Proc. Natl. Acad. Sci. USA*, 108:15097, 2011.
- [118] Michael Fleischhauer, Atac Imamoglu, and Jonathan P. Marangos. Electromagnetically induced transparency: Optics in coherent media. *Rev. Mod. Phys.*, 77:633, 2005.

- [119] Mete Atatüre, Jan Dreiser, Antonio Badolato, Alexander Högele, Khaled Karrai, and Atac Imamoglu. Quantum-dot spin-state preparation with near-unity fidelity. *Science*, 312:551, 2006.
- [120] Sandra C. Kuhn and Marten Richter. Hybrid density matrix approach as a factorization scheme for many-body systems: Illustrated by a quantum dot–continuum system. *Phys. Rev. B*, 91:155309, 2015.
- [121] Judith F. Specht, Andreas Knorr, and Marten Richter. Two-dimensional spectroscopy: An approach to distinguish förster and dexter transfer processes in coupled nanostructures. *Phys. Rev. B*, 91:155313, 2015.
- [122] K. Roszak, A. Grodecka, P. Machnikowski, and T. Kuhn. Phonon-induced decoherence for a quantum-dot spin qubit operated by raman passage. *Phys. Rev. B*, 71:195333, 2005.
- [123] A. Grodecka, P. Machnikowski, and J. Förstner. Phonon-assisted tunneling between singlet states in two-electron quantum dot molecules. *Phys. Rev. B*, 78:085302, 2008.
- [124] Weng W. Chow, Frank Jahnke, and Christopher Gies. Emission properties of nanolasers during the transition to lasing. *Light Sci. Appl.*, 3:e201, 2014.
- [125] Marduk Bolaños and Pablo Barberis-Blostein. Algebraic solution of the lindblad equation for a collection of multilevel systems coupled to independent environments. *Journal of Physics A: Mathematical and Theoretical*, 48:445301, 2015.
- [126] Upendra Harbola and Shaul Mukamel. Superoperator nonequilibrium green’s function theory of many-body systems; applications to charge transfer and transport in open junctions. *Phys. Rep.*, 465:191, 2008.
- [127] Dimitri van Heesch. Doxygen. <http://www.stack.nl/~dimitri/doxygen/>.
- [128] Satish Balay, Shrirang Abhyankar, Mark F. Adams, Jed Brown, Peter Brune, Kris Buschelman, Lisandro Dalcin, Victor Eijkhout, William D. Gropp, Dinesh Kaushik, Matthew G. Knepley, Lois Curfman McInnes, Karl Rupp, Barry F. Smith, Stefano Zampini, Hong Zhang, and Hong Zhang. PETSc Web page. <http://www.mcs.anl.gov/petsc>, 2017.
- [129] Satish Balay, Shrirang Abhyankar, Mark F. Adams, Jed Brown, Peter Brune, Kris Buschelman, Lisandro Dalcin, Victor Eijkhout, William D. Gropp, Dinesh Kaushik, Matthew G. Knepley, Lois Curfman McInnes, Karl Rupp, Barry F. Smith, Stefano Zampini, Hong Zhang, and Hong Zhang. PETSc users manual. Technical Report ANL-95/11 - Revision 3.7, Argonne National Laboratory, 2016.
- [130] Satish Balay, William D. Gropp, Lois Curfman McInnes, and Barry F. Smith. Efficient management of parallelism in object oriented numerical software libraries. In E. Arge, A. M. Bruaset, and H. P. Langtangen, editors, *Modern Software Tools in Scientific Computing*, pages 163–202. Birkhäuser Press, 1997.
- [131] V. Hernandez, J. E. Roman, and V. Vidal. SLEPc: Scalable Library for Eigenvalue Problem Computations. *Lect. Notes Comput. Sci.*, 2565:377–391, 2003.
- [132] Vicente Hernandez, Jose E. Roman, and Vicente Vidal. SLEPc: A scalable and flexible toolkit for the solution of eigenvalue problems. *ACM Trans. Math. Software*, 31(3):351–362, 2005.

- [133] J. E. Roman, C. Campos, E. Romero, and A. Tomas. SLEPc users manual. Technical Report DSIC-II/24/02 - Revision 3.7, D. Sistemes Informàtics i Computació, Universitat Politècnica de València, 2016.
- [134] Emmanuel Agullo, Patrick Amestoy, Maurice Bremond, Alfredo Buttari, Philippe Combes, Marie Durand, Aurélia Fevre, Abdou Guermouche, Guillaume Joslin, Jacko Koster, Jean-Yves L'Excellent, Stéphane Pralet, Chiara Puglisi, Francois-Henry Rouet, Wissam Sid-Lakhdar, Tzvetomila Slavova, Bora Ucar, and Clément Weisbecker. MUMPS: aMUlti-frontal Massively Parallel sparse direct Solver. <http://mumps.enseeiht.fr/index.php?page=credits>.
- [135] Xiaoye S. Li. An overview of SuperLU: Algorithms, implementation, and user interface. *ACM Trans.Math. Softw.*, 31:302, 2005.
- [136] George Karypis and et. al. ParMETIS - Parallel Graph Partitioning and Fill-reducing Matrix Ordering. <http://glaros.dtc.umn.edu/gkhome/metis/parmetis/overview>.
- [137] Cédric Chevalier and François Pellegrini. Pt-scotch: A tool for efficient parallel graph ordering. *Parallel Comput.*, 34(6):318–331, 2008.
- [138] Francois Pellegrini and et. al. SCOTCH and PT-SCOTCH. <http://www.labri.fr/perso/pelegrin/scotch/>.
- [139] R Tanaś and Z Ficek. Entangling two atoms via spontaneous emission. *J. Opt. B Quantum Semiclassical Opt.*, 6:S90, 2004.
- [140] Shaul Mukamel. *Principles of Nonlinear Optical Spectroscopy*. Oxford, 1995.
- [141] Julia Kabuss, Alexander Carmele, Tobias Brandes, and Andreas Knorr. Optically driven quantum dots as source of coherent cavity phonons: a proposal for a phonon laser scheme. *Phys. Rev. Lett.*, 109:054301, 2012.
- [142] Leon Droenner, Nicolas L. Naumann, Julia Kabuss, and Alexander Carmele. Collective enhancements in many-emitter phonon lasing. *arXiv:1706.07777*, 2017.
- [143] Yousef Saad. *Iterative methods for sparse linear systems*. SIAM, 2003.
- [144] Tommy Markstein. Helium-neon laser in betrieb. <https://de.wikipedia.org/wiki/Helium-Neon-Laser#/media/File:Henelaser.jpg>.
- [145] Stewart Wills. Micropillar + quantum dot = single-photon source. [https://www.osa-opn.org/home/newsroom/2016/january/micropillar\\_quantum\\_dot\\_single-photon\\_source/](https://www.osa-opn.org/home/newsroom/2016/january/micropillar_quantum_dot_single-photon_source/).
- [146] Olga Kocharovskaya. Amplification and lasing without inversion. *Phys. Rep.*, 219:175, 1992.
- [147] Paul Gartner. Two-level laser: Analytical results and the laser transition. *Phys. Rev. A*, 84:053804, 2011.
- [148] Mark Fox. *Quantum optics: an introduction*, volume 15. OUP Oxford, 2006.
- [149] DA Tieri, Minghui Xu, D Meiser, J Cooper, and MJ Holland. Theory of the crossover from lasing to steady state superradiance. *arXiv:1702.04830*, 2017.

- [150] Frank Jahnke, Christopher Gies, Marc Aßmann, Manfred Bayer, HAM Leymann, Alexander Foerster, Jan Wiersig, Christian Schneider, Martin Kamp, and Sven Höfling. Giant photon bunching, superradiant pulse emission and excitation trapping in quantum-dot nanolasers. *Nature communications*, 7, 2016.
- [151] Michael Gegg, T Sverre Theuerholz, Andreas Knorr, and Marten Richter. Fully quantized spaser physics: towards exact modeling of mesoscopic cqed systems. In *SPIE OPTO*, pages 93610Z–93610Z. International Society for Optics and Photonics, 2015.
- [152] Personal discussions with Günther Kewes and Andreas Ott at various SFB 951 events.
- [153] Günther Kewes, Kathrin Herrmann, Rogelio Rodríguez-Oliveros, Alexander Kuhlicke, Oliver Benson, and Kurt Busch. Limitations of particle-based spasers. *Phys. Rev. Lett.*, 118(23):237402, 2017.
- [154] Personal discussion with Alexander Govorov at the Plasmonics Workshop "Quantum Theory of Nanoparticle Plasmons: Methodological Aspects" 2016, Berlin.
- [155] H. Fröhlich. *Theory of dielectrics: dielectric constant and dielectric loss*. Oxford, 1949.
- [156] Yuan Zhang, Klaus Mølmer, and Volkhard May. Theoretical study of plasmonic lasing in junctions with many molecules. *Phys. Rev. B*, 94:045412, 2016.
- [157] Yuan Zhang and Klaus Mølmer. Analysis of a multi-mode plasmonic nano-laser with an inhomogeneous distribution of molecular emitters. *The Journal of Physical Chemistry C*, 2017.
- [158] P. D. Drummond and D. F. Walls. Quantum theory of optical bistability. II. Atomic fluorescence in a high-Q cavity. *Phys. Rev. A*, 23:2563, 1981.
- [159] S.S. Hassan, R.K. Bullough, R.R. Puri, and S.V. Lawande. Intensity fluctuations in a driven dicke model. *Phys. A*, 103:213, 1980.
- [160] S V Lawande, R R Puri, and S S Hassan. Non-resonant effects in the fluorescent Dicke model. I. Exact steady state analysis. *J. Phys. B*, 14:4171, 1981.
- [161] S. Schneider and G. J. Milburn. Entanglement in the steady state of a collective-angular-momentum (dicke) model. *Phys. Rev. A*, 65:042107, 2002.
- [162] L. Schneebeli, M. Kira, and S. W. Koch. Characterization of strong light-matter coupling in semiconductor quantum-dot microcavities via photon-statistics spectroscopy. *Phys. Rev. Lett.*, 101:097401, 2008.
- [163] Tony E. Lee, H. Häffner, and M. C. Cross. Collective quantum jumps of rydberg atoms. *Phys. Rev. Lett.*, 108:023602, 2012.
- [164] Yumian Su, Dieter Bimberg, Andreas Knorr, and Alexander Carmele. Collective light emission revisited: Reservoir induced coherence. *Phys. Rev. Lett.*, 110:113604, 2013.
- [165] C. Carr, R. Ritter, C. G. Wade, C. S. Adams, and K. J. Weatherill. Nonequilibrium phase transition in a dilute rydberg ensemble. *Phys. Rev. Lett.*, 111:113901, 2013.
- [166] Sam Genway, Weibin Li, Cenap Ates, Benjamin P. Lanyon, and Igor Lesanovsky. Generalized dicke nonequilibrium dynamics in trapped ions. *Phys. Rev. Lett.*, 112:023603, 2014.

- [167] L. J. Zou, D. Marcos, S. Diehl, S. Putz, J. Schmiedmayer, J. Majer, and P. Rabl. Implementation of the dicke lattice model in hybrid quantum system arrays. *Phys. Rev. Lett.*, 113:023603, 2014.
- [168] Elie Wolfe and S. F. Yelin. Certifying separability in symmetric mixed states of  $n$  qubits, and superradiance. *Phys. Rev. Lett.*, 112:140402, 2014.
- [169] Marlan O. Scully. Single photon subradiance: Quantum control of spontaneous emission and ultrafast readout. *Phys. Rev. Lett.*, 115:243602, 2015.
- [170] William Guerin, Michelle O. Araújo, and Robin Kaiser. Subradiance in a large cloud of cold atoms. *Phys. Rev. Lett.*, 116:083601, 2016.
- [171] Wolfgang Dür, Guifre Vidal, and J Ignacio Cirac. Three qubits can be entangled in two inequivalent ways. *Phys. Rev. A*, 62:062314, 2000.
- [172] H Haffner, W Hansel, CF Roos, J Benhelm, M Chwalla, T Korber, UD Rapol, M Riebe, PO Schmidt, C Becher, et al. Scalable multiparticle entanglement of trapped ions. *Nature*, 438:643, 2005.
- [173] Jacob D. Bekenstein and Marcelo Schiffer. The many faces of superradiance. *Phys. Rev. D*, 58:064014, 1998.
- [174] G. Rempe, R. J. Thompson, R. J. Brecha, W. D. Lee, and H. J. Kimble. Optical bistability and photon statistics in cavity quantum electrodynamics. *Phys. Rev. Lett.*, 67:1727, 1991.
- [175] R Bonifacio and LA Lugiato. Optical bistability and cooperative effects in resonance fluorescence. *Phys. Rev. A*, 18:1129, 1978.
- [176] H. M. Gibbs. *Optical Bistability: Controlling light with light*. Academic Press, 1985.
- [177] Mehmet Fatih Yanik, Shanhui Fan, Marin Soljačić, and John D Joannopoulos. All-optical transistor action with bistable switching in a photonic crystal cross-waveguide geometry. *Opt. Lett.*, 28:2506, 2003.
- [178] Dieter Bimberg. Talk at the School of Nanophotonics Block Seminar in Graal-Müritz, 2015.
- [179] A. Schenzle and H. Brand. Dynamic behaviour of optical bistability. *Optics Communications*, 31:401, 1979.
- [180] K Vogel and H Risken. Quantum-tunneling rates and stationary solutions in dispersive optical bistability. *Phys. Rev. A*, 38:2409, 1988.
- [181] CM Savage and HJ Carmichael. Single atom optical bistability. *IEEE J. Quant. Electr.*, 24:1495, 1988.
- [182] Anthony Zee. *Quantum field theory in a nutshell*. Princeton, 2010.
- [183] SRK Rodriguez, W Casteels, F Storme, I Sagnes, L Le Gratiet, E Galopin, A Lemaitre, A Amo, C Ciuti, and J Bloch. Dynamic optical hysteresis in the quantum regime. *arXiv preprint arXiv:1608.00260*, 2016.
- [184] W Casteels, F Storme, A Le Boité, and C Ciuti. Power laws in the dynamic hysteresis of quantum nonlinear photonic resonators. *Phys. Rev. A*, 93:033824, 2016.

- [185] H. J. Carmichael. Quantum fluctuations in absorptive bistability without adiabatic elimination. *Phys. Rev. A*, 33:3262, 1986.
- [186] M. Richter, Th. Renger, G. Renger, and A. Knorr. Nonperturbative theory for the optical response to strong light of the light harvesting complex II of plants: Saturation of the fluorescence quantum yield. *J. Chem. Phys.*, 127:075105, 2007.
- [187] Dieter H. E. Gross. *Microcanonical Thermodynamics: Phase Transitions in "Small" Systems*. World Scientific, 2001.
- [188] David J Wineland, John J Bollinger, Wayne M Itano, FL Moore, and DJ Heinzen. Spin squeezing and reduced quantum noise in spectroscopy. *Phys. Rev. A*, 46:R6797, 1992.
- [189] David J Wineland, John J Bollinger, Wayne M Itano, and DJ Heinzen. Squeezed atomic states and projection noise in spectroscopy. *Phys. Rev. A*, 50:67, 1994.
- [190] Masahiro Kitagawa and Masahito Ueda. Squeezed spin states. *Phys. Rev. A*, 47:5138, 1993.
- [191] D. Dylewsky, J. K. Freericks, M. L. Wall, A. M. Rey, and M. Foss-Feig. Nonperturbative calculation of phonon effects on spin squeezing. *Phys. Rev. A*, 93:013415, 2016.
- [192] G. S. Agarwal. Quantum statistical theories of spontaneous emission and their relation to other approaches. *Springer Tr. Mod. Phys.*, 74:25–38, 1974.
- [193] Jonathan D Pritchard, D Maxwell, Alexandre Gauguet, Kevin J Weatherill, MPA Jones, and Charles S Adams. Cooperative atom-light interaction in a blockaded rydberg ensemble. *Phys. Rev. Lett.*, 105:193603, 2010.
- [194] M. Saffman, T. G. Walker, and K. Mølmer. Quantum information with rydberg atoms. *Rev. Mod. Phys.*, 82:2313, 2010.
- [195] Ph. Tamarat, T. Gaebel, J. R. Rabeau, M. Khan, A. D. Greentree, H. Wilson, L. C. L. Hollenberg, S. Praver, P. Hemmer, F. Jelezko, and J. Wrachtrup. Stark shift control of single optical centers in diamond. *Phys. Rev. Lett.*, 97:083002, 2006.
- [196] P. Borri, W. Langbein, S. Schneider, U. Woggon, R. L. Sellin, D. Ouyang, and D. Bimberg. Ultralong dephasing time in ingaas quantum dots. *Phys. Rev. Lett.*, 87:157401, 2001.
- [197] Yu-Jung Lu, Jisun Kim, Hung-Ying Chen, Chihhui Wu, Nima Dabidian, Charlotte E Sanders, Chun-Yuan Wang, Ming-Yen Lu, Bo-Hong Li, Xianggang Qiu, et al. Plasmonic nanolaser using epitaxially grown silver film. *Science*, 337:450, 2012.
- [198] Yanwen Wu, Chengdong Zhang, N Mohammadi Estakhri, Yang Zhao, Jisun Kim, Matt Zhang, Xing-Xiang Liu, Greg K Pribil, Andrea Alù, Chih-Kang Shih, and Xiaoqin Li. Intrinsic optical properties and enhanced plasmonic response of epitaxial silver. *Advanced Materials*, 26:6106, 2014.
- [199] Thomas Hartsfield, Michael Gegg, Ping-Hsiang Su, Matthew R Buck, Jennifer A Hollingsworth, Chih-Kang Shih, Marten Richter, Han Htoon, and Xiaoqin Li. Semiconductor quantum dot lifetime near an atomically smooth ag film exhibits a narrow distribution. *ACS Photonics*, 3:1085, 2016.

- 
- [200] Peijun Yao, C Van Vlack, A Reza, M Patterson, MM Dignam, and Stephen Hughes. Ultrahigh purcell factors and lamb shifts in slow-light metamaterial waveguides. *Phys. Rev. B*, 80:195106, 2009.
- [201] Cole Van Vlack, Philip Trøst Kristensen, and Stephen Hughes. Spontaneous emission spectra and quantum light-matter interactions from a strongly coupled quantum dot metal-nanoparticle system. *Phys. Rev. B*, 85:075303, 2012.
- [202] Refractive index calculator. <https://refractiveindex.info/?shelf=main&book=A1203&page=Malitson-o>.
- [203] Marvin J Weber. *CRC handbook of laser science and Technology supplement 2: optical materials*, volume 8. CRC press, 1994.
- [204] John Adrian Bondy and Uppaluri Siva Ramachandra Murty. *Graph theory with applications*, volume 290. London: Macmillan, 1976.
- [205] Minghui Xu. Theory of steady-state superradiance. *PhD thesis*, 2016.
- [206] Guodong Shi, Daoyi Dong, Ian R Petersen, and Karl Henrik Johansson. Reaching a quantum consensus: master equations that generate symmetrization and synchronization. *IEEE Transactions on Automatic Control*, 61:374, 2016.
- [207] R. A. Horn and C. R. Johnson. *Topics in matrix analysis*. Cambridge, 1991.
- [208] V. Vedral, M. B. Plenio, M. A. Rippin, and P. L. Knight. Quantifying entanglement. *Phys. Rev. Lett.*, 78:2275, 1997.